From Nuclei to Compact Stars

Contents

1 Topics

The study of compact objects such as white dwarfs, neutron stars and black holes requires the interplay between nuclear and atomic physics together with relativistic field theories, e.g., general relativity, quantum electrodynamics, quantum chromodynamics, as well as particle physics. In addition to the theoretical physics aspects, the study of astrophysical scenarios characterized by the presence of at least one of the above compact object is focus of extensive research within our group, e.g. physics of pulsars. This research can be divided into the following topics:

- **Nuclear and Atomic Astrophysics**. We study the properties and processes occurring in compact stars in which nuclear and atomic physics have to be necessarily applied. We focus on the properties of nuclear matter under extreme conditions of density, pressure and temperature in the compact star interiors. The matter equation of state is studied in detail taking into account all the interactions between the constituents within a full relativistic framework.

- **White Dwarfs Physics and Structure**. The aim of this part of our research is the construction of the white dwarf structure within a self-consistent description of the equation of state of the interior together with the solution of the hydrostatic equilibrium equations in general relativity. Non-magnetized, magnetized, non-rotating and rotating white dwarfs are studied. The interaction and evolution of a central white dwarf with a surrounding disk, as occurred in the aftermath of white dwarf binary mergers, is also a subject of study.

- **White Dwarfs Astrophysics**. We are interested in the astrophysics of white dwarfs both isolated and in binaries. Magnetized white dwarfs, soft gamma repeaters, anomalous X-ray pulsars, white dwarf pulsars, cataclysmic variables, binary white dwarf mergers, and type Ia supernovae are studied. The role of a realistic white dwarf interior structure is particularly emphasized.

- **Neutron Stars Physics and Structure**. We calculate the properties of the interior structure of neutron stars using realistic models of the nuclear matter equation of state within the general relativistic equations of equilibrium. Strong, weak, electromagnetic and gravitational interactions have to be jointly taken into due account within a self-consistent fully relativistic framework. Non-magnetized, magnetized, non-rotating and rotating neutron stars are studied.

- **Neutron Stars Astrophysics**. We study astrophysical systems harboring neutron stars such as isolated and binary pulsars, low and intermediate X-ray binaries, inspiraling and merging double neutron stars. Most extreme cataclysmic events involving neutron stars and their role in the explanation of extraordinarily energetic astrophysical events such as gamma-ray bursts are analyzed in detail.

- **Radiation Mechanisms of Compact Objects**. We here study possible emission mechanisms of compact objects such as white dwarfs, neutron stars, and black holes. We are interested in the electromagnetic, neutrino and gravitational-wave emission in compact object magnetospheres, accretion disks surrounding them, as well as inspiraling and merging relativistic binaries (double neutron stars, neutron star-white dwarfs, white dwarf-white dwarf and neutron star-black holes). We also study the radiation from particle acceleration in the vicinity of stellar-mass and supermassive black holes by surrounding electromagnetic fields.

- **Exact and Numerical Solutions of the Einstein and Einstein-Maxwell Equations in Astrophysics**. We analyze the ability of analytic exact solutions of the Einstein and Einstein-Maxwell equations to describe the exterior spacetime of compact stars such as white dwarfs and neutron stars. For this we compare and contrast exact analytic with numerical solutions of the stationary axisymmetric Einstein equations. The problem of matching between interior and exterior spacetime is addressed in detail. The effect of the quadrupole moment on the properties of the spacetime is also investigated. Particular attention is given to the application of exact solutions in astrophysics, e.g. the dynamics of particles around compact stars and its relevance in astrophysical systems such as X-ray binaries and gamma-ray bursts.

- **Critical Fields and Non-linear Electrodynamics Effects in Astrophysics**. We study the conditions under which ultrastrong electromagnetic fields can develop in astrophysical systems such as neutron stars and in the process of gravitational collapse to a black hole. The effects of non-linear electrodynamics minimally coupled to gravity are investigated. New analytic and numeric solutions to the Einstein-Maxwell equations representing black holes or the exterior field of a compact star are obtained and analyzed. The consequences on extreme astrophysical systems, for instance gamma-ray bursts, are studied.

2 Participants

2.1 ICRANet

- C. L. Bianco (ICRANet, Italy)

- J. A. Rueda (ICRANet, Italy)

- L. Li (ICRANet, Italy)

- R. Moradi (ICRANet, Italy)

- R. Ruffini (ICRANet, Italy)

- N. Sahakyan (ICRANet, Armenia)

- G. Vereschagin (ICRANet, Italy)

- S.-S. Xue (ICRANet, Italy)

- Y. Wang (ICRANet, Italy)

2.2 External on going collaborations

- K. Boshkayev (Al-Farabi Kazakh National University, Kazakhstan)

- R. Camargo (Universidade do Estado de Santa Catarina, Florianópolis, Brazil)

- C. Cherubini (Università Campus Biomedico, Rome, Italy)

- J. G. Coelho (Universidade Tecnológica Federal do Paraná, Brazil)

- S. Filippi (Università Campus Biomedico, Rome, Italy)

- C. L. Fryer (University of Arizona; Los Alamos National Laboratory, USA)

- G. A. González (Universidad Industrial de Santander, Colombia)

- F. D. Lora-Clavijo (Universidad Industrial de Santander, Colombia)

- M. Malheiro (Instituto Tecnológico de Aeronáutica, Brazil)

- R. M. Jr. Marinho (Instituto Tecnológico de Aeronáutica, Brazil)

- G. Mathews (University of Notre Dame, USA)

- L. A. Nuñez (Universidad Industrial de Santander, Colombia)

- R. Riahi (Department of Science, Shahrekord Branch, Islamic Azad University, Iran)

- C. V. Rodrigues (Instituto Nacional de Pesquisas Espaciais, Brazil)

- J. F. Rodriguez (Universidad Industrial de Santander, Colombia)

- C. A. Z. Vasconcellos (Universidade Federal do Rio Grande do Sul, Brazil)

- J. I. Zuluaga (Universidad de Antioquia, Colombia)

2.3 Postdocs

- L. Becerra (Universidad Pontificia Católica de Chile, Chile)

- J. P. Pereira (Nicolaus Copernicus Astronomical Center, Polish Academy of Sciences, Poland)

2.4 Graduate Students

- E. A. Becerra (ICRANet; Sapienza University of Rome, Italy)

- S. Campion (ICRANet; Sapienza University of Rome, Italy)

- G. Nurbakyt (ICRANet; Sapienza Al-Farabi Kazakh National University, Kazakhstan)

- G. Zhumakhanova (ICRANet; Sapienza Al-Farabi Kazakh National University, Kazakhstan)

3 Publications 2021

3.1 Refereed Journals

3.1.1 Printed

1. Moradi, R. ; Rueda, J. A. ; Ruffini, R. ; Li, Liang ; Bianco, C. L. ; Campion, S. ; Cherubini, C. ; Filippi, S. ; Wang, Y. ; Xue, S. S., *Nature of the ultrarelativistic prompt emission phase of GRB 190114C*, Physical Review D 104, 063043, 2021.

   We address the physical origin of the ultrarelativistic prompt emission (UPE) phase of GRB 190114C observed in the interval $t_{\rm rf} = 1.9$–3.99 s, by the *Fermi*-GBM in 10 keV–10 MeV energy band. Thanks to the high signal–to–noise ratio of *Fermi*-GBM data, a time-resolved spectral analysis has evidenced a sequence of similar blackbody plus cutoff power-law spectra (BB+CPL), on ever decreasing time intervals during the entire UPE phase. We assume that during the UPE phase, the "*inner engine*" of the GRB, composed of a Kerr black hole (BH) and a uniform test magnetic field B_0, aligned with the BH rotation axis, operates in an overcritical field $|\mathbf{E}| \geq E_c$, where $E_c = m_e^2 c^3/(e\hbar)$, being m_e and $-e$ the mass and charge of the electron. We infer an $e^+\,e^-$ pair electromagnetic plasma in presence of a baryon load, *a PEMB pulse*, originating from a vacuum polarization quantum process in the *inner engine*. This initially optically thick plasma self-accelerates, giving rise at the transparency radius to the MeV radiation observed by *Fermi*-GBM. At times $t_{\rm rf} > 3.99$ s, the electric field becomes undercritical, $|\mathbf{E}| < E_c$, and the *inner engine*, as previously demonstrated, operates in the classical electrodynamics regime and generate the GeV emission. During both the "quantum" and the "classical" electrodynamics processes, we determine the time varying mass and spin of the Kerr BH in the *inner engine*, fulfilling the Christodoulou-Hawking-Ruffini mass-energy formula of a Kerr BH. For the first time, we quantitatively show how the *inner engine*,

by extracting the rotational energy of the Kerr BH, produces a series of PEMB pulses. We follow the quantum vacuum polarization process in sequences with decreasing time bins. We compute the Lorentz factors, the baryon loads and the radii at transparency, as well as the value of the magnetic field, B_0, assumed to be constant in each sequence. The fundamental hierarchical structure, linking the quantum electrodynamics regime to the classical electrodynamics regime, is characterized by the emission of *"blackholic quanta"* with a timescale $\tau \sim 10^{-9}$ s, and energy $\mathcal{E} \sim 10^{45}$ erg.

2. Campion, S.; Rueda, J. A.; Ruffini, R.; Xue, S. S., *Magnetic field screening in strong crossed electromagnetic fields*, Physics Letters B 820, 136562, 2021.

   We consider crossed electric and a magnetic fields ($\vec{B} = B\hat{z}$, $\vec{E} = E\hat{y}$), with $E/B < 1$, in presence of some initial number of $e^{\pm}$ pairs. We do not discuss here the mechanism of generation of these initial pairs. The electric field accelerates the pairs to high-energies thereby radiating high-energy synchrotron photons. These photons interact with the magnetic field via magnetic pair production process (MPP), i.e. $\gamma + B \rightarrow e^{+} + e^{-}$, producing additional pairs. We here show that the motion of all the pairs around the magnetic field lines generates a current that induces a magnetic field that shields the initial one. For instance, for an initial number of pairs $N_{\pm,0} = 10^{10}$, an initial magnetic field of 10^{12} G can be reduced of a few percent. The screening occurs in the short timescales $10^{-21} \leq t \leq 10^{-15}$ s, i.e. before the particle acceleration timescale equals the synchrotron cooling timescale. The present simplified model indicates the physical conditions leading to the screening of strong magnetic fields. To assess the occurrence of this phenomenon in specific astrophysical sources, e.g. pulsars or gamma-ray bursts, the model can be extended to evaluate different geometries of the electric and magnetic fields, quantum effects in overcritical fields, and specific mechanisms for the production, distribution, and multiplicity of the e-e+ pairs.

3. Ruffini, R. ; Moradi, R. ; Rueda, J. A. search by orcid ; Li, L. search by orcid ; Sahakyan, N. ; Chen, Y. -C. search by orcid ; Wang, Y. ; Aimuratov, Y. search by orcid ; Becerra, L. ; Bianco, C. L. ; Cherubini, C. ; Filippi, S. ; Karlica, M. ; Mathews, G. J. ; Muccino, M. ; Pisani, G. B. ; Xue, S. S., *The morphology of the X-ray afterglows and of the jetted GeV emission in long GRBs*, Monthly Notices of the Royal Astronomical Society 504,

5301, 2021.

We recall evidence that long gamma-ray bursts (GRBs) have binary progenitors and give new examples. Binary-driven hypernovae (BdHNe) consist of a carbon-oxygen core (CO_{core}) and a neutron star (NS) companion. For binary periods ~ 5 min, the CO_{core} collapse originates the subclass BdHN I characterized by (1) an outstanding supernova (SN; the *SN-rise*); (2) a black hole (BH), born from the NS collapse by SN matter accretion, leading to a GeV emission with luminosity $L_{GeV} = A_{GeV}t^{-\alpha_{GeV}}$, observed only in some cases; and (3) a new NS (νNS), born from the SN, originating from the X-ray afterglow with $L_X = A_X t^{-\alpha_X}$, observed in all BdHN I. We record 378 sources and present for four prototype GRBs 130427A, 160509A, 180720B, and 190114C: (1) spectra, luminosities, SN-rise duration; (2) A_X, $\alpha_X = 1.48 \pm 0.32$, and (3) the νNS spin time evolution. We infer (i) A_{GeV}, $\alpha_{GeV} = 1.19 \pm 0.04$ and (ii) the BdHN I morphology from time-resolved spectral analysis, three-dimensional simulations, and the GeV emission presence/absence in 54 sources within the Fermi-Large Area Telescope boresight angle. For 25 sources, we give the integrated and time-varying GeV emission, 29 sources have no GeV emission detected and show X/gamma-ray flares previously inferred as observed along the binary plane. The 25/54 ratio implies the GeV radiation is emitted within a cone of half-opening angle $60°$ from the normal to the orbital plane. We deduce BH masses of 2.3–$8.9 M_{\odot}$ and spin of 0.27–0.87 by explaining the GeV emission from the BH rotational energy extraction, while their time evolution validates the BH mass-energy formula.

4. Rueda, J. A. ; Ruffini, R., *The quantum emission of an alive black hole*, IJMPD 30, 2141003, 2021. Third Award Winning Essay of the *Gravity Research Foundation 2021 awards for essays on Gravitation*.

   A long march of fifty years of successive theoretical progress and new physics discovered using observations of gamma-ray bursts, has finally led to the formulation of an efficient mechanism able to extract the rotational energy of a Kerr black hole to power these most energetic astrophysical sources and active galactic nuclei. We here present the salient features of this long-sought mechanism, based on gravito-electrodynamics, and which represents an authentic shift of paradigm of black holes as forever *alive* astrophysical objects.

5. Moradi, R. ; Rueda, J. A. ; Ruffini, R. ; Wang, Y., *The newborn black hole in GRB 191014C proves that it is alive*, Astronomy & Astrophysics 649, A75, 2021.

   A multi-decade theoretical effort has been devoted to finding an efficient mechanism to use the rotational and electrodynamical extractable energy of a Kerr-Newman black hole (BH), to power the most energetic astrophysical sources such as gamma-ray bursts (GRBs) and active galactic nuclei (AGN). We show an efficient general relativistic electrodynamical process which occurs in the *"inner engine"* of a binary driven hypernova (BdHN). The *inner engine* is composed of a rotating Kerr BH of mass M and dimensionless spin parameter α, a magnetic field of strength B_0 aligned and parallel to the rotation axis, and a very low density ionized plasma. Here, we show that the gravitomagnetic interaction between the BH and the magnetic field induces an electric field that accelerates electrons/protons from the environment to ultrarelativistic energies emitting synchrotron radiation. We show that in GRB 190114C the BH of mass $M = 4.4\ M_\odot$, $\alpha = 0.4$ and $B_0 \approx 4 \times 10^{10}$ G, can lead to a high-energy ($\gtrsim$GeV) luminosity of 10^{51} erg s^{-1}. The *inner engine* parameters are determined by requiring: 1) that the BH extractable energy explains the GeV and ultrahigh-energy emission energetics, 2) that the emitted photons are not subjected to magnetic-pair production, and 3) that the synchrotron radiation timescale agrees with the observed high-energy timescale. We find for GRB 190114C a clear jetted emission of GeV energies with a semi-aperture angle of approximately 60° with respect to the BH rotation axis.

6. Uribe, J. D.; Becerra-Vergara, E. A.; Rueda, J. A., *Neutrino Oscillations in Neutrino-Dominated Accretion Around Rotating Black Holes*, Universe 7, 7, 2021.

   In the binary-driven hypernova model of long gamma-ray bursts, a carbon-oxygen star explodes as a supernova in presence of a neutron star binary companion in close orbit. Hypercritical (i.e. highly super-Eddington) accretion of the ejecta matter onto the neutron star sets in, making it reach the critical mass with consequent formation of a Kerr black hole. We have recently shown that, during the accretion process onto the neutron star, fast neutrino flavour oscillations occur. Numerical simulations of the above system show that a part of the ejecta keeps

bound to the newborn Kerr black hole, leading to a new process of hypercritical accretion. We here address, also for this phase of the binary-driven hypernova, the occurrence of neutrino flavour oscillations given the extreme conditions of high density (up to 10^{12} g cm^{-3}) and temperatures (up to tens of MeV) inside this disk. We estimate the behaviour of the electronic and non-electronic neutrino content within the two-flavour formalism ($\nu_e\nu_x$) under the action of neutrino collective effects by neutrino self-interactions. We find that in the case of inverted mass hierarchy, neutrino oscillations inside the disk have frequencies between $\sim (10^5$–$10^9)$ s^{-1}, leading the disk to achieve flavour equipartition. This implies that the energy deposition rate by neutrino annihilation ($\nu + \bar{\nu} \rightarrow e^- + e^+$) in the vicinity of the Kerr black hole, is smaller than previous estimates in the literature not accounting by flavour oscillations inside the disk. The exact value of the reduction factor depends on the ν_e and ν_x optical depths but it can be as high as ~ 5. The results of this work are a first step toward the analysis of neutrino oscillations in a novel astrophysical context and, as such, deserve further attention.

7. Campion, S. ; Rueda, J. A. ; Xue, S. S. ; Ruffini, R., *On the Magnetic Field Screening in Strong Crossed Electromagnetic Fields*, Astronomy Reports 65, 911, 2021.

It has been shown that a rotating black hole (BH hereafter) immersed in a test background magnetic field, of initial strength B0 and aligned parallel to the BH rotation axis, generates an induced electric field, which strength is proportional to the background magnetic field. We consider the configuration of crossed fields: $\vec{B} = B\hat{z}$ and $\vec{E} = E\hat{y}$. In this system, a huge number of pairs can be emitted and start to be accelerated to high energies, by means of the induced electric field, and emit synchrotron photons. These photons interact with the magnetic field via the magnetic pair production process (MPP hereafter), $\gamma + B \rightarrow e^+ + e^-$. The motion of all these pairs around the magnetic field lines generates also an induced magnetic field oriented in the opposite direction to the background one. This implies a reduction of the background magnetic field. The purpose of this study is to show if this reduction occurs, which implies a decreases the MPP efficiency and, consequently, the enhancement of the probability for the synchrotron photons to escape from the region and be detected.

8. Rueda, J. A., *An Update of the Binary-Driven Hypernovae Scenario of Long Gamma-Ray Bursts*, Astronomy Reports 65, 1026, 2021.

   I discuss some most recent theoretical and observational results on the inner engine of the high-energy (GeV) emission of long gamma-ray bursts (GRBs), within the context of the binary-driven hypernova (BdHN) model.

9. Jorge A. Rueda, Remo Ruffini, Rahim Moradi, Yu Wang, *A brief review of binary-driven hypernova*, IJMPD 30, 2130007, 2021.

   Binary-driven hypernova (BdHN) models long gamma-ray burst (GRB) as occurring in the binary systems involving a carbon–oxygen core (CO_{core}) and a companion neutron star (NS) or a black hole (BH). This model, first proposed in 2012, succeeds and improves upon the fireshell model and the induced gravitational collapse (IGC) paradigm. After nearly a decade of development, the BdHN model has reached a nearly complete structure, giving explanation to all the observables of long bursts into its theoretical framework, and has given a refined classification of long GRB according to the original properties of the progenitors. In this paper, we present a summary of the BdHN model and the physical processes at work in each of the envisaged Episodes during its occurrence and lifetime, duly contextualized in the framework of GRB observations.

3.1.2 Accepted for publication or in press

1. Uribe, J. D.; Rueda, J. A., *Neutrino Flavour Oscillations in Gamma-Ray Bursts*, to be published as a chapter in the book "New phenomena and new states of matter in the Universe: from quarks to Cosmos", Eds. Peter Hess, Thomas Boller and Cesar Zen Vasconcellos, World Scientific 2021.

   In the binary-driven hypernova model of long gamma-ray bursts, a carbon-oxygen star explodes as a supernova in presence of a neutron star binary companion in close orbit. Hypercritical (i.e. highly super-Eddington) accretion of the ejecta matter onto the neutron star sets in, making it reach the critical mass with consequent formation of a Kerr black hole. We have recently shown that, during the accretion process onto the neutron star, fast neutrino flavour oscillations occur. Nu-

merical simulations of the above system show that a part of the ejecta keeps bound to the newborn Kerr black hole, leading to a new process of hypercritical accretion. We address here the occurrence of neutrino flavour oscillations given the extreme conditions of high density (up to 10^{12} g cm^{-3}) and temperatures (up to tens of MeV) inside this disk. We estimate the evolution of the electronic and non-electronic neutrino content within the two-flavour formalism ($\nu_e \nu_x$) under the action of neutrino collective effects by neutrino self-interactions. We find that neutrino oscillations inside the disk have frequencies between $\sim (10^5 - 10^9)$ s^{-1}, leading the disk to achieve flavour equipartition. This implies that the energy deposition rate by neutrino annihilation ($\nu + \bar{\nu} \rightarrow e^- + e^+$) in the vicinity of the Kerr black hole, is smaller than previous estimates in the literature not accounting by flavour oscillations inside the disk. The exact value of the reduction factor depends on the ν_e and ν_x optical depths but it can be as high as ~ 5.

2. Rueda, J. A.; Ruffini, R., *An Inner Engine Based on Binary-Driven Hypernovae for the High-Energy Emission of Long Gamma-Ray Bursts*, to be published as a chapter in the book "New phenomena and new states of matter in the Universe: from quarks to Cosmos", Eds. Peter Hess, Thomas Boller and Cesar Zen Vasconcellos, World Scientific 2021.

A multi-decade theoretical effort has been devoted to finding an efficient mechanism to use the rotational and electromagnetic extractable energy of a Kerr-Newman black hole (BH) to power the most energetic astrophysical sources, gamma-ray bursts (GRBs) and active galactic nuclei (AGN). We show an efficient general relativistic electrodynamical process which occurs in the *"inner engine"* of a binary driven hypernova (BdHN). The *inner engine* is composed of a rotating Kerr BH, surrounded by a magnetic field of strength B_0, aligned and parallel to the rotation axis, and a very-low-density ionized plasma. The gravitomagnetic interaction between the Kerr BH and the magnetic field induces an electric field that accelerates charged particles from the environment. Along the BH rotation axis, the particles reach energies above 10^{18} eV hence contributing to ultrahigh-energy cosmic rays, and at other latitudes emit synchrotron radiation at GeV energies which explain the high-energy emission of long GRBs observed by Fermi-LAT.

3.1.3 Submitted for publication

1. Rueda, J. A.; Ruffini, R.; Kerr, R. P., *Gravitomagnetic interaction of a Kerr black hole with a magnetic field as the source of the jetted GeV radiation of gamma-ray bursts*, submitted for publication to MNRAS.

   We show that the gravitomagnetic interaction of a Kerr black hole (BH) with a surrounding magnetic field induces an electric field able to accelerate charged particles to ultra-relativistic energies in the vicinity of the BH. Along the BH rotation axis, electrons/protons can reach even thousands of PeV leading to ultrahigh-energy cosmic rays (UHECRs) from stellar-mass BHs in long gamma-ray bursts (GRBs) and from supermassive BHs in active galactic nuclei (AGN). At off-axis latitudes, the particles are accelerated to hundreds of GeV, and by synchrotron radiation emit high-energy GeV photons. Such a process occurs within approximately $60°$ around the BH rotation axis and with equatorial symmetry, hence forming a double-cone emission structure. The theoretical framework describing these acceleration and radiation processes, how they extract the rotational energy of the Kerr BH, as well as the consequences for the astrophysics of GRBs are outlined.

2. Campion, S.; Melon Fuksman, J. D.; J. A. Rueda, *Neutrino and gamma-ray production from proton-proton interactions in binary-driven hypernovae*, submitted for publication to EPJC.

   We estimate the neutrino emission from the decay chain of the π-meson and μ-lepton, produced by proton-proton inelastic scattering in energetic ($E_{\mathrm{iso}} \gtrsim 10^{52}$ erg) long gamma-ray bursts (GRBs), within the type I binary-driven hypernova (BdHN) model. The BdHN I progenitor is binary system composed of a carbon-oxygen star (CO_{core}) and a neutron star (NS) companion. The CO_{core} explosion as supernova (SN) triggers a massive accretion process onto the NS. For short orbital periods of few minutes, the NS reaches the critical mass, hence forming a black hole (BH). Recent numerical simulations of the above scenario show that the SN ejecta becomes highly asymmetric, creating a *cavity* around the newborn BH site, due to the NS accretion and gravitational collapse. Therefore, the electron-positron ($e^{\pm}$) plasma created in the BH formation, during its isotropic and expanding self-acceleration, engulfs different amounts of ejecta baryons along different directions, leading to a direction-dependent Lorentz factor. The protons engulfed

inside the high-density ($\sim 10^{23}$ particle/cm^3) ejecta reach energies in the range $1.24 \lesssim E_p \lesssim 6.14$ GeV and interact with the unshocked protons in the ejecta. The protons engulfed from the low density region around the BH reach energies ~ 1 TeV and interact with the low-density (~ 1 particle/cm^3) protons of the interstellar medium (ISM). The above interactions give rise, respectively, to neutrino energies $E_\nu \leq 2$ GeV and $10 \leq E_\nu \leq 10^3$ GeV, and for both cases we calculate the spectra and luminosity.

3. Moradi, R. ; Li, Liang ; Rueda, J. A. ; Ruffini, R. ; Sahakyan, N. ; Wang, Y., *X-ray and GeV afterglows and sub-TeV emission of GRB 180720B*, submitted for publication to ApJ.

We classify GRB 180720B, with redshift $z = 0.653$ and isotropic energy $E_{\mathrm{iso}} = 5.92 \times 10^{53}$ erg, as a binary-driven hypernova (BdHN) I. The binary progenitor with orbital period ~ 5 min is composed of a carbon-oxygen core (CO$_{\mathrm{core}}$) and a neutron star (NS) companion. The CO$_{\mathrm{core}}$ collapse generates a supernova (SN) and a new NS (νNS). From a time-resolved analysis, we identify the three components of this long-GRB subclass: the νNS, the NS companion, and the SN ejecta. The GRB Episodes are: 1) the first appearance of the SN (*"SN-rise"*), at $t_{\mathrm{rf}} = 4.84$ s from the GRB trigger; 2) the first appearance of the νNS (*"νNS-rise"*), at $t_{\mathrm{rf}} = 6.05$ s, from fallback accretion of SN ejecta, followed by the X-ray afterglow with a power-law luminosity $L_X \propto t^{-1.44 \pm 0.01}$; 3) the appearance of the black hole (*"BH-rise"*), formed from the NS companion collapse by accretion of SN ejecta, heralded by the first GeV emission at $t_{\mathrm{rf}} = 7.01$ s, followed by the ultrarelativistic prompt emission lasting 1.82 s. The observation of hard, soft X-ray flares and the GeV emission indicates a line-of-sight close to the binary plane. We infer from the X-rays the νNS period and magnetic field, $P_{\circ \mathrm{NS,0}} = 1.01$ ms and $B_{\mathrm{dip}} = 4.2 \times 10^{13}$ G. From the GeV emission originating in the BH rotational energy, we infer its mass, $M = 2.3 M_\odot$, and spin, $\alpha = 0.27$. We ascribe the sub-TeV emission observed by H.E.S.S. to a νNS glitch during its spindown.

Nature of the ultrarelativistic prompt emission phase of GRB 190114C

R. Moradi,[1,2,3,*] J. A. Rueda,[1,2,4,5,6,†] R. Ruffini,[1,2,7,‡] Liang Li,[1,2,7,§] C. L. Bianco,[1,2,6] S. Campion,[1,2]
C. Cherubini,[2,8,9] S. Filippi,[2,8,10] Y. Wang,[1,2,11,‖] and S. S. Xue[1,2]

[1]*ICRA and Dipartimento di Fisica, Università di Roma "La Sapienza",*
Piazzale Aldo Moro 5, I-00185 Roma, Italy
[2]*International Center for Relativistic Astrophysics Network, Piazza della Repubblica 10,*
I-65122 Pescara, Italy
[3]*INAF—Osservatorio Astronomico d'Abruzzo, Via M. Maggini snc, I-64100 Teramo, Italy*
[4]*ICRANet-Ferrara, Dipartimento di Fisica e Scienze della Terra, Università degli Studi di Ferrara,*
Via Saragat 1, I–44122 Ferrara, Italy
[5]*Dipartimento di Fisica e Scienze della Terra, Università degli Studi di Ferrara,*
Via Saragat 1, I–44122 Ferrara, Italy
[6]*INAF, Istituto di Astrofisica e Planetologia Spaziali, Via Fosso del Cavaliere 100, 00133 Rome, Italy*
[7]*INAF, Viale del Parco Mellini 84, 00136 Rome, Italy*
[8]*ICRA, University Campus Bio-Medico of Rome, Via Alvaro del Portillo 21, I-00128 Rome, Italy*
[9]*Department of Science and Technology for Humans and the Environment and Nonlinear Physics*
and Mathematical Modeling Lab, University Campus Bio-Medico of Rome,
Via Alvaro del Portillo 21, 00128 Rome, Italy
[10]*Department of Engineering, University Campus Bio-Medico of Rome, Nonlinear Physics*
and Mathematical Modeling Lab, Via Alvaro del Portillo 21, 00128 Rome, Italy
[11]*INAF—Osservatorio Astronomico d'Abruzzo, Via M. Maggini snc, I-64100, Teramo, Italy*

We address the physical origin of the ultrarelativistic prompt emission (UPE) phase of GRB 190114C observed in the interval $t_{\rm rf} = 1.9$–3.99 s, by the *Fermi*-GBM in 10 keV–10 MeV energy band. Thanks to the high signal-to-noise ratio of *Fermi*-GBM data, a time-resolved spectral analysis has evidenced a sequence of similar blackbody plus cutoff power-law spectra (BB + CPL), on ever decreasing time intervals during the entire UPE phase. We assume that during the UPE phase, the "*inner engine*" of the GRB, composed of a Kerr black hole (BH) and a uniform test magnetic field B_0, aligned with the BH rotation axis, operates in an overcritical field $|\mathbf{E}| \geq E_c$, where $E_c = m_e^2 c^3/(e\hbar)$, being m_e and $-e$ the mass and charge of the electron. We infer an e^+e^- pair electromagnetic plasma in presence of a baryon load, *a PEMB pulse*, originating from a vacuum polarization quantum process in the *inner engine*. This initially optically thick plasma self-accelerates, giving rise at the transparency radius to the MeV radiation observed by *Fermi*-GBM. At times $t_{\rm rf} > 3.99$ s, the electric field becomes undercritical, $|\mathbf{E}| < E_c$, and the *inner engine*, as previously demonstrated, operates in the classical electrodynamics regime and generate the GeV emission. During both the "quantum" and the "classical" electrodynamics processes, we determine the time varying mass and spin of the Kerr BH in the *inner engine*, fulfilling the Christodoulou-Hawking-Ruffini mass-energy formula of a Kerr BH. For the first time, we quantitatively show how the *inner engine*, by extracting the rotational energy of the Kerr BH, produces a series of PEMB pulses. We follow the quantum vacuum polarization process in sequences with decreasing time bins. We compute the Lorentz factors, the baryon loads and the radii at transparency, as well as the value of the magnetic field, B_0, assumed to be constant in each sequence. The fundamental hierarchical structure, linking the quantum electrodynamics regime to the classical electrodynamics regime, is characterized by the emission of "*blackholic quanta*" with a timescale $\tau \sim 10^{-9}$ s, and energy $\mathcal{E} \sim 10^{45}$ erg.

*rahim.moradi@inaf.it
†jorge.rueda@icra.it
‡ruffini@icra.it
§liang.li@icranet.org
‖yu.wang@uniroma1.it

I. INTRODUCTION

It is by now clear that gamma-ray bursts (GRBs), far from being a short single elementary process lasting less than 10^2 s, are possibly the most complex astrophysical systems in the Universe, an authentic fundamental physics

laboratory. A series of Episodes, corresponding to new different physical laws, take place on vastly different characteristic timescales ranging from quantum electrodynamics (QED) timescales of 10^{-21} s, to classical electrodynamics processes of 10^{-14} s, as well as to gravitational processes of 10^{-6} s, and to hydrodynamics timescales of 1 s and of 10^{7} s, and the GRB source lifetime can indeed be as long as 10^{17} s, i.e., the Universe lifetime (see [1], and references therein).

One of the most intriguing phenomena occurring in the most energetic long GRBs is the ultrarelativistic prompt emission (UPE) phase. In the case of GRB 190114C: (1) it takes place on a 2 s rest-frame time ($t_{\rm rf}$) interval, (2) it encompasses 40% of the GRB isotropic energy, and (3) it occurs in an originally optically thick domain reaching transparency in the keV-MeV energy range.

We address in this article the challenge of inferring, from spectral properties, on an ever-decreasing timescales, the nature of this new and yet unexplained process. We use: (A) The concepts previously developed for a self-accelerating optically thick $e^{+}e^{-}$ pair-electromagnetic-baryon plasma (PEMB pulse) originated from vacuum polarization produced by a overcritically charged Kerr-Newman black hole (BH) [2–7]. (B) A specific property of the PEMB pulse: the reaching of the transparency radius with $\Gamma \sim 100$ [3], which is essential to overcome the compactness problem of the UPE phase; see e.g., [8,9] (C) The Papapetrou-Wald solution [10,11] as an alternative to the charged Kerr-Newman BH as the source of vacuum polarization process. (D) The concept of an "effective charge", $Q_{\rm eff}$, which overcomes the difficulty of adopting the unexplained origin of a charged BH. This concept allows to explain in an "effective way" the electric field which arises from the gravitomagnetic interaction of a Kerr BH with a surrounding magnetic field, B_0. The effective charge has been used in the study of the "*inner engine*" of GRB 130427A [12] and GRB 190114C [13].

We address the UPE phase of GRB 190114C that, owing to its morphology, can be identified as a canonical binary driven hypernova (BdHN) of type I (see details below), observed with a viewing angle orthogonal to the orbital plane of the GRB binary progenitor. Indeed, a variety of episodes of GRB 190114C have been already identified and duly explained [1], including the x-ray afterglow [14] and the GeV emission [13].

It has been possible since the beginning of 2018 [1,14–17] to obtain specific new results thanks to a variety of factors, including the identification of new GRB paradigms, a novel time-resolved spectral analysis fulfilling stringent criteria of statistical significance [18–23], and three-dimensional, numerical smoothed-particle-hydrodynamic (SPH) simulations of BdHNe presented in Becerra *et al.* [24]. From these results, it has been concluded:

(A) There is clear evidence that the progenitors of long GRBs are binary systems composed of a carbon-oxygen (CO) star and a neutron star (NS) companion: the BdHN. The gravitational collapse of the iron core of the CO star leads to the SN and forms the newborn NS (νNS). When the binary period is short i.e., ~ 5 min, the SN ejecta hypercritically accretes onto the companion NS, leading to the formation of a BH [1]. These systems are known as BdHN of type I (BdHN I). This approach was successfully adopted in explaining the physical origin of the x-ray flares [25], further confirmed in Ruffni *et al.* [26].

(B) The accretion of the SN ejecta onto the νNS in BdHNe has given the opportunity to explain the underlying physical nature of the x-ray afterglow in GRB 130427A, GRB 160509A, GRB 160625B, GRB 180720A and GRB 190114C; see [14] and [15].

(C) The observations of a mildly relativistic phase in the GRB plateau and in the afterglow [25,26], have motivated the use of BdHNe model in order to explain the energetic of the GeV emission as originating from the extraction of rotational energy of a Kerr BH very close to the BH horizon, described by the *inner engine*, addressed in Ruffni *et al.* [12], Rueda and Ruffni [17].

The *inner engine* is composed of: (1) a Kerr BH with mass of M and angular momentum of J, (2) an asymptotically uniform magnetic field, B_0 aligned with the BH rotation axis, the Papapetrou-Wald solution [11], and (3) a very low density plasma composed of ions and electrons with density of 10^{-14} g cm^{-3}; see Ruffni *et al.* [12]. The effective charge, $Q_{\rm eff}$, of this system:

$$Q_{\rm eff} = 2B_0 JG/c^3, \qquad (1)$$

originates from the gravitomagnetic interaction of the Kerr BH with the surrounding magnetic field, B_0, being c and G the speed of light in vacuum and the gravitational constant, respectively; see Ruffni *et al.* [12], Rueda and Ruffni [17], and Moradi *et al.* [13].

In order to explain the GeV emission the *inner engine* operates in an undercritical electric field regime, i.e., $|\mathbf{E}| < E_c$, where $E_c = m_e^2 c^3/(e\hbar)$, being m_e and $-e$ the electron mass and charge, respectively, in presence of a magnetic field of $B_0 \sim 10^{10}$ G, assumed to be constant in the entire process of emission. During this process:

(1) electrons are injected close to the horizon with an initial Lorentz factor of $\gamma = 1$;

(2) electrons are accelerated by the electromagnetic fields of the *inner engine* and radiate synchrotron photons of GeV energies;

(3) the radiation does not occur continuously but is emitted in elementary events (quanta) of $\sim 10^{37}$ erg on a timescale of $\sim 10^{-14}$ s. This energy is paid by the rotational energy of the Kerr BH implying a corresponding decrease of the angular momentum J of the Kerr BH [12,13,17].

The emission of the quanta is repetitive. After the emission of each quanta, a new process occurs starting

from a new value $J^* = J - \Delta J$ of the angular momentum, with $\Delta J/J \sim 10^{-16}$, being ΔJ the angular momentum extracted to the Kerr BH by the event in each repetitive step [12,13].

In this article, we address the study of the UPE phase utilizing our previous background and being guided by: (1) the hierarchical structure of the UPE in GRB 190114C with characteristic spectral signature of a cutoff power-law and a blackbody component (CPL + BB); see Ruffni *et al.* [27]; (2) the *inner engine* model which has been already well tested for the GeV radiation in GRB 130427A [12] and GRB 190114C [13].

We recall that the electric field in the Papapetrou-Wald solution in the slow-rotation approximation is given by [12]:

$$E_r \approx -\frac{1}{2}\alpha B_0 \frac{r_+^2}{r^2},\qquad(2)$$

where r_+ is the outer event horizon and $\alpha \equiv cJ/(GM^2)$ is the dimensionless BH spin parameter.

The profound novelty characterizing the UPE phase is the assumption of an overcritical field, i.e., $|\mathbf{E}| \geq E_c$ around the Kerr BH in the *inner engine*. This overcritical field generates, via vacuum polarization, an optically thick

PEMB pulse which owing to its high density (here $\sim 10^8$ g cm^{-3}) and high interior pressure, self-accelerates to an ultrarelativistic regime and finally reaching the transparency point [7].

The hydrodynamic equations of the relativistic expanding PEMB pulses are integrated until the point of transparency when the MeV radiation becomes observable. The radius of transparency and Lorentz factor are explicitly evaluated. This solution was first addressed in Ruffni [3], Ruffni *et al.* [5–7]. This is the fundamental physical process which is assumed to be at the very ground of the description of the UPE phase and its spectral properties. Again, the energy in the overcritical field originates from the rotational energy of the Kerr BH in the Papapetrou-Wald solution.

An additional necessary step is how to carry out the matching of the overcritical regime, characterizing the UPE phase, its MeV radiation, and its intrinsic quantum nature, with the already analyzed undercritical regime following the UPE phase. This undercritical regime describes the GeV radiation and is dominated in the *inner engine* by a classical electrodynamics nature with very low density surrounding plasma.

For the determination of the parameters of the *inner engine*, we are guided by the time-resolved spectra analysis and existence of the hierarchical structure found in the UPE
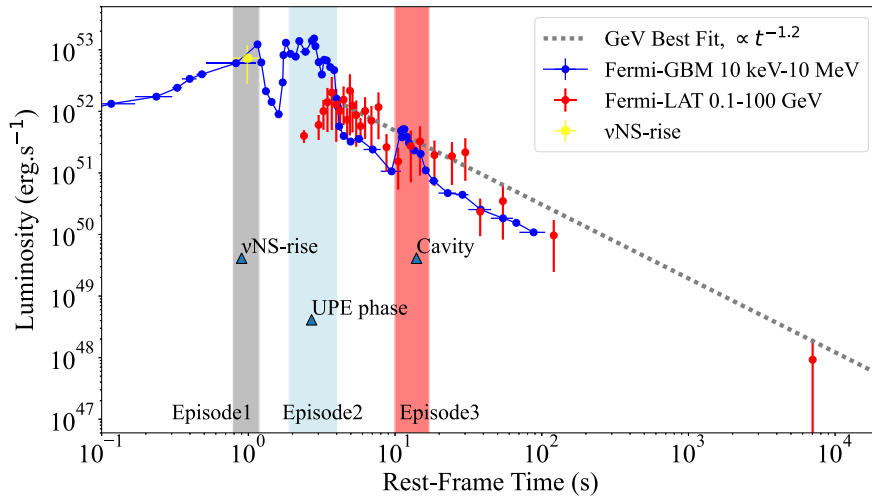
FIG. 1. Luminosity of the *Fermi*-GBM in the 10 keV–10 MeV energy band together with the luminosity of *Fermi*-LAT during and after UPE phase expressed in the rest-frame of the source. The light grey part shows the νNS–rise from $t_{\rm rf} = 0.79$ s to $t_{\rm rf} = 1.18$ s. The light blue part shows the UPE phase which is in the time interval $t_{\rm rf} = 1.9$–3.99 s, whose lower and upper edges correspond, respectively, to the moment of BH formation and to the moment which blackbody component disappears from the GBM data. The corresponding analysis for GRB 130427A, GRB 160509A and GRB 160625B is presented in [28]. The red part shows the Fermi-GBM the *cavity* introduced in Ruffni *et al.* [29]. The rest-frame 0.1–100 GeV luminosity light-curve of GRB 190114C after UPE phase is best fitted by a power-law with slope of 1.2 ± 0.04 and amplitude of 7.75×10^{52} erg s^{-1}
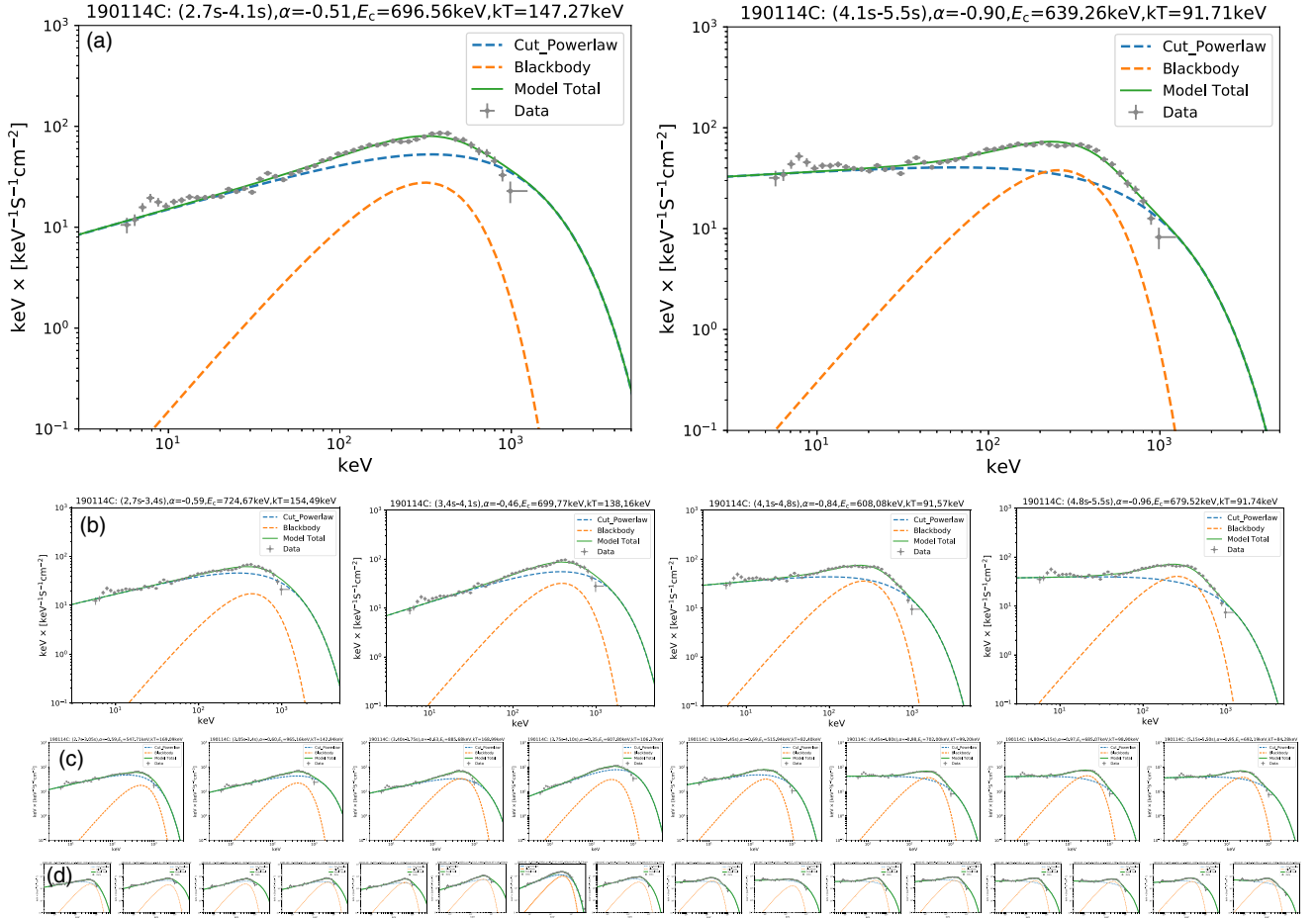
FIG. 2.   Time-resolved spectral analysis of UPE phase GRB 190114C: from $t = 2.7$ s ($t_{\rm rf} = 1.9$ s) to $t = 5.5$ s ($t_{\rm rf} = 3.9$ s). For the second iteration: (a) the time interval is divided into two parts, four parts for the third iteration; b, eight parts for the fourth iteration; (c) and sixteen parts for the fifth iteration; (d) respectively. The spectral fitting parameters for each iteration are reported in Table I. Plots are taken from Ruffni *et al.* [27] with permission of authors.
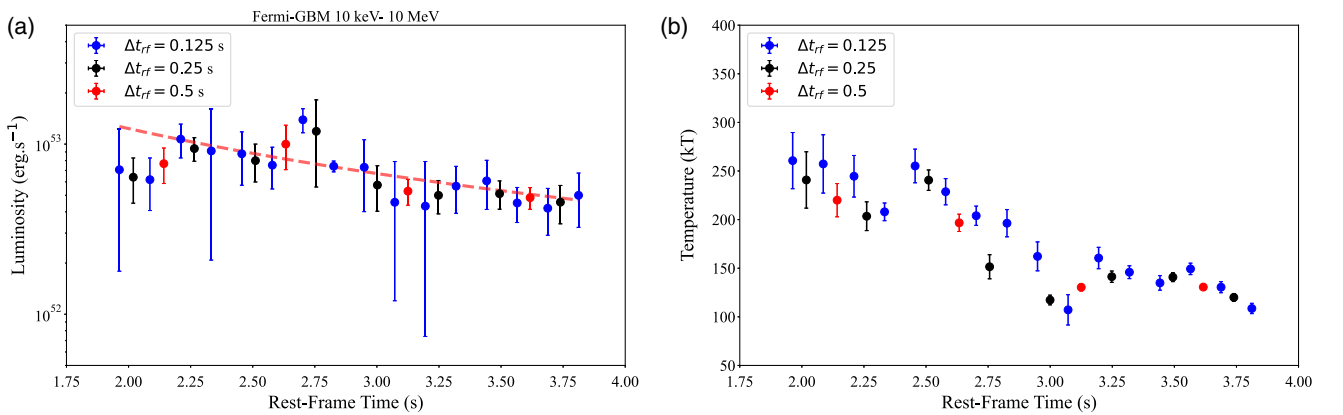
FIG. 3.   Luminosity [a] and rest-frame temperature [b] during the UPE observed by *Fermi*-GBM, obtained from analyses with $\Delta t = 0.125$ s (blue circles), $\Delta t = 0.25$ s (black circles) and $\Delta t = 0.5$ s (red circles) time resolutions reported in Table I. The luminosity is best fitted by a power-law of amplitude $(3.5 \pm 1.1) \times 10^{53}$ erg s^{-1} and power-law index -1.50 ± 0.30. The best fit of luminosity, obtained from $\Delta t_{\rm rf} = 0.125$ s time-resolved analysis, is in principle independent of the resolution of data analysis and is fulfilled in all iterative sequences.

phase [27]. Each successive iteration (rebinning) fulfills the total energy requirement and spectral structures in different timescales. We select as the fundamental iterative process the "only" one which allows the electric field to fulfill at the end of the UPE phase the constraint $|\mathbf{E}| = E_c$. This boundary condition determines the value of B_0 and is necessary to join the UPE phase to the classical electro-dynamics regime, originating the GeV radiation.

Similar to the case of the generation of GeV radiation from the *inner engine*, also the emission of the MeV radiation during the UPE phase is not continuous:

1. $e^+e^-\gamma$ plasma, in presence of the baryon load, is generated by the vacuum polarization close to horizon with initial bulk Lorentz factor $\Gamma = 1$ on a characteristic timescale of $\sim\hbar/(m_e c^2) \approx 10^{-21}$ s,

2. these PEMB pulses self-accelerate all the way to the point of transparency at which emit MeV radiation in an ultrarelativistic regime,

3. the process is again repetitive; at the end of each step the process restarts with a value of electric field given by Eq. (2), keeping the magnetic field constant, but with a new value of the BH dimensionless spin parameter $\alpha^* = \alpha - \Delta\alpha$, with $\Delta\alpha/\alpha \sim 10^{-9}$, being $\Delta\alpha$ the amount of dimensionless BH spin extracted to the Kerr BH by the event in each repetitive step.

The UPE phase stops in the sequence which allows the condition $|\mathbf{E}| = E_c$ to be reached at the right time.

In Sec. II, we recall three different Episodes identified in time-resolved spectral analysis of GRB 190114C. We focus on the spectral analysis of the Fermi-GBM (keV-MeV) and the Fermi-LAT (GeV) data during and after the UPE phase; see Fig. 1.

In Sec. III, we present the time-resolved analysis of the UPE phase as well as the appearance of the hierarchical structure of its spectra. These results were announced in Ruffni *et al.* [27] and here presented in an improved numerical analysis, with their theoretical modeling; see Fig. 2.

In Sec. IV, we outline the properties of the *inner engine*. This is composed of a uniform magnetic field aligned with the rotation axis of a Kerr BH, following the exact, mathematical solution of the Einstein-Maxwell equations given by Wald [11]. We here apply this solution to the astrophysical conditions occurring in a BdHN I.

In Sec. V, for $t_{\rm rf} > 3.99$ s, namely after the UPE phase, following Ruffni *et al.* [1,12], Rueda and Ruffni [17] and Moradi *et al.* [13], we proceed to the self-consistent determination of (a) the mass and spin of the BH, (b) the magnetic field B_0. These parameters are determined to fulfill the energetics of GeV radiation and its trans-parency with respect to the process of pair production by photon-magnetic field interaction. The mass and spin of BH at $t_{\rm rf} = 3.99$ s are, respectively, $M = 4.45\,M_\odot$ and $\alpha = 0.41$, and magnetic field is $B_0 \sim 10^{10}$ G.

In Sec. VI, we determine the mass and spin of BH at $t_{\rm rf} = 1.9$ s, $M = 4.53\,M_\odot$ and $\alpha = 0.54$. This result is consistent with the luminosity obtained from the time-resolved spectral analysis, during the UPE phase, and the above values of the mass and spin for $t_{\rm rf} > 3.99$ s given in Sec. V; see Figs. 3 and 4.
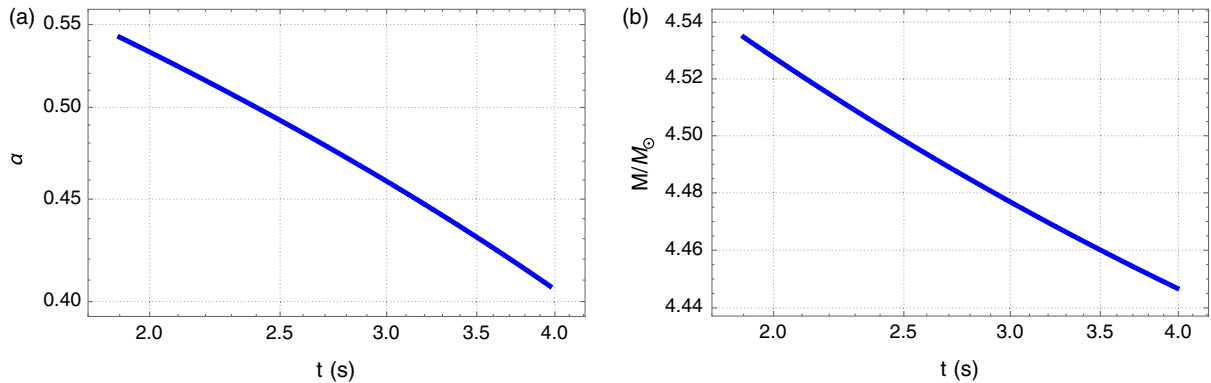
FIG. 4.   The decrease of the BH spin and mass, as a function of rest-frame time for GRB 190114C during the UPE phase, namely in the rest-frame time interval $t_{\rm rf} = 1.9$–3.99 s. The values of spin and mass at the moment when BH formed are, respectively, $M = 4.53\,M_\odot$ and $\alpha = 0.54$. At the moment when the UPE is over, i.e., at $t_{\rm rf} = 3.99$ s, are: $\alpha = 0.41$ and $M = 4.45\,M_\odot$.

In Sec. VII, we address the overcritical regime, $|\mathbf{E}| \geq E_c$, in order to have the vacuum polarization via Schwinger e^+e^- pair production [see discussion in [30]], in the UPE phase; see also Ruffni [3], Ruffni *et al.* [5–7].

In Sec. VIII, we assess the general formulation of the transparency of the MeV photons during the UPE phase.

In Sec. IX, we determine the magnetic field, $B_0 \sim 10^{17}$ G, inferred from the time-resolved spectral analysis with $\Delta t = 0.125$ s resolution, represented in Sec. III, corresponding to the emission at the transparency point of the 16 PEMB pulses with the repetition time of

$\tau = 0.125$ s. This sequence does not fulfill the boundary condition of the UPE phase i.e., $|\mathbf{E}| = E_c$ at $t_{\rm rf} = 3.99$ s; see Fig. 5.

In Sec. X, we obtain the lower limit of magnetic filed around the BH, $B_0 = 2.3 \times 10^{14}$ G, during the UPE phase by imposing $|\mathbf{E}| = E_c$ at $t_{\rm rf} = 3.99$ s, marking the end of UPE phase. We infer that the UPE phase results from emission at the transparency point of the $\sim 10^9$ PEMB pulses, with radiation timescale of $\tau_q \sim 10^{-9}$ s; see Fig. 6.

In Sec. XI, we make a comparison with other approaches In Sec. XII, we outline the conclusions of this article.
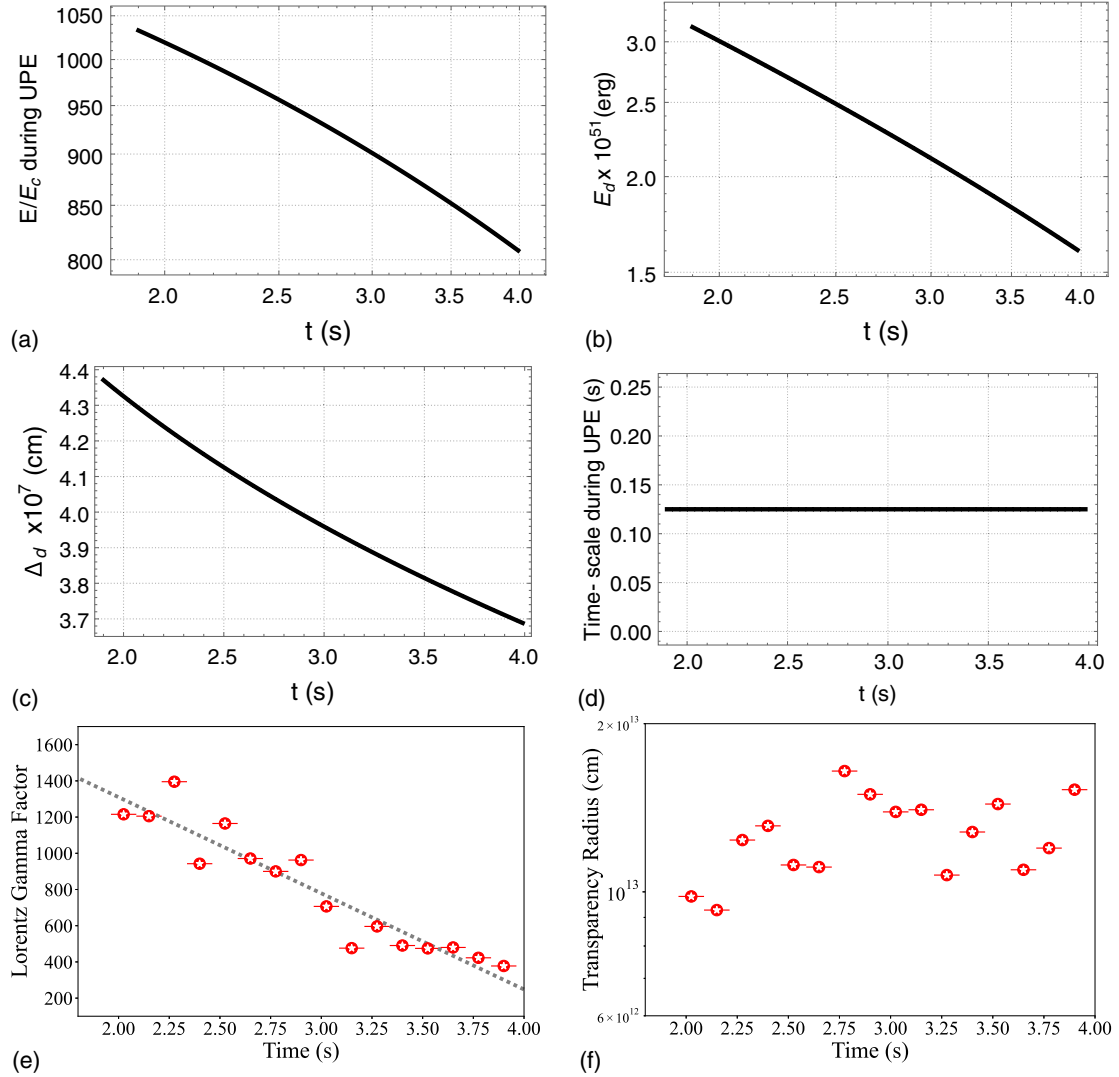
FIG. 5. The parameters of *inner engine* and transparency condition as a function of rest-frame time for GRB 190114C during the UPE phase, namely in the rest-frame time interval $t_{\rm rf} = 1.9$–3.99 s, obtained from a time-resolved analysis down to a $\Delta t = 0.125$ s time resolution reported in Table I. (a): The electric field during UPE phase which is clearly overcritical. (b): The energy of dyadoregion during the UPE phase obtained from Eq. (20). (c): The width of dyadoregion obtained from Eq. (23). (d): Timescale of radiation during the UPE phase. (e): The decrease of the Lorentz gamma factor, Γ, as a function of rest-frame time. (f): The evolution of transparency radius in the UPE phase of GRB 190114C. All values are obtained for magnetic field of, $B_0 = 1.8 \times 10^{17}$ G, calculated in Sec. IX.
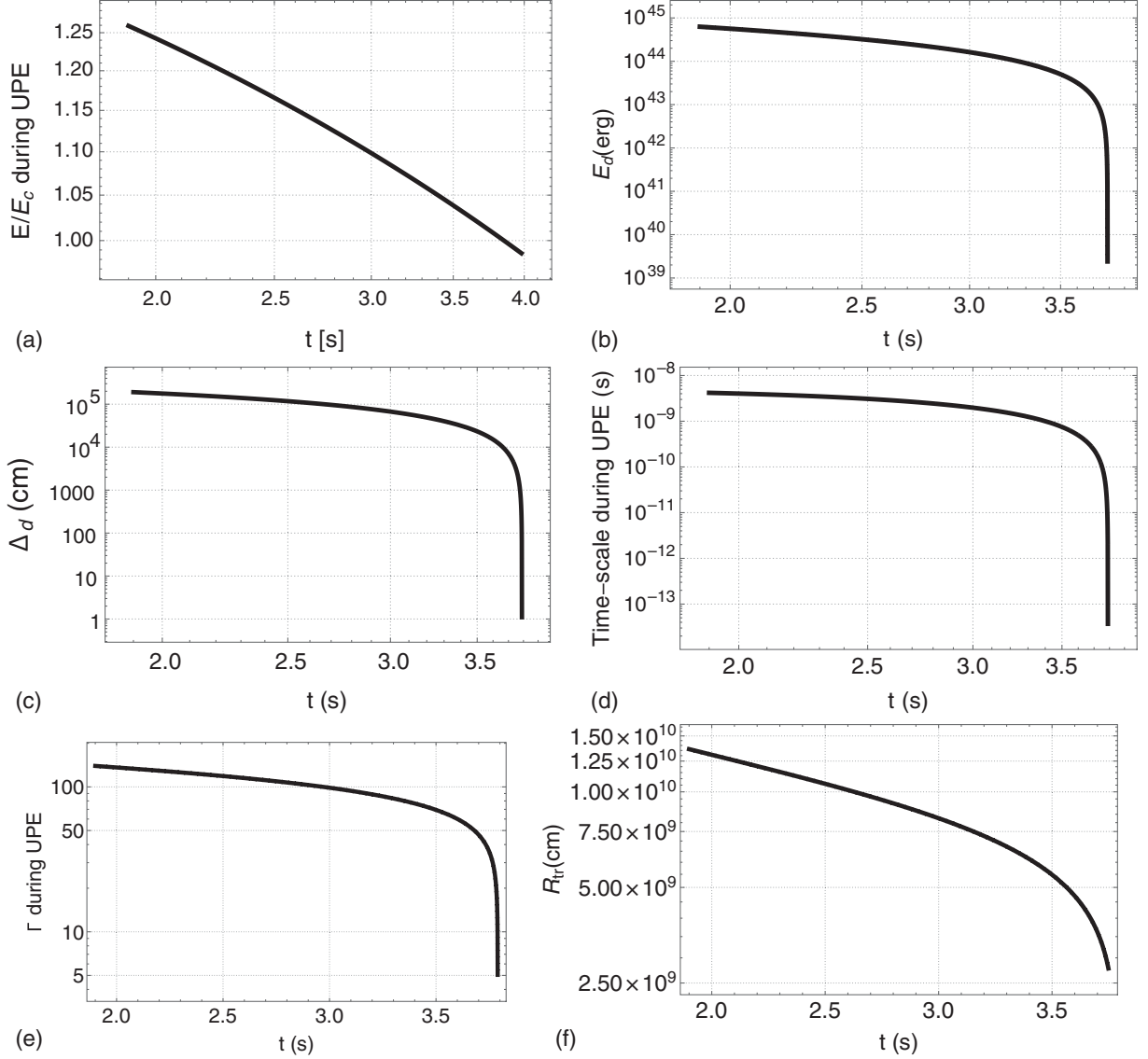
FIG. 6. The parameters of *inner engine* and transparency point, obtained for $B_0 = 2.3 \times 10^{14}$ G, as a function of rest-frame time for GRB 190114C during the UPE phase, namely in the rest-frame time interval $t_{\rm rf} = 1.9$–3.99 s. (a): The electric field during the UPE phase which is clearly overcritical and reaches its critical value at the end of the UPE phase ($t_{\rm rf} = 3.99$ s). (b): The energy of dyadoregion during the UPE phase obtained from Eq. (20). (c): The width of dyadoregion obtained from Eq. (23) which tends to zero at the end of UPE phase, indicating that the number of e^+e^- pairs are suppressed and the UPE phase is over. (d): Repetition timescale of the *inner engine* during the UPE phase obtained from Eq. (44). (e): The decrease of the Lorentz factor, Γ, as a function of rest-frame time. This indicates the fact that Γ tends to unity for the last layers which confirms the end of UPE is reached. (f): The evolution of transparency radius; see Sec. X.

II. *FERMI* DATA OF GRB 190114C

At $20\!:\!57\!:\!02.63$ UT on 14 January 2019, *Fermi*-GBM was triggered by GRB 190114C [31]. The *Fermi*-LAT had a boresight angle of 68 degrees at the trigger time, the GRB remained in the field of view of *Fermi*-LAT for 150 s. With the redshift of $z = 0.424$ [32] the isotropic energy of this burst is $E_{\rm iso} = (2.48 \pm 0.22) \times 10^{53}$ erg. Since BdHNe I are characterized by $E_{\rm iso} \gtrsim 10^{52}$ erg, we have identified GRB 190114C as a BdHN I and predict the occurrence of

an associated SN [33]. This prediction was followed by the successful observation of the SN associated with this burst [34]. The first GeV photon with probability more than 90% belonging to this GRB is a ~0.9 GeV photon observed at $t_{\rm rf} = 1.9$ s after the GBM trigger. The highest-energy photon is a 22.9 GeV event which is observed 15 s after the GBM trigger [35]. GRB 190114C has become since a prototype for identifying the BdHN I episodes.

Three different episodes have been identified in the *Fermi*-GBM data; see Fig. 1:

Episode 1 with an isotropic energy of $E_{iso} = (1.0 \pm 0.12) \times 10^{53}$ erg, occurs in the rest-frame time interval $t_{rf} = [0, 1.9]$ s, being $t_{rf} = 0$ s the *Fermi*-GBM rest-frame trigger time. It reveals a thermal component from $t_{rf} = 0.79$ s to $t_{rf} = 1.18$ s, in its spectral analysis, marking the rise of newly born NS (*νNS–rise*) with a corresponding isotropic energy of $E_{\nu NS}^{iso} = (2.82 \pm 0.13) \times 10^{52}$ erg.

Episode 2, with an isotropic energy of $E_{iso} = (1.47 \pm 0.2) \times 10^{53}$ erg, equivalent to 40% of isotropic energy of the GRB, lasts only 2 s. It occurs in the rest-frame time interval $t_{rf} = [1.9, 3.99]$ s. It encompasses three major events: (a) The formation of the BH, observation of the first GeV photon at $t_{rf} = 1.9$ s, see details in Ruffni *et al.* [12]. (b) An increase of the 0.1–100 GeV luminosity following a power-law of $L_{GeV} = 8.7 \times 10^{50} \, t^{+(1.77 \pm 0.28)}$ erg s^{-1}. (c) The energetically dominant UPE phase observed by *Fermi*-GBM in the 10 keV–10 MeV band, occurring in the entire interval $t_{rf} = 1.9$ s–3.99 s fulfilling a hierarchical structure signed by a spectrum composed of a thermal emission and a cutoff power-law component (CPL + BB); see Sec. III.

Episode 3, the "cavity", starts at $t_{rf} = 11$ s and ends at $t_{rf} = 20$ s. The presence of a "cavity" in GRB 190114C, carved out in the SN ejecta by the BH formation, has been confirmed in Ruffni *et al.* [29].

The GeV luminosity following the UPE phase is best fitted by the *decreasing* power-law of $L_{GeV} = (7.75 \pm 0.44) \times 10^{52} \, t^{-(1.2 \pm 0.04)}$ erg s^{-1}, with an isotropic energy of $E_{GeV} = (1.8 \pm 1.3) \times 10^{53}$ erg. The spectrum of *Fermi*-LAT in the 0.1–100 GeV energy band, after the UPE phase, is best fitted by a power-law [36]; see Fig. 1 and Moradi *et al.* [13] for more details.

All these results have been presented in Ruffni *et al.* [27], Ruffni *et al.* [29], Ruffni *et al.* [12] and Moradi *et al.* [13].

III. THE TIME-RESOLVED SPECTRAL ANALYSIS, THE HIERARCHICAL STRUCTURE, AND THE MEV LUMINOSITY OF THE UPE PHASE

Following the spectral analysis performed over the UPE phase from $t_{rf} = 1.9$ s to $t_{rf} = 3.9$ s (first iteration), we perform the spectral analysis over the 1 second intervals ($\Delta t_{rf} = 1$ s), namely [1.9s–2.9s] and [2.9s–3.9s](second iteration).

Each half intervals are further divided in half (third iteration), i.e., $\Delta t_{rf} = 0.5$ s: [1.9s–2.40s], [2.40s–2.9s], [2.9s–3.4s], and [3.4s–3.9s] and the corresponding spectral analysis is performed over each interval.

We further divide the UPE into 8 intervals of $\Delta t_{rf} = 0.25$ s (fourth iteration): [1.9s–2.15s], [2.15s–2.40s], [2.40s–2.65s], [2.65s–2.9s], [2.9s–3.15s], [3.15s–3.4s], [3.4s–3.65s], and [3.65s–3.9s], and perform the same spectral analysis over each interval.

We continue until the final iteration (fifth iteration), where the adequate signal-to-noise ratio S/N is fulfilled. The UPE is divided in 16 time intervals of $\Delta t_{rf} = 0.125$ s: [1.896s–2.019s], [2.019s–2.142s], [2.142s–2.265s], [2.265s–2.388s], [2.388s–2.511s], [2.511s–2.633s], [2.633s–2.756s], [2.756s–2.87s], [2.879s–3.002s], [3.002s–3.125s], [3.125s–3.248s], [3.248s–3.371s], [3.371s–3.494s], [3.494s–3.617s], [3.617s–3.739s], and [3.739s–3.862s] and perform the spectral analysis. After dividing into subintervals of 0.125 s one extra time interval of [3.862s–3.985s] has been added.

The spectral fitting of a cutoff power law plus black body (CPL + BB) is confirmed in each time interval and for each iterative process; see Table I, Fig. 2, Ruffni *et al.* [[27] for more details].

From a time-resolved analysis of the UPE phase, performed down to the fifth iteration, a hierarchical structure is obtained. It reveals a common spectral feature for each subinterval characterized by the CPL + BB best-fit model with a rest-frame temperature of $kT = 100$–300 keV and the ratio of blackbody flux (F_{BB}) to the total flux (F_{tot}) of:

$$0.1 \lesssim \frac{F_{BB}}{F_{tot}} \lesssim 0.5. \tag{3}$$

see Table I, Fig. 2 and Ruffni *et al.* [[27] for more information]

During the UPE phase the MeV luminosity is best fitted by

$$L_{MeV} = A_{MeV} t^{-\alpha_{MeV}}, \tag{4}$$

with slope $\alpha_{MeV} = 1.5 \pm 0.3$, and amplitude $A_{MeV} = (3.5 \pm 1.1) \times 10^{53}$ erg s^{-1}. This best fit is obtained from $\Delta t_{rf} = 0.125$ s time-resolved analysis and is fulfilled in all iterative sequences; see Table I and Figs. 1 and 3.

The existence of the thermal and the cutoff power-law components in the spectra of the UPE phase have been identified as the characteristic signature of $e^+ e^-$ pair creation in presence of baryons (PEMB pulse) originating from the vacuum polarization process [5–7,39]; see Sec. VII.

TABLE I. The parameters of the time-resolved spectral fits of the UPE phase of GRB 190114C, performed from $\Delta t_{\rm rf} = 2$ s down to subintervals of $\Delta t_{\rm rf} = 0.125$ s. The UPE phase extends from $t = 2.7$ s ($t_{\rm rf} = 1.9$ s) to $t = 5.5$ s ($t_{\rm rf} = 3.99$ s). Column 1; represents the time intervals in the observer's frame (Obs), column 2; the time intervals in the rest-frame (rf), column 3; the statistical significance (S) for each time interval, column 4; the power-law index of the cutoff power-law (CPL) component, column 5; the rest-frame cut-off energy, column 6; the rest-frame black body (BB) temperature, column 7; the Akaike Information Criterion/Bayesian Information Criterion (AIC/BIC), column 8; the BB flux ($F_{\rm BB}$), column 9; the CPL + BB or total flux ($F_{\rm tot}$), column 10; the ratio of the BB flux to the total flux, $F_{\rm BB}/F_{\rm tot}$ and, finally column 11; the isotropic energy in each time interval. As it can be seen from column 10, the $F_{\rm BB}/F_{\rm tot}$ remains almost constant in each iteration. The AIC (Akaike [37]) and the BIC (Schwarz *et al.* [38]) methods were used to select non-nested and nested models, respectively [see [18–23], for more information about these methods]. Table is taken from Ruffni *et al.* [27] with permission of authors.

$t_1 \sim t_2$ (s) Obs	$t_{rf,1} \sim t_{rf,2}$ (s) Rest-frame	S	α	E_c (keV)	kT (keV)	ΔDIC	$F_{\rm BB}$ (10^{-6}) (erg cm^{-2} s^{-1})	$F_{\rm tot}$ (10^{-6}) (erg cm^{-2} s^{-1})	$F_{\rm ratio}$	$E_{\rm tot}$ (erg)
$2.700 \sim 5.500$	$1.896 \sim 3.862$	418.62	$-0.71^{+0.02}_{-0.02}$	$717.6^{+25.4}_{-25.4}$	$159.0^{+3.6}_{-3.6}$	$-3344/6697/6719$	$22.49^{+3.21}_{-2.65}$	$111.10^{+11.60}_{-10.40}$	0.20	$1.50e+53$
$2.700 \sim 4.100$	$1.896 \sim 2.879$	296.60	$-0.51^{+0.02}_{-0.02}$	$696.6^{+31.9}_{-32.4}$	$209.7^{+9.3}_{-9.1}$	$-2675/5360/5381$	$24.67^{+6.93}_{-5.35}$	$142.50^{+23.90}_{-21.00}$	0.17	$9.64e+52$
$4.100 \sim 5.500$	$2.879 \sim 3.862$	318.07	$-0.90^{+0.02}_{-0.02}$	$639.3^{+31.9}_{-31.6}$	$130.6^{+2.5}_{-2.5}$	$-2529/5069/5090$	$25.55^{+2.97}_{-2.75}$	$80.98^{+9.68}_{-8.07}$	0.32	$5.48e+52$
$2.700 \sim 3.400$	$1.896 \sim 2.388$	204.30	$-0.59^{+0.03}_{-0.03}$	$724.7^{+44.5}_{-45.5}$	$220.0^{+17.1}_{-17.2}$	$-1882/3774/3796$	$18.55^{+44.5}_{-7.40}$	$123.90^{+29.20}_{-22.30}$	0.15	$4.19e+52$
$3.400 \sim 4.100$	$2.388 \sim 2.879$	225.88	$-0.46^{+0.04}_{-0.04}$	$699.8^{+47.8}_{-48.3}$	$196.7^{+8.9}_{-8.7}$	$-2032/4074/4095$	$31.78^{+9.60}_{-7.31}$	$161.40^{+47.10}_{-32.40}$	0.20	$5.46e+52$
$4.100 \sim 4.800$	$2.879 \sim 3.371$	233.97	$-0.84^{+0.03}_{-0.03}$	$608.1^{+42.1}_{-42.2}$	$130.4^{+3.7}_{-3.9}$	$-1880/3770/3792$	$23.94^{+4.20}_{-4.22}$	$85.37^{+14.83}_{-12.27}$	0.28	$2.89e+52$
$4.800 \sim 5.500$	$3.371 \sim 3.862$	227.90	$-0.96^{+0.03}_{-0.03}$	$679.5^{+49.1}_{-48.7}$	$130.6^{+3.1}_{-3.2}$	$-1809/3628/3649$	$27.18^{+4.01}_{-3.73}$	$78.20^{+11.40}_{-9.66}$	0.35	$2.65e+52$
$2.700 \sim 3.050$	$1.896 \sim 2.142$	148.59	$-0.59^{+0.03}_{-0.03}$	$547.7^{+44.2}_{-44.9}$	$240.8^{+29.2}_{-29.1}$	$-1187/2384/2406$	$19.67^{+17.96}_{-8.88}$	$103.20^{+30.60}_{-20.28}$	0.19	$1.75e+52$
$3.050 \sim 3.400$	$2.142 \sim 2.388$	145.04	$-0.60^{+0.02}_{-0.02}$	$965.2^{+28.5}_{-30.1}$	$203.5^{+14.8}_{-14.8}$	$-1320/2650/2671$	$22.87^{+8.88}_{-7.23}$	$152.00^{+24.00}_{-21.00}$	0.15	$2.57e+52$
$3.400 \sim 3.750$	$2.388 \sim 2.633$	134.60	$-0.63^{+0.04}_{-0.04}$	$885.7^{+70.9}_{-70.1}$	$240.6^{+10.5}_{-10.6}$	$-1224/2458/2480$	$41.02^{+11.09}_{-7.91}$	$129.10^{+32.40}_{-23.40}$	0.32	$2.18e+52$
$3.750 \sim 4.100$	$2.633 \sim 2.879$	187.77	$-0.35^{+0.06}_{-0.05}$	$607.8^{+57.1}_{-60.1}$	$151.5^{+12.4}_{-14.2}$	$-1428/2866/2887$	$23.92^{+12.46}_{-10.40}$	$192.00^{+101.70}_{-60.30}$	0.12	$3.25e+52$
$4.100 \sim 4.450$	$2.879 \sim 3.125$	171.81	$-0.69^{+0.04}_{-0.04}$	$515.9^{+43.6}_{-43.6}$	$117.3^{+5.0}_{-5.0}$	$-1271/2552/2573$	$19.19^{+4.89}_{-4.40}$	$92.71^{+27.69}_{-22.43}$	0.21	$1.57e+52$
$4.450 \sim 4.800$	$3.125 \sim 3.371$	230.14	$-0.98^{+0.04}_{-0.04}$	$702.0^{+78.1}_{-78.2}$	$141.3^{+5.8}_{-5.8}$	$-1254/2518/2539$	$26.76^{+6.41}_{-5.47}$	$80.73^{+17.95}_{-14.95}$	0.33	$1.37e+52$
$4.800 \sim 5.150$	$3.371 \sim 3.617$	166.30	$-0.97^{+0.04}_{-0.04}$	$685.1^{+80.9}_{-68.6}$	$140.8^{+4.6}_{-4.6}$	$-1218/2447/2468$	$31.83^{+6.85}_{-4.98}$	$82.51^{+15.62}_{-12.33}$	0.39	$1.40e+52$
$5.150 \sim 5.500$	$3.617 \sim 3.862$	161.51	$-0.95^{+0.04}_{-0.04}$	$692.2^{+79.1}_{-77.7}$	$120.0^{+4.0}_{-4.0}$	$-1203/2416/2438$	$23.19^{+5.38}_{-3.81}$	$73.57^{+18.69}_{-12.93}$	0.32	$1.24e+52$
$2.700 \sim 2.875$	$1.896 \sim 2.019$	117.09	$-0.58^{+0.05}_{-0.05}$	$470.5^{+74.4}_{-83.7}$	$261.5^{+29.0}_{-27.9}$	$-640/1291/1311$	$33.68^{+20.39}_{-14.33}$	$112.30^{+28.37}_{-25.73}$	0.30	$9.50e+51$
$2.875 \sim 3.050$	$2.019 \sim 2.142$	94.40	$-0.68^{+0.04}_{-0.05}$	$627.6^{+87.0}_{-91.5}$	$258.0^{+30.1}_{-28.7}$	$-664/1337/1359$	$28.45^{+20.42}_{-12.51}$	$98.14^{+35.60}_{-26.44}$	0.29	$8.30e+51$
$3.050 \sim 3.225$	$2.142 \sim 2.265$	106.62	$-0.59^{+0.03}_{-0.03}$	$957.1^{+34.1}_{-34.9}$	$245.3^{+21.5}_{-21.0}$	$-768/1547/1568$	$25.71^{+13.87}_{-9.03}$	$169.30^{+38.20}_{-31.60}$	0.15	$1.43e+52$
$3.225 \sim 3.400$	$2.265 \sim 2.388$	100.40	$-0.73^{+0.06}_{-0.05}$	$1275.9^{+208.9}_{-215.4}$	$208.6^{+9.1}_{-9.2}$	$-669/1349/1369$	$36.78^{+9.54}_{-8.93}$	$144.90^{+33.02}_{-27.63}$	0.25	$1.23e+52$
$3.400 \sim 3.575$	$2.388 \sim 2.511$	98.23	$-0.59^{+0.05}_{-0.05}$	$804.0^{+86.7}_{-82.3}$	$255.9^{+17.4}_{-17.4}$	$-702/1414/1436$	$42.19^{+19.41}_{-13.59}$	$139.30^{+48.30}_{-35.60}$	0.30	$1.18e+52$
$3.575 \sim 3.750$	$2.511 \sim 2.633$	93.84	$-0.65^{+0.04}_{-0.04}$	$916.3^{+64.6}_{-67.7}$	$229.3^{+13.6}_{-13.5}$	$-730/1471/1492$	$39.25^{+11.97}_{-10.71}$	$119.50^{+32.90}_{-25.45}$	0.33	$1.01e+52$
$3.750 \sim 3.925$	$2.633 \sim 2.756$	126.63	$-0.51^{+0.02}_{-0.02}$	$960.9^{+30.9}_{-31.4}$	$204.6^{+9.9}_{-10.0}$	$-808/1627/1648$	$57.70^{+15.81}_{-12.25}$	$221.10^{+35.60}_{-31.50}$	0.26	$1.87e+52$
$3.925 \sim 4.100$	$2.756 \sim 2.879$	141.61	$-0.27^{+0.06}_{-0.06}$	$412.7^{+12.2}_{-11.9}$	$196.8^{+14.0}_{-16.1}$	$-729/1468/1488$	$32.20^{+19.05}_{-18.86}$	$176.50^{+12.91}_{-11.21}$	0.18	$1.49e+52$
$4.100 \sim 4.275$	$2.879 \sim 3.002$	122.91	$-0.54^{+0.06}_{-0.06}$	$474.1^{+45.5}_{-46.2}$	$162.6^{+14.9}_{-14.8}$	$-758/1526/1547$	$24.26^{+17.09}_{-10.09}$	$116.10^{+52.40}_{-35.12}$	0.21	$9.82e+51$
$4.275 \sim 4.450$	$3.002 \sim 3.125$	122.62	$-0.64^{+0.08}_{-0.08}$	$365.0^{+44.9}_{-48.5}$	$107.5^{+15.7}_{-12.6}$	$-675/1360/1380$	$9.04^{+9.47}_{-5.69}$	$72.20^{+19.06}_{-14.95}$	0.13	$6.11e+51$
$4.450 \sim 4.625$	$3.125 \sim 3.248$	111.94	$-1.04^{+0.05}_{-0.05}$	$640.0^{+108.7}_{-106.1}$	$161.0^{+11.1}_{-10.8}$	$-640/1290/1310$	$22.34^{+9.36}_{-6.65}$	$68.54^{+11.70}_{-11.21}$	0.33	$5.80e+51$
$4.625 \sim 4.800$	$3.248 \sim 3.371$	123.33	$-0.95^{+0.05}_{-0.05}$	$694.2^{+96.8}_{-94.2}$	$146.3^{+6.7}_{-6.6}$	$-734/1477/1499$	$35.59^{+9.47}_{-8.00}$	$89.91^{+27.59}_{-18.82}$	0.40	$7.60e+51$
$4.800 \sim 4.975$	$3.371 \sim 3.494$	129.65	$-0.85^{+0.05}_{-0.05}$	$564.5^{+68.9}_{-71.9}$	$135.3^{+7.5}_{-7.6}$	$-744/1498/1519$	$30.78^{+11.12}_{-8.55}$	$96.58^{+31.02}_{-23.68}$	0.32	$8.17e+51$
$4.975 \sim 5.150$	$3.494 \sim 3.617$	107.36	$-1.10^{+0.04}_{-0.04}$	$820.5^{+115.0}_{-111.2}$	$149.7^{+5.9}_{-5.8}$	$-683/1376/1398$	$32.76^{+6.98}_{-5.92}$	$71.57^{+16.74}_{-11.99}$	0.46	$6.05e+51$
$5.150 \sim 5.325$	$3.617 \sim 3.739$	108.96	$-1.04^{+0.05}_{-0.05}$	$765.2^{+119.0}_{-115.8}$	$130.9^{+5.8}_{-5.8}$	$-697/1404/1426$	$26.14^{+7.02}_{-5.96}$	$66.70^{+20.48}_{-14.17}$	0.39	$5.64e+51$
$5.325 \sim 5.500$	$3.739 \sim 3.862$	121.57	$-0.88^{+0.06}_{-0.06}$	$635.3^{+88.7}_{-92.0}$	$108.9^{+5.3}_{-5.4}$	$-736/1483/1504$	$20.90^{+6.51}_{-5.15}$	$79.48^{+28.02}_{-21.03}$	0.26	$6.72e+51$

IV. THE PROPERTIES OF *INNER ENGINE*

The discovery of the *inner engine* obtained by incorporating the Papapetrou-Wald solution [10–13,17], around the newborn Kerr BH in the BdHNe I, in presence of the low density plasma of the cavity, see [29], was operative in the classical electrodynamics with $|\mathbf{E}| < E_c$ process and leading to the generation by synchrotron radiation of the GeV emission in GRB 130427A and GRB190114C. We also apply here this *inner engine* in the $|\mathbf{E}| > E_c$ regime to describe the quantum electrodynamics process.

Wald's work is based on the Papapetrou discovery [10] that Killing vectors are vector potential solutions of

sourceless Maxwell equations in vacuum spacetimes in the test field approximation (i.e., no metric backreaction). A linear combination of these two Killing vector solutions led Wald to the solution for a rotating BH immersed in a uniform magnetic field B_0, aligned with the rotation axis of the Kerr BH at infinity.

The electromagnetic field of the *inner engine* in the Carter's orthonormal tetrad is

$$E_{\hat{r}} = \frac{\hat{a}B_0}{\Sigma}\left[r\sin^2\theta - \frac{\hat{M}(\cos^2\theta+1)(r^2-\hat{a}^2\cos^2\theta)}{\Sigma}\right], \quad (5)$$

$$E_{\hat{\theta}} = \frac{\hat{a}B_0}{\Sigma}\sin\theta\cos\theta\sqrt{\Delta}, \quad (6)$$

$$B_{\hat{r}} = -\frac{B_0\cos\theta}{\Sigma}\left[-\frac{2\hat{a}^2\hat{M}r(\cos^2\theta+1)}{\Sigma}+\hat{a}^2+r^2\right], \quad (7)$$

$$B_{\hat{\theta}} = \frac{B_0 r}{\Sigma}\sin\theta\sqrt{\Delta}. \quad (8)$$

where $\Sigma = r^2 + \hat{a}^2\cos^2\theta$, $\Delta = r^2 - 2\hat{M}r + \hat{a}^2$, $\hat{M} = GM/c^2$, $\hat{a} = a/c = J/(Mc)$, being M and J the mass and angular momentum of the Kerr BH. The (outer) event horizon is located at $r_+ = (\hat{M} + \sqrt{\hat{M}^2 - \hat{a}^2})$.

The electromagnetic field in the polar direction $\theta = 0$ and at small angles from it is well approximated by [12,17]:

$$E_{\hat{r}} = -\frac{2B_0 JG}{c^3}\frac{(r^2-\hat{a}^2)}{(r^2+\hat{a}^2)^2} \quad (9)$$

$$E_{\hat{\theta}} = 0 \quad (10)$$

$$B_{\hat{r}} = \frac{B_0(-\frac{4GJ^2 r}{M(r^2+\hat{a}^2)}+a^2+r^2)}{(r^2+\hat{a}^2)} \quad (11)$$

$$B_{\hat{\theta}} = 0. \quad (12)$$

Equation (9) is the same as the radial electric field of the Kerr-Newman metric in the same tetrad just substituting to the charge Q of the Kerr-Newman solution the effective charge Q_{eff}, given by Eq. (1), see, e.g., [40]. Therefore, up to linear order in θ and in the dimensionless BH spin parameter $\alpha \equiv \hat{a}/(GM/c^2)$, the electric field can be written as

$$E_{\hat{r}} = -\frac{2B_0 JG}{c^3}\frac{(r^2-\hat{a}^2)}{(r^2+\hat{a}^2)^2} \approx -\frac{1}{2}\alpha B_0\frac{r_+^2}{r^2}, \quad (13)$$

which for spin values $\alpha \lesssim 0.7$, the available electrostatic energy is well approximated by

$$\mathcal{E} \approx \frac{(2B_0 JG/c^3)^2}{2r_+} = \frac{Q_{\text{eff}}^2}{2r_+} = 1.25 \times 10^{43}\frac{\beta^2\alpha^2\mu^3}{1+\sqrt{1-\alpha^2}} \text{ erg,} \quad (14)$$

where we have normalized the mass and magnetic field strength by, respectively, $\mu = M/M_\odot$ and $\beta = B_0/B_c$, being

$$B_c = E_c = \frac{m_e^2 c^3}{e\hbar} \approx 4.41 \times 10^{13} \text{ G,} \quad (15)$$

the critical field for vacuum polarization; see Ruffni *et al.* [12] for more details.

The values μ and β in this general equations will be determined as a function of astrophysical process operative in the *inner engine* in GRB 190114C. The corresponding description of the overcritical and the undercritical fields are represented in the next sections.

We adopt that the magnetic field and BH spin are parallel, therefore along the symmetry axis direction electrons in the surrounding ionized medium are repelled, while protons are pulled into the BH [see [12] for additional details].

V. THE MASS AND SPIN OF THE BH OF GRB 190114C

We here recall the self-consistent solution following the UPE phase, well tested in the case of GRB 130427A [12] and GRB 190114C [13] which fulfills three conditions: (1) The GeV energetics observed by the Fermi-LAT is paid by the extractable energy of the BH, i.e.: $E_{\text{GeV}} = E_{\text{extr}}$. (2) The magnetic e^+e^- pair production (MPP) process does not occur around the BH, therefore the GeV photons fulfill the transparency condition. (3) The timescale of the synchrotron radiation determines the timescale of observed GeV radiation.

Having these conditions, and assuming the minimum energy budget requirement;, the *inner engine* parameters at $t > t_{\text{rf}} = 3.99$ s, i.e., after the UPE phase, are: magnetic field strength $B_0 \approx 3.9 \times 10^{10}$ G, spin and BH mass, respectively, $\alpha = 0.41$ and $M = 4.45 \, M_\odot$. The corresponding BH irreducible mass is $M_{\text{irr}} = 4.35 \, M_\odot$ see Moradi *et al.* [13] for more details.

VI. DETERMINATION OF THE MASS AND SPIN OF THE BH DURING THE UPE PHASE

We have obtained in the previous section at $t_{\text{rf}} = 3.99$ s the values of mass and spin parameters of the BH and the magnetic field: $M = 4.45 \, M_\odot$, $\alpha = 0.41$, and $B_0 = 3.9 \times 10^{10}$ G, respectively. We now turn to the determination of the mass and spin of the BH during the UPE phase. The mass-energy formula of the Kerr BH ([41–43]; see also ch. 33 in [44]) is given by:

$$M^2 = \frac{c^2 J^2}{4G^2 M_{\mathrm{irr}}^2} + M_{\mathrm{irr}}^2. \tag{16}$$

We require that the energetics of the MeV radiation be explained by the extractable rotational energy of the Kerr BH, i.e.,

$$E_{\mathrm{MeV}} = E_{\mathrm{extr}} = (M - M_{\mathrm{irr}})c^2. \tag{17}$$

Therefore, the extractable energy is given by:

$$E_{\mathrm{extr}} = (M - M_{\mathrm{irr}})c^2 = \left(1 - \sqrt{\frac{1 + \sqrt{1 - \alpha^2}}{2}}\right) Mc^2. \tag{18}$$

The time derivative of Eq. (18) gives the luminosity

$$L_{\mathrm{MeV}} = -\frac{dE_{\mathrm{extr}}}{dt} = -\frac{dM}{dt}, \tag{19}$$

in which we assume that M_{irr} is constant for BH during the energy emission process.

From the luminosity of MeV radiation expressed in the rest-frame of the GRB, given by Eq. (4) in the time interval of the UPE phase (see also Fig. 3), and from the values of the spin and of the mass of the BH at $t_{\mathrm{rf}} = 3.99$ s, we can now work backward by integrating Eq. (19) and determine the BH mass and spin at the beginning of the UPE, when the BH is formed, namely at $t_{\mathrm{rf}} = 1.9$ s. We obtain $M = 4.53\ M_\odot$ and $\alpha = 0.54$, respectively.

This assumption demands that all the luminosity of UPE phase originates from the rotational energy of the BH. This point is going to be justified in the next sections.

VII. VACUUM POLARIZATION, DYADOREGION AND THE UPE PHASE

The UPE phase is characterized by an electric field $|\mathbf{E}| > E_c$ [7,26]. The problem of vacuum polarization due to the overcritical field has a vast literature which dates back to the concept of the dyadosphere [3] and dyadotorous in the Kerr-Newman geometry, developed in Cherubini *et al.* [30]. Dyado is from the Greek word "duados" for pair, indicating here the e^+e^- pairs. The dyadotorus is the region where the vacuum polarization processes occur around a rotating charged BH, leading to the production of e^+e^- pairs; see also [7] for details.

In order to evaluate this process in the present case, we adopt a description using the Kerr-Newman geometry for which an analytic formula for the energy contained in the dyadoregion has been derived in Cherubini *et al.* [30]. We have checked numerically that the energy of the dyadoregion in the Kerr-Newman geometry (see Eq. (20) below), setting the BH charge as the effective charge of the Papapetrou-Wald solution, $2B_0 JG/c^3$, is a good approximation of the one estimated numerically with the

Papapetrou-Wald solution. We have verified that the quantitative difference is at most 30%, which implies that this approximation does not affect our conclusions.

We can now evaluate the energy of e^+e^- pairs generated in the Papapetrou-Wald solution using the Kerr-Newman analogy. We use the Carter orthonormal frame, in which the flat spacetime Schwinger framework can be locally applied and determine the dyadoregion energy [see discussion in [30]]:

$$\begin{aligned}
E_{(r_+, r_{\mathrm{d}})} = {} & \frac{(2B_0 JG/c^3)^2}{4r_+}\left(1 - \frac{r_+}{r_{\mathrm{d}}}\right) + \frac{(2B_0 JG/c^3)^2}{4\hat{a}} \\
& \times \left[\left(1 + \frac{\hat{a}^2}{r_+^2}\right)\arctan\left(\frac{\hat{a}}{r_+}\right)\right. \\
& \left. - \left(1 + \frac{\hat{a}^2}{r_{\mathrm{d}}^2}\right)\arctan\left(\frac{\hat{a}}{r_{\mathrm{d}}}\right)\right],
\end{aligned} \tag{20}$$

where r_d is the radius of the dyadoregion

$$\left(\frac{r_d}{\hat{M}}\right)^2 = \frac{1}{2}\frac{\lambda}{\mu\epsilon} - \alpha^2 + \left(\frac{1}{4}\frac{\lambda^2}{\mu^2\epsilon^2} - 2\frac{\lambda}{\mu\epsilon}\alpha^2\right)^{1/2} \tag{21}$$

with $\epsilon = E_c M_\odot G^{3/2}/c^4 \approx 1.873 \times 10^{-6}$, and

$$\lambda = \frac{2B_0 JG/c^3}{\sqrt{GM}} = \frac{Q_{\mathrm{eff}}}{\sqrt{GM}}, \tag{22}$$

is the effective charge-to-mass ratio.

The characteristic width of the *dyadoregion*, i.e., the region around the BH where the electric field overcritical is

$$\Delta_{\mathrm{d}}(t) = r_d(t) - r_+(t). \tag{23}$$

VIII. TRANSPARENCY CONDITION IN THE UPE PHASE

The existence of overcritical fields in the UPE phase and the consequent production of an $e^+e^-\gamma$ plasma, have been addressed in Sec. VII.

In presence of an overcritical electric field around the BH, a sequence of events occur:

(1) An optically thick $e^+e^-\gamma$ plasma of total energy $E_{e^+e^-}^{\mathrm{tot}} = E_{\gamma,\mathrm{iso}}$ endowed with baryon load with a mass of M_B. The self-acceleration and expansion of such *PEMB pulses* has been described in Ruffni *et al.* [5]. The dynamics of the PEMB pulses due to the effect of baryonic matter (the remnant of the collapsed object) has been considered in [6]. The thermalization of the pair plasma is achieved almost instantaneously ($\sim 10^{-13}$ s) and expands due to its self-acceleration up to ultrarelativistic velocities ($\Gamma \sim 100$ in the case of long GRBs; [45,46]).

(2) The transparency of the $e^+e^-\gamma$ plasma. When the PEMB pulses expand with ultrarelativistic velocities, the $e^+e^-\gamma$ plasma becomes optically thin, a thermal radiation that has been called the Proper-GRB (P-GRB) is emitted [5,6]. The P-GRB is characterized by the observed thermal component; see Sec. II and Sec. III. The dynamics of the expanding plasma from the vicinity of the BH up to the transparency point is described by the plasma energy, $E_{e^+e^-}^{\text{tot}}$ and the baryon load parameter, $\mathcal{B} = M_B c^2 / E_{e^+e^-}^{\text{tot}}$ [5,6].

The total P-GRB energy in the comoving frame of each impulsive process is

$$
\begin{aligned}
E_{\text{P-GRB}}^{\text{com}} &= \int a T_{\text{com}}^4 dV_{\text{com}}, \\
&= a T_{\text{com}}^4 V_{\text{com}}
\end{aligned}
\tag{24}
$$

where a is radiation constant, T_{com} is the P-GRB temperature in the comoving frame and V_{com} is the volume of the PEMB pulses in the comoving frame.

Dividing Eq. (24) by the Doppler factor $\Gamma(1 - v/c)$ at transparency, i.e., when the P-GRB is emitted, being Γ and v the Lorentz factor and speed of the PEMB pulses, and assuming head-on emission; namely $\cos\vartheta = 1$ one can obtain:

$$
\frac{E_{\text{P-GRB}}^{\text{com}}}{\Gamma(1 - v/c)} = \frac{a T_{\text{com}}^4}{\Gamma(1 - v/c)} V_{\text{com}},
\tag{25}
$$

where we have assumed head-on emission and therefore fixed $\cos\vartheta = 1$ in the Doppler factor.

Since:

$$
\begin{aligned}
T_{\text{obs}} &= \frac{T_{\text{com}}}{\Gamma(1 - v/c)}, \\
E^{\text{obs}} &= \frac{E^{\text{com}}}{\Gamma(1 - v/c)}, \\
V_{\text{lab}} &= \frac{V_{\text{com}}}{\Gamma},
\end{aligned}
\tag{26}
$$

we have that:

$$
\begin{aligned}
E_{\text{P-GRB}}^{\text{obs}} &= a T_{\text{obs}}^4 \Gamma^3 (1 - v/c)^3 \Gamma V_{\text{lab}} \\
&= a T_{\text{obs}}^4 \Gamma^4 (1 - v/c)^3 4\pi R^2 \Delta_{\text{lab}},
\end{aligned}
\tag{27}
$$

where we have used the fact that $V_{\text{lab}} = 4\pi R^2 \Delta_{\text{lab}}$, where Δ_{lab} is the thickness of the PEMB pulses, and $a = 4\sigma/c$, being σ the Stefan-Boltzmann constant.

Moreover, we know from the condition of transparency

$$
\begin{aligned}
\tau &= \sigma_T (n_{e^+e^-} + \bar{Z} n_B) \Delta_{\text{lab}} \approx \sigma_T (\bar{Z} n_B) \Delta_{\text{lab}}, \\
&= \sigma_T \frac{\bar{Z} M_B}{m_N 4\pi R^2 \Delta_{\text{lab}}} \Delta_{\text{lab}} = 1,
\end{aligned}
\tag{28}
$$

where σ_T is the Thomson cross section, $\bar{Z}$ is the average atomic number of baryons ($\bar{Z} = 1$ for Hydrogen atom and $\bar{Z} = 1/2$ for general baryonic matter), m_N is nucleon mass and M_B is the baryon mass. Since the value of number density of e^+e^- can only be obtained numerically, for simplicity we assume here $n_{e^+e^-} \ll n_B$ and we have numerically checked that this assumption is indeed valid for the values of $\mathcal{B}$ considered here; namely $\mathcal{B} = 10^{-3}$–10^{-2}. In addition, we assume the constant slab approximation with a constant width Δ_{lab} in the laboratory frame following Ruffni *et al.* [5,6].

Therefore, the lower bound of the transparency radius is

$$
R^{\text{tr}} = \left(\frac{\sigma_T}{8\pi} \frac{M_B}{m_N} \right)^{1/2}.
\tag{29}
$$

By substituting Eq. (29) in Eq. (27), and dividing it by E_{iso}, one obtains:

$$
\frac{E_{\text{P-GRB}}^{\text{obs}}}{E_{\text{iso}}} = \frac{1}{2} a T_{\text{obs}}^4 \Gamma^4 (1 - v/c)^3 \sigma_T \frac{\mathcal{B}}{m_N c^2} \Delta_{\text{lab}},
\tag{30}
$$

where we used the fact that, by definition, $\mathcal{B} \equiv M_B c^2 / E_{\text{iso}}$.

Using the fact that:

$$
1 - v/c = \frac{1}{(1 + v/c)\Gamma^2} \simeq \frac{1}{2\Gamma^2},
\tag{31}
$$

where we assumed $v/c \sim 1$, that is certainly accurate at the transparency of the PEMB pulses, we have that:

$$
\frac{E_{\text{P-GRB}}^{\text{obs}}}{E_{\text{iso}}} = \frac{a T_{\text{obs}}^4}{16\Gamma^2} \sigma_T \frac{\mathcal{B}}{m_N c^2} \Delta_{\text{lab}}.
\tag{32}
$$

From the total energy conservation we have that:

$$
E_{\text{iso}} = E_{\text{P-GRB}}^{\text{obs}} + E_{\text{Kinetic}},
\tag{33}
$$

therefore

$$
1 = \frac{E_{\text{P-GRB}}^{\text{obs}}}{E_{\text{iso}}} + \frac{E_{\text{Kinetic}}}{E_{\text{iso}}}
\tag{34}
$$

where E_{Kinetic} is the kinetic energy of the baryonic PEMB pulses:

$$
E_{\text{Kinetic}} = (\Gamma - 1) M_B c^2.
\tag{35}
$$

By substituting Eq. (35) in Eq. (34) we have

$$
\mathcal{B} = \frac{1}{\Gamma - 1} \left(1 - \frac{E_{\text{P-GRB}}^{\text{obs}}}{E_{\text{iso}}} \right),
\tag{36}
$$

or, equivalently:

$$\Gamma = 1 + \mathcal{B}^{-1}\left(1 - \frac{E_{\text{P-GRB}}^{\text{obs}}}{E_{\text{iso}}}\right). \quad (37)$$

The radius of transparency, R^{tr}, is given by Eq. (29) in this theoretical approach:

$$R^{\text{tr}} = \left(\frac{\sigma_T}{8\pi}\frac{\mathcal{B}E_{\text{iso}}}{m_N c^2}\right)^{1/2}. \quad (38)$$

In general, from Eqs. (32) and (36), the values of $\mathcal{B}$ and Γ can be estimated by the values of $E_{\text{P-GRB}}^{\text{obs}}/E_{\text{iso}}$, T_{obs} and Δ_{lab}. Also, having E_{iso} and $\mathcal{B}$, we can obtain the transparency radius from Eq. (38).

IX. THE MAGNETIC FIELD INFERRED FROM THE $\Delta t = 0.125$ s TIME RESOLVED SPECTRAL ANALYSIS

As a specific example, we calculate the magnetic field and transparency parameters for the $\Delta t_{\text{rf}} = 0.125$ s time resolved interval, namely the fifth iteration analysis reported in Sec. III. Therefore, the UPE phase is assumed to be composed of 16 expanding PEMB pulses emitting an average isotropic energy of $E_{\text{iso}} \sim 10^{52}$ erg, with radiation timescale of $\tau_q = 0.125$ s, as reported in Table I.

Therefore, from (1) the ratio $E_{\text{P-GRB}}/E_{\text{iso}} = 0.3$, and (2) $E_{\text{P-GRB}} = E_{(r_+, r_d)}$, the electromagnetic energy stored in each expanding PEMB pulse should be $E_{(r_+, r_d)} = 0.3 \times E_{\text{iso}}$. Consequently, from Eq. (20) and the value of mass and spin parameter of the BH, the magnetic field needed to fulfill this energetic is $B_0 = 1.85 \times 10^{17}$ G. The Lorentz factor, $\Gamma \sim 1000$, the baryon load, $\mathcal{B} \sim 2 \times 10^{-3}$, and the radius of transparency, $R^{\text{tr}} \sim 10^{13}$ cm, are obtained using:

(i) the isotropic energy of each time interval, $E_{\text{iso}} \sim 10^{52}$ erg;

(ii) the ratio of black body energy to isotropic energy $E_{\text{P-GRB}}^{\text{obs}}/E_{\text{iso}} \sim 0.3$;

(iii) the value of black body temperature in keV reported in Table I;

(iv) the width of the dyadoregion at decoupling, $\Delta_{\text{lab}} = \Delta_d$ obtained from Eq. (23) for magnetic field of $B_0 = 1.85 \times 10^{17}$ G.

The results are shown in Fig. 5. It is appropriate to notice that the magnetic field of $B_0 = 1.85 \times 10^{17}$ G, obtained from the $\Delta t_{\text{rf}} = 0.125$ s time-resolved analysis, does not fulfill the boundary condition of the UPE phase, $|\mathbf{E}| = E_c$ at $t_{\text{rf}} = 3.99$ s. In the next section, we calculate the lowest limit of magnetic field and the minimum repetition time which fulfill the required boundary condition $|\mathbf{E}| = E_c$ at $t_{\text{rf}} = 3.99$ s.

X. THE LOWER LIMIT OF MAGNETIC FIELD DURING THE UPE PHASE

Having determined the boundary value of the magnetic field at $t_{\text{rf}} = 3.99$ s to be $B_0 = 3.9 \times 10^{10}$ G, we must now require that at $t_{\text{rf}} > 3.99$ s the electric to be undercritical, and overcritical inside the UPE phase. In Sec. VI, we have determined the overall behavior of the mass and spin of BH during the UPE since the moment of the formation of BH; see Fig. 4.

We set the value of B_0 in the UPE phase, i.e., at times $t_{\text{rf}} < 3.99$ s, such that the electric field therein is overcritical. The lower limit of the magnitude of magnetic field is determined in a way that in Eq. (13), $|E_{r_+}| = E_c$ at the end of the UPE phase; at $t_{\text{rf}} = 3.99$ s. For BH mass and spin parameter at the end of UPE, it implies a magnetic field of $\beta = B_0/B_c = 5.1$ or $B_0 = 2.3 \times 10^{14}$ G; see Fig. 6.

For $B_0 = 2.3 \times 10^{14}$ G and at the moment which BH is formed, namely $t_{\text{rf}} = 1.9$ s, $\lambda \approx 4.7 \times 10^{-5}$ [from Eq. (22)], which leads to $r_d = 1.15 r_+$. Having these values, the energy of dyadoregion at $t_{\text{rf}} = 1.9$ s is $E_d \approx 6.27 \times 10^{44}$ erg. The evolution of energy of dyadoregion is shown in Fig. 6(b).

The evolution of characteristic width of the dyadoregion is shown in Fig. 6(c). At $t_{\text{rf}} = 3.99$ s, the extent of the dyadoregion tends to zero confirming that not enough $e^+ e^-$ pairs are created and the UPE phase is finished.

A. The transparency condition obtained from the lower limit of magnetic field, $B_0 = 2.3 \times 10^{14}$ G

For $B_0 = 2.3 \times 10^{14}$ G, each expanding PEMB pulse; which are produced via vacuum polarization and self-expanded with different Lorentz factors, has an isotropic energy $\sim 10^{45}$ erg obtained from Eq. (20); see Fig. 6. The total isotropic energy of the UPE phase is $E_{\text{iso}}^{\text{UPE}} = 1.47 \times 10^{53}$ erg, therefore, this phase consists of $\sim 10^8$ impulses in the time interval 1.9–3.99 s. Radiation from each one of these PEMB pulse can be interpreted as a blackholic quantum introduced in Rueda and Ruffni [17].

As expressed in Sec. VIII, the key parameters for calculating the transparency radius of each impulse are: (1) its isotropic energy, E_{iso}, (2) the blackbody to isotropic energy ratio, $E_{\text{P-GRB}}^{\text{obs}}/E_{\text{iso}}$, (3) the blackbody temperature, (T_{obs}), and finally (4) the width $\Delta_{\text{lab}} = \Delta_d$.

From the *inner engine* theory, as presented in the previous subsection, for each impulse we have $E_{\text{iso}} \sim 10^{45}$ erg and the width of the dyadoregion at decoupling is $\Delta_d = 1.9 \times 10^5$ cm. From the hierarchical structure of UPE phase in this GRB presented by Eq. (3), we have $E_{\text{P-GRB}}^{\text{obs}}/E_{\text{iso}} \sim 0.3$ and the temperature $kT_{\text{obs}} \sim 150$ keV.

With these values of $E_{\text{P-GRB}}^{\text{obs}}/E_{\text{iso}}$, Δ_d, T_{obs}, and E_{iso}, we obtain via Eqs. (32), (36) and (38), the transparency radius of

$$R^{\text{tr}} = 9.4 \times 10^9 \text{ cm}, \quad (39)$$

the baryon load parameter

$$\mathcal{B} = 5.1 \times 10^{-3}, \quad (40)$$

and finally the Lorentz factor of

$$\Gamma \approx 139. \tag{41}$$

We have checked that these estimated values are in good agreement with the corresponding ones obtained from the numerical simulation of the PEMB pulses evolution. The corresponding values from the numerical simulation are: $R^{\text{tr}} = 9.3 \times 10^9$ cm, temperature $kT = 150$ keV, and Lorentz factor $\Gamma \sim 140$.

The evolution of the Lorentz gamma factor, Γ is shown in Fig. 6(e) indicating the fact that Γ tends to ~ 4 for the last shell which confirms the end of UPE is reached.

The evolution of transparency radius in the UPE of GRB 190114C, using the exact numerical values of energy and width of dyadoregion are also shown in Fig. 6(f).

B. The repetition time of sequence of the blackholic quanta

We now study the timescale of each blackholic quanta in which the system starts over. The new value of the electric field is set by the new values of the BH angular momentum and mass, $J = J_0 - \Delta J$ and $M = M_0 - \Delta M$, keeping the magnetic field value constant B_0 in which at $t_{\text{rf}} = 1.9$ s, i.e.,

$$\frac{\Delta J}{J} \approx \frac{\Delta M}{M} = 3.1 \times 10^{-9}. \tag{42}$$

Regarding the presence of the baryon load obtained from Eq. (36) in the acceleration process, we infer from the MeV luminosity, the evolution of the timescale $\tau_q(t)$ of the blackholic quantum by requiring it to explain the MeV emission, i.e.:

$$L_{\text{MeV}} = \frac{[1 - \mathcal{B}(\Gamma - 1)]E_{(r_+(t), r_d(t))}}{\tau_q(t)}. \tag{43}$$

In fact, the effect of baryon load is $(1 - \mathcal{B}\Gamma) \approx 0.3$. Therefore, we obtain for the timescale

$$\tau_q(t) = \frac{0.3E_{(r_+(t), r_d(t))}}{L_{\text{MeV}}}. \tag{44}$$

where the $E_{(r_+(t), r_d(t))}$ is the energy of dyadoregion obtained from Eq. (20), determined from the new values of J and M for each blackholic quanta and L_{MeV} is the MeV luminosity obtained from best fit represented by Eq. (4); the evolution of the blackholic timescale is shown in Fig. 6(d).

C. The approach of the $|\mathbf{E}| = E_c$ at the UPE phase boundary

From the above theoretical derivation, we can explicitly see that, for an iteration, such that the duration of each elementary process of the nth iteration is 10^{-9} s, namely

after 10^9 iterations, the physical model can be consistently implemented, deriving the necessary parameters characterizing the process, namely the energy of each PEMB pulse, the baryon load, the Lorentz factor, and the radius at transparency. From Fig. 6, it becomes clear that after $t_{\text{rf}} \sim 3.7$ s, the emission of quanta by the QED process becomes not effective and the classical regime is soon approached.

The lowest limit of the magnetic field to reach $|\mathbf{E}| = E_c$ occurs in an *inner engine* composed of a Kerr BH of initial mass of $M = 4.53 \, M_\odot$ and $\alpha = 0.51$, immersed with a uniform magnetic of $B_0 = 2.3 \times 10^{14}$ G with a radiation timescale of $\sim 10^{-9}$ s.

Indeed, the decrease of the magnetic field from $\beta = 5.1$ to $\beta = 8.9 \times 10^{-4}$ at $t_{\text{rf}} = 3.99$ s, can be explained as the result of the induced current created by pairs in the inward electric field, which screens the original magnetic field. This is a very interesting process that has consequences in different astrophysical scenarios. Therefore, we here limit ourselves to the above explanation and refer the reader for further details in the dedicated, separated publication [47].

All the above results: (1) are in perfect agreement with observational data; see Fig. 3 and, (2) overcome the compactness problem of the UPE phase. It is appropriate to mention all these results have been obtained guided by the hierarchical structure of the UPE phase.

XI. COMPARISON WITH OTHER APPROACHES

The magnetohydrodynamics of plasma accretion onto the Kerr BH was first addressed in Ruffini and Wilson [48] assuming he infinite conductivity condition, $F_{\mu\nu}U^\nu = 0$ implying $\mathbf{E} \cdot \mathbf{B} = 0$. In view of zero net charge on the surface of the BH, no process of energy extraction, neither by vacuum polarization nor by electromagnetic process was there possible [49].

Blandford and Znajek [50] returned on the same process and in order to overcome the difficulty of extracting energy and they introduced, in analogy with pulsar, the presence "*gaps*" [51,52].

Thorne and MacDonald [53], following Hanni and Ruffni [54], calculated the surface charge induced on the horizon of the Kerr BH immersed in the magnetic field in the Papapetrou-Wald solution [11]. Miniutti and Ruffni [55] explicitly manifested that the Papapetrou-Wald solution [11] implies $\mathbf{E} \cdot \mathbf{B} \neq 0$, and identified that the induced surface charge implies a quadrupolar distribution of electric field around the BH. These results were confirmed in [56]. Applying these works to the case of GRBs, it has been shown that the mathematical Papapetrou-Wald solution can be used in order to describe the *inner engine* of a GRB 130427A [12], which presents mechanism to extract the rotational energy of the Kerr BH. The process which occurs in the undercritical field regime leads to the

emission of synchrotron radiation in the GeV domain as well as ultrahigh energy cosmic rays (UHECRs) [13]. The synchrotron emission of the *inner engine* occurs near the BH horizon and is emitting in blackholic quanta [17].

The extrapolation to overcritical field regime, presented in this paper, leads to the explanation of the MeV radiation during the UPE phase.

In recent years, in parallel to the theoretical progresses in the field, computer simulations were also developed. These simulations point the fact that present plasma in any energy extracting scheme would screen the background electric field of the vacuum solution of Papapetrou-Wald from the magnetosphere; see e.g., Komissarov [57], Parfrey *et al.* [58]. These simulation mainly address the physics of active galactic nuclei (AGNs) and particularly attentive has been the review of their theoretical models indicated in Komissarov [57]. Their choice of parameters and physical processes are quite different from the ones we have used for the GRB analysis. In our GRB approach we have been guided by the theoretical explanation of a vast number of observations obtained from: (1) the unprecedented time-resolved spectral analysis of the UPE phase; (2) the power-law MeV luminosity observed by Fermi-GBM; and (3) the power-law GeV luminosity observed by Fermi-LAT. This allows us to identify the physical processes and parameters which had to be fulfilled in order to obtain the detailed acquired data. Their choice of parameters enforce $\mathbf{E} \cdot \mathbf{B} = 0$ condition so different from $\mathbf{E} \cdot \mathbf{B} \neq 0$ which has allowed us to obtain our results.

In our model, the magnetic field is left over by the collapse of the accreting NS to the BH, rooted in the surrounding material, and the electric field is created by the gravitomagnetic interaction of the spacetime rotation with the present magnetic field; see, e.g., Rueda *et al.* [14]. Following this procedure, and since the electric field is assumed to be overcritical, in a very short timescale $\sim \hbar/(m_e c^2) \approx 10^{-21}$ s, much shorter than any electromagnetic process, a dyadoregion originate dominated by the high density and high pressure of the neutral $e^+ e^- \gamma$ plasma [7].

The optically thick pair electromagnetic-baryon (PEMB) pulse self-accelerates to the ultra-relativistic regime and finally reaches the transparency point at the radius of $\sim 10^{10}$ cm. These classical results were obtained thanks to a collaboration with Wilson at Lawrence Livermore National Laboratory [5,6].

As soon as the BH is formed, the first and the most efficient process in action to produce the $e^+ e^-$ plasma and, consequently decreasing the rotational energy of BH, occurs through the Schwinger critical field pair production. Since an overwhelming amount of pair plasma is created in quantum timescales, the plasma expansion by its internal pressure starts well before any electric field screening.

This process takes a fraction of angular momentum of the Kerr BH. The BH then is left with a slightly smaller angular momentum $J^* = J - \Delta J$, with $\Delta J/J \sim 10^{-9}$, being

ΔJ the angular momentum, and the same magnetic field which leads to a new electric field created by the space-time rotation. As a result, the system starts a new process in presence of the same magnetic field B_0, kept rigorously constant and a new effective charge of $Q_{\mathrm{eff}}^* = Q_{\mathrm{eff}} - \Delta Q_{\mathrm{eff}}$ which $\Delta Q_{\mathrm{eff}} = 2B_0 \Delta J$.

This process continues till the moment that electric field is not overcritical anymore, and after that the sole electromagnetic process is at work. The expanding $e^+ e^- \gamma$ plasma sweeps away the matter in the cavity whose density after this process becomes $\sim 10^{-14}$ g cm^{-3}, and an undercritical electromagnetic field is left; see Ruffini *et al.* [29]. This low-density ionized plasma is needed to fulfill an acceleration of charged particles leading to the electrodynamical process around a newborn BH. In fact, this density is much below the Goldreich-Julian density $\rho_{\mathrm{GJ}} = 8 \times 10^{-12}$ g cm^{-3} obtained for the $B_0 = 3.9 \times 10^{10}$ G and $M = 4.45\ M_\odot$ and $a = 0.41M$. Moreover, the matter energy density inside the cavity is negligible comparing to the electromagnetic energy density, namely $\rho_M/(|B|^2 - |E|^2) \sim 10^{-14}$, while in Komissarov [57] this ratio is 0.05 or higher.

It is interesting that the *inner engine* operates as well in the supermassive BHs in active galactic nuclei in the $|\mathbf{E}| < E_c$ regime. In the case of M87, with a mass of a few $10^9\ M_\odot$, the repetition timescale is 0.68 d in the polar direction, with a quanta of $\mathcal{E} \sim 10^{45}$ erg [13].

XII. CONCLUSIONS

GRB 190114C has offered already the possibility of testing different Episodes of the BdHN I sequence by a time-resolved spectral analysis [1]; the νNS-rise [Becerra *et al.* in preparation], the formation of the BH triggering the UPE phase and the associated GeV emission (see Fig. 1), the formation of the cavity [29], the long-lasting emission in the X-ray afterglow from the spinning νNS [14], and in the GeV emission from the newly-formed BH [13].

The long lasting GeV radiation, with a luminosity following a power-law of $L_{\mathrm{GeV}} = (7.75 \pm 0.44) \times 10^{52}\ t^{-(1.2\pm0.04)}$ erg s^{-1}, has been shown to originate from the extraction of the rotational energy of a Kerr BH in a sequence of discrete "blackholic quanta" emission [17]. This process occurs in an *inner engine*, which is composed of an uniform magnetic field aligned with the rotation axis of the Kerr BH described by the Papapetrou-Wald solution [10,11] and immersed in a very low density fully ionized plasma with density as low as 10^{-14} g cm^{-3} [1,13,17,29].

One of the main results has been the concept of effective charge Q_{eff}, given by Eq. (1) driving the acceleration process in the *inner engine*.

The most unexpected result has been the discovery of hierarchical structure in the time-resolved spectral analysis on ever-decreasing timescales of the UPE phase of GRB 190114C by Ruffini *et al.* [27] and here updated in Sec. III. There, we have determined the spectral properties and

luminosities during and after the UPE phase, of the MeV emission observed by *Fermi*-GBM, and of the GeV emission observed by *Fermi*-LAT.

A new arena is open in this article linking the macroscopic hierarchical structure of the UPE phase to a microphysical sequence of discrete elementary events in a QED regime.

For the first time, we have here approached the energy extraction process from a Kerr BH by the general relativistic QED process occurring in the *inner engine*.

We have assumed that the electric field of the *inner engine* operates in an overcritical $|\mathbf{E}| > E_c$ during the UPE phase, and in an undercritical $|\mathbf{E}| < E_c$ just after the end of the UPE phase. A sharp separatix both in the theoretical treatment and in the observational properties of these two domains are evidenced.

The main result of this article is to have compared and contrasted the two different processes for explaining the MeV and GeV emissions of GRBs.

The first process, originating the MeV radiation, is dominated by the vacuum polarization originating from the overcritical field in the UPE phase. The overcritical field generates an initially optically thick $e^- e^- \gamma$-baryon plasma, which self-accelerates until reaching the point of transparency, a PEMB pulse. Typical values of $\Gamma \sim 100$ guarantee the avoidance of the compactness problem [8,9] in the UPE phase. We have shown that the magnetic field B_0 keeps a constant value during the UPE phase of order of $\sim 10^{14}$ G and reduces to 3.9×10^{10} G after the UPE phase.

The second process, originating the GeV emission, is based on the classical ultrarelativistic electrodynamics generated from the electrons injected in the magnetic field emitting synchrotron radiation close to the BH horizon, in selected energies with specific pitch angle dependence, see Fig. 9 in Ruffni *et al.* [12].

Both these processes originate from the rotational energy of the Kerr BH acting on a uniform magnetic field, aligned with the BH rotation axis, within Papapetrou-Wald solution.

The results presented here were expected since fifty years when the Christodoulou-Hawking-Ruffini mass-energy formula of the BH [41–43], as well as some of the pioneering works, using the vacuum polarization process of a BH, were established [3,59]. They were followed by fundamental contributions on the self-acceleration process of the $e^+ e^- \gamma$ optically thick plasma, PEMB pulses [3,5,6], and by the concepts of *dyadosphere* and *dyadotorus* [see [7], and references therein], which are the fundamental conceptual framework of this article. The revival of these concepts, as we explained in this article, has been made possible by the fundamental introduction of "*the effective charge*" overcoming the concept of a net charged BH and fulfilling, nevertheless, all the necessary electrodynamical process of an electrically charged BH.

The fact that all the properties of GRB 190114C have been confirmed to occur in GRB 130427A, GRB 160509A and GRB 160626B; see [28], allow us to extend and apply the analysis here performed for the *inner engine*, generally to all BdHNe I.

This has introduced a radical change by modifying the traditional energetic arguments based on the gravitational binding energy of massive particles geodesics, following a classical electrodynamics process in the Kerr metric occurring at very high density. Indeed, in [29], it has been shown how this *inner engine* operates most efficiently in a cavity in presence a very tenuous ionized plasma with density of 10^{-14} g cm^{-3} following a classical electrodynamics process. The *inner engine* equally works at high densities of the PEMB pulses in the quantum electrodynamics process. In both processes, the fundamental energetic role is being played by the rotational energy of the Kerr BH, which is converted by associated classical and quantum ultrarelativistic acceleration processes into the observed multiwavelength energy emissions and UHECRs. The application of the classical work of the innermost stable circular orbit (ISCO) of massive particles around Kerr BH, introduced in Ruffni and Wheeler [60], has been superseded in this new approach. The concepts of the dyadosphere and [3,5,6] and dyadotorus [30]s are the fundamental ones in this new electrodynamical scenario.

The most important result in this paper has been the understanding the role of hierarchical structure discovered in the time-resolved spectral analysis of the UPE phase, finally explained by their underlying quantum nature.

This long march was started by the intuitions announced in Ruffni *et al.* [27]. They have been here expanded and approached in their theoretical implication in this article. Although the motivations were clear, their detailed comprehension has needed further work which is here presented. We are ready to look at the implications of these results.

Thanks to the observation of GRB 190114C, which is by far the most complex fundamental physical system ever approached in Science, a new scenario is now open. The most unique complexity of BdHNe, their enormous energy emitted in an observer homogeneous Universe, see e.g., Ruffni *et al.* [61], and the special quantum and classical electrodynamics nature of their radiation make us wonder about the role GRB may play in the appearance of life in the Universe [62]. This new overarching conceptual description appears to be in sight thanks to the observation of GRB 190114C.

[1] R. Ruffini, R. Moradi, J. A. Rueda, L. Li, N. Sahakyan, Y. C. Chen, Y. Wang, Y. Aimuratov, L. Becerra, C. L. Bianco, C. Cherubini, S. Filippi, M. Karlica, G. J. Mathews, M. Muccino, G. B. Pisani, and S. S. Xue, Mon. Not. R. Astron. Soc. **504,** 5301 (2021).

[2] T. Damour and R. Ruffini, Phys. Rev. Lett. **35,** 463 (1975).

[3] R. Ruffini, in *49th Yamada Conference, Kyoto, Japan, 1998* [arXiv:astro-ph/9811232].

[4] T. Damour, R. S. Hanni, R. Ruffini, and J. R. Wilson, Phys. Rev. D **17,** 1518 (1978).

[5] R. Ruffini, J. D. Salmonson, J. R. Wilson, and S.-S. Xue, Astron. Astrophys. **350,** 334 (1999).

[6] R. Ruffini, J. D. Salmonson, J. R. Wilson, and S.-S. Xue, Astron. Astrophys. **359,** 855 (2000).

[7] R. Ruffini, G. Vereshchagin, and S. Xue, Phys. Rep. **487,** 1 (2010).

[8] M. Ruderman, in *Seventh Texas Symposium on Relativistic Astrophysics*, Annals of the New York Academy of Sciences Vol. 262, edited by P. G. Bergman, E. J. Fenyves, and L. Motz (1975), pp. 164–180.

[9] T. Piran, Rev. Mod. Phys. **76,** 1143 (2005).

[10] A. Papapetrou, Ann. L'Institut Henri Poincare Sect. (A) Phys. Theor. **4,** 83 (1966), http://www.numdam.org/item/AIHPA_1966__4_2_83_0/.

[11] R. M. Wald, Phys. Rev. D **10,** 1680 (1974).

[12] R. Ruffini, R. Moradi, J. A. Rueda, L. Becerra, C. L. Bianco, C. Cherubini, S. Filippi, Y. C. Chen, M. Karlica, N. Sahakyan, Y. Wang, and S. S. Xue, Astrophys. J. **886,** 82 (2019).

[13] R. Moradi, J. A. Rueda, R. Ruffini, and Y. Wang, Astron. Astrophys. **649,** A75 (2021).

[14] J. A. Rueda, R. Ruffini, M. Karlica, R. Moradi, and Y. Wang, Astrophys. J. **893,** 148 (2020).

[15] R. Ruffini, M. Karlica, N. Sahakyan, J. A. Rueda, Y. Wang, G. J. Mathews, C. L. Bianco, and M. Muccino, Astrophys. J. **869,** 101 (2018).

[16] Y. Wang, J. A. Rueda, R. Ruffini, L. Becerra, C. Bianco, L. Becerra, L. Li, and M. Karlica, Astrophys. J. **874,** 39 (2019).

[17] J. A. Rueda and R. Ruffini, Eur. Phys. J. C **80,** 300 (2020).

[18] L. Li, J.-J. Geng, Y.-Z. Meng, X.-F. Wu, Y.-F. Huang, Y. Wang, R. Moradi, Z. L. Uhm, and B. Zhang, Astrophys. J. **884,** 109 (2019).

[19] L. Li, Astrophys. J. Suppl. Ser. **242,** 16 (2019).

[20] L. Li, Astrophys. J. Suppl. Ser. **245,** 7 (2019).

[21] L. Li, Astrophys. J. **894,** 100 (2020).

[22] L. Li, F. Ryde, A. Pe'er, H.-F. Yu, and Z. Acuner, Astrophys. J. Suppl. Ser. **254,** 35 (2021).

[23] L. Li and B. Zhang, Astrophys. J. Suppl. Ser. **253,** 43 (2021).

[24] L. Becerra, C. L. Ellinger, C. L. Fryer, J. A. Rueda, and R. Ruffini, Astrophys. J. **871,** 14 (2019).

[25] R. Ruffini, Y. Wang, Y. Aimuratov, U. Barres de Almeida, L. Becerra, C. L. Bianco, Y. C. Chen, M. Karlica, M. Kovacevic, L. Li, J. D. Melon Fuksman, R. Moradi, M. Muccino, A. V. Penacchioni, G. B. Pisani, D. Primorac, J. A. Rueda, S. Shakeri, G. V. Vereshchagin, and S.-S. Xue, Astrophys. J. **852,** 53 (2018).

[26] R. Ruffini, L. Becerra, C. L. Bianco, Y. C. Chen, M. Karlica, M. Kovačević, J. D. Melon Fuksman, R. Moradi, M. Muccino, G. B. Pisani, D. Primorac, J. A. Rueda, G. V. Vereshchagin, Y. Wang, and S. S. Xue, Astrophys. J. 2018) 151 **,869**).

[27] R. Ruffini, L. Li, R. Moradi, J. A. Rueda, Y. Wang, S. S. Xue, C. L. Bianco, S. Campion, J. D. Melon Fuksman, C. Cherubini, S. Filippi, M. Karlica, and N. Sahakyan, arXiv:1904.04162.

[28] L. Li, R. Ruffini, J. A. Rueda, R. Moradi, Y. Wang, and S. S. Xue, arXiv:1910.12615.

[29] R. Ruffini, J. D. Melon Fuksman, and G. V. Vereshchagin, Astrophys. J. **883,** 191 (2019).

[30] C. Cherubini, A. Geralico, H. J. A. Rueda, and R. Ruffini, Phys. Rev. D **79,** 124002 (2009).

[31] R. Hamburg, P. Veres, C. Meegan, E. Burns, V. Connaughton, A. Goldstein, D. Kocevski, and O. J. Roberts, GRB Coordinates Network **23707,** 1 (2019).

[32] J. Selsing, J. Fynbo, K. Heintz, D. Watson, and S. Dyrbye, GRB Coordinates Network **23695** (2019).

[33] R. Ruffini, R. Moradi, Y. Aimuratov, U. Barres, V. A. Belinski, C. L. Bianco, Y. C. Chen, C. Cherubini, S. Filippi, D. M. Fuksman, M. Karlica, L. Li, D. Primorac, J. A. Rueda, N. Sahakyan, Y. Wang, and S. S. Xue, GRB Coordinates Network **23715,** 1 (2019).

[34] A. Melandri, L. Izzo, P. D'Avanzo, D. Malesani, M. Della Valle, E. Pian, N. R. Tanvir, F. Ragosta, F. Olivares, R. Carini, E. Palazzi, S. Piranomonte, P. Jonker, A. Rossi, D. A. Kann, D. Hartmann, C. Inserra, E. Kankare, K. Maguire, S. J. Smartt *et al.*, GRB Coordinates Network **23983** (2019).

[35] D. Kocevski, N. Omodei, M. Axelsson, and E. Burns, and the Fermi-LAT team, GRB Coordinates Network (2019).

[36] Y. Wang, L. Li, R. Moradi, and R. Ruffini, arXiv:1901.07505.

[37] H. Akaike, IEEE Trans. Autom. Control **19,** 716 (1974).

[38] G. Schwarz *et al.*, Ann. Stat. **6,** 461 (1978).

[39] R. Ruffini, J. D. Salmonson, J. R. Wilson, and S.-S. Xue, Astron. Astrophys. Suppl. Ser. **138,** 511 (1999).

[40] *Physics and Astrophysics of Neutron Stars and Black Holes*, edited by R. Giacconi and R. Ruffini (North-Holland Pub. Co., Amsterdam, New York, 1978).

[41] D. Christodoulou, Phys. Rev. Lett. **25,** 1596 (1970).

[42] D. Christodoulou and R. Ruffini, Phys. Rev. D **4,** 3552 (1971).

[43] S. W. Hawking, Phys. Rev. Lett. **26,** 1344 (1971).

[44] C. W. Misner, K. S. Thorne, and J. A. Wheeler, *Gravitation* (Freeman and Co., San Francisco, 1973).

[45] A. G. Aksenov, R. Ruffini, and G. V. Vereshchagin, Phys. Rev. Lett. **99,** 125003 (2007).

[46] A. G. Aksenov, R. Ruffini, and G. V. Vereshchagin, Phys. Rev. D **79,** 043008 (2009).

[47] S. Campion, J. Rueda, R. Ruffini, and S. Xue, Phys. Lett. B **820,** 136562 (2021).

[48] R. Ruffini and J. R. Wilson, Phys. Rev. D **12,** 2959 (1975).

[49] C. Cherubini, S. Filippi, A. Loppini, R. Moradi, R. Ruffini, Y. Wang, and S.-S. Xue, Phys. Rev. D **97,** 064038 (2018).

[50] R. D. Blandford and R. L. Znajek, Mon. Not. R. Astron. Soc. **179,** 433 (1977).

[51] P. A. Sturrock, Astrophys. J. **164,** 529 (1971).

[52] M. A. Ruderman and P. G. Sutherland, Astrophys. J. **196,** 51 (1975).

[53] K. S. Thorne and D. MacDonald, Mon. Not. R. Astron. Soc. **198,** 339 (1982).

[54] R. S. Hanni and R. Ruffini, Phys. Rev. D **8,** 3259 (1973).

[55] G. Miniutti and R. Ruffini, Nuovo Cimento B Ser. **115**, 751 (2000).

[56] B. Punsly, *Black Hole Gravitohydromagnetics*, Vol. 355 (Springer-Verlag Berlin Heidelberg, 2008).

[57] S. S. Komissarov, Mon. Not. R. Astron. Soc. **359**, 801 (2005).

[58] K. Parfrey, A. Philippov, and B. Cerutti, Phys. Rev. Lett. **122**, 035101 (2019).

[59] T. Damour and R. Ruffini, Phys. Rev. D **14**, 332 (1976).

[60] R. Ruffini and J. A. Wheeler, Phys. Today **24**, No. 1, 30 (1971).

[61] R. Ruffini, D. J. Song, and S. Taraglio, Astron. Astrophys. **190**, 1 (1988).

[62] P. Chen and R. Ruffini, Astronomy Reports **59**, 469 (2015).

Magnetic field screening in strong crossed electromagnetic fields

S. Campion [a,b], J.A. Rueda [a,b,c,d,e,*], R. Ruffini [a,b,f,g], S.S. Xue [a,b]

[a] *ICRA, Dipartimento di Fisica, Sapienza Università di Roma, P.le Aldo Moro 5, 00185 Rome, Italy*
[b] *International Center for Relativistic Astrophysics Network Piazza della Repubblica 10, I-65122 Pescara, Italy*
[c] *ICRANet-Ferrara, Dipartimento di Fisica e Scienze della Terra, Università degli Studi di Ferrara, Via Saragat 1, I–44122 Ferrara, Italy*
[d] *Dipartimento di Fisica e Scienze della Terra, Università degli Studi di Ferrara, Via Saragat 1, I–44122 Ferrara, Italy*
[e] *INAF, Istituto de Astrofisica e Planetologia Spaziali, Via Fosso del Cavaliere 100, 00133 Rome, Italy*
[f] *Université de Nice Sophia Antipolis, CEDEX 2, Grand Château Parc Valrose, Nice, France*
[g] *INAF, Viale del Parco Mellini 84, 00136 Rome, Italy*

ARTICLE INFO

ABSTRACT

We consider crossed electric and a magnetic fields $\left(\vec{B} = B\,\hat{z},\ \vec{E} = E\,\hat{y}\right)$, with $E/B < 1$, in presence of some initial number of $e^{\pm}$ pairs. We do not discuss here the mechanism of generation of these initial pairs. The electric field accelerates the pairs to high-energies thereby radiating high-energy synchrotron photons. These photons interact with the magnetic field via magnetic pair production process (MPP), i.e. $\gamma + B \rightarrow e^{+} + e^{-}$, producing additional pairs. We here show that the motion of all the pairs around the magnetic field lines generates a current that induces a magnetic field that shields the initial one. For instance, for an initial number of pairs $N_{\pm,0} = 10^{10}$, an initial magnetic field of 10^{12} G can be reduced a few percent. The screening occurs in the short timescales $10^{-21} \leq t \leq 10^{-15}$ s, i.e. before the particle acceleration timescale equals the synchrotron cooling timescale. The present simplified model indicates the physical conditions leading to the screening of strong magnetic fields. To assess the occurrence of this phenomenon in specific astrophysical sources, e.g. pulsars or gamma-ray bursts, the model can be extended to evaluate different geometries of the electric and magnetic fields, quantum effects in overcritical fields, and specific mechanisms for the production, distribution, and multiplicity of the $e^{-}e^{+}$ pairs.

1. Introduction

The process of screening of a strong electric field by means of the creation of electron-positron ($e^{\pm}$) pairs through quantum electrodynamics (QED) particles showers has been studied for many years. Recently, it was shown in [1] that an electric field as high as $E \sim \alpha_f E_{cr}$, where α_f is the fine structure constant and $E_{cr} = m_e^2 c^3/(e\hbar) \approx 1.32 \times 10^{16}$ V/cm is the critical field for vacuum polarization (see [2] for a review), cannot be maintained because the creation of particle showers depletes the field. To the best of our knowledge, no analog conclusion has been reached for a magnetic field. The main topic of this paper is to build a simple model to analyze the magnetic field screening (MFS) process owing to the motion of $e^{\pm}$ pairs in a region filled by magnetic $\vec{B}$ and electric $\vec{E}$ fields.

The basic idea of the screening process is explained by the following series steps:

1. An initial number of $e^{\pm}$ is placed in a region filled by $\vec{E}$ and $\vec{B}$, with $E/B < 1$, $B \leq B_{cr} = m_e^2 c^3/(e\hbar) \approx 4.4 \times 10^{13}$ G and then $E < E_{cr}$. These initial pairs could have been the result of vacuum breakdown, but we do not discuss here their creation process.

2. The initial pairs are accelerated by $\vec{E}$ and emit radiation via the curvature/synchrotron mechanism (or their combination), due to the $\vec{B}$ field.

3. The photons create a new $e^{\pm}$ pairs via the magnetic pair production process (MPP), $\gamma + B \rightarrow e^{-} + e^{+}$.

4. Also these new pairs are accelerated, radiate photons and circularize around the magnetic field lines. This circular motion generates a current that induces a magnetic field, $\vec{B}_{ind}$, oriented in the opposite direction with respect to the original one, thereby screening it. Due to the creation of new charged particles and to the proportionality between the strength of the fields, also the electric field is screened.

---

* Corresponding author at: International Center for Relativistic Astrophysics Network Piazza della Repubblica 10, I-65122 Pescara, Italy.
 E-mail address: jorge.rueda@icra.it (J.A. Rueda).

5. Since the series of the previous processes occurs at every time t, they could develop a particle shower.

A possible astrophysical scenario in which this study finds direct application is in the process of high-energy (MeV and GeV) emission from a BH in long gamma-ray bursts (GRBs), in view of the recently introduced "*inner engine*" [3,4] in the binary-driven hypernova (BdHN) model (see, e.g., [5–7]). The *inner engine* is composed of the newborn rotating BH, surrounded by the magnetic field (inherited from the collapsed NS) and low-density ionized matter from the SN ejecta, and it is responsible of the high-energy (GeV) emission observed in the GRB. The gravitomagnetic interaction of the rotating BH and the magnetic field induces an electric field which accelerates e^- which emit GeV photons by synchrotron radiation [3]. It has been argued in [7] that the magnetic field surrounding the BH could exceed the critical value, i.e. $B > B_{cr}$. Therefore, a situation in which $E \gtrsim E_{cr}$ could occur leading to a vacuum polarization process [2]. This could be the seed of the $e^\pm$ pairs we start with. If the MFS occurs, the optical depth for synchrotron photons could decrease sufficiently to allow them to freely escape from the region near the BH and become observable. Therefore, the physical process that we present here could be necessary to lead to the astrophysical conditions derived in [3] for the explanation of the GeV emission observed in long GRBs.

In this article, we build a first, simplified framework to study the problem of the MFS by $e^\pm$ pairs. We analyze the whole screening process for the specific configuration of perpendicular fields: $\vec{E} = E\ \hat{y}$ for the electric field and $\vec{B} = B\ \hat{z}$ for the magnetic field.

2. Particles dynamics

In this section, we start to build the equations that describe the particles dynamics and their creation.

The equations of motion of a particle immersed in an EM field[1] read (see, e.g., [8,9])

$$\frac{d\vec{r}}{dt} = c\vec{\beta}, \tag{1a}$$

$$\frac{d\vec{\beta}}{dt} = \frac{e}{mc\gamma}\left[\vec{E} + \vec{\beta}\times\vec{B} - \vec{\beta}(\vec{E}\cdot\vec{\beta})\right], \tag{1b}$$

$$\frac{d\gamma}{dt} = \frac{e}{mc}\left(\vec{E}\cdot\vec{\beta}\right) - \frac{I}{mc^2}, \tag{1c}$$

where I is the energy loss per unit time due to the radiation emitted by an accelerated particle. Following [10], we use the energy loss in the quantum regime written as:

$$I \equiv \left|-\frac{dE}{dt}\right| = \frac{e^2\ m^2\ c^3}{\sqrt{3}\ \pi\ \hbar^2}\overline{H}(\chi), \tag{2}$$

with $\overline{H}(\chi)$ defined in [10]. The parameter χ is defined as $\chi \equiv \varepsilon_*/2\ \varepsilon_e$ (see [10], and references therein for details), where $\varepsilon_* = \hbar\omega_*$ is the *critical photons energy*, with:

$$\omega_* = \frac{3e\gamma^2}{2mc}\sqrt{\left(\vec{E}+\vec{\beta}\times\vec{B}\right)^2 - \left(\vec{\beta}\cdot\vec{E}\right)^2}, \tag{3}$$

and being $\varepsilon_e = \gamma m_e c^2$ the electron/positron energy. For $\chi \gtrsim 1$, the particle radiates in the so-called quantum regime while, for $\chi < 1$, the particle radiates in the classical regime (see also Section 5.5). Equation (2) is valid in both regimes.

The radiation emitted by an accelerating particle with Lorentz factor γ is seen by an observer at infinity as confined within a cone of angle $\sim 1/\gamma$. Therefore, for ultra-relativistic particles ($\gamma \gg 1$), the radiated photons are seen to nearly follow the particle's direction of motion. We denote by ϕ the angle between the particle/photon direction and the magnetic field. Consistently, the square root in Eq. (3) already takes into account the relative direction between the photons and the fields.

The screening process starts when electrons are emitted inside the region where both $\vec{E}$ and $\vec{B}$ are present and proceeds through the series of steps described in section 1. The evolution with time of the photon number can be written as

$$\frac{dN_\gamma}{dt}(t,\phi) = N_\pm(t,\phi)\ \frac{I(t)}{\varepsilon_\gamma^e(t)}, \tag{4}$$

where I is the intensity in Eq. (2) and $N_\pm$ is the number of created pairs via the MPP process. The number of pairs is strictly related to the number of photons. Then, the equation for the evolution of the number of created pairs $N_\pm$ can be written as

$$\frac{dN_\pm}{dt}(t,\phi) = N_\gamma(t)\ R_A^e(t,\phi)\ c, \tag{5}$$

where R_A^e is the attenuation coefficient for the MPP process (see section 4).

3. Magnetic field equation

Let us introduce the curvature radius of the particle's trajectory [10]

$$\frac{1}{R_c} = \left|\frac{d\vec{\beta}}{cdt}\right| = \frac{e}{\gamma mc^2}\sqrt{\left(\vec{E}_{tot}+\vec{\beta}\times\vec{B}_{tot}\right)^2 - \left(\vec{\beta}\cdot\vec{E}_{tot}\right)^2}, \tag{6}$$

where B_{tot} and E_{tot} are the total magnetic and electric fields, respectively, as defined below.

The motion of a particle in the present EM field can be considered as the combination between acceleration along the z-direction, and in a series of coils around the magnetic field lines, in the $x-y$ plane. The linear number density of the particles on a path dl is defined as $n_\lambda = dN_\pm/dl$, while the current density in the two directions is $\vec{J}_\perp = e\ \vec{\beta}_\perp n_\lambda c$ and $\vec{J}_\parallel = e\ \vec{\beta}_\parallel n_\lambda c$, with $\beta_\perp = (\beta_x^2 + \beta_y^2)^{1/2}$ and $\beta_\parallel = \beta_z$.

The infinitesimal induced magnetic field $d\vec{B}_{ind}$ generated by the current of an element of the coil $dl = |d\vec{l}|$ is:

$$d\vec{B}_{ind} = \frac{J_\perp}{c}\frac{d\vec{l}\times\Delta\vec{r}}{\left|\Delta\vec{r}\right|^3} = \frac{J_\perp}{c}\frac{\left|d\vec{l}\right|}{\left|\Delta\vec{r}\right|^2}\hat{n} = e\ \beta_\perp\frac{dN_\pm}{dl}\frac{dl}{\left|\Delta\vec{r}\right|^2}\hat{n}, \tag{7}$$

where $\Delta\vec{r}$ is the vector connecting an element of the coil, in the $x-y$ plane, with an element of the coil axes and $\hat{n}$ is the versor normal to the $\Delta\vec{r}-d\vec{l}$ plane (since $d\vec{l}$ and $\Delta\vec{r}$ are always perpendicular). The only non-zero component of the magnetic field vector is the one parallel to the coil axes. Then, we have only $dB_z = dB\sin\theta$, where $\sin(\theta) = R_c(t)/\left|\Delta\vec{r}\right|$ and $\left|\Delta\vec{r}\right| = \sqrt{z^2 + R_c(t)^2}$, with z the height on the coil axes. At the coil center ($z = 0$) and writing $dl = c\ dt$, we obtain

$$\frac{dB_{z,ind}}{dt} = e\frac{\beta_\perp(t)}{R_c(t)^2}\frac{dN_\pm}{dt}. \tag{8}$$

Here $B_{tot}(t) = B_0 - B_{ind}(t)$ is the total magnetic field; B_0 is the initial background magnetic field. Fig. 1 shows a schematic representation of the screening process.

---

[1] We use throughout cgs-Gaussian units in which the magnetic and electric fields share the same dimensions (g$^{1/2}$ cm$^{-1/2}$ s^{-1}). We also use a -2 signature so the spacetime metric is $\eta_{\mu\nu} = (1, -1, -1, -1)$.
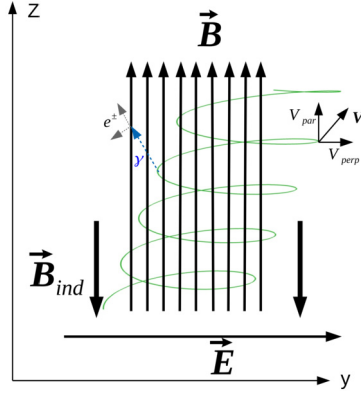
Fig. 1. Schematic representation of the screening process for perpendicular fields $(\vec{B} = B\,\hat{z}, \ \vec{E} = E\,\hat{y})$. The green lines represent the coils of the particles path.

4. Pair production rate

In Eq. (5), we introduced the attenuation coefficient for the magnetic pair production R_A^e. Hereafter, we refer to as $\zeta \equiv R_A^e c$ the MPP rate. In [11], it was derived the expression for the pair production rate, in the observer frame at rest, in strong perpendicular electric and magnetic fields ($\vec{E} \cdot \vec{B} = 0$).

4.1. Production rate for perpendicular fields

In the present configuration of the fields, we study the pair production for a general direction propagation of photons. Let us consider a photon with energy ε_γ and momentum vector $\hbar\vec{k}$, with director cosines $(\eta_x, \ \eta_y, \ \eta_z)$. Following [11], we apply a Lorentz transformation along the x-direction to a new frame, K', where there is no electric field; we calculate all the necessary quantities and the rate in K' and, finally, we transform them back to the lab frame.

We introduce the photon four-momentum as $k^{\,\mu} = (\omega/c, \vec{k})$ and the four-vector for the photon direction as $\eta^{\,\mu} = (1, \vec{k}/k^0)$, with k^0 the time component of $k^{\,\mu}$, i.e. the photon energy. The photon energy and director cosines in the K' frame are (1, 2, 3 stand for x, y, z):

$$\varepsilon'_\gamma = \gamma^* \left(1 - \beta^* \eta^1\right) \varepsilon_\gamma \tag{9a}$$

$$\eta'^1 = \frac{k^0}{k'_0} \Lambda^1_{\ \nu} \eta^{\,\nu} = \frac{\varepsilon_\gamma}{\varepsilon'_\gamma} \gamma^* \left(\eta^1 - \beta^*\right) \tag{9b}$$

$$\eta'^2 = \frac{\varepsilon_\gamma}{\varepsilon'_\gamma} \eta^2, \ \ \eta'^3 = \frac{\varepsilon_\gamma}{\varepsilon'_\gamma} \eta^3, \tag{9c}$$

where $\varepsilon_\gamma = \hbar k^0$. The component of the magnetic field in the K' frame perpendicular to the propagation direction of the photons, is given by:

$$\vec{B}' \times \vec{\eta}' = \left(B'_\| \hat{e}'_\| + B'_\perp \hat{e}'_\perp\right) \times \hat{e}'_\| = B'_\perp \left(\hat{e}'_\perp \times \hat{e}'_\|\right) = B'_\perp, \tag{10}$$

where $\hat{e}'$ are the basis vectors of the K' frame. The vector $\vec{B}'_\perp = \left(-B'_z \eta'_y, \ B'_z \eta'_x\right)$ and then, from Eq. (9), we get the magnitude of $B'_\perp$ as a function of the fields, the photon director cosines and energy in the laboratory frame:

$$B'_\perp = B_z \sqrt{1 - \frac{E_y^2}{B_z^2}} \frac{\varepsilon_\gamma}{\varepsilon'_\gamma} \sqrt{\eta_y^2 + \gamma^{*2} (\eta_x - \beta^*)^2}. \tag{11}$$

The pair production rate in the K' frame is given by [11]:

$$\zeta' = 0.23 \frac{\alpha_f c}{\lambda_c} \frac{B'_\perp}{B_{cr}} \exp\left(-\frac{4}{3} \Psi^{-1}\right), \tag{12a}$$

$$\Psi = \frac{1}{2} \left(\frac{\varepsilon'_\gamma}{mc^2}\right) \left(\frac{B'_\perp}{B_{cr}}\right). \tag{12b}$$

The expression for the rate in Eq. (12a) is valid as long as $\Psi \ll 1$ (see below section 5.1).

The pair production rate in the laboratory frame, K (observer at infinity), is given by $\zeta = \zeta'/\gamma^*$, that can be rewritten as a function of the variables in the K frame as

$$\zeta = 0.23 \frac{\alpha_f c}{\lambda_c} \frac{B_z}{B_{cr}} \left(1 - \frac{E_y^2}{B_z^2}\right) \frac{\sqrt{\eta_y^2 \left(1 - \frac{E_y^2}{B_z^2}\right) + \left(\eta_x - \frac{E_y}{B_z}\right)^2}}{1 - \frac{E_y}{B_z}\eta_x}$$

$$\times \exp\left\{-\frac{8}{3} \frac{mc^2}{\varepsilon_\gamma} \frac{B_{cr}}{B_z} \left[\eta_y^2 \left(1 - \frac{E_y^2}{B_z^2}\right) + \left(\eta_x - \frac{E_y}{B_z}\right)^2\right]^{-1/2}\right\}. \tag{13}$$

One can write the photon momentum director cosines $\vec{\eta}$ as a function of the electron velocity $\vec{\beta}$, the polar Θ and azimuthal Φ angles of emission in the comoving frame:

$$\eta_x = \frac{\sin\Theta \cos\Phi + \beta_x \left[\gamma + \frac{(\gamma-1)}{\beta^2}\nu\right]}{\gamma(1+\nu)} \tag{14a}$$

$$\eta_y = \frac{\sin\Theta \sin\Phi + \beta_y \left[\gamma + \frac{(\gamma-1)}{\beta^2}\nu\right]}{\gamma(1+\nu)} \tag{14b}$$

$$\eta_z = \frac{\cos\Theta + \beta_z \left[\gamma + \frac{(\gamma-1)}{\beta^2}\nu\right]}{\gamma(1+\nu)}, \tag{14c}$$

where $\nu = \beta_x \sin\Theta \cos\Phi + \beta_y \sin\Theta \sin\Phi + \beta_z \cos\Theta$ and γ the $e^\pm$ Lorentz factor. Selecting specific photons emission angles in the comoving frame (e.g. $\Theta = \Phi = \pi/2$), we can now integrate our set of equations.

5. Results

We now present the results of the numerical integration of the set of equations described in the previous sections, with the related initial conditions (hereafter ICs). In our calculations, we adopt the electric and magnetic field strengths proportional to each other, i.e.:

$$E(t) = \Upsilon B(t), \tag{15}$$

where $0 < \Upsilon \le 1$ since we are interested in analyzing situations of magnetic dominance. We have selected three values of reference, $\Upsilon = 1/2, \ 1/10$, and $1/100$. The proportionality is requested at any time, so when $B(t)$ changes, $E(t)$ changes accordingly to keep Υ constant. These combined effects affect the motion of particles and, consequently, all the successive processes giving rise to the screening.

5.1. Initial conditions and MPP rate

In order to apply Eq. (13), the condition $\Psi \ll 1$ (expressed in the K' frame) must be satisfied. Transforming back ϵ'_γ and $B'_\perp$ to the original K frame (where both fields are present), we obtain the following condition for Ψ:

Table 1

Maximum initial upper values for B_0 (in unit of the critical field B_{cr}) and γ_0, for the three initial emission directions of the particles, for the three selected values of Υ, necessary in order to satisfy the condition given in Eq. (16).

Υ	Direction	$B_0(B_{cr})$	γ_0
$\frac{1}{2}$	y	0.1	3.66
	z	0.1	7.098
	Generic	0.1	6.48
$\frac{1}{10}$	y	0.1	3.71
	z	0.1	22.66
	Generic	0.1	4.18
$\frac{1}{100}$	y	0.1	3.71
	Generic	0.1	3.81

$$\Psi = \frac{3}{4} \frac{e\hbar}{m\,c} \frac{B^2}{B_{cr}} \gamma^2 \sqrt{\beta_y{}^2\left(1 - \frac{E^2}{B^2}\right) + \left(\frac{E}{B} - \beta_x\right)^2}$$
$$\times \sqrt{\eta_y{}^2\left(1 - \frac{E^2}{B^2}\right) + \left(\eta_x - \frac{E}{B}\right)^2} \ll 1. \tag{16}$$

This condition brings with it three conditions for the initial values of the variables: B_0, γ_0, and particles direction of emission (contained in the initial velocities $\vec{\beta}_0$ and in the director cosines of the photons $\vec{\eta}$). Then, we need to choose the right values for the three parameters in order to apply Eq. (13) for the rate.

We proceed first by choosing specific emission directions for the particles. We select three directions of reference: 1) along the $\hat{y}$-axis; 2) along the $\hat{z}$-axis; 3) a direction characterized by polar and azimuth angles, respectively, $\theta = 75°$ and $\phi = 30°$ (hereafter we refer to this direction as "*generic*" or "*G*"). For each direction, we have chosen the initial value of the magnetic field B_0 and, consequently, the maximum value of particles Lorentz factor γ_0. Table 1 lists the values of B_0 and γ_0 for each emission direction and for the selected values of Υ that satisfy the condition in Eq. (16), and the one for a classical treatment of the problem (see section 6).

For the values in Table 1, we have integrated our system of equations varying the initial number of emitted particles, $N_{\pm,0} = 1$, 10^3, 10^6, 10^{10}, with $N_{\gamma,0} = 0$; $N_{\gamma,0} = 10^3$, with $N_{\pm,0} = 1$. Each numerical integration stops when $\gamma = 1$, i.e. when the particle has lost all of its energy. We start the integration at $t_0 = 10^{-21}$ s and the previous condition is reached at $t_f \sim 3 \times 10^{-17}$–$10^{-15}$ s, depending on the specific initial conditions.

Fig. 2 shows an appreciable decrease of $\vec{B}$ is obtained for high values of $N_{\pm,0}$ ($\geqslant 10^{10}$), with particles emitted along the $\hat{y}$ direction (as expected) and increasing Υ. For particles emitted along the *generic* direction, the screening increases for $\Upsilon = 1/2 \to 1/10$, while decreases for $\Upsilon = 1/10 \to 1/100$.

We obtain no exponential growth of the produced number of pairs, e.g. for $N_{\pm,0} = 10^{10}$, only 10^2–10^3 new pairs are created, and for $N_{\pm,0} = 10^6$, only a few are created. This result tells us that the MPP process is not being efficient for all the cases in the time interval in which the particles lose their energy. When $N_{\pm,0}$ is high ($\sim 10^{10}$ or larger), the increase in the number of particles is mainly due to the larger number of photons rather than to a larger pair production rate.

5.2. Magnetic field screening

Fig. 2 shows the screening of the magnetic field for $B_0 = 0.1\ B_{cr}$, $N_{\pm,0} = 10^{10}$ and different γ_0, operated by particles emitted initially: 1) for $\Upsilon = 1/2$ and $1/10$, along the three directions
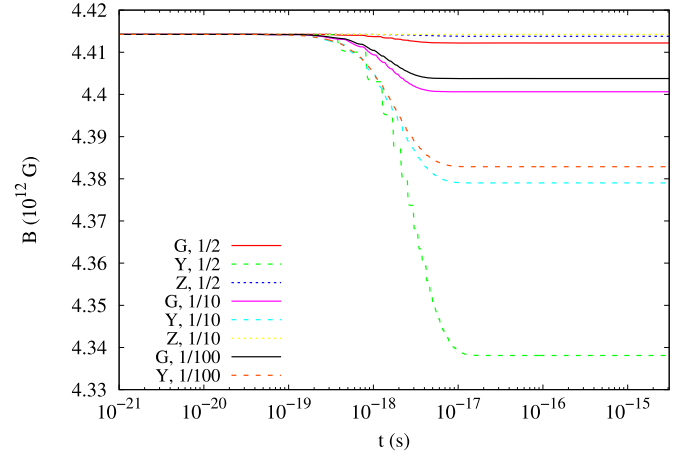
Fig. 2. The magnetic field decrease with time for the three values of $\Upsilon = 1/2$, $1/10$, $1/100$ (and $B_0 = 0.1\ B_{cr}$), operated by an initial number of particles $N_{\pm,0} = 10^{10}$ emitted initially along the three directions "*generic*", $\hat{y}$ and $\hat{z}$ (only for $\Upsilon = 1/2$ and $1/10$), is shown. For the case of emission along the $\hat{z}$ direction, the decrease cannot be appreciated because of the small magnitude of the decrease itself.
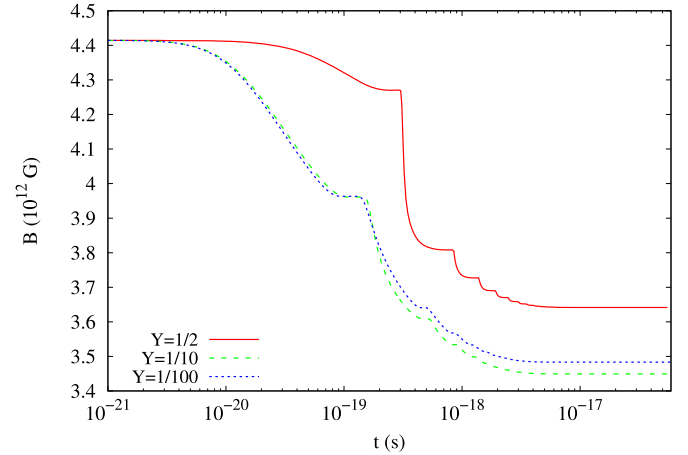
Fig. 3. The magnetic field decrease is shown, for $B_0 = 0.1\ B_{cr}$ and $N_{\pm,0} = 10^{15}$ emitted initially along the *generic* direction, for $\Upsilon = 1/2$, $1/10$, $1/100$, with Lorentz factor $\gamma_0 = 6.48$, 4.18, 3.81, respectively.

generic, y and z; 2) for $\Upsilon = 1/100$, along the *generic* and $\hat{y}$ directions.[2]

Fig. 3 shows the screening of the magnetic field for $B_0 = 0.1\ B_{cr}$, when $N_{\pm,0} = 10^{15}$ particles are emitted along the *generic* direction. The three curves correspond to the three values of Υ.

Figs. 2 and 3 tell us that the larger the initial number of particles, the faster the magnetic field screening. It can be also seen that in all cases the screening process is stepwise (even if in some cases it is smoothed out) due to the dependence of Eq. (8) on γ, β_x, and β_y, which have an oscillatory behavior owing to the continuous competition between gain and loss of energy.

5.3. Photons energy

We here show the results for the photons energy and number. Fig. 4 shows the photons energy $\varepsilon_\gamma(t)$ for $\Upsilon = 1/2$, $B_0 = 0.1\ B_{cr}$, $N_{\pm,0} = 10^{10}$ and particles emitted in the three considered directions. As before, the oscillatory behavior is due to the evolution of

---

[2] Since the integration time is not equal for all cases, we have extended a few solutions with their last constant value until the end time of the longer solution.
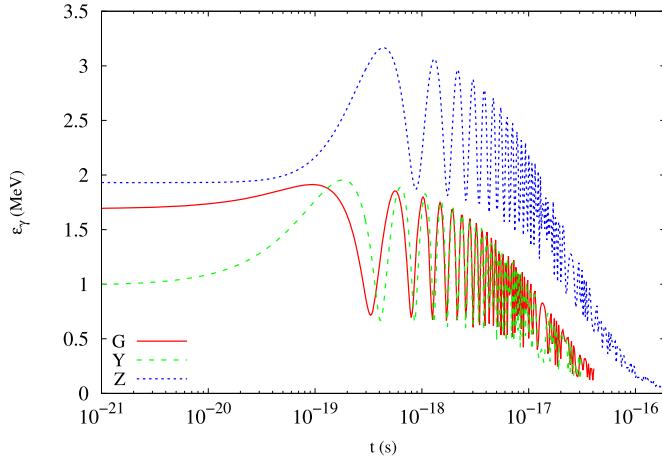
Fig. 4. Evolution of the photons energy for: $\Upsilon = 1/2$, $B_0 = 0.1\,B_{cr}$ and $N_{\pm,0} = 10^{10}$ emitted along the three directions.
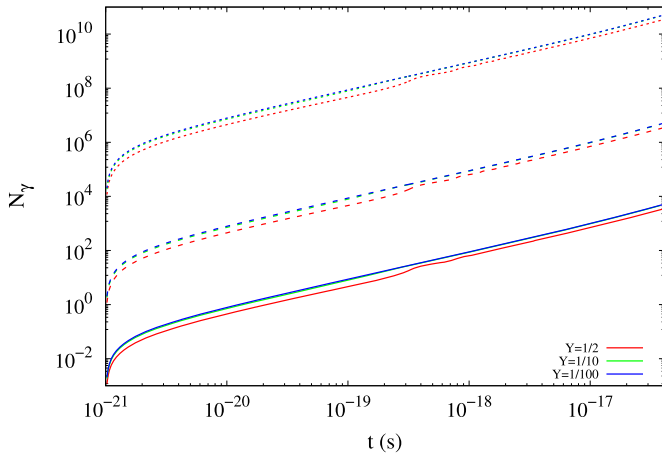
Fig. 5. Number of photons created by different values of the initial number of emitted particles $N_{\pm,0} = 10^3$ (continuous lines), 10^6 (dashed lines), 10^{10} (dotted lines). Here we consider particles emitted along the *generic* direction, with $B_0 = 0.1\,B_{cr}$, for $\Upsilon = 1/2$ (red lines), 1/10 (green lines), 1/100 (blue lines). The curves for $\Upsilon = 1/10$ and 1/100 are almost overlapped.

γ, β_x, β_y that corresponds to a competition between acceleration of the particle (due to $\vec{E}$) and emission of radiation (due to $\vec{B}$).

Fig. 5 shows the number of synchrotron photons created by $N_{\pm,0} = 10^3$, 10^6, 10^{10}, emitted along the *generic* direction, for the three values of Υ. We notice that, for each $N_{\pm,0}$, a decrease of Υ leads to the creation of a larger number photons. Since to a decrease of Υ it corresponds a decrease of the electric to magnetic field ratio (see Eq. (15)), this implies that a larger number of synchrotron photons is produced hence a larger number of secondary pairs. Moreover, we notice that an exponential growth of N_γ is present and their final value $N_{\gamma,f}$ is always one order of magnitude larger than $N_{\pm,f}$.

5.4. Screening and circularization timescales

In order to use Eq. (8) for the induced magnetic field, specific conditions on the processes time scales need to be satisfied. We define the circularization time as $t_c = 2\pi R_c/(\beta c)$, namely the time the particle spends to complete one "*orbit*" around the magnetic field line.[3] We define the screening timescale as $t_{screen}(t) =$

---

[3] Here, we approximate the coil as perfectly circular due to the short timescale and since we are interested only in its order of magnitude.

$|B(t)/\dot{B}(t)|$. For $t_c < t_{screen}$, the magnetic field can be considered stationary in the considered time interval, and we can use Eq. (8). For $t_{screen} \lesssim t_c$ instead, the assumptions of stationary field are no longer valid.

For all the studied ICs, we find that $t_c < t_{screen}$ or $\ll t_{screen}$. Instead for $N_{\pm,0} > 10^{15}$, t_{screen} becomes smaller than t_c (even if for not all the integration time). Then, we exclude this IC from our study.

5.5. Further conditions for the magnetic pair production

We turn to analyze the reason of the paucity that we find in the MPP process. The parameter χ has a twofold role: 1) it sets the energy of the emerging pairs; 2) it sets a threshold for the efficiency of the MPP process. If $0.01 \lesssim \chi \leq 1$, the emerging pairs share equally the photon energy. Instead, if $\chi > 1$ or $\gg 1$, one of the pairs tends to absorb almost all the energy of the photon, and the other takes the remaining energy (see [12] for details). It has been shown that the pair production is not expected to occur with significant probability unless $\chi \gtrsim 0.1$ (see e.g. [12] and references therein). For all the ICs in Table 1, $0.1 < \chi < 1$. Then, a production of pairs through the MPP process is expected and the emerging pairs share almost equally the parent photons energy.

A further rule-of-thumb condition for MPP was derived in [13] (see also [11,14]), where it is shown that the pair production occurs whenever $\varepsilon_\gamma \times B_\perp \gtrsim 10^{18.6} = 3.98 \times 10^{18}$, with ε_γ the photon energy and $B_\perp$ the perpendicular (to the photon propagation direction) component of the magnetic field. Inserting an electric field (perpendicular to $\vec{B}$), one has

$$\varepsilon_\gamma \times B \left[\left(\eta_x - \frac{E}{B} \right)^2 + \eta_y^2 \left(1 - \frac{E^2}{B^2} \right) \right]^{1/2} \gtrsim 10^{18.6}. \qquad (17)$$

For all the analyzed cases, this condition is satisfied since it spans values between 10^{18} and 10^{23} (depending upon the ICs), even if not at all the integration times.

6. Conditions for classical approach

We turn now to validate our semi-classical treatment of the screening problem. Quantum-mechanical effects are not important when the electron's cyclotron radius $R_L = cp/eB$ is larger than de Broglie wavelength $\lambda = \hbar/p$ (see [15]), where $p = m\gamma\beta c$ is the electron's momentum. This corresponds to the following request for the magnetic field strength: $B \leq B_{cr}\,\beta^2\,\gamma^2$. Moreover, in presence of an electric field E, the work exerted by the electric force over a de Broglie wavelength, $eE\lambda$, must be smaller than the electron's rest mass-energy, mc^2. This condition translates into $E < \gamma\beta E_{cr} = \gamma\beta B_{cr}$. For the parameters adopted in Table 1, the above two conditions are well satisfied, so we do not expect the electrons in our system to experience quantum-mechanical effects, thereby validating the present semi-classical approach. In cases where the above conditions fail to be satisfied, e.g. in presence of overcritical fields, quantum-mechanical effects occur and the semi-classical approach for the dynamics and for the radiation production mechanisms is no longer valid. In those cases, the equation for the quantum synchrotron transitions rate suggested in [16] should be used. We here limit ourselves to physical situations in which the semi-classical treatment remains accurate (see Table 1).

The above considerations can be also verified by looking at the particle's Landau levels. The energy of a particle immersed in strong background magnetic field is given by (see e.g. [12])

$$E_j = \sqrt{|\vec{p}_\parallel|^2 c^2 + m^2 c^4 + 2m^2 c^4 \frac{B}{B_{cr}}\, j}, \qquad (18)$$
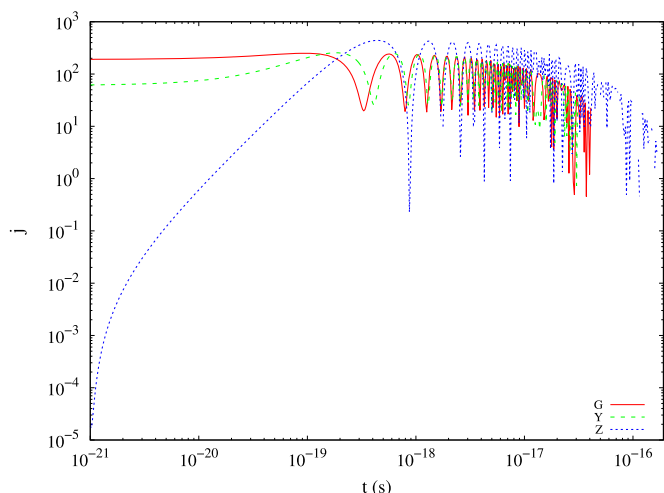
Fig. 6. Evolution of the Landau levels for the ICs (with $B_0 = 0.1 \, B_{\mathrm{cr}}$, $N_\pm = 10^{10}$ and particles emitted along the three directions G, y and z) for $\Upsilon = 1/2$. For $\Upsilon = 1/10$ and for the curves oriented along G and y directions, with $\Upsilon = 1/100$, the curves have almost the same behavior and values of the ones for $\Upsilon = 1/2$.

where j is the number of occupied (Landau) energy levels and $p_\parallel$ its momentum component parallel to the magnetic field, $p_\parallel = p_z = \gamma m \beta_z c$. For given values of $(\gamma, \ \beta_z, \ B)$, from Eq. (18) we can extract j: $j = B_{\mathrm{cr}}/2B \left[\gamma^2 \left(1 - \beta_z^2 \right) - 1 \right]$. The use of a classical treatment is allowed when the number of Landau levels is large, i.e. $\gg 1$. We show in Fig. 6 the value of j as a function of time, for the ICs in Table 1. High values of j are reached for all the studied cases. We have found that $j \lesssim$ or $\ll 1$ for: 1) $\Upsilon = 1/100$ and particles emitted along the $\hat{z}$ direction (j oscillates between $10^{-3} - 10^0$), and 2) $B_0 > 0.1 B_{\mathrm{cr}}$.

7. Conclusions

In this article, we have built a simplified model to study the MFS by $e^\pm$ pairs also in presence of a crossed electric field. Before to resume the results of our study, three important comments need to be considered about the model and the results obtained:

1. We have constructed one-particle equations to describe the particles motion as a fluid. This assumption can be justified by the following considerations. Since we are considering strong fields, the particles are bound to follow almost the same trajectory. Further, the flux of particles can be treated as a fluid, since it obeys to the continuity equation. The particles flux along the lateral surface of the tube flux can be approximated to zero, while the ones through the upper and lower surfaces are equal since e^- and e^+ move in opposite directions.
2. Because of Eq. (15), also the electric field is screened. This effect can be justified considering that the creation of new charged particles leads to the formation of a current which screens the electric field. The elaboration of a more detailed treatment of this phenomenon goes beyond the scope of the present article and is left for a future work.
3. The screening is mainly operated by the initial particles injected in the system. Under the studied conditions and time interval, the MPP is not sufficiently efficient. In fact, the photons energy is of the order of a few MeV, so the $e^\pm$ pairs gain an energy just a bit higher than their rest-mass energy. As a consequence, they do not make many "*loops*" around the $\vec{B}$ lines and emit photons with almost the same energy. This leads to a lower MPP rate.

We have shown that the screening increases (up to a few percent) if one increases the initial number of pairs, from $N_{\pm,0} = 10^6$ to $10^{10} - 10^{15}$. It also depends on the initial direction of emission of the particles. The major effect occurs when the particles are emitted in the *generic* and $\hat{y}$ directions, since the screening is produced by orthogonal component (respect to the $\hat{z}$-axis) of the particle velocity.

A further dependence is related to the parameter Υ. A decrease of Υ enhances the efficiency of the screening since, because of Eq. (15), it leads to a decrease of the electric field strength. Consequently, the synchrotron process is more efficient and a higher number of photons is created. This also implies an increase of the MPP rate $\zeta(t)$. We can also notice the following features:

1. **Fixing Υ:** the screening is larger if the particles are emitted initially along the $\hat{y}$-axis; it is lower if they are emitted along the *generic* direction.
2. **Fixing the $\hat{y}$ direction:** the screening increases if we increase the value of Υ.
3. **Fixing the *generic* direction:** the screening increases if we decrease Υ (even if not linearly).

The first feature is related to the particle orthogonal velocity, $\beta_\perp$, which is larger for particles emitted along the $\hat{y}$-axis, with respect to particles emitted along the *generic* direction. The other two points are related to the dependence of the equation for the magnetic field, and in particular of the rate, on $\left(\vec{\beta}, \ \vec{\eta}, \ \Upsilon \right)$. Concerning the second point, we have verified that: 1) an increase of Υ leads to an increase of $\beta_\perp$; 2) in the time interval $10^{-21} \leq t \lesssim t^* = 5 \times 10^{-18}$ s, being t^* the time when the magnetic field starts to drop down, the rate $\zeta(t)$ for $\Upsilon = 1/10$ and $1/100$ is higher than the one for $\Upsilon = 1/2$. For $t > t^*$, even if the rate for $\Upsilon = 1/2$ is just little higher than for $\Upsilon = 1/10$, $1/100$, it is higher enough to explain a wider decrease of $\vec{B}$ for larger Υ, for particles along the $\hat{y}$ direction. This implies also a higher value for the respective $dN_\pm/dt$. For the third point, analyzing Eq. (8), together with Eqs. (13), one can derive analytically that a decrease of Υ leads to a stronger MPP rate $\zeta(t)$. Moreover, a decrease of Υ implies a lower value for the particle Lorentz factor. In Fig. 5, we have also shown that a decrease of Υ leads to a stronger synchrotron emission, with the related increase of N_γ. Then, since $dN_\pm/d\tilde{t} = N_\gamma(\tilde{t}) \ \tilde{\zeta}(\tilde{t})$ and $d\tilde{B}_{tot}/d\tilde{t} \propto \gamma^{-2} \times dN_\pm/d\tilde{t} = \gamma^{-2} \times N_\gamma(\tilde{t}) \times \tilde{\zeta}(\tilde{t})$, the discussions above imply that lower values of Υ lead to a stronger screening.

We conclude that the screening effect occurs under physical conditions reachable in extreme astrophysical systems, e.g. pulsars and gamma-ray bursts. For the present analyzed physical conditions, the decrease of the magnetic field from its original value can be of up to a few percent. This study has been the first one on this subject and in view of this, we have adopted some simplified assumptions that we have detailed and analyzed, and which have allowed us to get a clear insight on the main physical ingredients responsible for this effect. There is still room for improvements of the model, for instance, by considering different configuration of the electric and magnetic fields, overcritical fields strengths, among others. All the above considerations are essential to scrutinize the occurrence of the magnetic field screening process, and consequently for the interpretation of the astrophysical systems in which similar extreme physical conditions are at work.

Declaration of competing interest

The authors declare that they have no known competing financial interests or personal relationships that could have appeared to influence the work reported in this paper.

References

[1] A. Fedotov, N. Narozhny, G. Mourou, G. Korn, Limitations on the attainable intensity of high power lasers, Phys. Rev. Lett. 105 (8) (2010) 080402.

[2] R. Ruffini, G. Vereshchagin, S.-S. Xue, Electron-positron pairs in physics and astrophysics: from heavy nuclei to black holes, Phys. Rep. 487 (1–4) (2010) 1–140, https://doi.org/10.1016/j.physrep.2009.10.004, arXiv:0910.0974.

[3] R. Ruffini, R. Moradi, J.A. Rueda, L. Becerra, C.L. Bianco, C. Cherubini, S. Filippi, Y.C. Chen, M. Karlica, N. Sahakyan, Y. Wang, S.S. Xue, On the GeV emission of the type I BdHN GRB 130427A, Astrophys. J. 886 (2) (2019) 82, https://doi.org/10.3847/1538-4357/ab4ce6, arXiv:1812.00354.

[4] J.A. Rueda, R. Ruffini, The blackholic quantum, Eur. Phys. J. C 80 (4) (2020) 300, https://doi.org/10.1140/epjc/s10052-020-7868-z, arXiv:1907.08066.

[5] L. Becerra, C.L. Ellinger, C.L. Fryer, J.A. Rueda, R. Ruffini, SPH simulations of the induced gravitational collapse scenario of long gamma-ray bursts associated with supernovae, Astrophys. J. 871 (2019) 14, https://doi.org/10.3847/1538-4357/aaf6b3, arXiv:1803.04356.

[6] Y. Wang, J.A. Rueda, R. Ruffini, L. Becerra, C. Bianco, L. Becerra, L. Li, M. Karlica, Two predictions of supernova: GRB 130427A/SN 2013cq and GRB 180728A/SN 2018fip, Astrophys. J. 874 (2019) 39, https://doi.org/10.3847/1538-4357/ab04f8, arXiv:1811.05433.

[7] J.A. Rueda, R. Ruffini, M. Karlica, R. Moradi, Y. Wang, Magnetic fields and afterglows of BdHNe: inferences from GRB 130427A, GRB 160509A, GRB 160625B, GRB 180728A, and GRB 190114C, Astrophys. J. 893 (2) (2020) 148, https://doi.org/10.3847/1538-4357/ab80b9, arXiv:1905.11339.

[8] L.D. Landau, E.M. Lifshitz, The Classical Theory of Fields, 1971.

[9] J.D. Jackson, Classical Electrodynamics, 1999.

[10] S.R. Kelner, A.Y. Prosekin, F.A. Aharonian, Synchro-curvature radiation of charged particles in the strong curved magnetic fields, Astron. J. 149 (1) (2015) 33.

[11] J. Daugherty, I. Lerche, On pair production in intense electromagnetic fields occurring in astrophysical situations, Astrophys. Space Sci. 38 (2) (1975) 437–445.

[12] J.K. Daugherty, A. Harding, Pair production in superstrong magnetic fields, Astrophys. J. (1983) 761–773.

[13] P. Sturrock, A model of pulsars, Astrophys. J. 164 (1971) 529.

[14] A.K. Harding, E. Tademaru, L. Esposito, A curvature-radiation-pair-production model for gamma-ray pulsars, Astrophys. J. 225 (1978) 226–236.

[15] J. Daugherty, I. Lerche, Theory of pair production in strong electric and magnetic fields and its applicability to pulsars, Phys. Rev. D 14 (2) (1976) 340.

[16] A. Sokolov, I. Ternov, V. Bagrov, D. Gal'Tsov, V.C. Zhukovskii, Radiation-induced self-polarization of the electron spin for helical motion in a magnetic field, Sov. Phys. J. 11 (5) (1968) 4–7.

The morphology of the X-ray afterglows and of the jetted GeV emission in long GRBs

R. Ruffini,[1,2,3,4,5]★ R. Moradi,[1,2,6]★ J. A. Rueda [1,2,7,8,9]★ L. Li,[1,2,6] N. Sahakyan,[10,1] Y.-C. Chen [1,2]
Y. Wang,[1,2,6] Y. Aimuratov,[1,2,11,18] L. Becerra,[1,2,12] C. L. Bianco,[1,2,9] C. Cherubini,[1,13,14] S. Filippi,[1,13,15]
M. Karlica,[1,2] G. J. Mathews,[1,16] M. Muccino,[17] G. B. Pisani[1,2] and S. S. Xue[1,2]

[1]*ICRANet, Piazza della Repubblica 10, I-65122 Pescara, Italy*
[2]*ICRA, Dipartimento di Fisica, Università di Roma 'La Sapienza', Piazzale Aldo Moro 5, I-00185 Roma, Italy*
[3]*ICRANet-Rio, Centro Brasileiro de Pesquisas Físicas, Rua Dr. Xavier Sigaud 150, 22290-180 Rio de Janeiro, Brazil*
[4]*Université de Nice Sophia-Antipolis, Grand Château Parc Valrose, 06103 Nice, CEDEX 2, France*
[5]*INAF, Viale del Parco Mellini 84, I-00136 Rome, Italy*
[6]*INAF – Osservatorio Astronomico d'Abruzzo, Via M. Maggini snc, I-64100 Teramo, Italy*
[7]*ICRANet-Ferrara, Dipartimento di Fisica e Scienze della Terra, Università degli Studi di Ferrara, Via Saragat 1, I-44122 Ferrara, Italy*
[8]*Dipartimento di Fisica e Scienze della Terra, Università degli Studi di Ferrara, Via Saragat 1, I-44122 Ferrara, Italy*
[9]*INAF, Istituto di Astrofisica e Planetologia Spaziali, Via Fosso del Cavaliere 100, I-00133 Rome, Italy*
[10]*ICRANet-Armenia, Marshall Baghramian Avenue 24a, Yerevan 0019, Republic of Armenia*
[11]*Fesenkov Astrophysical Institute, Observatory 23, 050020 Almaty, Kazakhstan*
[12]*Instituto de Astrofísica, Facultad de Física, Pontificia Universidad Católica de Chile, Av. Vicuña Mackenna 4860, Macul, 8970117 Santiago, Chile*
[13]*ICRA, University Campus Bio-Medico of Rome, Via Alvaro del Portillo 21, I-00128 Rome, Italy*
[14]*Department of Science and Technology for Humans and the Environment and Nonlinear Physics and Mathematical Modeling Lab, University Campus Bio-Medico of Rome, Via Alvaro del Portillo 21, I-00128 Rome, Italy*
[15]*Department of Engineering, University Campus Bio-Medico of Rome, Nonlinear Physics and Mathematical Modeling Lab, Via Alvaro del Portillo 21, I-00128 Rome, Italy*
[16]*Center for Astrophysics, Department of Physics, University of Notre Dame, Notre Dame, IN 46556, USA*
[17]*Instituto Nazionale di Fisica Nucleare, Laboratori Nazionali di Frascati, I-00044 Frascati, Italy*
[18]*Al-Farabi Kazakh National University, al-Farabi avenue 71, 050040 Almaty, Kazakhstan*

ABSTRACT

We recall evidence that long gamma-ray bursts (GRBs) have binary progenitors and give new examples. Binary-driven hypernovae (BdHNe) consist of a carbon–oxygen core (CO_{core}) and a neutron star (NS) companion. For binary periods $\sim$5 min, the CO_{core} collapse originates the subclass BdHN I characterized by (1) an outstanding supernova (SN; the '*SN-rise*'); (2) a black hole (BH), born from the NS collapse by SN matter accretion, leading to a GeV emission with luminosity $L_{GeV} = A_{GeV}\, t^{-\alpha_{GeV}}$, observed only in some cases; and (3) a new NS (νNS), born from the SN, originating from the X-ray afterglow with $L_X = A_X\, t^{-\alpha_X}$, observed in all BdHN I. We record 378 sources and present for four prototype GRBs 130427A, 160509A, 180720B, and 190114C: (1) spectra, luminosities, SN-rise duration; (2) A_X, $\alpha_X = 1.48 \pm 0.32$, and (3) the νNS spin time evolution. We infer (i) A_{GeV}, $\alpha_{GeV} = 1.19 \pm 0.04$ and (ii) the BdHN I morphology from time-resolved spectral analysis, three-dimensional simulations, and the GeV emission presence/absence in 54 sources within the *Fermi*-Large Area Telescope boresight angle. For 25 sources, we give the integrated and time-varying GeV emission, 29 sources have no GeV emission detected and show X/gamma-ray flares previously inferred as observed along the binary plane. The 25/54 ratio implies the GeV radiation is emitted within a cone of half-opening angle $\approx$60° from the normal to the orbital plane. We deduce BH masses of 2.3–8.9 $M_\odot$ and spin of 0.27–0.87 by explaining the GeV emission from the BH rotational energy extraction, while their time evolution validates the BH mass–energy formula.

Key words: black hole physics – binaries: general – gamma-ray bursts – transients: supernovae.

1 INTRODUCTION

The year 2021 marks the 50th anniversary of the paper 'Introducing the black hole' (Ruffini & Wheeler 1971) and of the black hole (BH)

mass–energy formula (Christodoulou 1970; Christodoulou & Ruffini 1971; Hawking 1971; Hawking 1972). Since those days, interest in BHs has spread worldwide and their study represents one of the most innovative fields of fundamental physics and astrophysics. There has also been an exponential growth of observational and theoretical developments that are finally reaching the momentous result of unveiling the process of rotational energy extraction from a rotating Kerr BH. We indicate the path of this discovery in

★ E-mail: ruffini@icra.it (RR); rahim.moradi@icranet.org (RM); jorge.rueda@icra.it (JAR)

this paper. This realization has allowed for the identification of the code of gamma-ray bursts (GRBs): one of the most complex sequences of a very large number of non-repetitive classical and quantum events, each of which are characterized by specific spectral and temporal properties. In parallel, a new arena for fundamental physics has been revealed by the dubbed '*blackholic quantum*' (Rueda & Ruffini 2020). This enormous conceptual progress has not been reached straightforwardly: it has come from an intense dedicated process with continuous feedback between theoretical understanding, unprecedented panchromatic observational progress, and modification of basic interpretation paradigms: they have all been truly essential. We first summarize in this introduction some of the contributions which have initiated this most complex inquiry into the the most powerful energy source in the Universe and identify the rotational energy of a Kerr BH as their energy source.

1.1 The initial 'golden age' of relativistic astrophysics

The first breakthrough in relativistic astrophysics was the discovery of pulsars in 1967 (Hewish et al. 1968), and the discovery of a pulsar in the core of the Crab Nebula (Staelin & Reifenstein 1968; Reifenstein, Brundage & Staelin 1969). The identification of the energy source of the pulsar with a fast rotating newly born neutron star (NS); the new NS (νNS), coincident with the supernova (SN) explosion led to a new paradigm in SN understanding (Shklovskij 1969). As we show in this paper, we are gaining a deeper understanding of both of SNe and of the role of the νNS in the binary-driven hypernova (BdHN) systems.

The second breakthrough came from the launch in 1970 of the first X-ray telescope, observing in the 2–20 keV energy band: the *Uhuru* satellite (see e.g. Giacconi & Ruffini 1978; Giacconi 2003). *Uhuru* paved the way for a crucial working method in developing a multiwavelength collaboration with optical and radio observatories. Thanks to the theoretical understanding, this led to the discovery, inside our own galaxy, of a large number of binary X-ray sources composed of a main-sequence star and a companion NS (like Hercules X-1 and Centaurus X-3) and a binary system composed of a main-sequence star and a BH, which gave the first evidence for the discovery of a BH in our Galaxy (see Ruffini 1974; Giacconi & Ruffini 1978, for details). It was soon realized that these binary X-ray sources would themselves further evolve as the companion main-sequence star would undergo an SN explosion on time-scales of 10^8 yr (Ruffini 1974). In view of the limited number of such binary X-ray sources in our Galaxy, the expected observational rate of the final evolution of such binary systems would be of the order of 10^{-8} events per yr in our Galaxy. The point that was missed at the time was the existence of the process of '*induced gravitational collapse*', which was identified years later (Ruffini et al. 2001; Rueda & Ruffini 2012). This implies an unprecedented energy emission of $\sim 10^{54}$ erg, making them observable from all galaxies in the entire Universe: if the number of galaxies in our past light-cone is taken into account, the expected observational rate of the final evolution of such binary X-ray sources in the entire Universe is of the order of 10–100 events per yr. *The third breakthrough* was the introduction in 1971 of the BH mass–energy formula by Christodoulou, Hawking, Ruffini (Christodoulou 1970; Christodoulou & Ruffini 1971; Hawking 1971, 1972), and the BH extractable energy by reversible and irreversible transformation (in geometric $c = G = 1$ units):

$$M^2 = \frac{J^2}{4M_{irr}^2} + M_{irr}^2, \tag{1a}$$

$$S = 16\pi M_{irr}^2 \tag{1b}$$

$$\delta S = 32\pi M_{irr}\delta M_{irr} \geq 0, \tag{1c}$$

where J, M, M_{irr}, and S are the angular momentum, mass, irreducible mass, and horizon surface area of the BH, respectively.

Again in this article, we indicate the path to observe for the first time the BH extractable energy process, which can be as high as 29% of the BH mass for an extreme Kerr BH. We measure as well the BH mass and spin in selected BdHN.

Just at the end of this 'initial golden age of relativistic astrophysics', the discovery of GRBs was publicly announced in 1974 February at the annual meeting of the American Association for the Advancement of Science, in San Francisco (see details in Gursky & Ruffini 1975). In that meeting, observations by the Vela 5 and Vela 6 satellites were presented. These satellites operated in the 3–12 keV X-ray energy band and, for the first time, in the 150–750 keV (Vela 5) and 300–1500 keV (Vela 6) gamma-ray energy bands. Tens of gamma-ray events per year of unknown origin, lasting for a few seconds, and originating outside the Solar system, were named 'gamma-ray bursts' (details in Klebesadel, Strong & Olson 1973; Strong 1975).

What has became clear only recently, and further clarified in this article, is that precisely the late catastrophic evolution of the binary X-ray sources leads to the BdHNe: the progenitors of a class of long GRBs. Indeed, these highest luminosity energy sources in the Universe are observed to occur at a rate of 10–100 events per yr, consistent with the order of magnitude estimate given above.

We proceed to focus on the most recent developments, selecting crucial observational milestones, theoretical developments, and define the interpretation paradigms that have recently led to a unified understanding of the GRBs.

1.2 The largest ever multiwavelength observational efforts

The earliest evidence for high-energy radiation above 100 MeV from GRBs was the observations by the Energetic Gamma-Ray Experiment Telescope (*EGRET*), operating in the energy range $\sim$ 20 MeV–30 GeV, onboard of the Compton Gamma-Ray Observatory (*CGRO*, 1991–2000). The detection was triggered by the Burst And Transient Source Experiment (*BATSE*), operating in energy range of $\sim$20–2000 keV. *EGRET* has detected five GRBs that, from our understanding today, were long-duration bursts: GRB 910503, GRB 910601, GRB 930131, GRB 940217, and GRB 940301 (see e.g. Kanbach 1996, and references therein). Unfortunately, no redshift was known at the time.

A new epoch started with the launch of the *Beppo-Sax* satellite in 1996, joining the expertise of the X-ray and gamma-ray communities. Its gamma-ray burst monitor (GRBM) operating in the 40–700 keV energy band determined the trigger of the GRB, and two wide-field cameras operating in the 2–30 keV X-ray energy band allowed the localization of the source to within arcminutes resolution. This enabled a follow-up with the narrow-field instruments (NFI) in the 2–10 keV energy band.

Beppo-SAX achieved three major results:

(i) The discovery of the X-ray afterglow (GRB 970228; Costa et al. 1997), characterized by an X-ray luminosity decreasing with a power law with index of $\alpha_X = -1.48 \pm 0.32$ (see de Pasquale et al. 2006, as well as Li et al. 2015, 2018b; Pisani et al. 2016). In this article, we specifically address the astrophysical origin of the afterglow.

(ii) The determination of the accurate positions by the NFI, transmitted to the optical (van Paradijs et al. 1997) and radio telescopes (Frail et al. 1997), allowed the determination of the GRB cosmological redshifts. The first redshift was measured for GRB 970508 (Metzger et al. 1997), using the LRIS instrument of the Keck II telescope (Oke et al. 1995). The derived distances of $\approx$5–10 Gpc confirmed their cosmological origin and their unprecedented energetics, $\approx 10^{50}$–10^{54} erg, thus validating our hypothesis derived from first principles (Damour & Ruffini 1975; Ruffini 1998).

(iii) The discovery of the temporal and spatial coincidence of GRB 980425 with SN 1998bw (Galama et al. 1998), which suggested the connection between GRBs and SNe, was soon supported by many additional events (see e.g. Woosley & Bloom 2006; Della Valle 2011; Hjorth & Bloom 2012; Li et al. 2012, 2018a). The astrophysical origin of this coincidence is addressed in this article within the BdHN approach.

The Neil Gehrels *Swift* Observatory (hereafter indicated as *Swift*) followed in 2004. It was conceived as a panchromatic space observatory dedicated to the observations of GRBs. The GRB trigger is detected by the large field of view of its Burst Alert Telescope (BAT; Barthelmy et al. 2005), operating in the hard X-ray band. This is followed up by the fast and automatic observations of the onboard narrow fields instruments XRT (Burrows et al. 2005) and UVOT (Roming et al. 2005) operating in the soft/medium X-ray and in the optical/UV bands, respectively. The BAT telescope operates in the 15–150 keV energy band and can detect the GRB prompt emission while accurately determining its position in the sky within 3 arcmin. Within 90 s, *Swift* can repoint the XRT telescope, operating in the 0.3–10 keV energy range, and relay promptly the burst position to the ground. Unfortunately, this does not allow the establishment of the initial *Swift*-XRT detection prior to the *Swift*-BAT trigger, as later explained in this article.

Thanks to the *Swift* satellite, the number of detected GRBs increased rapidly to 1300 sources with known redshifts (see e.g. Giommi et al. 2020). By analysing the light curve of some long GRBs, Nousek et al. (2006) and Zhang et al. (2006) discovered three power-law segments in the XRT flux light curves prior to the afterglow emission (see also Li et al. 2015, 2018a). We refer in this article to these segments as the 'Nousek–Zhang power laws'. All the X-ray afterglow observations considered in this article refer to *Swift*-XRT observation.

The high-energy astrophysics era of GRB observations started with the launch of *AGILE* in 2007 (Tavani et al. 2009) with the onboard Gamma-Ray Imaging Detector (*GRID*) operating in the 30 MeV–50 GeV energy range. *AGILE* was soon followed by the launch in 2008 June of the *Fermi* satellite, having onboard the gamma-ray burst monitor (GBM) operating in the 8 keV–40 MeV energy range (Meegan et al. 2009) and the Large Area Telescope (LAT) operating in the 20 MeV–300 GeV energy range (Atwood et al. 2009).

AGILE-GRID detected the first long GRB with emission above 100 MeV and with a photometric redshift of $z = 1.8$, GRB 080514B (Giuliani et al. 2008). It was followed four months later by the detection of GRB 080916C (Greiner et al. 2009) by *Fermi* with one of the largest isotropic energies ever detected, $E_{iso} = (4.07 \pm 0.86) \times 10^{54}$ erg, and a photometric redshift of $z = 4.35$. These were followed by a large number of long GRBs observed by LAT with both GeV emission and with a well-defined z. All the high-energy long GRBs considered in this article are based on the first and second *Fermi*-LAT GRB catalogues (Ackermann et al. 2013; Ajello et al. 2019).

The leading observations from space observatories were followed by a multitude of equally essential observations from ground-based observatories spanning the globe. The leading role was taken by the largest optical telescopes, e.g. the VLT from ESO with its X-shooter instrument (Vernet et al. 2011) and radio telescopes. This vastest ever multiwavelength observational campaign has been recently further extended to the very-high-energy (VHE) domain with the GRB detection by observatories on the ground. This is the case of the observations of GRB 190114C by the Imaging Atmospheric Cherenkov Telescopes MAGIC (see Fig. 1 and MAGIC Collaboration 2019a), designed to detect VHE gamma-rays from 30 GeV to more than 50 TeV (see e.g. Aleksić et al. 2016a, b), the observations of GRB 180720B by H.E.S.S (see Fig. 2 and Abdalla et al. 2019), operating in the energy range from tens of GeV to tens of TeV (see e.g. Aharonian et al. 2006), as well as GRB 190829A (Chand et al. 2020), which we also address in this article.

1.3 The short GRBs with binary NS progenitors

One of the main results of the observations of the *CGRO* satellite (Murdin 2000) was the isotropic distribution of the GRBs when expressed in galactic coordinates (Meegan et al. 1992). This result gave the first preliminary indication of the cosmological nature of GRBs. This was later confirmed by irrefutable evidence from the observations of *Beppo-Sax*, as mentioned above. An additional result was the clear indication of the existence of two different classes of GRBs: the short and the long GRBs (Kouveliotou et al. 1993). This classification has been confirmed and further extended as we recall in Section 2, now duly expressing all quantities, after *Beppo-Sax*, in the rest frame of the source.

The first proposal of successfully relating a GRB to an astrophysical cosmological source came from the vision of Bohdan Paczynski and collaborators, who identified the progenitors of short GRBs (S-GRBs) with merging NS binaries (see e.g. Paczynski 1986; Eichler et al. 1989; Narayan, Piran & Shemi 1991; Mao & Paczynski 1992; Narayan et al. 1992; Narayan, Paczynski & Piran 1992). This result was later confirmed by *Beppo-Sax* (Li & Paczyński 1998, 2000, 2006; Berger 2014). Complementary information came from the localization of S-GRBs at large off-sets from their host galaxies and with no star formation evidence (see e.g. Fox et al. 2005; Gehrels et al. 2005; Berger 2014). The following fundamental discovery came from the identification of the first S-GRB in the GeV band by *AGILE*. The first observation of an S-GRB was done by *AGILE* who detected GRB 090510A at a spectroscopic redshift of $z = 0.903$, with $E_{iso} = (3.95 \pm 0.21) \times 10^{52}$ erg, and a significant GeV emission $E_{LAT} = (5.78 \pm 0.60) \times 10^{52}$ erg. On the basis of the observed energetics of this source, and its spectral properties, we proposed that in this S-GRB we witness the birth of a BH, which we associate with the onset of the GeV emission: the signature of this event (Ruffini et al. 2016a).

This identification further evolved with the introduction of the two subclasses of short bursts (Ruffini et al. 2015b, 2016a, b; Aimuratov et al. 2017). The first subclass corresponds to short bursts with isotropic energies $E_{iso} < 10^{52}$ erg (in the rest-frame 1–10^4 keV energy band) and rest-frame spectral peak energies $E_{p,i} < 2$ MeV. These are expected to originate when the NS–NS merger leads to a single massive NS (M-NS) with a mass below the NS critical mass. We have called these sources short gamma-ray flashes (S-GRFs).

GRB 190114C
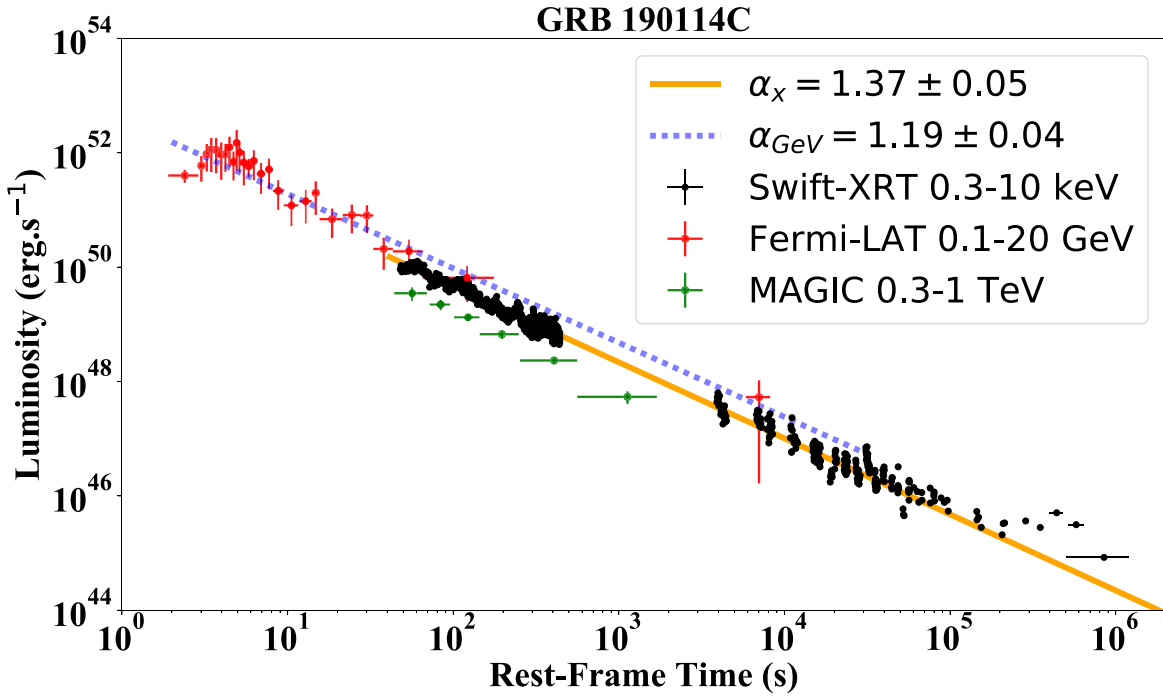
Figure 1. Luminosity of BdHN I 190114C: the black data points represent the rest-frame 0.3–10 keV luminosity obtained from *Swift*-XRT. It follows a decaying power law with index $\alpha_X = 1.37 \pm 0.05$. The red data points show the rest-frame 0.1–20 GeV luminosity observed by *Fermi*-LAT. It follows a decaying power law with amplitude $(4.6 \pm 0.6) \times 10^{52}$ erg s^{-1} and index $\alpha_{GeV} = 1.19 \pm 0.04$. The green data points show the rest-frame 0.3–1 TeV luminosity obtained from MAGIC. Details are given in Sections 4, 5, and 8.

GRB 180720B
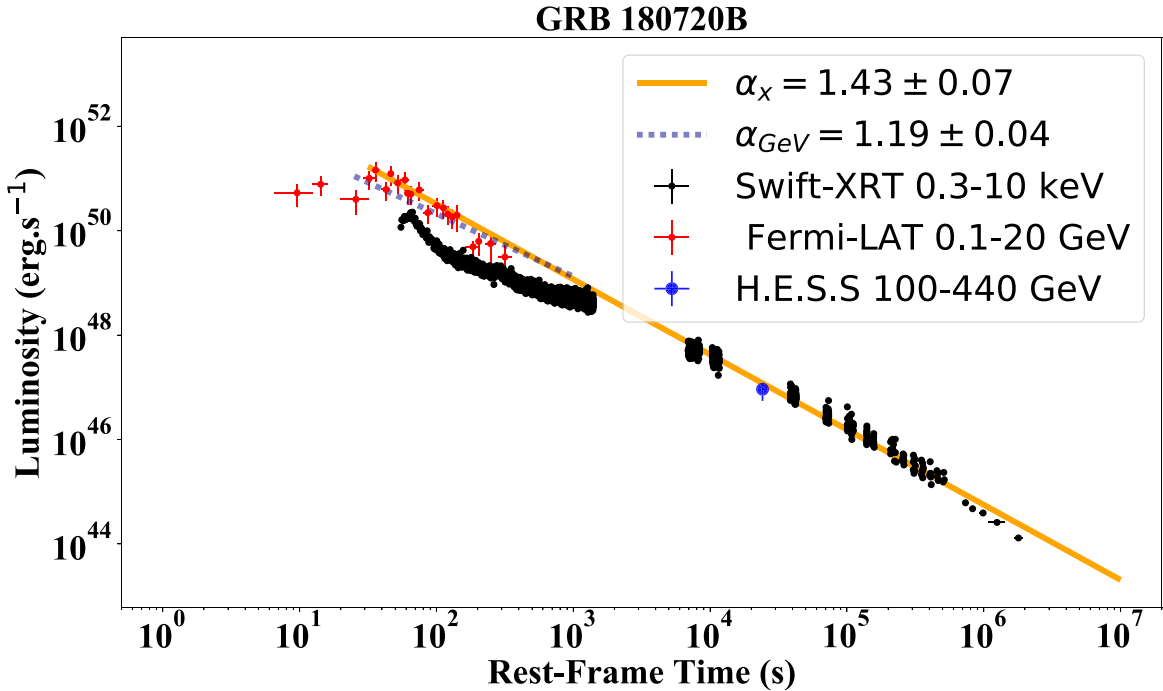
Figure 2. Luminosity of BdHN I 180720B: the black data points represent the rest-frame 0.3–10 keV luminosity obtained from *Swift*-XRT. It follows a decaying power law with index $\alpha_X = 1.43 \pm 0.07$. The blue data point shows the rest-frame 100–440 GeV luminosity observed by H.E.S.S. The red data points show the rest-frame 0.1–20 GeV luminosity observed by *Fermi*-LAT. It follows a decaying power law with amplitude $(5.4 \pm 0.6) \times 10^{52}$ erg s^{-1} and index $\alpha_{GeV} = 1.19 \pm 0.04$. Details are given in Sections 4, 5, and 8.
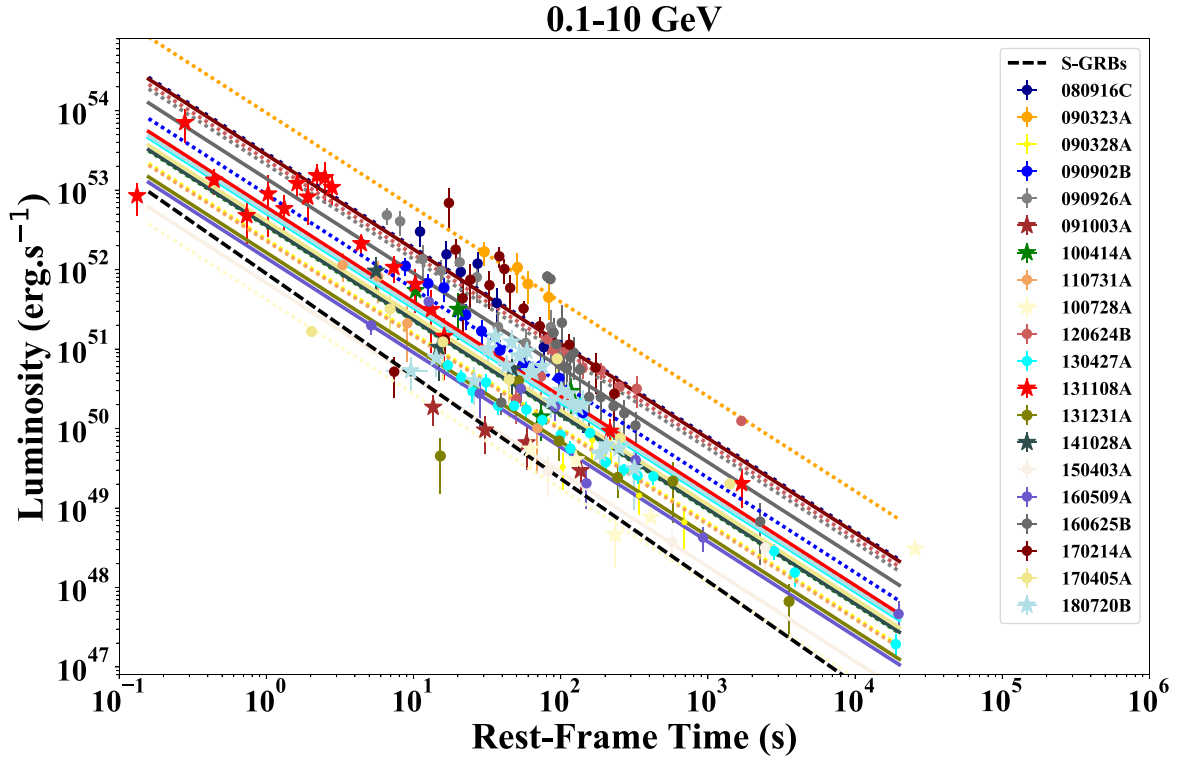
0.1-10 GeV

Figure 3. The rest-frame 0.1–10 GeV isotropic luminosity of 20 selected BdHNe with LAT emission. The solid red line marks the common power-law behaviour of the GeV emission for BdHNe with slope $\alpha_{\rm GeV} = 1.19 \pm 0.04$; the shaded grey area encloses all the luminosity light curves of the selected BdHNe. The dashed black line marks the common power-law behaviour of the GeV emission in S-GRBs with a slope of $\gamma = 1.29 \pm 0.06$.

The second subclass corresponds to short bursts with $E_{\rm iso} \gtrsim 10^{52}$ erg and $E_{\rm p,i} \gtrsim 2$ MeV. It was assumed that these sources, in analogy with the prototype GRB 090510, originate from an NS–NS merger in which the merged core overcomes the NS critical mass and gravitationally collapses to form a BH. We have called these sources genuine S-GRBs (see Ruffini et al. 2016a, 2019c); six of such S-GRBs have been identified, all emitting GeV emission with a decaying luminosity of index $\alpha_{\rm GeV,short} = -1.29 \pm 0.06$ (Ruffini et al. 2019c); see Fig. 3 in Section 8.

We show how, by following these pathfinding works on S-GRBs, we have progressed in formulating the theory of the BdHNe: the theory of long GRBS based on binary progenitors. Before this, however, we summarize the traditional long GRB models based upon a single progenitor.

1.4 Long GRBs in the traditional model

A review of the traditional long GRB model is facilitated by the extensive book by Bing Zhang and many references therein (Zhang 2018). As recounted there, the papers by Rees & Meszaros (1992), Mészáros & Rees (1997), and Woosley (1993) have characterized this traditional model. Rees & Meszaros (1992) proposed a single BH as the origin of GRBs emitting an ultrarelativistic blast wave, whose expansion follows the Blandford–McKee self-similar solution (Blandford & McKee 1976). Woosley (1993) linked the GRB origin to a Kerr BH emitting an ultrarelativistic jet originating from the accretion of toroidal material on to the BH. The BH was assumed to be produced from the direct collapse of a massive star, a 'failed' SN leading to a large BH of approximately 5 $M_\odot$, possibly as high as 10

$M_\odot$, a 'collapsar'. We will address this interesting idea within our BdHN model in Section 9.

In these ultrarelativistic blast wave models, the afterglow is explained by the synchrotron/synchrotron self-Compton (SSC) emission from accelerated electrons when the blast wave of $\Gamma \sim 1000$ is slowed down by the circumburst medium (Waxman & Piran 1994; Sari & Piran 1995; Sari 1997; Wijers, Rees & Meszaros 1997; Sari, Piran & Narayan 1998).

As pointed out by Zhang (2018), these ultrarelativistic blast wave models have been applied to explain a vast number of observations:

(i) The X-ray afterglow as well as the steep and shallow decay in the 'Nousek–Zhang' phase, the X-ray, and the gamma-ray flares.
(ii) The optical and radio emissions.
(iii) The high-energy emission in the GeV band observed in some long GRBs by *Fermi*-LAT.

An example of this method is the recent case of GRB 190114C, in which the traditional approach has been applied:

(i) To jointly explain the emissions in the TeV observed recently by MAGIC (MAGIC Collaboration 2019a, b; Mirzoyan et al. 2019); see Fig. 1.
(ii) To explain the emission in the MeV and GeV bands observed by the *Fermi* GBM and LAT satellites in the jetted emission.
(iii) To explain the emission in the MeV and keV bands observed by *Swift* including the emission in the optical and radio emissions.

In the traditional model, all of these emissions occur jointly using the kinetic energy of an ultrarelativistic blast wave with Lorentz

Table 1. Alphabetic ordered list of the acronyms used in this work.

Extended wording	Acronym
Binary-driven hypernova	BdHN
Black hole	BH
Carbon–oxygen star	CO-star
Fallback-powered kilonova	FB-KN
Gamma-ray burst	GRB
Gamma-ray flash	GRF
Gamma-ray flash kilonovae	GR-K
Massive neutron star	M-NS
Neutron star	NS
New neutron star	νNS
Short gamma-ray burst	S-GRB
Short gamma-ray flash	S-GRF
Supernova	SN
Supernova rise	SN-rise
Ultrashort gamma-ray burst	U-GRB
White dwarf	WD
X-ray flash	XRF

factor Gamma $\sim 10^3$, emitting at distances of $\sim 10^{16}$–10^{18} cm, implying total energies reaching 10^{55} erg.

This approach, however, encounters some contradictions with model-independent constraints. Moreover, there is no requirement that these different emission processes be explained by a single origin, i.e. the kinetic energy of a blast wave. As we are going to show in this article, each one of the above mentioned emissions finds its reason for existence in different specific processes originating in different specific episodes during the BdHN evolution. Each episode implies a different process and less demanding energy requirements.

1.5 The role of binary systems as progenitors of long GRBs

The role of binary systems as progenitors of long GRBs in our approach involves three assumptions:

(i) That all long GRBs, not only the S-GRBs, originate from binary systems. These binaries are composed of different combinations of CO_{core}, NS, white dwarfs (WDs), BH, and νNS; see Table 1. We classify all GRBs in nine different subclasses on the basis of their energetics, their spectra, and their duration expressed in the rest frame of the source. Only in *some* of these subclasses the presence of a BH occurs (see e.g. Ruffini et al. 2016b, 2018c; Wang et al. 2019); see in detail in Section 2.

(ii) We focus on BdHNe with a binary progenitor composed of a CO-star and a companion binary NS. As the CO_{core} gravitationally collapses, it gives origin to an SN and its iron core collapses to form a νNS. The hypercritical accretion of the SN ejecta on the companion NS leads, for binary periods $\lesssim 5$ min, to the formation of a BH. This happens when the NS critical mass is reached and overcome (Becerra et al. 2016). We denote these systems as BdHNe I in which a BH is formed. The BdHNe I are characterized by an isotropic energy, estimated by the *Fermi*-GBM, in the range $10^{52} < E_{iso} < 10^{54}$ erg. In the opposite case, i.e. for longer binary periods, a more M-NS originates from the SN hypercritical accretion process (Wang et al. 2019). These BdHNe II are characterized by $10^{50} < E_{iso} < 10^{52}$ erg (Ruffini et al. 2016b). The BdHNe III are characterized by binaries with even longer periods, so with more widely separated components, leading to an even weaker energy emission with $10^{48} < E_{iso} < 10^{50}$ erg.

(iii) We make use of recent theoretical results in the study of the hypercritical accretion of the SN ejecta both on the companion NS

and the νNS (see e.g. Becerra et al. 2016, 2019; Ruffini et al. 2016b, 2018a; Rueda et al. 2020). We rely on the three-dimensional (3D) simulations performed with a new smoothed particle hydrodynamics (SPH) code developed in collaboration with Los Alamos National laboratory (see e.g. Becerra et al. 2019, and reference therein). We here give special attention to this procedure in order to reconstruct the morphology of the BdHNe, which has a strong dependence on the viewing angle as a result of the binary nature of the progenitor. We use the observations of the GeV emission observed by *Fermi*-LAT present only in *some* BdHN to infer their morphology and visualize its nature by SPH simulations (see Sections 6 and 7 and Fig. 4).

1.6 The role of the binary progenitor in the SN associated with long GRBs

Contrary to the case of S-GRBs, the necessity of a binary progenitor in long GRBs did not arise from the very beginning, and possibly the most important observational piece of evidence of this need can be identified in the temporal and spatial coincidence of GRB 980425 (Pian et al. 2000) and SN 1998bw (Galama et al. 1998), and the subsequent systematic spectroscopic analysis of additional GRB-SN associations (see Cano et al. 2017, for a review).

There are two key observational aspects of the SNe associated with GRBs pointing to a relevant role of binary interactions: (1) they are of type Ic, namely both hydrogen and helium lack in their spectra, and (2) the spectral lines are broad-lined implying their ejecta expand at very high expansion velocities of the order of 10^4 km s^{-1}, implying kinetic energies of up to 10^{52} erg, the reason for which they have been dubbed HN (Cano et al. 2017).

The first feature, namely that these SNe are of type IC implies that they possibly originate from helium stars, CO_{core}, or Wolf–Raye stars that have rid of their outermost layers (see e.g. Smith et al. 2011). Indeed, it has been recognized that a binary companion would most efficiently help in stripping off the pre-SN star outermost layers by tidal effects, multiple mass-transfer, and common-envelope episodes (see e.g. Nomoto & Hashimoto 1988; Iwamoto et al. 1994; Fryer et al. 2007; Yoon, Woosley & Langer 2010; Smith et al. 2011).

The second feature, namely the observed high-expansion velocities of the SN ejecta, is more delicate and less straightforward to account for in theoretical models. In the BdHN model, numerical simulations in Ruffini et al. (2018a) have shown that the explosion of the GRB within the SN might transfer to it sufficient energy and momentum to convert an initial ordinary SN into an HN. Therefore, broad-lined SNe or HNe in the BdHN model does not necessarily need to be born as such, instead they can be the outcome of the GRB feedback into the SN (see also Becerra et al. 2019). Evidence of such a transition from an SN into an HN in a BdHN has been observationally identified in GRB 151027A (see Ruffini et al. 2018c, for details).

In addition, binary interactions may enforce corotation of the pre-SN star (i.e. the CO_{core}) thereby spinning it up to high rotation rates. For BdHN I, this implies a rotation period of the CO_{core} of the order of minutes, so a rotational energy $\sim 10^{50}$ erg (Wang et al. 2019). Of course, this cannot explain directly an observed kinetic energy of 10^{52} erg. The core collapse of the iron core of this rotating CO_{core}, by angular momentum conservation, implies the birth of a millisecond period νNS, which may well power the SN by injecting into it energies of the order of 10^{52} erg (see Wang et al. 2019; Rueda et al. 2020, for more details). It may also happen that binary interactions spin-up the CO_{core} beyond corotation bringing it to even to higher rotation rates ~ 1 rad s^{-1} (see e.g. Nakamura et al. 2014;
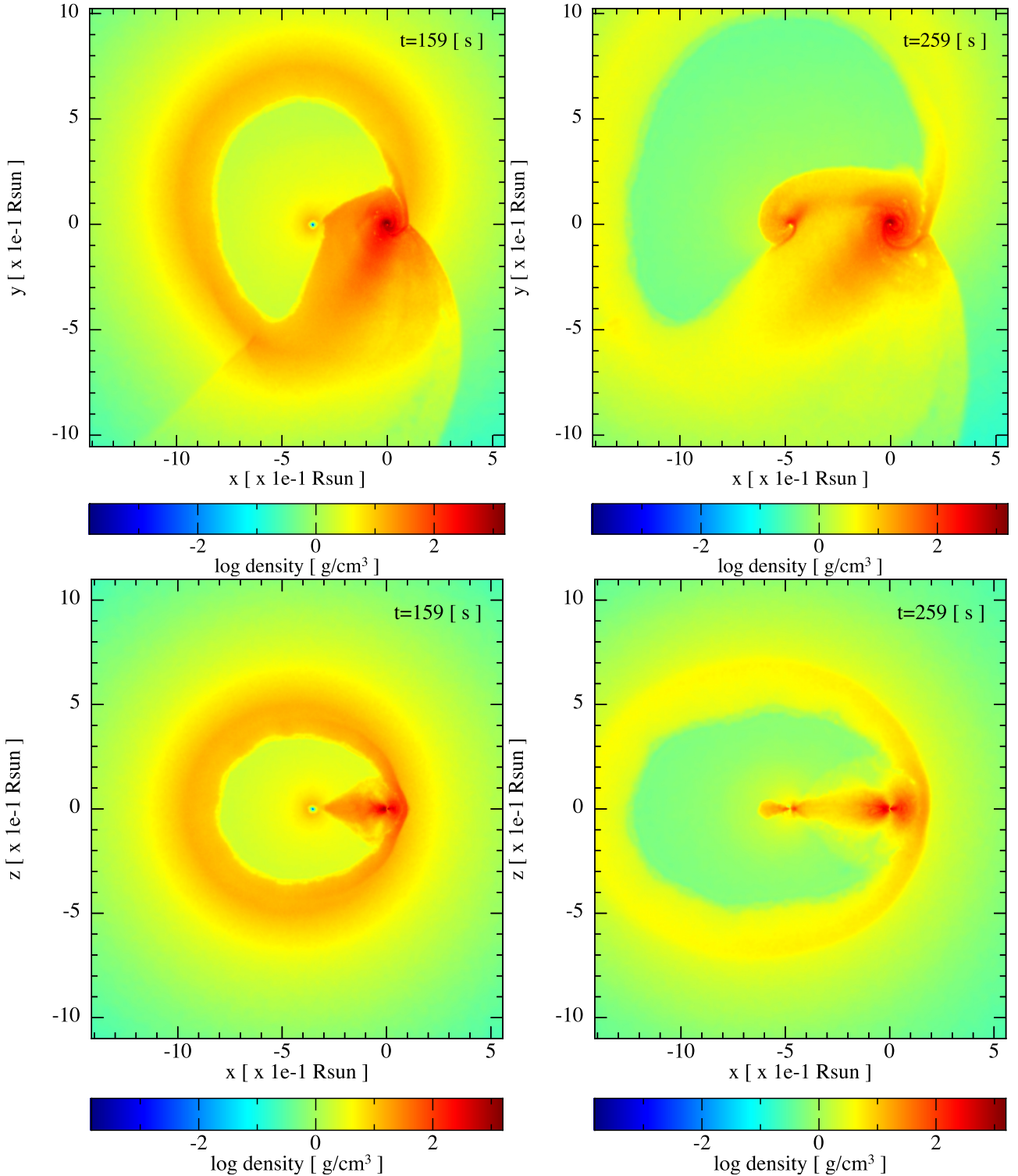
Figure 4. An SPH simulation from Becerra et al. (2019) of the exploding CO-star as the SN in the presence of a companion NS: Model '25m1p08E' (see table 2 therein). The CO-star is obtained from the evolution of a 25 $M_\odot$ zero-age main-sequence (ZAMS) progenitor that leads to a pre-SN CO-star mass $M_{CO} = 6.85\ M_\odot$. The initial mass of the νNS (formed at the centre of the SN) is 1.85 $M_\odot$ and the one of the NS companion is $M_{NS} = 2\ M_\odot$. The initial orbital period is 4.8 min. The upper panels show the mass density on the binary equatorial plane and the lower ones correspond to the plane orthogonal to it, at two selected times from the SN explosion ($t = 0$ of the simulation), 159 and 259 s. The reference system is rotated and translated so that the x-axis is along the line that joins the νNS and the NS, and the axis origin $(0, 0)$ is located at the NS position. For this simulation, the NS collapses reaching the secular axisymmetric instability point with a mass 2.26 $M_\odot$ and angular momentum $1.24 GM_\odot^2/c$, while the νNS is stable with mass and angular momentum, respectively, 2.04 $M_\odot$ and $1.24 GM_\odot^2/c$. Up to the final simulation time, the binary system kept bound although the binary orbit widens, reaching an orbital period of 16.5 min and an eccentricity of $\epsilon = 0.6$. The collapse of the NS to the newly formed BH, characteristic of a BdHN I, occurs at $t = 21.6$ min.

Gilkis 2018; Fujisawa et al. 2019), which would imply a much larger rotational energy of a few 10^{52} erg, ready to be used in the SN event.

There is increasing observational evidence on the high energetics of up to 10^{52} erg and the complex nature of the SN from the X- and gamma-ray precursors to the prompt radiation in long GRBs (see e.g. Wang et al. 2019). In order to account for such a complexity, we have dubbed these early phases of the BdHN as 'SN-rise' (Li et al. 2019). The *SN-rise* triggers the entire BdHN, so it includes the SN explosion as well as the feedback of the hypercritical accretion on to the νNS and on to the binary companion NS. We dedicate Section 3 to their analysis giving examples in the case of BdHN I and II.

We can conclude that the binary progenitor of the BdHN model provides a natural explanation of the observational features of the SN associated with long GRBs. Having said this, it is now appropriate to discuss the formation of the CO_{core}–NS binary progenitors of the BdHN from the stellar evolution viewpoint.

It is well known from the stellar evolution theory and observations that massive binaries might evolve to form binaries composed of compact objects, e.g. WD–WD, NS–WD, NS–NS and NS–BH. Leaving aside specific technical details, traditional evolutionary paths lead the compact remnant of the more massive star, after undergoing SN, to common-envelope phase with the companion, and after the collapse of the companion star leading to the second SN, the system forms a compact-object binary provided it keeps bound (Fryer, Woosley & Hartmann 1999; Dominik et al. 2012; Postnov & Yungelson 2014). It is very interesting that alternative evolutionary scenarios have been recently proposed in the X-ray binary and SN community leading to the so-called *ultrastripped* binaries used to explain NS–NS and low-luminosity SNe (see e.g. Tauris et al. 2013; Tauris, Langer & Podsiadlowski 2015, for details). The binary in these cases, after first SN, experiences multiple mass-transfer phases leading to the expulsion of the hydrogen and helium shells of the secondary. As proposed in Becerra et al. (2015) and Fryer et al. (2015), these evolutionary scenarios are a plausible path to form CO_{core}–NS binary progenitors of BdHN.

From the above descends the question of whether such a population of binaries might or not include the progenitors of the BdHN. The orbital periods of the binary at the end of the evolution in these population synthesis codes are 50–5000 h (Tauris et al. 2013). They have been used as a main channel to form NS–NS, but the formation of NS–BH binaries, which are the final outcome left by BdHN I, have not been up to now considered in population synthesis numerical codes. One of the main reasons for this is that the physical processes involved in a BdHN I, occurring when shorter orbital periods of the order of minutes are allowed, lead to BH formation and they have not accounted for yet in these numerical codes. This is certainly a major research that deserves to be pursued in the near future.

We refer to Fryer et al. (2015) for additional details on the following estimation of the BdHN progenitor population. Ultrastripped binaries are expected to be 0.1–1 per cent of the total SN (Tauris et al. 2013), which is estimated to be 2×10^4 Gpc^{-3} yr^{-1} (see e.g. Guetta & Della Valle 2007). The population densities of BdHN II/III and BdHN I have been estimated to be $\sim$100 and $\sim$1 Gpc^{-3} yr^{-1}, respectively (Ruffini et al. 2016b). The above numbers imply, for instance, that BdHN I would comprise of only the 0.5 per cent of the ultrastripped binaries. These estimates confirm, in passing, the rareness of the GRB phenomenon.

Since 2018, our research on BdHN has acquired a different status by promoting technical progress in the visualization and in the data analysis, as well as in the introduction of new theoretical paradigms and identification of new astrophysical regimes that we further extend in this article. We start with a specific example of BdHN simulation.

1.7 A specific BdHN I SPH simulation

In Fig. 4, we show the results of a specific SPH simulation of a BdHN I from Becerra et al. (2019). It represents the implosion of a CO_{core} of 6.85 M$_\odot$ giving origin to the explosion of an SN in presence of a binary companion NS of $M_{NS} = 2$ M$_\odot$. An additional NS of 1.85 M$_\odot$ originates from the collapse of the Fe-core within the CO_{core} (the green dot at the centre of the SN in the two left figures). We indicate as νNS this newborn neutron star, in order to differentiate it from the binary companion NS. The two upper panels correspond to the mass density in the binary equatorial plane of the binary progenitor, which we label for short as 'seen in the orbital plane'. The lower panels correspond to viewing in a plane orthogonal to the equatorial plane of the binary progenitor, indicated for short as 'seen from the top'. This figure well summarizes the central role of the SN in triggering the BDHN1 phenomenon: by first creating the νNS and the accreting SN ejecta both on the νNS and the binary NS companion. The sequence of the accretion process is followed in these Figs 159 s and 259 s. Following the hypercritical accretion process, the νNS reaches a mass and angular momentum, 2.04 M$_\odot$ and $1.24GM_\odot^2/c$, respectively. Up to the final simulation time. Similarly, the binary NS companion collapses reaching the secular axisymmetric instability point with a mass of 2.26 M$_\odot$ and angular momentum $1.24GM_\odot^2/c$ at $t = 21.6$ min. In this model, the initial binary period of the circular orbit is 4.8 min. The binary orbit then widens, reaching an orbital period of 16.5 min and an eccentricity of $\epsilon = 0.6$. We are going to give specific examples in selected GRBs of this process in Section 10 with the determination of the mass and spin of the newborn BH. This figure is also essential in emphasizing the implications of the different viewing angles implied by the binary nature of the progenitors, which have been also neglected in the traditional approach.

We further exemplify, in the next two sections, the large amount of results inferred on the BdHN nature utilizing the two above viewing angles.

1.8 The upper limits on the Lorentz Γ factor and nature of the afterglow

The observations of BdHN I 'seen in the orbital plane' have been addressed in a series of articles based essentially on the X-ray observations made with the XRT detector in *Swift* (see e.g. Ruffini et al. 2018a, and references therein). They have been essential in identifying model-independent upper limits on the Lorenz Γ factors of the emission regions during the gamma-ray flare, the X-ray flares phase, the flare-plateau, and the early afterglow phases (the Nousek–Zhang phase), following the initial ultrarelativistic prompt radiation phase.

The traditional approach had shown that gamma-ray spikes in the prompt emission occur at $\sim$10^{15}–10^{17} cm with Lorentz gamma factor $\Gamma \sim 10^2$–10^3 (e.g. Li 2020). Using a novel data analysis, we have shown that the time of occurrence, duration, luminosity, and total energy of the X-ray flares correlate with E_{iso}. A crucial feature has been identified in the observation of thermal emission in the X-ray flares that we have shown occurs at radii $\sim$10^{12} cm with $\Gamma \lesssim 4$. The upper limit of Lorentz factor, $\Gamma \lesssim 2$, has been there established in the analysis of the X-ray flares. Equally, an upper limit $\Gamma \lesssim 3$ has been set in the transition from a SN to an HN in GRB 151027A (Ruffini et al. 2018c). Finally, the limit $\Gamma \lesssim 2$ has been established in the thermal emission in the early part of the afterglow phase of GRB 130427A (Ruffini et al. 2018b).

The enormous kinetic energy of an ultrarelativistic blast wave needed in the traditional approach to explain the energy source of

the afterglow has been therefore superseded: the above mentioned stringent upper limits on the Γ factors exclude any ultrarelativistic motion.

The origin of the afterglow of long GRBs and these mildly relativistic processes have been successfully identified in the synchrotron emission produced by relativistic electrons in the SN ejecta, powered by the hypercritical accretion of the SN into the spinning νNS of 1.5 $M_\odot$ and its pulsar-like emission (Ruffini et al. 2018b; Wang et al. 2019; Rueda et al. 2020). From the amplitude of their decaying X-ray luminosities observed by *Swift*-XRT (Pisani et al. 2016), the spin of the νNS and the strength and structure of its magnetic field in specific BdHN I and II have recently been obtained (Rueda et al. 2020).

It is important that the synchrotron process occurring in the interaction of the SN ejecta with the νNS requires a much smaller energy to explain the nature of the afterglow in our present approach based on the hypercritical accretion from the SN on to the νNS (Wang et al. 2019; Rueda et al. 2020) than the ones purported in the ultrarelativistic blast waves.

1.9 The '*inner engine*' of BdHN I

The observations of the BdHN I 'seen from the top' are the main topic of this article. They lead to an identification of the morphology of BdHN I, to the origin of the MeV, GeV, and TeV emissions observed by the GBM and LAT instruments onboard the *Fermi* satellite, the *MAGIC* and the H.E.S.S telescopes, as well as a contribution to ultrahigh-energy cosmic rays (UHECRs) from GRBs (see e.g. Rueda & Ruffini 2020). Particularly important has been the recent identification of the physical process occurring in the '*inner engine*' originating from the GeV emission as 'seen from the top' in GRB 130427A, also confirmed in three additional BdHN I GRB 160509A, GRB 160625B, and GRB 190114C (Li et al. 2019; Ruffini et al. 2019c).

In these works:

(i) We have proposed that the *inner engine* of a BdHN I is composed of a Kerr BH in a non-stationary state, embedded in a uniform magnetic field B_0 aligned with the BH rotation axis, as modelled by the Papapetrou–Wald solution of the Einstein–Maxwell equations (Papapetrou 1966; Wald 1974), and surrounded by an extremely low density ionized plasma of 10^{-14} g cm^{-3}. Using GRB 130427A as a prototype, we have shown that this *inner engine* acts in a sequence of *elementary impulses* emitting '*blackholic quanta*' (Rueda & Ruffini 2020). The repetition time of the emission of each '*blackholic quantum*' of energy $\mathcal{E} \sim 10^{37}$ erg is $\sim 10^{-14}$ s at the beginning of the process. Then, it slowly increases with the time evolution. Electrons are accelerated to ultrarelativistic energy near the BH horizon and propagate along the polar axis, $\theta = 0$. They can reach energies of $\sim 10^{18}$ eV, and partially contribute to UHECRs. When propagating along $\theta \neq 0$ through the magnetic field B_0 they give rise to the synchrotron emission of GeV and TeV photons. The *inner engine* operates within a 'cavity' formed during the hypercritical accretion of the SN ejecta on to the NS binary companion, and during the BH formation (Ruffini, Melon Fuksman & Vereshchagin 2019b). This result is the first step towards identifying the BdHN I morphology, presented in this article.

(ii) It has been shown that the multiwavelength emissions corresponding to the above acceleration process leading to synchrotron radiation occur in a jet with a half-opening angle of $60°$ from the normal to the binary plane. The jetted emission occurs in selected energy bands in the MeV, GeV, TeV, and UHECR.

(iii) This result has been applied to GRB 130427A, and we here show that it applies generally to all BdHN I as a consequence of the novel morphology identified in this article.

(iv) We have evaluated the total GeV emission in GRB 130427A and identified its decaying luminosity in the GeV range with a power-law index of $\alpha_{\mathrm{GeV}} = -1.19 \pm 0.04$, using the first and the second *Fermi*-GRB catalogues (Ackermann et al. 2013; Ajello et al. 2019). In this article, we generalize this result to all BdHN I emitting GeV radiation.

1.10 On the measure of the BH mass and spin in BdHN I

For the first time, in Ruffini et al. (2019c) it was shown how to extract the rotational energy of a Kerr BH in an astrophysical system, using GRB 130427A as a prototype. This was made possible making use of the the mass–energy formula of the Kerr BH (Christodoulou 1970; Christodoulou & Ruffini 1971; Hawking 1971, 1972), given in equation (1a). There, it was shown how through the '*inner engine*' activity the energetics of the GeV emission could originate near the BH horizon and be explained using the extractable energy of the BH, keeping constant the BH *irreducible mass*. In turn, this has led to the first measure of the initial mass and spin of the BH at its moment of formation: $M = 2.3$ $M_\odot$, its spin, $\alpha = a/M = 0.47$. This article is dedicated to extend this classic result to all BdHN I, where sufficient GeV emission data are available. This same procedure will be soon extended to active galactic nuclei with BH masses up to 10^{10} $M_\odot$.

1.11 Structure of the article

We first give in Section 2 an outline of the nine GRB subclasses presented in Ruffini et al. (2016b), with a brief summary of their initial states (*in-state*), their final state (out-state), their energetics, and spectral properties in the gamma-rays both in the MeV and in the GeV emissions. We also recall the binary mergers that include the NS–NS binaries leading to the two classes of S-GRBs.

In Section 3, we summarize the previous results (Li et al. 2019) on the analysis of the SN-rise of BdHNe I and II obtained from *Fermi*-GBM, and present their relation with the X-ray afterglow observed by *Swift*-XRT.

In Section 4, following our previous works (Ruffini et al. 2018b; Wang et al. 2019; Rueda et al. 2020), we study properties of the X-ray afterglow of BdHNe and we determine the spin of the νNS in two BdHNe I, two BdHNe II, and one BdHN III system.

In Section 5, we analyse the properties of the GeV emission in BdHNe I updated following the second GRB catalogue presented by *Fermi*-LAT, which covers the first 10 yr of its operations, from 2008 August 4 to 2018 August 4 (Ajello et al. 2019). We address the 378 BdHNe I with known cosmological redshift; see the list of BdHNe I in Pisani et al. (2016), Ruffini et al. (2018a), and also the updated list in Appendix A. We then consider only the 54 BdHN I with the boresight angle of *Fermi*-LAT smaller than $75°$ at the trigger time. We give the details of the 25 BdHNe I with observed GeV radiation, out of the 54. For each of them, we list in Table 5 the cosmological redshift, the $E_{\mathrm{p,i}}$ of the spectrum, the $E_{\gamma,\mathrm{iso}}$ of the source, the *Fermi* GCN, the boresight angle, the E_{LAT}, the likelihood test statistic (TS), and some additional distinguishing properties. In Table 6 for the 29 BdHNe I, we then give the cosmological redshift, the $E_{\mathrm{p,i}}$ of the spectrum, the $E_{\gamma,\mathrm{iso}}$ of the source, the *Fermi* GCN, the boresight angle, and some distinguishing properties of the associated X-ray emissions.

In Section 6, we explain the nature of the these BdHNe in terms of a novel morphology of the binary system. The BdHN I have a conical

structure normal to the equatorial plane of the binary progenitor. When the observations are made with a viewing angle lying in the orbital plane of the binary progenitor then the GeV emission is not observable. In this case, only the gamma-ray flare, the X-ray flares, and the X-ray plateau remain observable. From the ratio $N_{LAT}/N_{tot} = 25/54$, we infer the presence in the BdHN I of a conical structure of approximately 60° around the normal to the plane of the binary progenitors. Within this cone all emissions are observable, namely the X-ray, the gamma-ray, the GeV and TEV emission, and UHECRs. For larger inclination angle as confirmed theoretically in Ruffini et al. (2018c, 2019c), the GeV radiation is not observable and only flaring activities are observed following the prompt radiation phase.

In Section 7, we show that this novel geometry is indeed present in the recent 3D SPH numerical simulations at the moment of BH formation in a BdHN (Becerra et al. 2019).

In Section 8, for each of the 25 BdHNe I, we provide the 0.1–10 GeV luminosity light curves as a function of the time in the rest frame of the source. We obtain a power-law fit $L_n = A_n t^{-1.19 \pm 0.04}$ erg s^{-1} and report the amplitude A_n and the luminosity at 10 s from the beginning of the prompt radiation, L_{10s}, with their associated uncertainties. We also provide a correlation between L_{10s} and $E_{\gamma,iso}$.

In Section 9, we determine the values of the mass and spin of the BH and the strength of the magnetic field surrounding the BH in the '*inner engine*' of the selected BdHNe I. We also show the process of hypercritical accretion of the SN on a companion NS gives in all cases origin to the newborn BH.

In Section 10, we confirm (1) the central role of the SN in giving rise to its hypercritical accretion on the νNS and the newly born BH, to the afterglow observed by SWIFT and to the high-energy GeV and TeV emission observed by Fermi-LAT, (2) that the MeV–GeV energetic range is explainable by extractable rotational energy of a Kerr BH operating n the '*inner engine*' and this result allows the determination of the initial mass and spin of the BH, and (3) the power-law evolution of the 0.1–100 GeV luminosity after the prompt phase arises from the slowing down rate of the BH spin, keeping constant the irreducible mass M_{irr} of the BH.

We finally proceed to the general conclusions in Section 11. Before proceeding, we indicate in Table 1 the alphabetic ordered list of acronyms used in this work.

2 SUBCLASSES OF GRBS AND DEFINITIONS OF BDHN

We address the specific role of the X-ray emission observed by the *Swift* satellite as well as the MeV–GeV radiation observed by the *Fermi* satellite in order to further characterize the nine subclasses of GRBs presented in Ruffini et al. (2016b) and updated in Ruffini et al. (2018a), Wang et al. (2019), and here further updated in Section 4 and Appendix A. In Table 2, we summarize for each GRB subclass their name, the number of observed sources with cosmological redshift, and their progenitors characterizing their 'in-state'.

In all cases, the GRB progenitors are binary systems composed of various combinations of CO$_{core}$, of NSs, of WDs, and of BHs. The 'out-state' of the corresponding mergers or accretion processes have been represented in fig. 7 in Ruffini et al. (2016b) where we also presented the interesting possibility that 'out-states' of the GRB subclasses can become the 'in-states' of new GRB subclasses. In particular, we indicate an example in which the 'out-state' of a BdHN I can become the 'in-state' of an S-GRB.

In this article, we focus only on long GRBs with BdHN progenitors (Ruffini et al. 2016b): binary systems composed of a CO$_{core}$,

exploding as SN Ic, and an NS binary companion. The presence of such an NS binary companion in close orbit can explain the removing of the outer layers of hydrogen and helium of the massive star leading to the CO$_{core}$ (see e.g. Ruffini et al. 2001; Rueda & Ruffini 2012; Fryer, Rueda & Ruffini 2014).

As noted in the introduction, when the CO$_{core}$ gravitationally collapses, it gives origin to an SN and its Fe core collapses to form a νNS. The entire dynamics and evolution of the BdHN is essentially based on these three different components and their interplay: the SN explosion (SN-rise), the νNS undergoing an overcritical accretion process of the SN ejecta, and the binary companion NS also undergoes an overcritical accretion process of the SN ejecta that monotonically increases the binary NS companion mass. In compact binary systems, this accretion causes the NS to reach its critical mass leading to the formation of a newborn BH (Becerra et al. 2015, 2016); see also Fig. 4.

We first address the SN hypercritical accretion on to the binary NS companion: the outcome is a strong function of the compactness of the binary system and its binary orbital period.

When the orbital period is as short as 5 min, the hypercritical accretion proceeds at higher rates and the companion NS reaches its critical mass leading to:

(i) the formation of a BH and consequently a formation of a new binary system composed of a BH and a νNS (Fryer et al. 2014);

(ii) the emission of a very energetic GRB in the range of $10^{52} \lesssim E_{iso} \lesssim 10^{54}$ erg and, peak energy in the range of 0.2 MeV $< E_{p,i} <$ 2 MeV lasting a few seconds known as the ultrarelativistic prompt emission phase (UPE);

(iii) the onset of the prolonged power-law GeV emission, triggered by the formation of the newborn BH, with a luminosity described in the rest frame of the source

$$L_{GeV} = A_{GeV} \left(\frac{t}{1\,s} \right)^{-\alpha_{GeV}} , \qquad (2)$$

with $\alpha_{GeV} = 1.19 \pm 0.04$. One of the main results in this paper is to show that this radiation is present only in a subset of BdHN and the explanation of this result will lead to the determination of the conical BdHN morphology, see Section 8.

These systems have been indicated as BdHN I (Becerra et al. 2015, 2016; Ruffini et al. 2015b, 2016b, 2019c; Wang et al. 2019).

The first list of the BdHNe I was composed of 161 sources spanning 12 yr of *Swift*/XRT observation activity till 2015 presented in Pisani et al. (2016) which was further extended to 173 sources in Ruffini et al. (2018a) up through the end of 2016 which led to a total of 345 BdHNe I within 1997–2016 observed by other satellites like *Fermi* and *Konus*-WIND in addition to *Swift*. This list is further extended here to 378 BdHN I till 2018 December (see Appendix A and Table 2).

When the orbital period of the binary system is $\gtrsim$5 min, the hypercritical accretion is not sufficient to trigger the collapse of the NS companion into a BH: therefore, no GeV emission can be produced nor be observed. Therefore, an M-NS is formed. In these systems, the observed peak energy is in the range 4 keV $< E_{p,i} <$ 300 keV and the isotropic energy is the range of $10^{48} \lesssim E_{iso} \lesssim 10^{52}$ erg, as observed by the *Fermi*-GBM. They have been indicated as X-ray flashes (XRF) in contrast with the more energetic BdHN I (Becerra et al. 2015, 2016; Ruffini et al. 2015b, 2016b). We here use for the XRFs the name BdHN II, according to Wang et al. (2019). A canonical example has been given in Wang et al. (2019); see Table 2.

BdHNe III have the same composition as BdHNe II, but the binary is further detached. No BH is formed and no GeV radiation

Table 2. Summary of the GRB subclasses. In addition to the subclass name, we report the number of GRBs for each subclass. We recall as well the 'in-state' representing the progenitors and the 'out-state' and the $E_{p,i}$ and $E_{\gamma,iso}$ for each subclass. The GeV emission is indicated in the last column: for long GRBs it appears only in BdHN I and BdHN IV (BH-SN) while, for short bursts, it appears only for S-GRBs. In all sources with GeV emission, it is $\gtrsim 10^{52}$ erg.

Class	Type	Number	In-state	Out-state	$E_{p,i}$ (MeV)	$E_{\gamma,iso}$ (erg)	$E_{iso,Gev}$ (erg)
Binary driven	I	378	CO star–NS	νNS–BH	~ 0.2–2	$\sim 10^{52}$–10^{54}	$\gtrsim 10^{52}$
hypernova	II	(49)	CO star–NS	νNS–NS	~ 0.01–0.2	$\sim 10^{50}$–10^{52}	–
(BdHN)	III	(19)	CO star–NS	νNS–NS	~ 0.01	$\sim 10^{48}$–10^{50}	–
	IV	0	CO star–NS	BH	–	$> 10^{54}$	$\gtrsim 10^{53}$
	I	18	NS–NS	MNS	~ 0.2–2	$\sim 10^{49}$–10^{52}	–
Binary	II	6	NS–NS	BH	~ 2–8	$\sim 10^{52}$–10^{53}	$\gtrsim 10^{52}$
merger	III	(1)	NS–WD	MNS	~ 0.2–2	$\sim 10^{49}$–10^{52}	–
(BM)	IV	(1)	WD–WD	NS/MWD	< 0.2	$< 10^{51}$	–
	V	(0)	NS–BH	Direct BH	$\gtrsim 2$	$> 10^{52}$	–

is produced nor observed. This subclass is characterized by binary systems widely separated and weaker energy emission with E_{iso} in the range of 10^{48}–10^{50} erg.

As we will see in Section 10, the most energetic BdHN I originate from extremely tight binary systems with the companion NS grazing the radius of the CO_{core}. It is therefore conceivable that in some systems the NS companion merges with the CO_{core} just prior to the SN explosion leading to the possible direct formation of a BH, a concept envisaged by Woosley (1993) in the failed SN scenario. We have left such a possibility opened in an additional BdHN IV family; see Table 2.

The hypercritical accretion of the SN ejecta on to the νNS leads to the pulsar-like emission that gives rise to the X-ray afterglow emission observed by *Swift* (Rueda et al. 2020). This is a property intrinsic to the nature of the model and shared by all BdHN subclasses. It is therefore natural to expect, as has been verified, that the luminosity of the X-ray afterglows of *all* long GRBs, in all BdHN subclasses, follow a common decaying power law of

$$L_X = A_X \left(\frac{t}{1\,s}\right)^{-\alpha_X}, \tag{3}$$

with $\alpha_X = 1.48 \pm 0.32$, including the SN-rise, when averaged over all BdHN I up to 10^6 s (Pisani et al. 2016). The different amplitudes, A_X, and power-law indices, α_X, of the X-ray afterglow luminosity can be used to determine the spin and magnetic field of the νNS (Wang et al. 2019; Rueda et al. 2020).

Before leaving this topic, we mention a few cases of X-ray afterglows in BdHN II and BdHN III. Each BdHN II and BdHN III must be also characterized by an X-ray afterglow originating from the accretion of the SN ejecta into the νNS. Their power-law index α_X coincides with the one of BdHN I, although the difference in the total angular momentum of the binary progenitors and its conservation leads necessarily to a smaller value of the amplitude A_X in equation (3), to a corresponding lower value of the νNS spin, and to a smaller value of the SN-rise; see Fig. 5.

In the rest of this article, we mainly examine the properties of BdHN I with special attention to:

(i) their SN-rise emission;
(ii) the power-law decay of the X-ray emission of the afterglow observed by *Swift*, measured in the cosmological rest frame of the source;
(iii) the corresponding GeV emission observed by *Fermi*-LAT, centring on the identification of the BdHN morphology to explain the absence of this emission in a subclass of BdHN I.

3 THE SN-RISE IN BDHN I AND BDHN II: FERMI OBSERVATION

The trigger of all BdHNe is represented by the gravitational collapse of the CO_{core} that gives origin to an SN and its Fe-core collapses to form a νNS. We have indicated the first appearance of the SN as the SN-rise. In BdHN I, the SN-rise is characterized by the presence of the thermal component in the *Fermi*-GBM data with isotropic energy of $\sim 10^{52}$ erg (see Fryer et al. 2014; Li et al. 2019; Ruffini et al. 2019a). In BdHN II, the SN-rise is weaker and has no thermal component in the *Fermi*-GBM data with energy of $\sim 10^{50}$ erg (see Li et al. 2019; Ruffini et al. 2019a; Wang et al. 2019; Fig. 6 and Table 3). In this article, we just recall the observation of the SN-rise in four BdHNe I: GRB 130427A, GRB 160509A, GRB 180720B, and GRB 190114C, as well as in two BdHNe II: GRB 180728A and GRB 190829A. In Fig. 6, we show the spectra of the SN-rise in the aforementioned sources and in Fig. 7 we show their corresponding luminosity.

4 THE AFTERGLOWS OF BDHN I, BDHN II, AND BDHN III: THE SWIFT OBSERVATIONS

Following the CO_{core} gravitational collapse and the appearance of the SN-rise, which characterizes all BdHN subclasses, the hypercritical accretion of the SN ejecta on to the νNS and the magnetic field of the νNS leads to the pulsar-like emission powering the X-ray afterglow observed by the *Swift* satellite (Rueda et al. 2020).

We present four afterglows of BdHN I (Fig. 7), two afterglows of BdHNe II, and one afterglow of BdHNe III (Fig. 5). In each case, we also reproduce the SN-rise presented in the previous section (see Figs 5 and 7).

The BdHN I in GRB 130427A, GRB 190114C, GRB 180720B, and GRB 160509A follow a decaying luminosity consistent with equation (3) (see Fig. 7):

(i) GRB 130427A with amplitude $(3.65 \pm 0.63) \times 10^{52}$ erg s^{-1} and power-law index $\alpha_X = 1.24 \pm 0.02$.
(ii) GRB 160509A with amplitude $(22.68 \pm 24.00) \times 10^{52}$ erg s^{-1} and power-law index $\alpha_X = 1.22 \pm 0.09$.
(iii) GRB 180720B with amplitude $(112.67 \pm 93.89) \times 10^{52}$ erg s^{-1} and power-law index $\alpha_X = 1.43 \pm 0.07$.
(iv) GRB 190114C with amplitude $(5.14 \pm 2.03) \times 10^{52}$ erg s^{-1} and power-law index $\alpha_X = 1.37 \pm 0.05$.

The BdHNe II in GRB 180728A and GRB 190829A follow a decaying luminosity consistent with equation (3) (see Wang et al. 2019; Figs 5a and b):
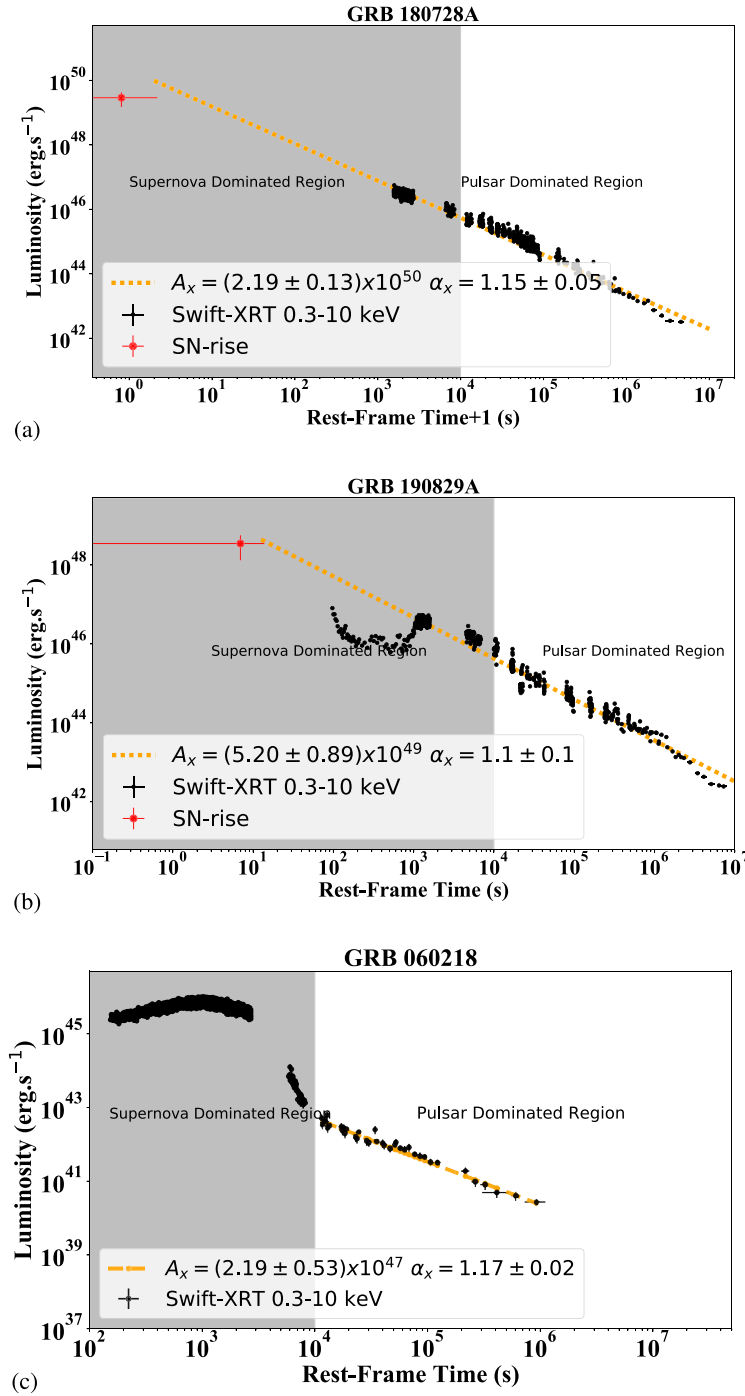
Figure 5. The X-ray afterglow luminosity observed by *Swift*-XRT that follow a decaying power law: (a) GRB 180728A (BdHN II) with amplitude $(2.19 \pm 0.13) \times 10^{50}$ erg s^{-1} and power-law index $\alpha_X = 1.15 \pm 0.05$. (b) GRB 190829A (BdHN II) with amplitude $(5.20 \pm 0.89) \times 10^{49}$ erg s^{-1} and power-law index $\alpha_X = 1.1 \pm 0.1$. (c) GRB 060218 (BdHN III) with amplitude $(2.19 \pm 0.53) \times 10^{47}$ erg s^{-1} and power-law index $\alpha_X = 1.17 \pm 0.02$. The fallback material of the SN on the νNS produce this X-ray afterglow emission (Rueda et al. 2020). In Section 4.1, we report the result of the simultaneous fit of the X-ray afterglow of all types of BdHN in order to find the universal power-law index. As shown in Ruffini et al. (2018a, c), until $\sim 10^4$ s the gamma/X-ray afterglow is mainly produced by the SN kinetic energy (*SN dominated region*) and its interaction with the magnetic field of the νNS. After 10^4 s, as shown by Ruffini et al. (2018b), the role of νNS becomes prominent (*pulsar dominated region*).

(i) GRB 180728A with amplitude $(2.19 \pm 0.13) \times 10^{50}$ erg s^{-1} and power-law index $\alpha_X = 1.15 \pm 0.05$.

(ii) GRB 190829A with amplitude $(5.20 \pm 0.89) \times 10^{49}$ erg s^{-1} and power-law index $\alpha_X = 1.1 \pm 0.1$.

As an example of the X-ray afterglow luminosity of a BdHN III, we indicate the case of GRB 060218 where the X-ray luminosity, as in the case of BdHNe I and II, follows a decaying power-law consistent with equation (3), with an amplitude $(2.19 \pm 0.53) \times 10^{47}$ erg s^{-1}
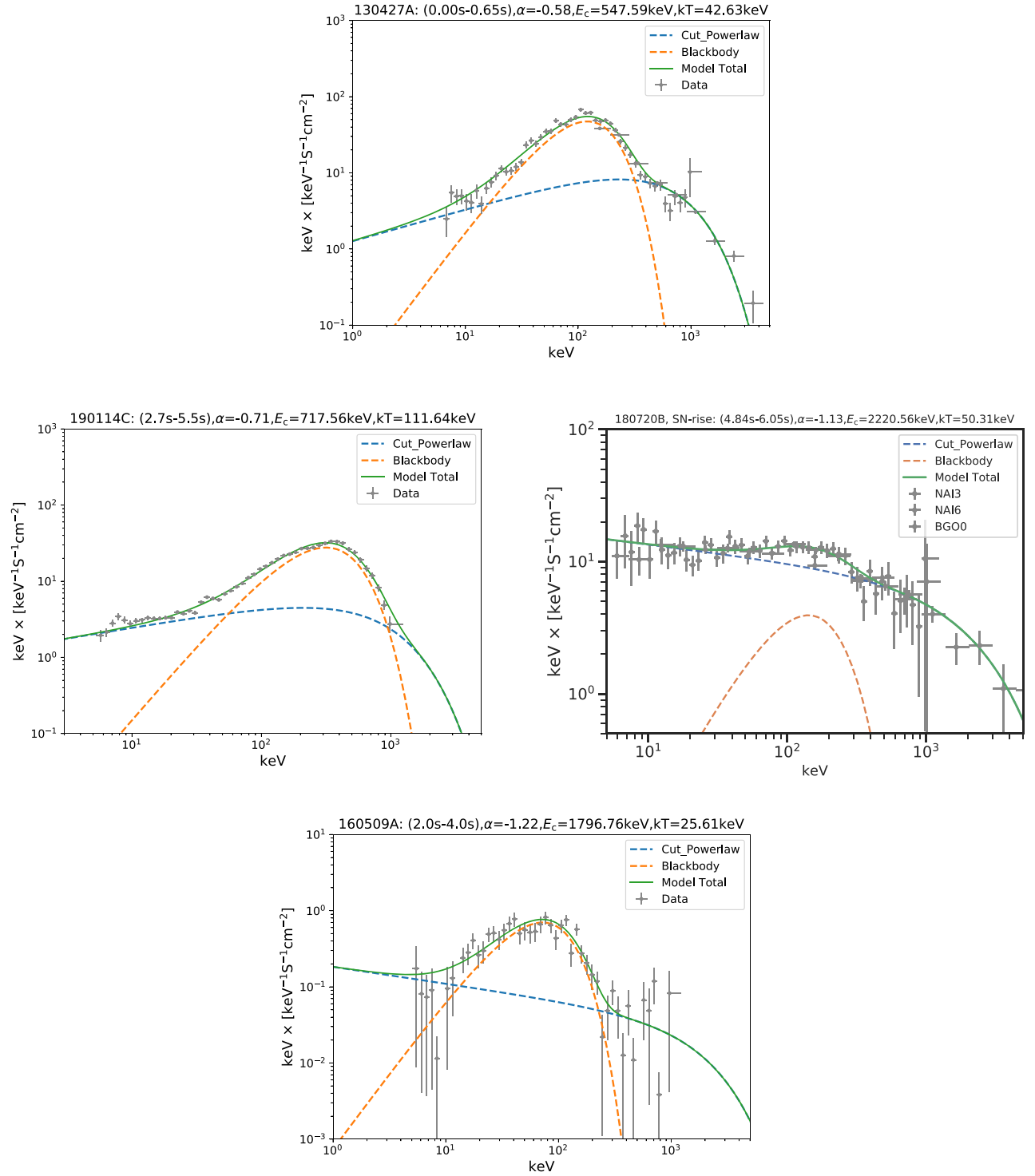
Figure 6. The spectrum of the SN-rise of GRB 160509A as observed by *Fermi*-GBM in the energy range of 8–900 keV. Upper left: SN-rise spectrum of BdHN I 130427A, well fitted by a CPL + BB model, from 0 to 0.65s ($t_{rf} \simeq 0.49s$); the spectral index α is -0.58, cut-off energy E_c is 547.59 keV, and the BB temperature is 42.63 keV in the observer's frame. Upper right: The spectra of SN-rise of BdHN I 190114C corresponding to $t = 1.12$ s ($t_{rf} = 0.79s$) to $t = 1.68$ s ($t_{rf} = 1.18s$), which is best fit by a CPL + BB model, with a low-energy photon index α of -0.71, and a peak energy E_c of 524.7 keV, and a BB temperature 18.42 keV. Time is reported in both the observer's frame and the rest frame. Spectral parameters of the best fit are presented in the observer's frame. Lower left: SN-rise spectrum of BdHN I 180720B, well fitted by a CPL + BB model, from 4.84 to 6.05 s ($t_{rf} \simeq 0.s$); the spectral index α is -1.13, cut-off energy E_c is 2220.569 keV, and the BB temperature is 50.31 keV in the observer's frame. Lower right: SN-rise spectrum of BdHN I 160509A, well fitted by a CPL + BB model, from 2.0 to 4.0 s ($t_{rf} \simeq 0.s$); the spectral index α is -1.22., cutoff energy E_c is 1796.76 keV, and the BB temperature is 25.66 keV in the observer's frame.

Table 3. The properties of the SN-rise in BdHN I: GRB 190114C, GRB 130427A, GRB 160509A, and GRB 160625B; and the properties of the SN-rise in BdHN II: GRB 180728A.

GRB	t_1–t_2 (s) (Observation)	Duration (s) (Rest)	Flux (erg cm^{-2} s^{-1})	E_{sh} (10^{52} erg) (SN-rise)	E_{iso} (erg) (Total)	Temperature (keV) (Rest)	Redshift	Reference (For SN-rise)
190114C	1.12–1.68	0.39	$1.06^{+0.20}_{-0.20}(10^{-4})$	$2.82^{+0.13}_{-0.13}$	$(2.48 \pm 0.20) \times 10^{53}$	$27.4^{+45.4}_{-25.6}$	0.424	Melandri et al. (2019)
130427A	0.0–0.65	0.49	$2.14^{+0.28}_{-0.26}(10^{-5})$	$0.65^{+0.17}_{-0.17}$	$\sim 1.40 \times 10^{54}$	$44.9^{+1.5}_{-1.5}$	0.3399	Xu et al. (2013)
160509A	2.0–4.0	0.92	$1.82^{+1.23}_{-0.76}(10^{-6})$	$1.47^{+0.6}_{-0.6}$	$\sim 1.06 \times 10^{54}$	$25.6^{+4.8}_{-4.7}$	1.17	Tam et al. (2017)
160625B	0–2.0	0.83	$6.8^{+1.6}_{-1.6}(10^{-7})$	$1.09^{+0.2}_{-0.2}$	$\sim 3.00 \times 10^{54}$	$36.8^{+1.9}_{-1.9}$	1.406	This paper
180728A	−1.57 to 1.18	0.83	$4.82^{+1.16}_{-0.82}(10^{-8})$	$7.98^{+1.92}_{-1.34} \times 10^{49}$	$2.76^{+0.11}_{-0.10} \times 10^{51}$	-	0.117	Izzo et al. (2018)
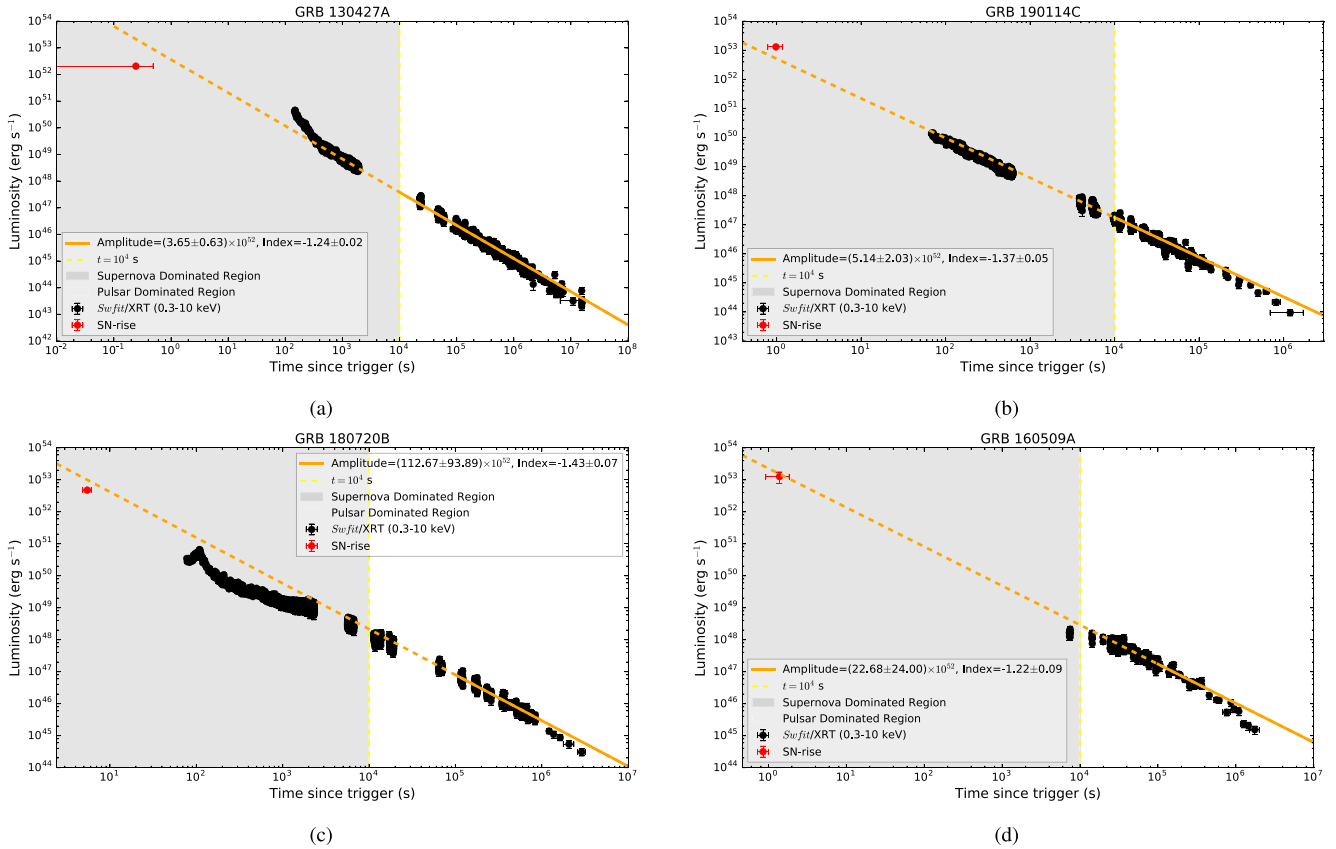
Figure 7. X-ray afterglow luminosities of four BdHNe I observed by *Swift*-XRT that follow a decaying power law: (a) GRB 130427A (BdHNe I) with amplitude $(3.65 \pm 0.63) \times 10^{52}$ erg s^{-1} and power-law index $\alpha_X = 1.24 \pm 0.02$. (b) GRB 190114C with amplitude $(5.14 \pm 2.03) \times 10^{52}$ erg s^{-1} and power-law index $\alpha_X = 1.37 \pm 0.05$. (c) GRB 180720B with amplitude $(112.67 \pm 93.89) \times 10^{52}$ erg s^{-1} and power-law index $\alpha_X = 1.43 \pm 0.07$. (d) GRB 160509A with amplitude $(22.68 \pm 24.00) \times 10^{52}$ erg s^{-1} and power-law index $\alpha_X = 1.22 \pm 0.09$. The red points show the luminosity of SN-rise in each BdHN. The fallback of material from the SN on to the νNS produces this X-ray afterglow emission (Rueda et al. 2020). As shown in Ruffini et al. (2018a, c), till $\sim 10^4$ s the gamma/X-ray afterglow is mainly produced by the SN kinetic energy (*SN dominated region*) and its interaction with the magnetic field of the νNS. After 10^4 s, as shown by Ruffini et al. (2018b), the role of νNS becomes prominent (*pulsar dominated region*).

and power-law index $\alpha_X = 1.17 \pm 0.02$. This is consistent with $\alpha_X = 1.2 \pm 0.1$ obtained by Campana et al. (2006; see Fig. 5c).

We can then reach the following general conclusions:

(i) The X-ray afterglow is present in all three BdHN subclasses: BdHN I, BdHN II, and BdHN III.

(ii) The X-ray afterglow is always present in *all* of the 378 BdHNe I (see Appendix A).

(iii) This result clearly indicates the spherical symmetry, or a very wide-angle emission of the X-ray afterglow.

4.1 The spin of the νNS

In Ruffini et al. (2018b), Rueda et al. (2020), and Wang et al. (2019), the bolometric luminosity contributing to the optical and X-ray bands by the νNS rotational energy loss by magnetic braking has been modelled for the emission at late times $t \gtrsim 10^4$ s of the 'Nousek–Zhang' (flare-plateau-afterglow, FPA phase). This allows the inference of the initial rotation period of the νNS as well as its magnetic field structure. The origin of the long GRB afterglows at this phase is the interaction between the SN ejecta and the spinning magnetized νNS and their synchrotron emission (Ruffini et al. 2018b).

Since the νNS is just born, it must be rapidly rotating and contains abundant rotational energy:

$$E_{\rm rot} = \frac{1}{2} I \Omega^2, \qquad (4)$$

where I is the moment of inertia and $\Omega = 2\pi / P_{\nu\rm NS}$ is the angular velocity. For a νNS with a period of $P_{\nu\rm NS} = 1$ ms, $M = 1.4$ M$_\odot$, $R = 10$ km, the moment of inertia is $I \sim 10^{45}$ g cm^2. This leads to a total rotational energy of $E \sim 2 \times 10^{52}$ erg.

We assume that the rotational energy of the νNS provides the energy budget of the X-ray radiation via synchrotron emission of the electrons (Ruffini et al. 2018b):

$$E_{\rm rot} = E_{\rm X}. \qquad (5)$$

This is reminiscent of the extraction of the BH rotational energy via synchrotron radiation of electrons radiating in the GeV energy band (Ruffini et al. 2019c).

Therefore, using the equation (4) and substituting the equation (3)

$$\frac{\mathrm{d}E_X}{\mathrm{d}t} = L_{\rm X}(t) = A_{\rm X} \left(\frac{t}{1\mathrm{s}}\right)^{-\alpha_{\rm x}} = -I\Omega\dot{\Omega}. \qquad (6)$$

The best fit to the X-ray luminosity of equation (3), together with equation (6), allow an estimate of the spin of the νNS in *all* BdHNe, as well as their spin evolution (see Table 4 and Fig. 8).

In Table 4, we report the physical quantities of three BdHNe I, GRB 130427A, GRB 180720B, and GRB 190114C, together with two BdHNe II, GRB 180728A and GRB 190829A, as well as one BdHN III, GRB 060218; assuming a νNS of mass and radius, respectively, 1.4 M$_\odot$ and 10^6 cm. The νNS emission is not able to explain the emission of the 'Nousek–Zhang' phase at early times 10^2–10^4 s. As it is shown in Ruffini et al. (2018b, c), that emission is mainly powered by the mildly relativistic SN kinetic energy that we refer to as the *SN dominated region*. After 10^4 s, as shown by Ruffini et al. (2018b), the role of νNS becomes prominent, referred to as the *pulsar dominated region*.

The first main results of this paper are: (1) the first identification of the SN-rise, (2) the agreement of the extrapolated luminosity of the X-ray afterglow with the luminosity of the SN-rise, and (3) the measurement of the νNS period, leading to the power-law emission of the afterglow (see Fig. 7). The two process of the SN-rise energetics and the νNS dynamics appear to be strongly correlated.

5 BDHN I: THE FERMI-LAT OBSERVATIONS

5.1 BdHNe I observed by Fermi-LAT

We now address the 378 BdHNe I with known redshifts (see Pisani et al. 2016; Ruffini et al. 2018a; Appendix A): out of them, we are first interested in the 25 BdHNe I emitting GeV radiation and within the boresight angle of *Fermi*-LAT, i.e. $\theta < 75°$, at the time of the trigger, since exposure drops quickly for larger angles (Ajello et al. 2019). They have as well a TS value >25, which means the GeV photons are excluded at the 5σ level from background sources. We follow the first and second *Fermi* catalogues (Ackermann et al. 2013; Ajello et al. 2019) for the time-resolved likelihood spectral analysis. Therefore, we divide the data into logarithmic spaced bins and, if the TS value of each bin is smaller than 16, we merge the time bin with the next one and repeat the likelihood analysis. In Table 5, we indicate in the first column the name of the BdHNe I, in the second their measured redshift, we report in the third column the $E_{\rm p,i}$ obtained from the *Fermi* data, we estimate in the fourth column the

$E_{\gamma,\rm iso}$, which is itself larger than the 10^{52} erg. In the fifth column, the *Fermi* GCN numbers are shown. In the sixth column, the values of $E_{\rm LAT}$ are provided and finally we add the boresight angle of the LAT $\theta < 75°$ and the TS values of these GRBs observed by LAT.

5.2 BdHNe I without GeV emission and geometry of the BdHNe I

We now turn to an additional unexpected result obtained in the analysis of the BdHNe I subtended within the 75° of the *Fermi*-LAT boresight angle: the existence of 29 BdHNe I without observed GeV emission (see Table 6). Although the distribution of the boresight angle and redshift is analogous to the one of the 25 sources considered in Section 5, no GeV emission is observed.

Some BdHNe I of this group have been observed previously by *Swift* and have been identified as sources of (i) gamma and hard X-ray flares, (ii) soft X-ray flares, and of (iii) the extended thermal emission (see Ruffini et al. 2018a, for details). A particular example has been given by GRB 151027A in Nappo et al. (2017) and Ruffini et al. (2018c). There, we assumed that the viewing angle of these sources lies in the equatorial plane of the progenitor system (see Section 1 and Fig. 4). As we will show in this article, in none of these sources GeV radiation can be observed due to the new morphology discovered in the BdHNe I (see next section).

6 MORPHOLOGY OF BDHN I

We here assume that the 25 sources considered in Table 5, all emitting in the GeV have a viewing angle close to the normal of the plane. This assumption is confirmed in Ruffini et al. (2019c) where indeed the high-energy GeV–TeV radiations are emitted in direction close to the BH rotation axis.

The remaining 29 sources in Table 6 have a viewing angle in the equatorial plane of the binary progenitor and in that case only flaring activities in gamma and X-ray are observable, i.e. no GeV–TeV emission, as explicitly shown in Ruffini et al. (2018c, 2019c). This allows us to introduce a new morphology for the BdHNe I and predict specific observational properties.

We now look at the ratio between the number of GRBs with an observed GeV radiation, $N_{\rm LAT}$, and the total number of GRBs, $N_{\rm tot}$, both within the LAT 75° boresight angle. We assume that: (1) BdHNe I follow the same cosmological isotropic distribution of all GRBs first observed by the BATSE instrument onboard the CGRO satellite (see e.g. Meegan et al. 1992; Paciesas et al. 1999); (2) all orientations of the BdHNe I with respect to the LAT detector are equally probable; (3) the GeV emitting region is a two-side cone whose opening angle is the same for all sources. Under these assumptions, we can then estimate the half-opening angle of a single cone ϑ as

$$1 - \cos\vartheta = \frac{N_{\rm LAT}}{N_{\rm tot}}. \qquad (7)$$

Our search in the LAT data[1] gives $N_{\rm LAT} = 25$ and $N_{\rm tot} = 54$, leading to $\vartheta \approx 60°$. Therefore, in BdHN I the GeV emission comes from a wide-angle emission, as it is schematically shown in Fig. 9. This is in agreement with theory of synchrotron radiation produced around the Kerr BH along the rotation axis (see details in Ruffini et al. 2019c).

Therefore, we have identified a *new* morphology of the BdHN I (see Figs 9 and 10). The identification of this morphology has been possible thanks to the analysis of the GeV emission in this paper, by

---

[1] https://fermi.gsfc.nasa.gov/ssc/observations/types/grbs/lat_grbs/table.php

Table 4. Observational properties of three BdHN I, GRB 130427A, GRB 180720B, and GRB 190114C together with two BdHNe II 180728A and 190829A as well as one BdHN III, GRB 060218 and inferred physical quantities of the νNS of the corresponding BdHN model that fits the GRB data. Column 1: GRB name; column 2: identified BdHN type; column 3: cosmological redshift (z); column 4: the isotropic energy released ($E_{\rm iso}$) in gamma-rays; column 5: νNS rotation period ($P_{\nu \rm NS}$) at 10^4 s, column 6: The isotropic energy of the X-ray afterglow ($E_{\rm X}$). We assume the NS mass of 1.4 M$_\odot$ and the NS radius of 10^6 cm for all these cases.

GRB	Type	Redshift	$E_{\rm iso}$ (erg)	$P_{\nu \rm NS} @ 10^4$ s (ms)	$E_{\rm X}$(after10^4 s) (erg)	$A_{\rm X}$ (erg s^{-1})	$\alpha_{\rm X}$
130427A	BdHN I	0.34	9.2×10^{53}	1.15	1.67×10^{52}	$(3.65 \pm 0.63) \times 10^{52}$	1.24 ± 0.02
180720B	BdHN I	0.654	6.8×10^{53}	0.66	4.99×10^{52}	$(112.67 \pm 93.89) \times 10^{52}$	1.43 ± 0.07
190114C	BdHN I	0.42	1.5×10^{53}	2.19	4.60×10^{51}	$(5.14 \pm 2.03) \times 10^{52}$	1.37 ± 0.05
180728A	BdHN II	0.117	2.3×10^{51}	7.74	3.68×10^{50}	$(2.19 \pm 0.13) \times 10^{50}$	1.15 ± 0.05
190829A	BdHN II	0.0785	2.2×10^{50}	10.31	2.07×10^{50}	$(5.20 \pm 0.89) \times 10^{49}$	1.10 ± 0.06
060218	BdHN III	0.033	5.4×10^{49}	285.81	2.69×10^{47}	$(2.19 \pm 0.53) \times 10^{47}$	1.17 ± 0.02
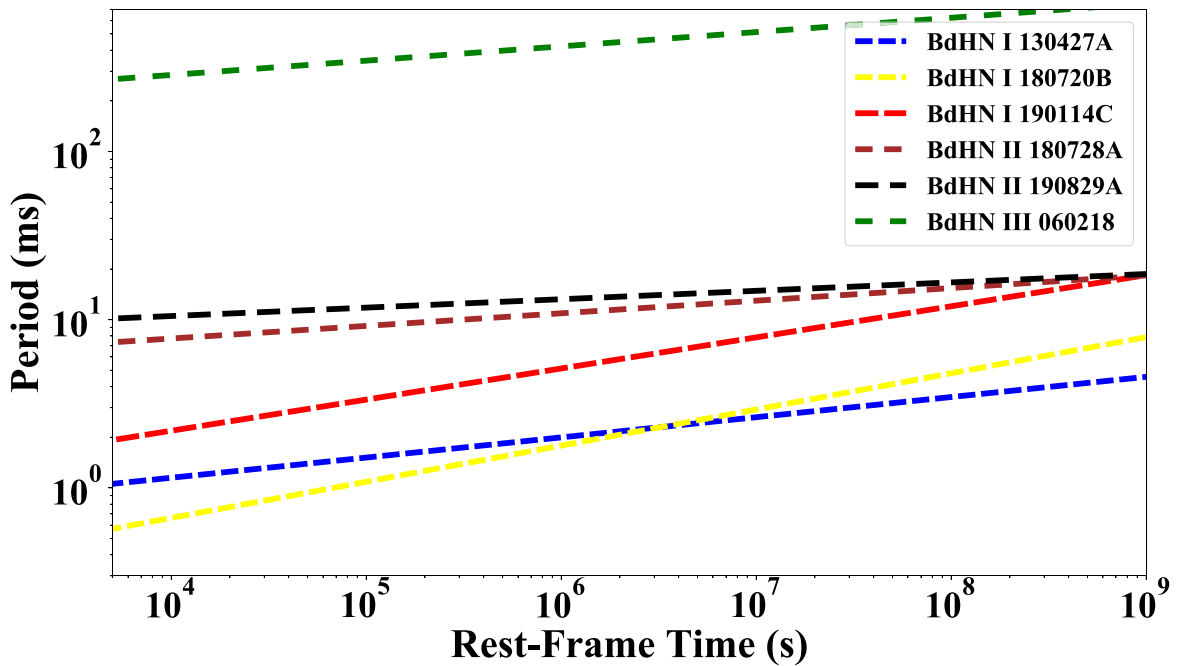
Figure 8. The evolution of the νNS period of six BdHNe, as a function of rest-frame time. The values of the νNS period at 10^4 s, namely in the pulsar dominated region of the afterglow are tabulated in Table 4. The trend of the νNS period indicates that the rotational energy is being released due to the radiation losses in the keV band revealing itself as the X-ray afterglow luminosity.

the soft and hard X-ray flares in Ruffini et al. (2018a), the extended thermal emission in Nappo et al. (2017), and Ruffini et al. (2018a) in GRB 151027A. In this identification, we have been guided by the large number of numerical simulations describing the accretion of the SN ejected material around the NS companion (see Figs 4 and 10, and its idealized representation in Fig. 9; see Becerra et al. 2016, 2019, for additional details).

What can be concluded from the above results is that in BdHNe I, the GeV emission is only detectable when the viewing angle is less than $\approx 60°$ from the normal to the plane and the BdHN I is 'seen from the top' (see the left-hand plot in Fig. 9). Whenever the viewing angle is within $60°$ from the orbital plane, no GeV emission is observed, though X-ray and gamma-ray flares are observed (see right-hand plot in Fig. 9).

Therefore, the second main result of this paper is the identification of the BdHN I morphology and its explanation within the BdHN I model.

7 SPH SIMULATION OF BDHNE I

The numerical simulations at the moment of BH formation in a BdHN I is presented in Becerra et al. (2016, 2019). 3D views of the density distribution at the moment of the BH formation in a BdHN I are shown Fig. 10. These plots correspond to the simulation of the SN ejecta expansion in the presence of the NS companion. The simulation is performed using an SPH code in which the SN ejecta material is evolved with N point-like particles, in the present case 16 million, with different masses and their motion is followed under the NS gravitational field. The orbital motion of the NS around the SN explosion centre is also taken into account as the NS star gravitational mass changes via the hypercritical accretion process. The latter was modelled independently estimating the accretion rate on to the NS via the Bondi–Hoyle formalism. For the initial conditions of the simulation, an homologous velocity distribution in free expansion was adopted and a power-law initial density profile of the SN matter was modelled by populating the inner layers with more particles (see

Table 5. Prompt and GeV emission of the 25 long GRBs inside the *Fermi*-LAT boresight angle and with GeV photons detected. The columns list: the source name, z, $E_{p,i}$, $E_{\gamma,iso}$, E_{LAT} in 0.1–10 GeV, the position of the source from the LAT boresight θ, the likelihood TS. The E_{LAT} includes only the energy in the observed time duration, which does not cover the whole GeV emission period, and is different for each GRB, so we put a symbol '$\gtrsim$' to indicate that the value is the lower limit.

GRB	z	$E_{p,i}$ (MeV)	$E_{\gamma,iso}$ (10^{52} erg)	Fermi GCN	E_{LAT} (10^{52} erg)	θ (deg)	TS
080916C	4.35	2.27 ± 0.13	407 ± 86	8246	230 ± 10	48.8	1450
090323A	3.57	2.9 ± 0.7	438 ± 53	9021	120 ± 20	57.2	150
090328A	0.736	1.13 ± 0.08	14.2 ± 1.4	9044	2.7 ± 0.4	64.6	107
090902B	1.822	2.19 ± 0.03	292.0 ± 29.2	9867	47 ± 2	50.8	1832
090926A	2.106	0.98 ± 0.01	228 ± 23	9934	149 ± 8	48.1	1983
091003A	0.897	0.92 ± 0.04	10.7 ± 1.8	9985	0.8 ± 0.3	12.3	108
091127	0.49	0.05 ± 0.01	0.81 ± 0.18	10204	0.03 ± 0.02	25.8	34
091208B	1.063	0.25 ± 0.04	2.10 ± 0.11	10266	$\gtrsim 0.41 \pm 0$	55.6	20
100414A	1.368	1.61 ± 0.07	55.0 ± 0.5	10594	7 ± 1	69	81
100728A	1.567	1.00 ± 0.45	72.5 ± 2.9	11006	0.9 ± 0.3	59.9	32
110731A	2.83	1.21 ± 0.04	49.5 ± 4.9	12221	15 ± 2	3.4	460
120624B	2.197	1.39 ± 0.35	347 ± 16	13377	22 ± 2	70.8	312
130427A	0.334	1.11 ± 0.01	92 ± 13	14473	8.6 ± 0.4	47.3	163
130518A	2.488	1.43 ± 0.38	193 ± 1	14675	15 ± 5	41.5	50
131108A	2.40	1.27 ± 0.05	51.20 ± 3.83	15464	37 ± 4	23.78	870
131231A	0.642	0.27 ± 0.01	21.50 ± 0.02	15640	1.6 ± 0.3	38	110
141028A	2.33	0.77 ± 0.05	76.2 ± 0.6	16969	9 ± 2	27.5	104.5
150314A	1.758	0.86 ± 0.01	70.10 ± 3.25	17576	1.8 ± 0.7	47.13	27.1
150403A	2.06	0.95 ± 0.04	87.30 ± 7.74	17667	1.1 ± 0.4	55.2	37
150514A	0.807	0.13 ± 0.01	1.14 ± 0.03	17816	0.06 ± 0.05	38.5	33.9
160509A	1.17	0.80 ± 0.02	84.5 ± 2.3	19403	10 ± 1	32	234
160625B	1.406	1.3 ± 0.1	337 ± 1	19581, 19604	17 ± 1	41.46	961.33
170214A	2.53	0.89 ± 0.04	392 ± 3	20675, 20686	53 ± 4	33.2	1571
170405A	3.51	1.20 ± 0.42	241.01 ± 52.02	20990, 20986	16 ± 7	52.0	56
180720B	0.654	1.06 ± 0.24	68.2 ± 2.2	22996, 23042	2.2 ± 0.2	49.1	975

Fryer et al. 2014; Becerra et al. 2016, 2019, for additional details). Figs 4 and 10 correspond to an initial binary system formed by a $2\,M_\odot$ NS and the CO_{core} obtained from a progenitor with $M_{ZAMS} = 30\,M_\odot$. When the CO_{core} collapses and explodes, it ejects $7.94\,M_\odot$ and leads a νNS of $1.5\,M_\odot$ at its centre. The initial binary period is about 5 min, corresponding to a binary separation of $\approx 1.5 \times 10^{10}$ cm.

The new morphology of the BdHNe I presented here and in the previous section leads to a difference in the observed energy spectra and time variability for sources with viewing angle in the plane, or normal to the orbital plane of the binary progenitor. We infer that our 25 BdHNe I, with viewing angles less than $\approx 60°$ from the normal to the orbital plane of the binary progenitor, 'seen from the top', have larger $E_{\gamma,iso}$ than the ones with a viewing angle lying in the plane of the binary system (see Tables 5 and 6). This explains the association/non-association of the GeV emission with bright GRBs often mentioned in the current literature (see Cenko et al. 2011; Racusin et al. 2011, and fig. 4 in Nava 2018).

An additional issue in the traditional approach (see e.g. Racusin et al. 2011; Beniamini et al. 2015, and sections 3 and 4 in Nava 2018) is also solvable: the sources that are seen with a viewing angle lying in the orbital plane have stronger flaring activities in the X-ray afterglow when compared to the 25 emitting in the GeV range. Therefore, the ratio between E_{iso} and the luminosity in the X-ray afterglow is systematically smaller than in the 25 with GeV emission. This offers a different explanation than the one presented in the traditional approach. However, all of these matters that have already been mentioned in Ruffini et al. (2018c) need a new operational definition of $E_{\gamma,iso}$, taking into due account the hard and soft X-ray flares and the extended thermal emission (see also Ruffini et al. 2019b).

Another important specific feature of the new morphology of BdHN I is the presence of the νNS formed at the centre of the exploding SN (see Fig. 4 and Becerra et al. 2016, 2019). We have shown that the νNS manifests itself through the synchrotron emission by relativistic electrons injected from it into the expanding magnetized SN ejecta, as well as through its pulsar emission that explain the early and late optical and X-ray afterglow, respectively, allowing the inference of the νNS rotation period (see Ruffini et al. 2018b). A smoking gun of this picture, namely the verification of the νNS activity following the above mechanism, both in XRFs (BdHNe II) and in BdHNe I, and the connection of the inferred rotation period of the νNS to the one of the CO-star and to the orbital period, from angular momentum conservation, has been explicitly shown in the GRB 180728A (BdHN II) and GRB 130427A (BdHN I) and GRB 190114C (BdHN I) (see Wang et al. 2019 for details).

8 THE LUMINOSITY POWER-LAW BEHAVIOUR IN BDHNE MEASURED IN THE REST FRAME

In the following, we fit simultaneously the luminosity light curves of all the 25 BdHNe with GeV emission expressed in their rest frame. We assume the same power-law decay index for all of them, but allow different amplitude values. This assumption is consistent with our model, moreover, it is a benefit for those GRBs with limited data that cannot be fitted solely.

Table 6. List of 29 BdHNe I inside the *Fermi*-LAT boresight angle and with no GeV photons detected: 29 BdHNe I with redshift taken from (Ruffini et al. 2016b) from 2008, when *Fermi* started to operate, till the end of 2016. All of them are within the boresight of *Fermi*-LAT, but no detected GeV photons. For each source the columns list: z, $E_{\gamma,\mathrm{iso}}$, E_p, GCN number, position of the source from LAT boresight θ, whether there was a detection by LAT, and additional information.

GRB	z	E_p (MeV)	$E_{\gamma,\mathrm{iso}}$ ($\times 10^{52}$ erg)	*Fermi* GCN	θ (deg)	GeV observed	Comments
081222	2.77	0.51 ± 0.03	27.4 ± 2.7	8715	50.0	No	
090424A	0.544	0.27 ± 0.04	4.07 ± 0.41	9230	71.0	No	
090516A	4.109	0.14 ± 0.03	99.6 ± 16.7	9415	20.0	No	Clear X-ray flare
100615A	1.398	0.21 ± 0.02	5.81 ± 0.11	10851	64.0	No	
100728B	2.106	0.32 ± 0.04	3.55 ± 0.36	11015	57.1	No	
110128A	2.339	0.46 ± 0.01	1.58 ± 0.21	11628	45.0	No	
111228A	0.716	0.060 ± 0.007	2.75 ± 0.28	12744	70.0	No	
120119A	1.728	0.52 ± 0.02	27.2 ± 3.6	12874	31.4	No	
120712A	4.175	0.64 ± 0.13	21.2 ± 2.1	13469	42.0	No	
120716A	2.486	0.4 ± 0.04	30.2 ± 3.0	13498	63.0	No	
120909A	3.93	0.87 ± 0.01	87 ± 10	13737	66.0	No	
130528A	1.250	0.27 ± 0.18	18.01 ± 2.28	14729	60.0	No	X-ray flare
130925A	0.347	0.14 ± 0.04	3.23 ± 0.37	15261	22.0	No	X-ray flare
131105A	1.686	0.55 ± 0.08	34.7 ± 1.2	15455	37.0	No	
140206A	2.73	1.1 ± 0.03	144.24 ± 19.20	15790	46.0	No	Clear X-ray flare
140213A	1.2076	0.176 ± 0.004	9.93 ± 0.15	15833	48.5	No	
140423A	3.26	0.53 ± 0.04	65.3 ± 3.3	16152	44.0	No	
140623A	1.92	1.02 ± 0.64	7.69 ± 0.68	16450	32.0	No	
140703A	4.13	0.91 ± 0.07	1.72 ± 0.09	16512	16.0	No	
140907A	1.21	0.25 ± 0.02	2.29 ± 0.08	16798	16.0	No	X-ray flare
141220A	1.3195	0.42 ± 0.02	2.44 ± 0.07	17205	47.0	No	
150301B	1.5169	0.45 ± 0.10	2.87 ± 0.42	17525	39.0	No	
150821A	0.755	0.57 ± 0.03	14.7 ± 1.1	18190	57.0	No	
151027A	0.81	0.62 ± 0.11	3.94 ± 1.33	18492	10.0	No	Clear X-ray flare
151111A	3.5	0.25 ± 0.04	3.43 ± 1.19	18582	50.0	No	X-ray flare observed
161014A	2.823	0.64 ± 0.06	10.1 ± 1.7	20051	69.0	No	
171222A	2.409	0.1 ± 0.01	20.73 ± 1.7	22272, 22277	43	No	
180703A	0.67	0.58 ± 0.05	3.15 ± 0.7	23889, 22896	44	No	
180728A	0.117	0.1 ± 0.02	3.15 ± 0.7	23055, 23067	35	No	
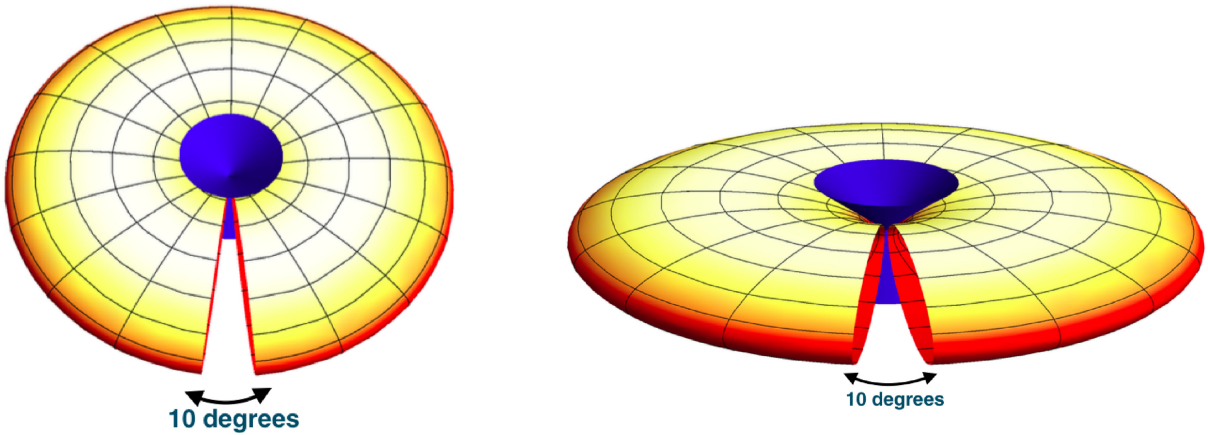
Figure 9. Schematic plot for showing the morphology of the BdHNe I. The GeV emission is detectable when the viewing angle is less than the 60° from the normal to the orbital plane. Left-hand panel is the situation in which the detectors can observe GeV and prompt emissions and the right-hand panel is the one for which GeV emission is not detectable and only gamma-ray and X-ray flares are detectable. The 10° cuts in both figures indicate the low-density region in Fig 10 through which the prompt radiation phase can be 'seen in the orbital plane'. The existence of such a 10° cut was first identified by the SPH simulation quoted in Becerra et al. (2016, 2019) and further confirmed in GRB 151027A (Ruffini et al. 2018c).

We limit our analysis of the light curves after the BdHN I prompt emission, when the GeV luminosity is already in the asymptotic power-law regime. We assume the power-law

$$L_n(t) = A_n t^{\alpha_{\mathrm{GeV}}},\qquad(8)$$

describing the rest-frame 0.1–100 GeV isotropic luminosity light curve of nth BdHN I. In the simultaneous fitting, we perform the Levenberg–Marquardt method to perform the minimization (Gill & Wright 1981). The basic idea of fitting is to minimize the χ^2; when fitting one curve to one equation, the χ^2 is minimized. To fit N curves
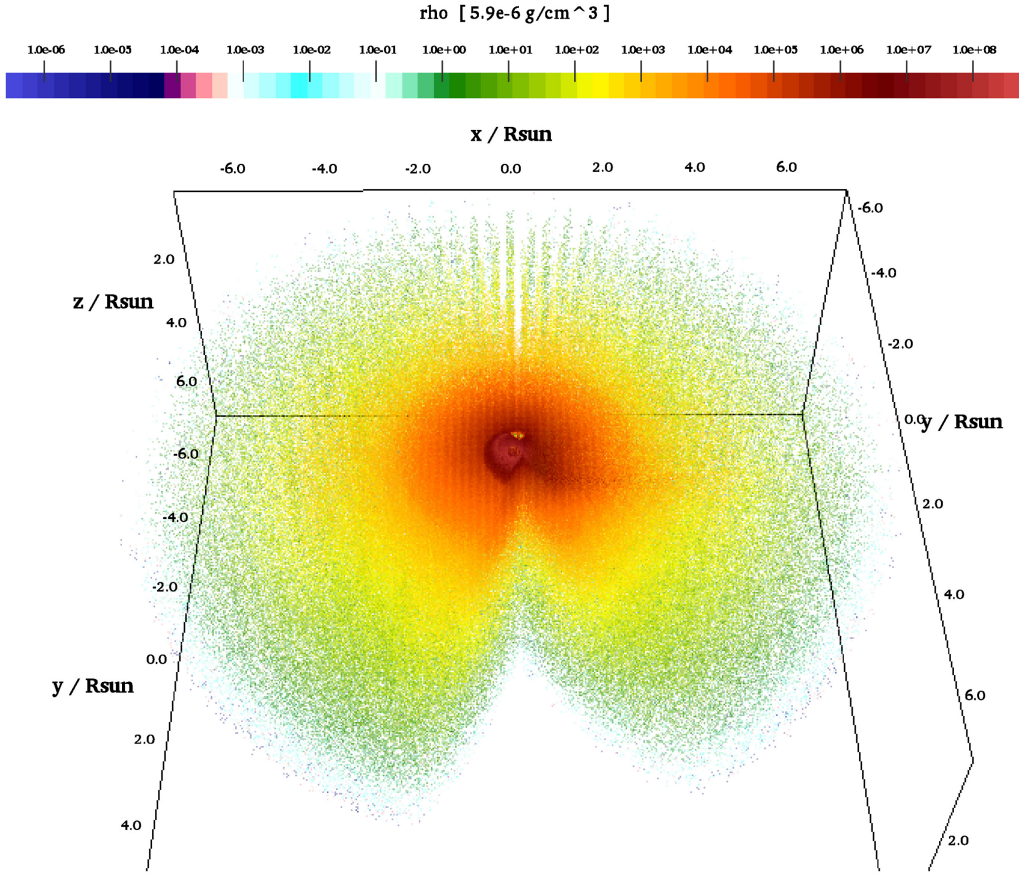
Figure 10. 3D, half-hemisphere views of the density distribution of the SN ejecta at the moment of BH formation in a BdHN I. The simulation is performed with an SPH code that follows the SN ejecta expansion under the influence of the NS companion gravitational field including the effects of the orbital motion and the changes in the NS gravitational mass by the hypercritical accretion process. The initial conditions of the SN ejecta are set as a homologous velocity distribution in free expansion and the mass distribution is modelled with 16 millions point-like particles (see Becerra et al. 2016, 2019, for additional details). The binary parameters of this simulation are: the NS companion has an initial mass of 2.0 M$_\odot$; the CO-star, obtained from a progenitor with ZAMS mass $M_{\rm ZAMS} = 30$ M$_\odot$, leads to a total ejecta mass of 7.94 M$_\odot$ and to a 1.5 M$_\odot$ νNS, the orbital period is $P \approx 5$ min (binary separation $a \approx 1.5 \times 10^{10}$ cm). The distribution of the ejecta is not axially symmetric; it is strongly influenced by the rotation of the system and accretion occurring in the binary component (see Fig. 4). Particularly relevant for the observations is the low-density region of $\approx 10°$ which allows the sources with viewing angle in the equatorial plane to detect the prompt radiation phase. This has been qualitatively indicated in Fig. 9. In these sources, only a fraction of approximately 10 per cent of the prompt radiation can be detectable, they are the only ones able to trigger the *Fermi*-GBM and the remaining 90 per cent will not have detectable prompt radiation (see Ruffini et al. 2018c). Figure is taken from Ruffini et al. (2018c) with the kind permission of the authors.

to N equations simultaneously, the sum of the χ^2 values should be minimized. The related equations are

$$\chi^2 = \sum_{n=1}^{N} \chi_n^2, \qquad (9)$$

$$\chi_n^2 = \sum_{i=1}^{M} \frac{1}{\sigma_{ni}^2}(L_{ni} - L_n(t_{ni}, A_n, \alpha_{\rm GeV}))^2, \qquad (10)$$

where n represents each BdHN I, i represents each data point in a given BdHN I, A_n is the amplitude of a power-law function for the nth BdHN I, and $\alpha_{\rm GeV}$ is the common power-law index shared for all the BdHNe I. Thus, for the nth BdHN I, at time t_{ni}, the observed luminosity is L_{ni}, and the predicted luminosity is $L_n(t_{ni}, A_n, \alpha)$. The value of χ^2 represents the difference between the best power-law fitting and all the observed data; it is a summation of individual χ_n^2, which represents the difference between the power-law fitting and the observed value of each GRB.

Out of 25 BdHNe I presented in Table 5, we perform the fitting for only 20 GRBs that have more than two data points in their luminosity light curves. Therefore, for the fitting of BdHNe I, there are 20 bursts and each one has its power-law function. Consequently, there are in total 17 parameters, including 20 amplitudes, and 1 power-law index. The fitting gives a power-law index of $\alpha_{\rm GeV} = 1.19 \pm 0.04$, i.e.:

$$L_n = A_n\, t^{-1.19\pm0.04}, \qquad (11)$$

which is plotted in Fig. 3 and the amplitudes of each GRB, A_n, with the uncertainty are shown in Table 7. This inferred power-law index is similar to the one obtained from fitting the GeV flux, $f_\nu(t)$ (see e.g. Kumar & Barniol Duran 2009; Panaitescu 2017), in which the power-law index is $\alpha_{\rm GeV} = 1.2 \pm 0.2$ and $\alpha_{\rm GeV} = 1.2 \pm 0.4$, respectively.

In our approach, we adopt an alternative interpretation of these power laws: instead of using the flux expressed in arrival time, we use the luminosity expressed in the rest frame of the source. Since the luminosity is proportional to the flux, i.e. $L = 4\pi d_L^2(1 + z)^{\alpha_{\rm GeV}-2}f_\nu$, where d_L is the luminosity distance, this similarity of the power-law index is not surprising. The advantage of using luminosity expressed in the rest frame of the source, instead of flux in arrival time, is that one can determine the intrinsic energy loss of the system that produces the GeV radiation, regardless of differences in the redshift

Table 7. Fitting parameters of the 0.1–10 GeV power-law luminosity when measured in the rest frame of 20 BdHNe with GeV emission: amplitude of the 0.1–10 GeV luminosity, A_n, and its uncertainty, the inferred 0.1–10 GeV luminosity at 10 s from the fitting and its uncertainty. The common power-law index is $\alpha_{\rm GeV} = 1.19 \pm 0.04$. Out of 25 BdHNe emitting GeV emission, we performed the fitting for 20 GRBs that have more than two data points in their luminosity light curves. GRBs 091127, 091208B, 130518A, 150314A, 150514A have only two data points in their GeV luminosity light curves.

BdHN	A_n (Amplitude)	Uncertainty of A_n	L_{10s}	Uncertainty of L_{10s}
080916C	2.9×10^{53}	$^{+9.1}_{-7.4} \times 10^{52}$	1.88×10^{52}	$^{+1.1}_{-1.0} \times 10^{52}$
090323A	9.4×10^{53}	$^{+3.5}_{-2.9} \times 10^{53}$	6.04×10^{52}	$^{+3.8}_{-1.4} \times 10^{52}$
090328A	2.4×10^{52}	$^{+1.1}_{-0.7} \times 10^{52}$	1.5×10^{51}	$^{+1.0}_{-0.9} \times 10^{51}$
090902B	8.9×10^{52}	$^{+2.5}_{-2.0} \times 10^{52}$	5.7×10^{51}	$^{+3.3}_{-3.0} \times 10^{51}$
090926A	2.1×10^{53}	$^{+5.9}_{-4.8} \times 10^{52}$	1.4×10^{52}	$^{+7.9}_{-7.3} \times 10^{51}$
091003A	5.7×10^{51}	$^{+1.7}_{-1.5} \times 10^{51}$	3.7×10^{50}	$^{+2.1}_{-2.0} \times 10^{50}$
100414A	3.5×10^{52}	$^{+1.4}_{-1.1} \times 10^{52}$	2.3×10^{51}	$^{+1.4}_{-1.3} \times 10^{51}$
100728A	4.2×10^{51}	$^{+1.9}_{-1.5} \times 10^{51}$	2.7×10^{50}	$^{+1.9}_{-1.6} \times 10^{50}$
110731A	2.3×10^{52}	$^{+0.8}_{-0.5} \times 10^{52}$	1.8×10^{51}	$^{+0.9}_{-0.8} \times 10^{51}$
120624B	2.4×10^{53}	$^{+8.2}_{-6.2} \times 10^{52}$	1.6×10^{52}	$^{+9.6}_{-8.5} \times 10^{51}$
130427A	5.1×10^{52}	$^{+2.1}_{-2.0} \times 10^{51}$	3.3×10^{51}	$^{+1.3}_{-1.3} \times 10^{51}$
131108A	6.1×10^{52}	$^{+9.1}_{-8.9} \times 10^{51}$	3.9×10^{51}	$^{+2.0}_{-1.9} \times 10^{51}$
131231A	1.64×10^{52}	$^{+7.9}_{-5.4} \times 10^{51}$	1.1×10^{51}	$^{+7.3}_{-6.1} \times 10^{50}$
141028A	3.6×10^{52}	$^{+1.2}_{-1.1} \times 10^{52}$	2.3×10^{51}	$^{+1.4}_{-1.3} \times 10^{51}$
150403A	6.8×10^{51}	$^{+3.0}_{-2.3} \times 10^{51}$	4.3×10^{50}	$^{+2.9}_{-3.0} \times 10^{50}$
160509A	1.4×10^{52}	$^{+4.9}_{-3.8} \times 10^{51}$	8.9×10^{50}	$^{+5.4}_{-4.1} \times 10^{50}$
160625B	1.4×10^{53}	$^{+4.6}_{-3.4} \times 10^{52}$	8.7×10^{51}	$^{+5.2}_{-4.6} \times 10^{51}$
170214A	2.8×10^{53}	$^{+7.4}_{-5.9} \times 10^{52}$	1.8×10^{52}	$^{+1.0}_{-0.9} \times 10^{52}$
170405A	4.1×10^{52}	$^{+1.1}_{-1.0} \times 10^{52}$	2.5×10^{51}	$^{+1.5}_{-1.4} \times 10^{51}$
180720B	5.4×10^{52}	$^{+6.6}_{-6.1} \times 10^{51}$	3.5×10^{51}	$^{+2.2}_{-2.1} \times 10^{50}$

of the sources. This allows us following our recent understanding of the BdHN I 130427A (see Ruffini et al. 2019c, and references therein), to relate the GeV radiation to the slowing down of the BH spin (see Section 10).

After obtaining the best power-law parameters for the luminosity light curve for each BdHNe I, we check the correlation between the GeV luminosity at 10 s from equation (11) using the fitted parameters and the isotropic energy $E_{\gamma,\rm iso}$. The power-law fitting gives (see Fig. 11)

$$L_{10s} = (4.7 \pm 1.2) \times 10^{48} \, (E_{\rm iso}/10^{52})^{\,1.3 \pm 0.3}, \tag{12}$$

and the fitting parameters for each GRB including their uncertainties are shown in Table 7. Furthermore, we estimate the energy released in the GeV band by each GRB in the 0.1–10^4 s time interval, i.e.:

$$E_{0.1-10^4 \rm s} = A_{\rm GRB} \int_{0.1}^{10000} t^{-1.19} \, {\rm d}t \ , \tag{13}$$

and the derived $E_{0.1-10^4 \rm s}$ are shown in Table 8. The parameters $E_{0.1-10^4 \rm s}$ and $E_{\gamma,\rm iso}$ (isotropic energy of the prompt emission in γ band) are also correlated by a power-law relation (see Fig. 11):

$$E_{0.1-10^4 \rm s} = (4.4 \pm 1.5) \times 10^{50} \, (E_{\rm iso}/10^{52})^{1.4 \pm 0.3}. \tag{14}$$

This positive correlation indicates that the BdHNe I with higher isotropic energy are also more luminous and more energetic in the GeV emission.

9 THE DETERMINATION OF THE MASS AND SPIN OF THE BH IN BDHNE I

The theoretical progress introduced in Ruffini et al. (2019c) has identified the GeV radiation as originating in the *inner engine* of BdHN I. There, for the first time, it has been shown that indeed the rotational energy of a Kerr BH can be extracted for powering an astrophysical system. The *inner engine* is composed of (i) a non-stationary Kerr BH, (ii) a uniform magnetic field of $\sim 10^{10}$G aligned with the rotation axis, and (iii) the presence of a very tenuous fully ionized electron–nuclei plasma. The fundamental new conceptual breakthrough introduced by the physics of the *inner engine* is developed in parallel papers (see e.g. Rueda & Ruffini 2020). The main goal here is to show, using our recently published results, that the rotational energy of the Kerr BH is indeed sufficient to explain the energetics of the GeV emission. In turn, this allows us to determine here the mass and spin of the Kerr BH in each BdHN I.

We here apply the self-consistent solution already well tested in the case of GRB 130427A (Ruffini et al. 2019c) and GRB 190114C (Moradi et al. 2019) for determining the three parameters of the *inner engine*, namely the mass and spin of the BH as well as the strength of the surrounding magnetic field B_0. The values are obtained satisfying three conditions:

(i) The energy budget for the observed GeV luminosity is provided by the extractable rotational energy of a Kerr BH (see equation (1a); see equation 34 in Ruffini et al. 2019c).

(ii) The magnetic field B_0 fulfills the transparency condition for the propagation of the GeV radiation imposed by the e^+e^- pair
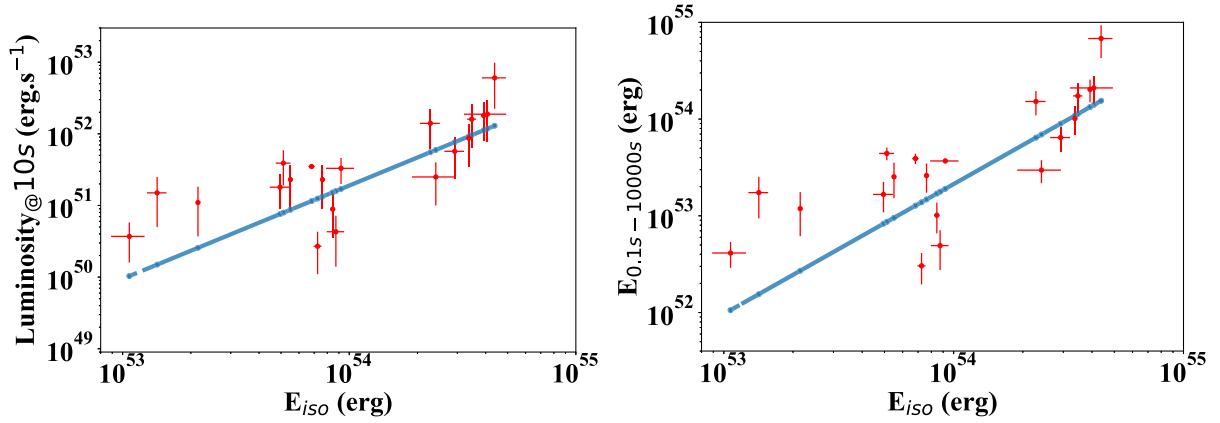
Figure 11. Left: The *Fermi*-LAT luminosity at 10 s in the energy range 0.1–10 GeV versus the isotropic gamma-ray energy from 1 keV to 10 MeV. The BdHNe are listed in Table 7. Right: The *Fermi*-LAT energy from 0.1 to 10^4 s versus isotropic gamma-ray energy from 1 keV to 10 MeV. See the corresponding values in Table 8.

Table 8. Results of $E_{0.1-10^4\text{s}}$ and related error of 20 BdHNe. $E_{0.1-10^4\text{s}}$ is the total GeV energy (in erg) emitted from 0.1 to 10^4 s. GRBs 091127, 091208B, 130518A, 150314A, 150514A are excluded since they have only two data points in their GeV luminosity light curves.

BdHN	$E_{0.1-10^4\text{s}}$	Uncertainty of $E_{0.1-10^4\text{s}}$
080916C	2.1×10^{54}	6.6×10^{53}
090323A	6.8×10^{54}	2.5×10^{54}
090328A	1.73×10^{53}	7.9×10^{52}
090902B	6.4×10^{53}	1.8×10^{53}
090926A	1.54×10^{54}	5.60×10^{53}
091003A	4.12×10^{52}	1.58×10^{52}
100414A	2.53×10^{53}	1.18×10^{53}
100728A	3.0×10^{52}	1.6×10^{52}
110731A	1.6×10^{53}	5.8×10^{52}
120624B	1.7×10^{54}	7.2×10^{53}
130427A	3.6×10^{53}	1.8×10^{52}
131108A	4.4×10^{53}	1.2×10^{53}
131231A	1.2×10^{53}	6.3×10^{52}
141028A	2.6×10^{53}	1.1×10^{53}
150403A	4.9×10^{52}	1.7×10^{52}
160509A	1.1×10^{53}	3.5×10^{52}
160625B	1.1×10^{54}	3.3×10^{53}
170214A	2.1×10^{54}	5.3×10^{53}
170405A	3.0×10^{53}	7.9×10^{52}
180720B	3.8×10^{53}	4.7×10^{52}

Table 9. The mass, M, the spin parameter, $\alpha = J/M^2$, and surrounding magnetic field, B_0, in 11 BdHNe I, out of the 25 long GRBs in Table 5. The high-quality GeV data of this sample allows for a measurement of the lower limit of their 'inner engine' parameters; see equation (1a).

Source	α	$M(\alpha)$ ($M_\odot$)	M_{irr} ($M_\odot$)	B_0 10^{10} G
BdHN I 080916C	0.87	8.9	7.6	1.9
BdHN I 090902B	0.59	5.3	5	2.8
BdHN I 090926A	0.76	8.4	7.7	2.1
BdHN I 110713A	0.37	4.7	4.6	4.5
BdHN I 130427A	0.40	2.3	2.24	4.1
BdHN I 130518A	0.50	2.5	2.4	3.3
BdHN I 131108A	0.56	4.7	4.4	2.9
BdHN I 160509A	0.41	2.4	2.3	4
BdHN I 170214A	0.80	2.8	2.5	2.1
BdHN I 170405A	0.45	3.4	3.3	3.7
BdHN I 180720B	0.27	2.3	2.29	6

production process in the *inner engine* (see equation 35 in Ruffini et al. 2019c).

(iii) The 'quantized' emission of the GeV radiation is determined by the density of the plasma and by the synchrotron radiation time-scale (Ruffini et al. 2019c) (see equation 36 in Ruffini et al. 2019c).

The high-quality GeV data in 11 BdHNe I out of the 25 long GRBs in Table 5 allow us to determine the starting point of the decreasing luminosity, by identifying the transition of the power-law dependence of the GeV luminosity from a positive to a negative slope (see Ruffini et al. 2019c, for more information). This enables us to calculate the lower limit of the mass, M, spin parameter of the BH, α, the corresponding irreducible mass of the BH, M_{irr}, which remains constant during the energy extraction process, and finally the surrounding magnetic field strength, B_0, as reported in Table 9. The values of the masses $M > 2.21 \, M_\odot$ and spin parameters of $\alpha < 0.71$ of the BH for BdHNe I presented in Table 9 show the consistency

with the upper limit of the critical mass of the NS in Rhoades & Ruffini (1974) and the mass and spin of rotating NSs computed in Cipolletta et al. (2015); see Fig. 12.

This has indeed been addressed in recent works (Ruffini et al. 2019c), where we have developed a complementary theory and its related analysis to identify the physical conditions that have to be enforced in order to extract the rotational energy of a Kerr BH. We have there addressed an approach of considering a Kerr BH placed in a uniform magnetic field of 10^{10} G aligned along the BH symmetry axis, fulfilling the Einstein–Maxwell equations via the Papapetrou–Wald solution (Papapetrou 1966; Wald 1974) modelling the *inner engine* that produces the MeV, GeV, and TeV radiation and UHECRs as well (Rueda & Ruffini 2020).

10 SPIN-DOWN OF THE BH IN BDHNE I

Following our previous work (Ruffini et al. 2019c), we can turn now from the luminosity expressed in the rest frame of the sources, see equation (11), and from the initial values of the spin and mass of the BH expressed in Section 9, to derive the slowing down of the BH due to the energy loss in the GeV emission.
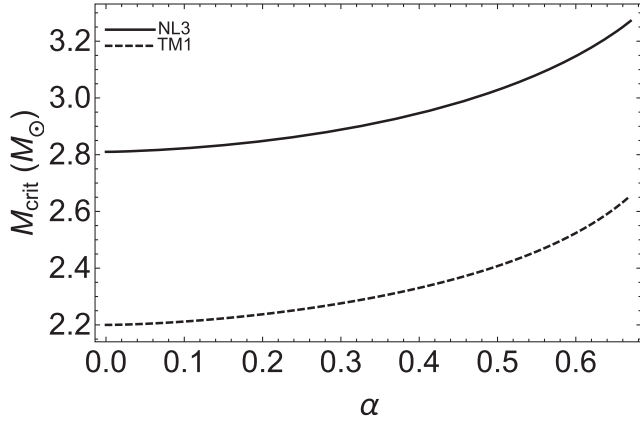
Figure 12. NS critical mass as a function of the spin parameter α for the NL3 and TM1 EOS. We recall that the maximum spin parameter of a uniformly rotating NS is $\alpha_{\max} \approx 0.71$, independently of the NS EOS (see e.g. Cipolletta et al. 2015).

The relation of the luminosity and the extractable rotational energy is (see equation 39 in Ruffini et al. 2019c)

$$L = -\frac{dE_{\text{extr}}}{dt} = -\frac{dM}{dt}. \tag{15}$$

For each BH during the GeV emission process the M_{irr} is constant. Utilizing the best fit obtained for the GeV luminosity $L_{\text{GeV}} = A_{\text{GeV}}\, t^{-1.2}$ erg s^{-1}, we obtain a relation for the loss of mass energy of the BH by integrating equation (15):

$$M = M_0 + 5At^{-0.2} - 5At_0^{-0.2}, \tag{16}$$

where M_0 is the initial mass of the newborn BH tabulated in Table 9. From the mass–energy formula of the BH, we have (Ruffini et al. 2019c)

$$a = \frac{J}{M} = 2M_{\text{irr}}\sqrt{1 - \frac{M_{\text{irr}}^2}{(M_0 + 5At^{-0.2} - 5At_0^{-0.2})^2}}, \tag{17}$$

where M_0 is the initial mass of the BH presented in Table 9 as M α at time t_0 at which the decaying part of GeV luminosity begins.

As indicative examples, we show in Fig. 13 the decrease of the BH spin, $\alpha = a/M = J/M^2$, as a function of time in GRBs 090902B, 131108A, and 170405A.

The third main results of this paper are: the identification of the rotational energy extraction from a Kerr BH and the consequent measure of the BH mass and spin.

11 CONCLUSIONS

The unprecedented observations of GRBs, pioneered by the *Beppo-Sax* satellite, have developed into the largest ever observational multiwavelength effort in astrophysics: starting with the *Swift*, BAT, and XRT instruments in the X-ray band; see Fig. 14, progressing with the *AGILE* and with *Fermi*-GBM in the MeV–GeV bands. These have worked in synergy with hundreds of optical, radio, and VHE telescopes worldwide including MAGIC (see Fig. 1) and H.E.S.S. (see Fig. 2).

This unprecedented observational effort assisted by parallel theoretical developments has allowed in this article the achievement of a new understanding of three new basic properties of the BdHNe: the first appearance of the SN triggering the entire BdHN process, the SN-rise; the presence of a mildly relativistic afterglow in the

X-ray in *all* BdHN; the identification in *all* BdHN of the origin of the high-energy emission in an *inner engine* driven by a newborn BH; the description of their morphology. We show, for the first time, the extractable energy of a Kerr BH as an astrophysical energy source, which has allowed the inference of the BH mass and spin.

In Section 2, we first recall that binary systems have an important role in understanding both short and long GRBs and we report the progress in the classification of GRBs in nine different subclasses (see e.g. Wang et al. 2019, and references therein). We then focus on the BdHNe: long GRB model with progenitors composed of CO_{core} and the binary NS companion. The CO_{core} undergoes gravitational collapses that gives origin to an SN and the collapse of its Fe-core produces a νNS.

We also there recall the fundamental role of the hypercritical accretion of the SN into the companion binary NS and into the νNS determine the BdHNe further evolution (see Fig. 4 and Pisani et al. 2016; Ruffini et al. 2016b, 2018c; Wang et al. 2019 for further details). The SN accretion on to the νNS gives origin to the X-ray afterglow emission, while the SN accretion on to the companion NS leads to different outcomes as a function of the binary period. For periods shorter than 5 min, the hypercritical accretion on to the companion NS is sufficient for the NS to overcome its critical mass and gravitationally collapse to a BH. The BH formation characterizes a BdHN I with an isotropic energy in the range of 10^{52} erg $\lesssim E_{\text{is}} \lesssim 10^{54}$ erg. We here show that it gives origin, *only in some* of them, to the GeV emission observed by *Fermi*-LAT. For larger binary periods, no BH is formed and consequently no GeV radiation is observed, the hypercritical SN accretion leads to an M-NS with an isotropic energy in the range of 10^{50} erg $\lesssim E_{\text{is}} \lesssim 10^{52}$ erg. We refer to these binaries as BdHN II paradigm. The same occurs for more detached binary systems leading to a BdHN III, where the isotropic energy is in the range of 10^{48} erg $\lesssim E_{\text{iso}} \lesssim 10^{50}$ erg.

In Section 3, we have given the spectral properties of the first appearance of the SN-rise in BdHN I and in BdHN II and also differentiate their energetics.

In Section 4, we have related the SN-rise luminosity to the X-ray luminosity of the afterglow in all three BdHNe types. It is a fortunate coincidence that we have recently understood the origin of the afterglow as a consequence of the SN hypercritical accretion on the νNS. This process is dominated by a mildly relativistic synchrotron pulsar-like emission with Lorentz factor $\Gamma \sim 2$ that gives rise to the X-ray afterglow (Ruffini et al. 2018b; Wang et al. 2019; Rueda et al. 2020), and we have also related their X-ray luminosity to the NS spin. This has allowed us to represent in Fig. 8 the afterglows for two BdHNe I, for two BdHNe II, and one BdHN III and estimate in Table 4 the initial spin value of the νNS. What is most remarkable is that the X-ray afterglow is present in *all* BdHN types which implies that, unlike the GeV emission, which as we show in this article to be necessarily beamed, the X-ray afterglow emission is necessarily isotropic. What is equally relevant is that independently of the differences among these four subclasses of BdHN, the X-ray afterglow luminosity emission is consistent with a power-law index of -1.48 ± 0.32 as measured from the *Swift* observations (Pisani et al. 2016), and a common energy source well explained by the rotational energy of the νNS.

The *first main result of this paper* identification of the SN-rise and the measurement of the νNS spin originating the power-law emission of the afterglow (see Figs 7 and 8). The two process of the SN-rise energetics and the νNS dynamics appear to be strongly correlated.

We then turn in Section 5 to consider only the case of BdHN I and their *Fermi*-GBM and LAT observations. In Appendix A, we update
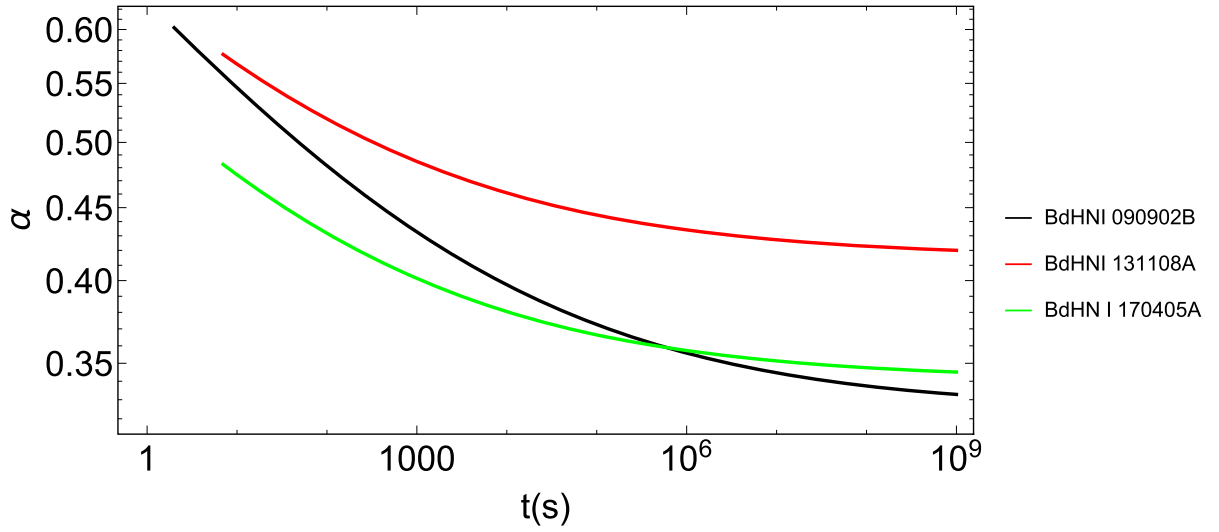
Figure 13. The BH spin as a function of rest-frame time. The initial values of the spin and mass of the BH for GRB 090902B are $\alpha = 0.59$ and $M(\alpha) = 5.3$ $M_\odot$; for 131108A: $\alpha = 0.56$ and $M(\alpha) = 4.7$ $M_\odot$; and for 170405A: $\alpha = 0.45$ and $M(\alpha) = 3.4$ $M_\odot$. This behaviour of the spin parameter indicates that the rotational energy of the BH is decreasing due to the radiation losses in the GeV energy band.
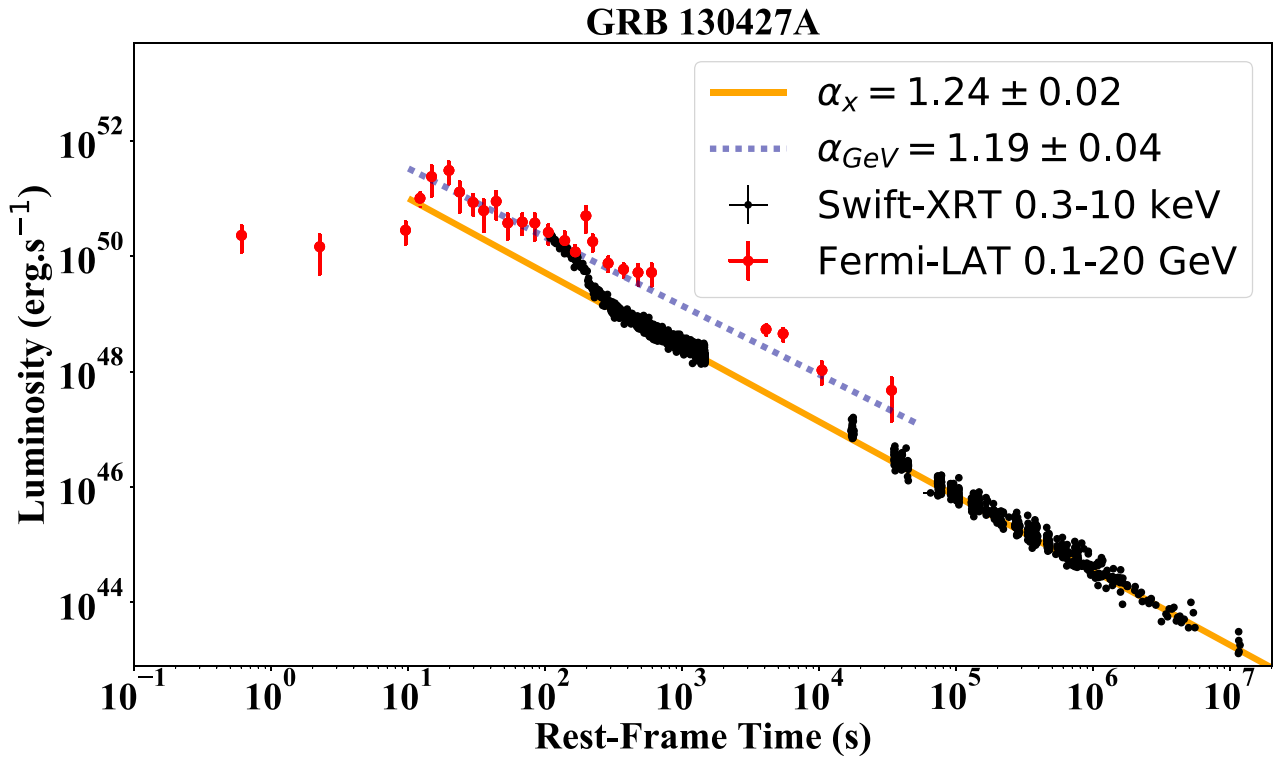
Figure 14. Luminosity of BdHN I 130427A: the black data points represent the rest-frame 0.3–10 keV luminosity obtained from *Swift*-XRT. It follows a decaying power law with amplitude $(3.65 \pm 0.63) \times 10^{52}$ erg s^{-1} and index $\alpha_X = 1.24 \pm 0.02$. The red data points show the rest frame in 0.1–20 GeV luminosity observed by *Fermi*-LAT. It follows a decaying power law with an amplitude of $(5.1 \pm 0.2) \times 10^{52}$ erg s^{-1} and index $\alpha_{GeV} = 1.19 \pm 0.04$. Details are given in Sections 4, 5, and 8.

our previous classification of BdHN I following Pisani et al. (2016), Ruffini et al. (2016b, 2018c) reaching the total number of 378 BdHN I, *all* of them are characterized by

(i) a measured cosmological redshift;

(ii) a prompt emission of $T_{90} > 2$ s, measured by *Fermi*-GBM, with isotropic energy larger than 10^{52} erg;

(iii) a decaying X-ray afterglow, measured by *Swift*-XRT, characterized by a luminosity decreasing with a mean power law with index of $\alpha_X = -1.48 \pm 0.32$.

Contrary to the case of the X-ray afterglow, universally present in *all* BdHN types, the GeV radiation is present *only in some* BdHN I. No GeV emission occurs in BdHN II and BdHN III. We first explore the possibility that the non-detection of GeV radiation in

some of BdHNe I could be due to the observational limitation of the LAT field of view, i.e. because of the boresight angle smaller than 75°. Indeed, we find that only $N_{tot} = 54$ out of the 378 BdHNe I are inside the boresight angle of *Fermi*-LAT. What is unexpected is that only $N_{LAT} = 25$ out of these 54 BdHNe I exhibit the GeV emission observed by *Fermi*-LAT. For each of these 25 sources, we have given the basic parameters in Table 5. The corresponding data of the remaining 29 BdHN I, without observed GeV radiation, are given in Table 6.

In Section 6, we have assumed that *all* BdHNe I, like all GRBs are homogeneously distributed in space (see e.g. Meegan et al. 1992; Paciesas et al. 1999), we have inferred that the emission of the GeV radiation occurs in two opposite cones each of half-opening angle of ~60° from the normal to the binary plane.

We duly recall as well that the visualization of the morphology has been made possible thanks to a close collaboration with LANL (see Becerra et al. 2016, 2019, for additional details), leading to the results well illustrated in the simulation presented in Figs 4 and 10. We then conclude from this simulation that all of the 25 LAT sources are actually 'seen from the top' that allows us to fully observe the conical emission of 60° half-opening angle. For the remaining 29 BdHN I without an observed GeV emission, we provide evidence that when the *Swift* data are available, gamma-ray flares and hard and soft X-ray flares as well as extended thermal emissions are observed in these systems (Ruffini et al. 2018a, c), and that these sources have a viewing angle laying in the 'orbital plane' of the binary progenitor system.

We conclude that we are faced with a new morphology of the BdHN I that depends significantly on the viewing angle, 'seen from the top', normal to the binary orbital plane when the GeV emission is observed, or seen 'in the plane' of the binary when the observation of the GeV radiation is impeded by the accreting binary material (see Figs 4, 9, and 10). This is reminiscent of the morphology encountered in some AGNs (see e.g. the AGN IC 310 in Aleksić et al. 2014).

The second main result of this paper is the identification of the BdHN I conical morphology and its explanation within the BdHN I model.

We then recall some theoretical progresses in understanding the origin of the GeV emission:

(i) The identification of the three components of the GRB *inner engine* in GRB 130427A (Ruffini et al. 2019c), composed of a Kerr BH with a magnetic field B_0 aligned with the BH rotation axis, both embedded in a tenuous ionized plasma composed of electrons and ions, has represented a turning point in the study of BdHN I. The electrodynamics of this *inner engine*, based on the Papapetrou–Wald solution (Papapetrou 1966; Wald 1974; Ruffini et al. 2019c), leads to a high-energy emission in two opposite lobes in the MeV, GeV, and TeV radiation as well as narrowly beamed UHECR along the BH polar axis (Moradi et al. 2019).

(ii) This high-energy emission, unlike the traditional models, that implies ultrarelativistic baryonic motion with $\Gamma \sim 10^3$ at 10^{16}–10^{18} cm occurs very close to the BH horizon.

(iii) The energy source is the extractable energy of the BH (Christodoulou 1970; Christodoulou & Ruffini 1971; Hawking 1971, 1972; see equation 1a), and is emitted in a sequence of impulsive process, the '*blackholic quanta*', occurring on a time-scale of 10^{-14} s (Rueda & Ruffini 2020).

On the basis of these results, we have examined the physical origin of the GeV emission observed by *Fermi*-LAT both in BdHN I. We find that the luminosity of the GeV emission as a function of time in the rest frame of the source fulfils a universal decaying power-law

dependence with index of -1.19 ± 0.04; see Fig 3. This has allowed: (1) to verify that indeed the entire GeV radiation observed by *Fermi*-LAT can be energetically expressed in terms of the rotational energy of the Kerr BH; (2) following the procedures in Ruffini et al. (2019c) to evaluate the mass and spin of the BH (see Table 9); and (3) to explicitly compute the slowing down rate of the BH spin due to the GeV emission (see Fig. 13).

It has been possible for some of the 25 sources with the best data:

(i) To compute the lower limit of the initial value of the BH masses, M, and show their consistency with the absolute upper limit of the NS critical mass (Rhoades & Ruffini 1974), and the upper limit of the NS mass of $M = 2.21$ M$_\odot$ and spin parameter of $\alpha < 0.71$ computed in Cipolletta et al. (2015).

(ii) To evaluate the value of the spin, a, and show the consistency with the canonical upper limit $\alpha = a/M \leq 1$.

(iii) By combining the value of the spin of the νNS observed from the afterglow (see Table 4), the time intervening between the SN-rise and the UPE phase, the mass estimate of the BH in GRB 190114C and in GRB 090926A and in GRB 180720B, we infer that necessarily in these system we are observing the presence of a BdHN precursor with a companion NS grazing the surface of the CO$_{core}$.

The third main results of this paper is the identification of the rotational energy extraction from a Kerr BH as the origin of the GeV emission and allowing the consequent measure of the BH mass and spin.

All the above three main results are important: the underlying proof that indeed we can use the extractable rotational energy of a Kerr BH for explaining the high-energy jetted emissions of GRBs and AGNs stands alone. Even more subtle is the fact that the jetted emission does not originate from massive ultrarelativistic jetted emissions, but from very special energy-saving ultrarelativistic quantum and classical electrodynamical processes originating in the high-energy jetted emission. We were waiting for this result for 49 yr, since the writing of equation (1a).

Far from completing an era, GRBs are a fertile ground to discover new physical laws. In front of us: the identification of the nature of the SN-rise, the constituent of the UPE emission, the further application of the *blackholic* energy (Rueda & Ruffini 2020), and the identification of their timescales ranging from 10^{-15} s to 10^{17} s.

Division at NASA/GSFC and the High Energy Astrophysics Division of the Smithsonian Astrophysical Observatory.

DATA AVAILABILITY

The data underlying this article are available in Appendix A of the article.

REFERENCES

Abdalla H. et al., 2019, Nature, 575, 464
Ackermann M. et al., 2013, ApJS, 209, 11
Aharonian F. et al., 2006, A&A, 457, 899
Aimuratov Y. et al., 2017, ApJ, 844, 83
Ajello M. et al., 2019, ApJ, 878, 52
Aleksić J. et al., 2014, Science, 346, 1080
Aleksić J. et al., 2016a, Astropart. Phys., 72, 61
Aleksić J. et al., 2016b, Astropart. Phys., 72, 76
Amati L. et al., 2000, Science, 290, 953
Atwood W. B. et al., 2009, ApJ, 697, 1071
Barraud C. et al., 2003, A&A, 400, 1021
Barthelmy S. D. et al., 2005, Space Sci. Rev., 120, 143
Becerra L., Cipolletta F., Fryer C. L., Rueda J. A., Ruffini R., 2015, ApJ, 812, 100
Becerra L., Bianco C. L., Fryer C. L., Rueda J. A., Ruffini R., 2016, ApJ, 833, 107
Becerra L., Ellinger C. L., Fryer C. L., Rueda J. A., Ruffini R., 2019, ApJ, 871, 14
Beniamini P., Nava L., Duran R. B., Piran T., 2015, MNRAS, 454, 1073
Berger E., 2014, ARA&A, 52, 43
Blandford R. D., McKee C. F., 1976, Phys. Fluids, 19, 1130
Burrows D. N. et al., 2005, Space Sci. Rev., 120, 165
Campana S. et al., 2006, Nature, 442, 1008
Cano Z., Wang S.-Q., Dai Z.-G., Wu X.-F., 2017, Adv. Astron., 2017, 8929054
Cenko S. B. et al., 2006, ApJ, 652, 490
Cenko S. B. et al., 2011, ApJ, 732, 29
Chand V. et al., 2020, ApJ, 898, 42
Christodoulou D., 1970, Phys. Rev. Lett., 25, 1596
Christodoulou D., Ruffini R., 1971, Phys. Rev. D, 4, 3552
Cipolletta F., Cherubini C., Filippi S., Rueda J. A., Ruffini R., 2015, Phys. Rev. D, 92, 023007
Costa E. et al., 1997, Nature, 387, 783
de Pasquale M. et al., 2006, A&A, 455, 813
Damour T., Ruffini R., 1975, Phys. Rev. Lett., 35, 463
Della Valle M., 2011, Int. J. Mod. Phys. D, 20, 1745
Dominik M., Belczynski K., Fryer C., Holz D. E., Berti E., Bulik T., Mandel I., O'Shaughnessy R., 2012, ApJ, 759, 52
Eichler D., Livio M., Piran T., Schramm D. N., 1989, Nature, 340, 126
Fox D. B. et al., 2005, Nature, 437, 845
Frail D. A., Kulkarni S. R., Nicastro L., Feroci M., Taylor G. B., 1997, Nature, 389, 261
Frontera F. et al., 1998, ApJ, 493, L67
Fryer C. L., Woosley S. E., Hartmann D. H., 1999, ApJ, 526, 152
Fryer C. L. et al., 2007, PASP, 119, 1211
Fryer C. L., Rueda J. A., Ruffini R., 2014, ApJ, 793, L36
Fryer C. L., Oliveira F. G., Rueda J. A., Ruffini R., 2015, Phys. Rev. Lett., 115, 231102
Fujisawa K., Okawa H., Yamamoto Y., Yamada S., 2019, ApJ, 872, 155
Galama T. J. et al., 1998, Nature, 395, 670
Gehrels N. et al., 2005, Nature, 437, 851
Giacconi R., 2003, Rev. Mod. Phys., 75, 995
Giacconi R., Ruffini R., eds, 1978, Physics and Astrophysics of Neutron Stars and Black Holes. North Holland Publishing Co., Amsterdam
Gilkis A., 2018, MNRAS, 474, 2419
Gill P. R., Murray W., Wright M. H., 1981, 500, 136
Giommi P. et al., 2020, A&A, 642, A141
Giuliani A. et al., 2008, A&A, 491, L25

Greiner J. et al., 2009, A&A, 498, 89
Guetta D., Della Valle M., 2007, ApJ, 657, L73
Gursky H., Ruffini R., eds, 1975, Astrophysics and Space Science Library Neutron Stars, Black Holes and Binary X-ray Sources . Springer-Verlag, Berlin
Hawking S. W., 1971, Phys. Rev. Lett., 26, 1344
Hawking S. W., 1972, Commun. Math. Phys., 25, 152
Hewish A., Bell S. J., Pilkington J. D. H., Scott P. F., Collins R. A., 1968, Nature, 217, 709
Hjorth J., Bloom J. S., 2012, The Gamma-Ray Burst - Supernova Connection. Cambridge Univ. Press, Cambridge, p. 169
Hurley K. et al., 2000, ApJ, 534, L23
in 't Zand J. J. M. et al., 1998, ApJ, 505, L119
in't Zand J. J. M. et al., 2001, ApJ, 559, 710
Iwamoto K., Nomoto K., Höflich P., Yamaoka H., Kumagai S., Shigeyama T., 1994, ApJ, 437, L115
Izzo L. et al., 2018, GCN Circ., 23142, 1
Kanbach G., 1996, Mem. Soc. Astron. Ital., 67, 161
Klebesadel R. W., Strong I. B., Olson R. A., 1973, ApJ, 182, L85
Kouveliotou C., Meegan C. A., Fishman G. J., Bhat N. P., Briggs M. S., Koshut T. M., Paciesas W. S., Pendleton G. N., 1993, ApJ, 413, L101
Kumar P., Barniol Duran R., 2009, MNRAS, 400, L75
Li L., 2020, ApJ, 894, 100
Li L.-X., Paczyński B., 1998, ApJ, 507, L59
Li L.-X., Paczyński B., 2000, ApJ, 534, L197
Li L.-X., Paczyński B., 2006, MNRAS, 366, 219
Li L. et al., 2012, ApJ, 758, 27
Li L. et al., 2015, ApJ, 805, 13
Li L., Wang Y., Shao L., Wu X.-F., Huang Y.-F., Zhang B., Ryde F., Yu H.-F., 2018a, ApJS, 234, 26
Li L., Wu X.-F., Lei W.-H., Dai Z.-G., Liang E.-W., Ryde F., 2018b, ApJS, 236, 26
Li L., Ruffini R., Rueda J. A., Moradi R., Wang Y., Xue S. S., 2019, preprint (arXiv:1910.12615)
MAGIC Collaboration, 2019a, Nature, 575, 455
MAGIC Collaboration, 2019b, Nature, 575, 459
Mao S., Paczynski B., 1992, ApJ, 388, L45
Meegan C. A., Fishman G. J., Wilson R. B., Paciesas W. S., Pendleton G. N., Horack J. M., Brock M. N., Kouveliotou C., 1992, Nature, 355, 143
Meegan C. A. et al., 2008, GCN Circ., 8100, 1
Meegan C. et al., 2009, ApJ, 702, 791
Melandri A. et al., 2019, GCN Circ.
Mészáros P., Rees M. J., 1997, ApJ, 482, L29
Metzger M. R., Djorgovski S. G., Kulkarni S. R., Steidel C. C., Adelberger K. L., Frail D. A., Costa E., Frontera F., 1997, Nature, 387, 878
Mirzoyan R., et al., 2019, GCN Circ.
Moradi R., Rueda J. A., Ruffini R., Wang Y., 2019, A&A, preprint (arXiv:1911.07552)
Murdin P., ed., 2000, Compton Gamma Ray Observatory (CGRO). Institute of Physics Publishing, Bristol, p. 4537
Nakamura K., Kuroda T., Takiwaki T., Kotake K., 2014, ApJ, 793, 45
Nappo F. et al., 2017, A&A, 598, A23
Narayan R., Piran T., Shemi A., 1991, ApJ, 379, L17
Narayan R., Paczynski B., Piran T., 1992, ApJ, 395, L83
Nava L., 2018, Int. J. Mod. Phys. D, 27, 1842003
Nomoto K., Hashimoto M., 1988, Phys. Rep., 163, 13
Nousek J. A. et al., 2006, ApJ, 642, 389
Oke J. B. et al., 1995, PASP, 107, 375
Paciesas W. S. et al., 1999, ApJS, 122, 465
Paczynski B., 1986, ApJ, 308, L43
Panaitescu A., 2017, ApJ, 837, 13
Papapetrou A., 1966, Annales de L'Institut Henri Poincare Section (A) Physique Theorique, 4, 83
Pian E. et al., 2000, ApJ, 536, 778
Pisani G. B. et al., 2016, ApJ, 833, 159
Pisani G. B. et al., 2018, in EPJ Web Conf., 168, 04002
Postnov K. A., Yungelson L. R., 2014, Living Rev. Relativ., 17, 3
Racusin J. L. et al., 2011, ApJ, 738, 138

Rees M. J., Meszaros P., 1992, MNRAS, 258, 41

Reifenstein E. C., Brundage W. D., Staelin D. H., 1969, Phys. Rev. Lett., 22, 311

Rhoades C. E., Ruffini R., 1974, Phys. Rev. Lett., 32, 324

Roming P. W. A. et al., 2005, Space Sci. Rev., 120, 95

Rueda J. A., Ruffini R., 2012, ApJ, 758, L7

Rueda J. A., Ruffini R., 2020, Eur. Phys. J. C, 80, 300

Rueda J. A., Ruffini R., Karlica M., Moradi R., Wang Y., 2020, ApJ, 893, 148

Ruffini R., 1974, in Astrophysics and Gravitation: Proceedings of the Sixteenth Solvay Conference on Physics. Editions de l'Universite de Bruxelles, Brussels, p. 349

Ruffini R., 1998, in Sato H., Sugiyama N., eds, Frontiers Science Series 23: Black Holes and High Energy Astrophysics. Universal Academic Press Inc., Tokyo, Japan, p. 167

Ruffini R., Wheeler J. A., 1971, Phys. Today, 24, 30

Ruffini R., Bianco C. L., Fraschetti F., Xue S.-S., Chardonnet P., 2001, ApJ, 555, L117

Ruffini R. et al., 2015a, Astron. Rep., 59, 626

Ruffini R. et al., 2015b, ApJ, 798, 10

Ruffini R. et al., 2016a, ApJ, 831, 178

Ruffini R. et al., 2016b, ApJ, 832, 136

Ruffini R. et al., 2018a, ApJ, 852, 53

Ruffini R., Karlica M., Sahakyan N., Rueda J. A., Wang Y., Mathews G. J., Bianco C. L., Muccino M., 2018b, ApJ, 869, 101

Ruffini R. et al., 2018c, ApJ, 869, 151

Ruffini R. et al., 2019a, preprint (arXiv:e-prints)

Ruffini R., Melon Fuksman J. D., Vereshchagin G. V., 2019b, ApJ, 883, 191

Ruffini R. et al., 2019c, ApJ, 886, 82

Ruffini R., Bianco C. L., Fraschetti F., Xue S.-S., Chardonnet P., 2001, ApJ, 555, L117

Sari R., 1997, ApJ, 489, L37

Sari R., Piran T., 1995, ApJ, 455, L143

Sari R., Piran T., Narayan R., 1998, ApJ, 497, L17

Shirasaki Y. et al., 2008, PASJ, 60, 919

Shklovskij I. S., 1969, Supernovae. Interscience Publishers, New York, NY (USA)

Smith N., Li W., Silverman J. M., Ganeshalingam M., Filippenko A. V., 2011, MNRAS, 415, 773

Staelin D. H., Reifenstein Edward C. I., 1968, Science, 162, 1481

Strong I. B., 1975, Cosmic Gamma-Ray Bursts. D. Reidel Publishing Co., Dordrecht, Holland, p. 47

Tam P.-H. T., He X.-B., Tang Q.-W., Wang X.-Y., 2017, ApJ, 844, L7

Tauris T. M., Langer N., Moriya T. J., Podsiadlowski P., Yoon S.-C., Blinnikov S. I., 2013, ApJ, 778, L23

Tauris T. M., Langer N., Podsiadlowski P., 2015, MNRAS, 451, 2123

Tavani M. et al., 2009, A&A, 502, 995

van Paradijs J. et al., 1997, Nature, 386, 686

Vernet J. et al., 2011, A&A, 536, A105

Wald R. M., 1974, Phys. Rev. D, 10, 1680

Wang Y., Rueda J. A., Ruffini R., Becerra L., Bianco C., Becerra L., Li L., Karlica M., 2019, ApJ, 874, 39

Waxman E., Piran T., 1994, ApJ, 433, L85

Wijers R. A. M. J., Rees M. J., Meszaros P., 1997, MNRAS, 288, L51

Woosley S. E., 1993, ApJ, 405, 273

Woosley S. E., Bloom J. S., 2006, ARA&A, 44, 507

Xu D. et al., 2013, ApJ, 776, 98

Yoon S.-C., Woosley S. E., Langer N., 2010, ApJ, 725, 940

Zhang B., 2018, The Physics of Gamma-Ray Bursts. Cambridge Univeristy Press, Cambridge, UK

Zhang B., Fan Y. Z., Dyks J., Kobayashi S., Mészáros P., Burrows D. N., Nousek J. A., Gehrels N., 2006, ApJ, 642, 354

SUPPORTING INFORMATION

Supplementary data are available at *MNRAS* online.

stab724.pdf

Please note: Oxford University Press is not responsible for the content or functionality of any supporting materials supplied by the authors. Any queries (other than missing material) should be directed to the corresponding author for the article.

This paper has been typeset from a TEX/LATEX file prepared by the author.

World Scientific
www.worldscientific.com

The quantum emission of an alive black hole*

J. A. Rueda[†,‡,§,¶,‖,††] and R. Ruffini[†,‡,**,‡‡]

†*ICRANet, Piazza della Republica 10,*
I–65122 Pescara, Italy

‡*ICRA, Dipartimento di Fisica,*
Sapienza Università di Roma, P.le Aldo Moro 5,
I–00185 Rome, Italy

§*ICRANet-Ferrara,*
Dipartimento di Fisica e Scienze della Terra,
Università degli Studi di Ferrara,
Via Saragat 1, I–44122 Ferrara, Italy

¶*Dipartimento di Fisica e Scienze della Terra,*
Università degli Studi di Ferrara,
Via Saragat 1, I–44122 Ferrara, Italy

‖*INAF, Istituto de Astrofisica e Planetologia Spaziali,*
Via Fosso del Cavaliere 100, 00133 Rome, Italy

*****INAF, Viale del Parco Mellini 84,*
00136 Rome, Italy
††*jorge.rueda@icra.it*
‡‡*ruffini@icra.it*

A long march of 50 years of successive theoretical progress and new physics discovered using observations of gamma-ray bursts has finally led to the formulation of an efficient mechanism able to extract the rotational energy of a Kerr black hole to power these most energetic astrophysical sources and active galactic nuclei. We here present the salient features of this long-sought mechanism, based on gravito-electrodynamics, and which represents an authentic shift of paradigm of black holes as forever "*alive*" astrophysical objects.

Keywords: Gamma-ray bursts; black hole physics.

1. Introduction

Traditionally, rotating black holes (BHs) have been described by the Kerr[1] and the Kerr–Newman (for nonzero charge) metrics[2] which adopt the spacetime to

fulfill: (i) matter vacuum, (ii) asymptotic flatness, and (iii) global stationarity. These conditions led to the primordial view of BHs either as "*dead*" objects or as sinks of energy. Subsequently, it was realized that BHs, much as the thermodynamical systems, may interact with their surroundings leading to reversible and irreversible transformations.[3,4] This result led to the one of the most important concepts in BH physics and astrophysics, i.e. the BH mass-energy formula[4]:

$$M^2 = \left(M_{\mathrm{irr}} + \frac{Q^2}{4GM_{\mathrm{irr}}} \right)^2 + \frac{c^2}{G^2} \frac{J^2}{4M_{\mathrm{irr}}^2}, \qquad (1)$$

which relates the BH mass, M, to three independent parameters: its irreducible mass, M_{irr}, charge, Q, and angular momentum, J. The expression of the BH mass-energy (1) was soon confirmed by Ref. 5.

It turns immediately out from Eq. (1) that the BH extractable energy

$$E_{\mathrm{extr}} = (M - M_{\mathrm{irr}})c^2, \qquad (2)$$

could reach up to 50% of Mc^2 in a maximally charged BH (charge-to-mass ratio equal to unity), and up to 29% in a maximally rotating BH (spin to mass ratio equal to unity). This extraordinary result swung the attention of the astrophysics community to the alternative view of "*alive*" BHs since their energy could be extracted and be used to power astrophysical sources! This novel view of BHs was shaped in "Introducing the black hole" by Ref. 6 (see also "On the energetics of black holes" by Ruffini in Ref. 7), and since then it has permeated, for 50 years as of this writing, relativistic astrophysics both theoretically and experimentally.

The most energetic known astrophysical sources, gamma-ray bursts (GRBs) and active galactic nuclei (AGNs), were soon identified as primary candidates to be powered by BHs. GRBs, the most powerful transient objects in the sky, release energies of up to a few 10^{54} erg in just a few seconds, which implies that their luminosity in gamma-rays, in the time interval of the event, compares to the luminosity of all the stars of the universe in our past light-cone! GRBs have been thought to be powered (somehow) by stellar-mass BHs, while AGNs, releasing up to 10^{46} erg s^{-1} for billion years are thought to be powered by supermassive BHs.

However, since the theoretical formulation of the BH mass-energy formula and the introduction of the concept of extractable energy, every theoretical effort to find a specific mechanism able to efficiently extract the BH energy has been vanified by the implausibility of their actual realization in nature. An example was the *gedanken* Penrose's process which was shown by the authors to be physically not implementable on the ground of traditional physical considerations.[8] A new physics was needed!.

We have recently introduced in Refs. 9 and 10 the BH "*inner engine*" to explain the high-energy (in the GeV domain) radiation observed in energetic long GRBs,

which efficiently extracts the rotational energy of the newborn Kerr BH via a novel gravito-electrodynamical process occurring at the crossroad between quantum electrodynamics and general relativity. We have been guided by our GRB model based on binary-driven hypernova (BdHN) scenario (see Sec. 2), which proportioned us with the main ingredients that such a mechanism should have a Kerr BH, fully ionized matter, and a magnetic field. We have also shown in Ref. 10 that the same mechanism, duly extrapolated to large BH masses, works as well in AGN and can be a copious source of ultrahigh-energy cosmic rays (UHECRs). We summarize in this note the most important properties of this long-sought BH *inner engine* and how it paves the way to a still novel view of BHs as *forever alive* astrophysical objects.

2. Binary-Driven Hypernovae

Let us start by briefly introducing the BdHN model[11–14] of long GRBs. The BdHN proposes as GRB progenitor a binary system composed of a carbon-oxygen (CO) star and a neutron star (NS) companion. The gravitational collapse of the iron core of the CO star forms a newborn NS (νNS) at its center and expels the stellar outermost layers in a supernova/hypernova (SN/HN) explosion. Some of the ejecta fallback onto the νNS and some other reach the companion, therefore a hypercritical (i.e. highly super-Eddington) accretion process is triggered on both NSs. The accretion onto the νNS lasts short but is sufficient to spin it up to millisecond rotation rates. For compact binaries (orbital periods $\sim 5\,\mathrm{min}$), the accretion onto the NS companion makes it to reach, in matter of seconds, the critical mass for gravitational collapse, consequently forming a rotating (Kerr) BH. We have called these long GRBs in which there is BH formation as BdHN of type I (BdHN I) and their isotropic energy release is in the range 10^{53}–$10^{54}\,\mathrm{erg}$. Numerical simulations of the above process in one, two and three dimensions have been performed and have confirmed the occurrence of the above succession of physical events.[11,13–15] Figure 1 shows an example of three-dimensional simulation taken from Ref. 11. Since BdHN I keeps bound after the explosion, it naturally forms NS-BH binaries (see Ref. 16 for details).

But not all BdHNs form BHs, up to now, 380 BdHNs I have been identified.[17] In fact, in binaries with longer orbital periods, e.g. of the order of tens of minutes to hours, the accretion occurs at much lower rates and no BH is formed. The outcome is a BdHN II, a long GRB releasing energies 10^{51} to $10^{53}\,\mathrm{erg}$,[18] leading to a NS-NS binary. Even less energetics may occur for longer binary periods, we call them BdHNs III. The theoretical understanding of BdHNs I, II and III has allowed to distinguish their relevant physical processes in the observational data of long GRBs.

Detailed time-resolved analysis of the lightcurves and spectra of BdHN I has revealed the separated role of the νNS in the afterglow emission, and of the newborn BH in the GeV emission. The X-ray afterglow observed by the Neil Gehrels *Swift* satellite, characterized by a decreasing luminosity described by a power-law,
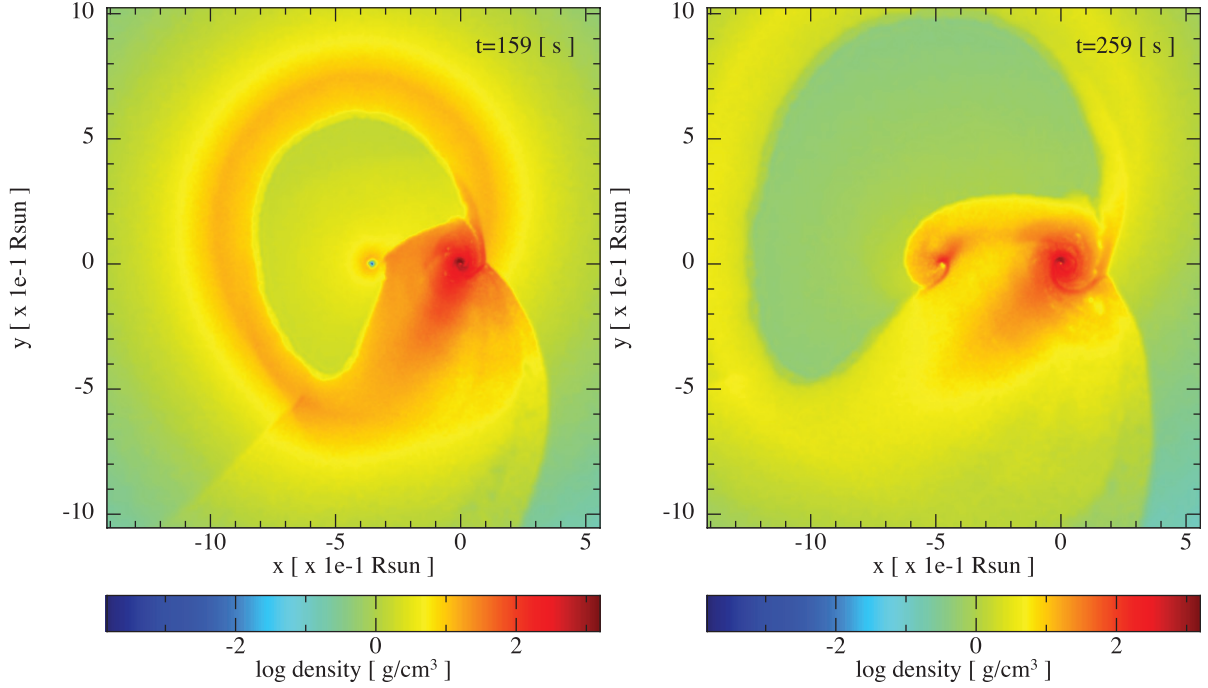
Fig. 1. Three-dimensional, numerical smoothed particle hydrodynamics (SPH) simulation taken from[11] of the SN explosion of a CO star in the presence of a binary companion NS. The orbital period is 4.8 min. The pre-SN CO star mass is $M_{CO} = 6.85 M_\odot$ (evolved star from a $25 M_\odot$ zero-age main-sequence progenitor), the νNS (formed at the center of the SN) mass is $1.85 M_\odot$ and the NS companion mass is $2 M_\odot$. The panels show the mass density on the binary equatorial plane at two selected times from the SN explosion ($t = 0$ of the simulation), 159 s and 259 s. The reference system is rotated and translated so that the x-axis is along the line that joins the νNS and the NS, and the axis origin $(0,0)$ is located at the NS position. In this simulation, the NS collapses with a mass $2.26 M_\odot$ and angular momentum $1.24\, G\, M_\odot^2/c$, while the νNS is stable with mass and angular momentum, respectively, $2.04 M_\odot$ and $1.24\, G\, M_\odot^2/c$.
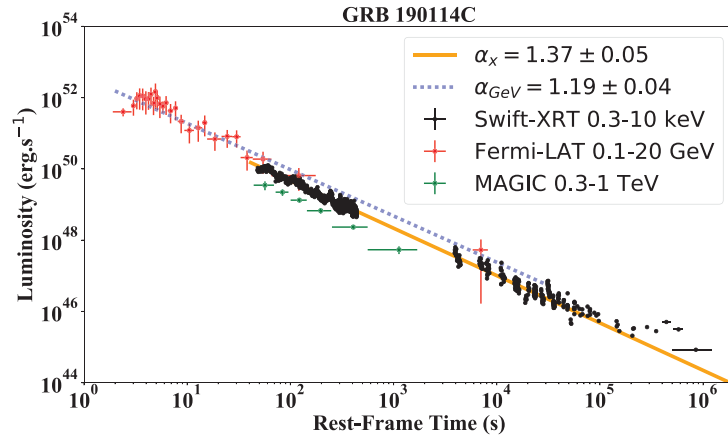
Fig. 2. (Color onine) Luminosity of BdHN I 190114C: the black data points represent the rest-frame 0.3–10 keV luminosity obtained from *Swift*-XRT. It follows a decaying power-law with index $\alpha_X = 1.37 \pm 0.05$. The red data points show the rest-frame 0.1–20 GeV luminosity observed by *Fermi*-LAT. It follows a decaying power-law with amplitude $(4.6 \pm 0.6) \times 10^{52}$ erg s^{-1} and index $\alpha_{GeV} = 1.19 \pm 0.04$. The green data points show the rest-frame 0.3–1 TeV luminosity obtained from MAGIC. Figure taken from Ref. 17 with the permission of the authors.

originates from the synchrotron radiation produced by ultra-relativistic electrons in the expanding SN ejecta, threaded by the magnetic field of the νNS, and further powered by the νNS pulsar-like emission.[18–20] Therefore, the νNS rotational energy powers the X-ray afterglow emission and we have used this fact to infer from the X-ray data the νNS spin, as well as the strength and structure of its magnetic field in several sources (see, e.g. Refs. 19 and 20).

The analysis of the GeV emission, characterized by a decreasing luminosity also well fitted by a power-law (but different with respect to the one of the X-rays), explained by the rotational energy extraction from the newborn rotating BH, has allowed to infer for the first time in GRB 130427A,[9] GRB 190114C[21] and in many other sources in Ref. 17, the BH mass and spin, as well as the geometrical properties of the GeV emission. The observed lightcurve in the X- and in the high-energy (GeV and beyond) gamma-rays of GRB 190114C is shown in Fig. 2.

3. The Black Hole *Inner Engine*

We turn now to give qualitative and quantitative details of the BH *inner engine*. The newborn BH in a BdHN I is embedded in the magnetic field inherited from the NS,[20] and sits at the center of a "*cavity*" of very-low density[22] of material from the HN ejecta (see Fig. 1). For GRB 190114C, such a density has been estimated to be of the order of $10^{-14}\,\mathrm{g\,cm^{-3}}$. The *cavity* is carved during the accretion and subsequent gravitational collapse of the NS leading to the BH. The magnetic field remains anchored to the material and did not participate in the BH formation (see Ref. 20 for details on the magnetic field surrounding the newborn Kerr BH in a BdHN I).

The Kerr BH in the *cavity* is not isolated, it is surrounded by a magnetic field of strength B_0, asymptotically parallel and aligned with the BH rotation axis, and by a fully ionized, very-low-density plasma. The plasma is essential to the electro-dynamical performance of the energy extraction process since it feeds the system with the particles to be accelerated. The operation procedure of the BH *inner engine* leads the mass and spin of the BH to be, instead of constant, decreasing functions of time, keeping constant the BH irreducible mass. The electrons accelerate to ultrahigh energy at expenses of the BH rotational energy, and release it via electron-synchrotron photons that carry it off to infinity.

A quantitative description of this physical situation can be obtained by means of the solution of the Einstein-Maxwell equations of a Kerr BH embedded in a test, asymptotically aligned, uniform magnetic field,[23,24] hereafter the Papapetrou–Wald solution. The BH rotation and the aligned magnetic field induce an electric field that for moderate dimensionless spin values, is mainly radial and inwardly directed. The intensity of this electric field decreases with the square of the distance, has a maximum value at the BH horizon and on the rotation axis ($\theta = 0$), and changes sign at $3\cos\theta_\pm - 1 = 0$. We show in Fig. 3 the electric and magnetic field lines in the Papapetrou–Wald solution. The electric field is inwardly-directed in the northern
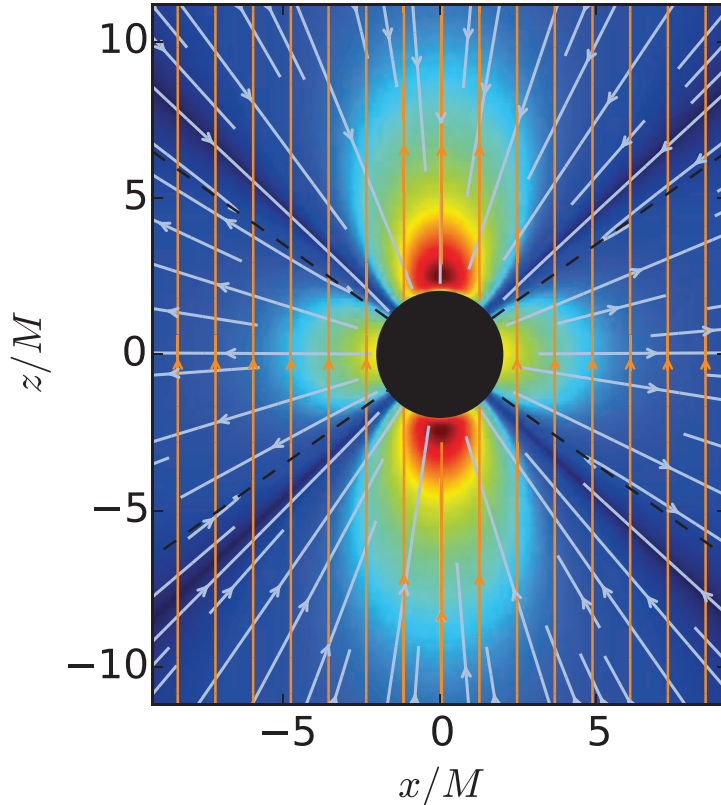
Fig. 3. (Color online) Electric (blue lines) and magnetic (golden lines) field lines of the Papapetrou–Wald solution in the xz plane in Cartesian coordinates. The BH spin parameter is here set to $a/M = 0.3$ and the magnetic field and the BH spin are aligned and parallel. The background is a density-plot of the electric field energy density which is decreasing from red to blue. The BH horizon is the black-filled disk. Distances are in units of M and the fields in units of B_0. In the northern hemisphere, the electric field is inwardly-directed in the region covered by spherical polar angles (measured clockwise) $-\theta_\pm < \theta < \theta_\pm$, where $\theta_\pm \approx 55°$. By equatorial symmetry, in the southern hemisphere it happens in $\pi - \theta_\pm < \theta < \pi + \theta_\pm$. Electrons located in these northern and southern hemisphere cones of semi-aperture angle of $\approx 60°$ are outwardly accelerated with appropriate pitch angles leading to GeV photons. Clearly, being anisotropic, this "jetted" emission is not always visible. This feature is crucial for inferring the morphology of BdHN I from the high-energy (GeV) data of long GRBs.[17] Figure taken from Ref. 17 with permission of the authors.

hemisphere for spherical polar angles (measured clockwise) $-\theta_\pm < \theta < \theta_\pm$, where $\theta_\pm = \arccos(\sqrt{3}/3) \approx 55°$ (see Fig. 3). Because of the equatorial symmetry, it also points inward in the southern hemisphere for $\pi - \theta_\pm < \theta < \pi + \theta_\pm$. There, electrons are outwardly-accelerated.

The mathematical role of the Papapetrou–Wald solution[23,24] in the BH *inner engine* have led to a profound change of paradigm,[9] namely the introduction of the effective charge given by the product of J and B_0:

$$Q_{\text{eff}} = \frac{G}{c^3} 2J B_0. \qquad (3)$$

It must be stressed that this charge works as an effective interpretation of the induced electric field which decreases as $1/r^2$ but, actually, the BH is uncharged as it can be shown by integrating the induced surface charge on the whole BH

horizon surface. Thus, we are in presence of BHs having "*charge without charge*", the electric field arises from the gravitomagnetic interaction of the Kerr BH with the magnetic field. This effective charge, however, allows to finally understand the successful use of a Kerr–Newman BH for the analysis of quantum electrodynamical processes in the field of a rotating BH.[25]

We are now able to elaborate, with the use of quantum electrodynamics and general relativity, a novel and physically more complete treatment of the GRB high-energy engine in a globally neutral system, therefore satisfying Eq. (1) but with $Q = 0$!.

4. The *Blackholic Quantum*

The operation of the *inner engine* is based on three components naturally present in a BdHN I: (i) the Kerr metric that describes the gravitational field produced by the newborn, rotating BH; (ii) an asymptotically uniform magnetic field around it, fulfilling the Papapetrou–Wald solution (see Fig. 3); (iii) a very-low-density plasma around the newborn BH composed of ions and electrons of $10^{-14} \, \mathrm{g \, cm^{-3}}$.[22] The BH *inner engine* operates the following precise steps:

(1) The gravitomagnetic interaction of the BH spin and the magnetic field induce an electric field as given by the Papapetrou–Wald solution. For an aligned and parallel magnetic field to the BH spin, the electric field is nearly radial and inwardly directed about the BH rotation axis up to an angle $\theta_{\pm}$ (see Fig. 3).

(2) The induced electric field accelerates electrons outwardly. The number of electrons that can be accelerated is set by the energy stored in the electric field which, as shown in Ref. 10, can be expressed in the quantum form:

$$\mathcal{E} = \hbar \, \Omega_{\mathrm{eff}}, \tag{4}$$

where Ω_{eff} is linearly proportional to the BH angular velocity, so depending on the BH mass and spin, and with the proportionality constant depending upon the magnetic field strength, the Planck mass, and the neutron mass. The expression evidences the nature of the underlying physical process generating the electric field and the BH horizon: the electrodynamics of the Papapetrou–Wald solution, the origin of the magnetic field from the NS, and the smooth BH formation from the induced gravitational collapse of the NS by accretion.

(3) The maximum possible electron acceleration/energy is set by the electric potential energy difference from the horizon to infinity,[10] $\Delta\Phi = e \, a \, B_0/c$.

(4) Along the polar (rotation) axis, radiation losses are absent, therefore electrons can accelerate all the way to reach $\Delta\Phi \approx 10^{18}$ eV, becoming a source of UHE-CRs.

(5) At off-axis latitudes, the electrons emit synchrotron radiation responsible of the observed GeV emission.

(6) After this, the energy $\mathcal{E}$ has been used and emitted. The process restarts with a new angular momentum $J = J_0 - \Delta J$, being ΔJ the angular momentum extracted to the Kerr BH by the event.

The above steps are repeated, with the same efficiency, if the density of plasma is sufficient, namely if the number of the particles is enough to cover the new value of the energy, $\mathcal{E}$. Therefore, the *inner engine* evolves in a sequence of "*elementary processes*", each emitting a well-defined, precise amount of energy $\mathcal{E}$, the *blackholic quantum*. As an example, we note that for a magnetic field strength $B_0 = 10^{11}$ G, BH mass $M = 3M_\odot$ and spin $\alpha = cJ/(GM^2) = 0.5$, the *blackholic quantum* of energy is $\mathcal{E} \approx 3.4 \times 10^{37}$ erg, and electrons can be accelerated to energies as large as $\Delta\Phi \approx 10^7$ erg $= 6.6 \times 10^{18}$ eV!.

At first sight, one could think this energy can not power the 10^{53}–10^{54} erg emitted at GeV energies in a long GRB. However, $\mathcal{E}$ is the energy of each *elementary process*, each *blackholic quantum* which, as we shall see, occurs on timescales as short as 10^{-15} s. This leads to luminosities of a few 10^{51} erg s^{-1}, just as the one observed (see Fig. 2). Indeed, in this short timescale only a small fractional angular momentum $\Delta J/J \sim 10^{-16}$ of the Kerr BH is extracted off. Therefore, the process must occur over and over all the way to the resolvable timescales by gamma-ray detectors, e.g. milliseconds and beyond. In fact, a BH angular momentum $\Delta J/J \sim 0.1$ is extracted in the timescale of a few seconds, leading to an extracted energy $E_{\mathrm{extr}} \sim 0.1 M c^2$ that explains the observed energy.

5. Polar and Off-Polar Acceleration

Along the polar axis, $\theta = 0$, the electric and magnetic fields are parallel (see Fig. 3). Since the electron is accelerated by the electric field, this implies that the electron pitch angle, i.e. the angle between the electron's injection velocity (into the magnetic field) and the magnetic field is zero. Consequently, no radiation losses (by synchrotron emission) occur for motion along the BH rotation axis. Electrons are accelerated outward along the rotation axis gaining the total electric potential energy, $\Delta\Phi \sim 10^{18}$ eV. Most of this energy is gained at distance scales of the order of the BH horizon, therefore this acceleration occurs on timescales GM/c^3 of a few microseconds. This implies that these ejected electrons may contribute to UHECRs at 10^{18} eV with a power $\sim 10^{42}$ erg s^{-1}.

At off-axis latitudes, the electric and magnetic field cross each other, implying non-zero pitch angles of the accelerated electrons. Figure 4 shows contours of constant pitch angle for electrons moving in the electromagnetic field of the Papapetrou–Wald solution shown in Fig. 3.

During the acceleration, the Lorentz factor increases linearly with time up to an asymptotic, maximum value.[9] This maximum value is set by the balance between the energy gain by acceleration in the electric field, and energy loss by synchrotron radiation. This maximum electron energy leads to photon energies in the GeV regime for the above pitch angles. For instance, in the case of BH spin $\alpha = 0.5$ and
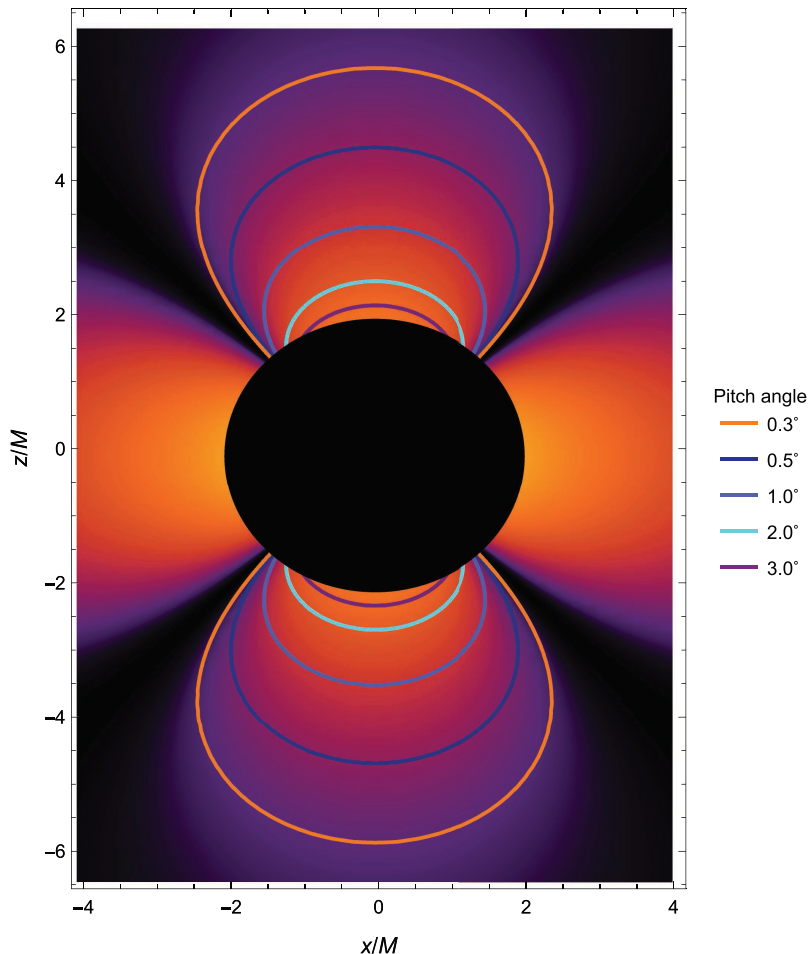
Fig. 4.   Contours of constant electron pitch angle in the electromagnetic field of the Papapetrou–Wald solution of Fig. 3. The BH is indicated by the filled black disk. The background colormap indicates the electric field energy density (the lighter the more intense). Electrons with these pitch angles emit GeV photons in the approximately conical region with a semi-aperture angle $\theta_\pm \approx 60°$ (dark boundary; see also Fig. 3). This "*jetted*" emission is essential to infer the BdHN I morphology from the GeV emission data of long GRBs.[17] Figure taken from Ref. 21 with permission of the authors.

$B_0 = 10^{11}$ G, electrons moving with a pitch angle of $2°$ reach an energy of $2\,$GeV, and radiate photons of $1\,$GeV (in the energy range of *Fermi*-LAT) with a timescale $3 \times 10^{-16}\,$s.

6. Inferring the BH Mass and Spin

We require three physical and astrophysical conditions to obtain the three BH *inner engine* parameters, the BH mass and spin, M and α, as well as the strength of the magnetic field surrounding the BH, B_0. We closely follow the treatment presented in Refs. 9, 17 and 21. The three conditions are as follows: (1) the GeV energetics is paid by the extractable energy of the BH; (2) the system is transparent to GeV photons produced by the synchrotron radiation of the accelerated electrons; (3) the synchrotron radiation timescale explains the observed GeV emission timescale. This constraint implies that the GeV emission is emitted from electrons being accelerated

with appropriate pitch angles (see Fig. 4). Such pitch angles occur within a cone of approximately 60° from the BH rotation axis.

From the above, we have inferred, for instance, for GRB 190114C: $B_0 \approx 3.9 \times 10^{10}$ G, spin and BH mass, respectively, $\alpha = 0.41$ and $M = 4.45 M_\odot$. The BH irreducible mass is $M_{\rm irr} = 4.35 M_\odot$. We have applied a minimum energy requirement, namely that $E_{\rm extr}$ equals the observed energy at GeV energies, so these values are lower limits. The BH *inner engine* can be extremely long-lasting, it can continue to radiate more than the observed (10^4 s of emission) $E_{\rm GeV}$. Because of the power-law behavior of the GeV luminosity, most of the energy is emitted in this early evolution, and just a small higher value of mass and spin can make the system to work for much longer times. For example, let us assume that this observed power-law luminosity (see Fig. 2) extends to longer times, we can check that a BH with $\alpha = 0.46$, $M = 4.50 M_\odot$, and $M_{\rm irr} = 4.38 M_\odot$ can power a 25% larger GeV emission energy, keeping the BH radiating for 1000 yr!.

In Ref. 17, we applied this method to several BdHNs I and inferred BH masses 2.3–8.9$M_\odot$ and spin 0.27–0.87. Besides explaining the GeV emission from the BH energy extraction, the time evolution validates, time by time, the BH mass-energy formula.

7. Conclusions

The *inner engine* uses an efficient gravito-electrodynamical process that explains the GeV emission of long GRBs. The gravito-magnetic interaction of the Kerr BH spin with the surrounding magnetic field induces an electric field which accelerates electrons from the BH vicinity. The kinetic energy gained by electrons is radiated off to infinity by synchrotron emission due to the presence of the magnetic field.

It is worth stressing that there is no bulk motion: each electron is accelerated to a maximum energy set by the balance between electric acceleration and synchrotron radiation losses. The electron-synchrotron photons have energies in the GeV domain. The radiation of the BH *inner engine*, e.g. at keV to MeV energies is negligible (with respect to the observed values). The observed radiation in the keV to MeV energy domains is explained by a different mechanism in a BdHN I; see, e.g. Ref. 20. The request that the observed GeV emission be paid by the extractable (rotational) energy of the Kerr BH has allowed us to estimate, for the first time, the mass and spin of BHs in long GRBs. Since we have here used only the GeV observational data, these values of the BH mass and spin must be considered as lower limits. In fact, we have shown that even a small higher mass (or spin) of the BH can guarantee even larger and longer emission of the BH *inner engine*, and in view of the decaying power-law behavior of the GeV emission, it may last forever!.

Before closing, it is worth to recall some crucial aspects of the BH *inner engine*. (I) The nature of the emission results from considering the physical process leading to the electric and magnetic fields and the BH formation. (II) This is fundamental to show that the emission process leading to the observed luminosity is not continuous but discrete. (III) The timescale of the emission in GRBs is too short to

be probed directly by current observational facilities. Direct evidence of the value and discreteness might come out instead from the observation of large BHs of 10^8–$10^{10} M_\odot$ in AGN. For instance, in the case of M87*, for $M = 6 \times 10^9 M_\odot$, $\alpha = 0.1$, and $B_0 = 10\,G$, the BH *inner engine* theory predicts a high-energy (GeV) emission with a luminosity of a few $10^{43}\,\mathrm{erg\,s^{-1}}$, with a timescale of up to tenths of seconds, while the timescale for UHECRs emission is of the order of half a day.

All the above results are important. The underlying proof that indeed we can use the extractable rotational energy of a Kerr BH to explain the high-energy *jetted* emissions of GRBs and AGN stands alone. The *jetted* emission does not originate from ultra-relativistic acceleration of matter in bulk (massive jets), but from very special energy-saving general relativistic and electrodynamical processes leading to the emission of *blackholic quanta* of energy.[10] We were waiting for this result for fifty years since "Introducing the black hole"[6] and the writing of Eq. (1). We are happy to have given the evidence of the successful operation of the BH *inner engine* in this 50th anniversary.

References

1. R. P. Kerr, *Phys. Rev. Lett.* **11** (1963) 237 (1963).
2. E. T. Newman, E. Couch, K. Chinnapared, A. Exton, A. Prakash and R. Torrence, *J. Math. Phys.* **6** (1965) 918.
3. D. Christodoulou, *Phys. Rev. Lett.* **25** (1970) 1596.
4. D. Christodoulou and R. Ruffini, *Phys. Rev. D* **4** (1971) 3552.
5. S. W. Hawking, *Commun. Math. Phys.* **25** (1972) 152.
6. R. Ruffini and J. A. Wheeler, *Phys. Today* **24** (1971) 30.
7. C. DeWitt and B. S. DeWitt, *Proc. Ecole d'Et de Physique Thorique*: *Les Astres Occlus*, Vol. 23 of Les Houches Summer School, Gordon and Breach (Gordon and Breach, New York, 1973).
8. R. Penrose and R. M. Floyd, *Nature Phys. Sci.* **229** (1971) 177.
9. R. Ruffini *et al.*, *Astrophys. J.* **886** (2019) 82, arXiv:1812.00354.
10. J. A. Rueda and R. Ruffini, *Eur. Phys. J. C* **80** (2020) 300, arXiv:1907.08066.
11. L. Becerra, C. L. Ellinger, C. L. Fryer, J. A. Rueda and R. Ruffini, *Astrophys. J.* **871** (2019) 14, arXiv:1803.04356.
12. J. A. Rueda and R. Ruffini, *Astrophys. J.* **758** (2012) L7, arXiv:1206.1684.
13. C. L. Fryer, J. A. Rueda and R. Ruffini, *Astrophys. J.* **793** (2014) L36, arXiv:1409.1473.
14. L. Becerra, C. L. Bianco, C. L. Fryer, J. A. Rueda and R. Ruffini, *Astrophys. J.* **833** (2016) 107, arXiv:1606.02523.
15. L. Becerra, F. Cipolletta, C. L. Fryer, J. A. Rueda and R. Ruffini, *Astrophys. J.* **812** (2015) 100, arXiv:1505.07580.
16. C. L. Fryer, F. G. Oliveira, J. A. Rueda and R. Ruffini, *Phys. Rev. Lett.* **115** (2015) 231102, arXiv:1505.02809.
17. R. Ruffini *et al.*, *Mon. Not. R. Astron. Soc.* (2021), arXiv:2103.09142.
18. Y. Wang, J. A. Rueda, R. Ruffini, L. Becerra, C. Bianco, L. Becerra, L. Li and M. Karlica, *Astrophys. J.* **874** (2019) 39, arXiv:1811.05433.
19. R. Ruffini, M. Karlica, N. Sahakyan, J. A. Rueda, Y. Wang, G. J. Mathews, C. L. Bianco and M. Muccino, *Astrophys. J.* **869** (2018) 101, arXiv:1712.05000.

20. J. A. Rueda, R. Ruffini, M. Karlica, R. Moradi and Y. Wang, *Astrophys. J.* **893** (2020) 148, arXiv:1905.11339.

21. R. Moradi, J. A. Rueda, R. Ruffini and Y. Wang, arXiv:1911.07552.

22. R. Ruffini, J. D. Melon Fuksman and G. V. Vereshchagin, *Astrophys. J.* **883** (2019) 191.

23. A. Papapetrou, *Ann. de L'Institut Henri Poincare Sec. A Phys. Theorique* **4** (1966) 83.

24. R. M. Wald, *Phys. Rev. D* **10** (1974) 1680.

25. T. Damour and R. Ruffini, *Phys. Rev. Lett.* **35** (1975) 463.

**Astronomy
&
Astrophysics**

The newborn black hole in GRB 191014C proves that it is alive

R. Moradi[1,2,3], J. A. Rueda[1,2,4,5,6], R. Ruffini[1,2,7], and Y. Wang[1,2,3]

[1] ICRANet, Piazza della Repubblica 10, 65122 Pescara, Italy
e-mail: `rahim.moradi@icranet.org, jorge.rueda@icra.it, ruffini@icra.it`
[2] ICRA, Dipartimento di Fisica, Sapienza Università di Roma, P.le Aldo Moro 5, 00185 Rome, Italy
[3] INAF, Osservatorio Astronomico d'Abruzzo, Via M. Maggini snc, 64100 Teramo, Italy
[4] ICRANet-Ferrara, Dipartimento di Fisica e Scienze della Terra, Università degli Studi di Ferrara, Via Saragat 1, 44122 Ferrara, Italy
[5] Dipartimento di Fisica e Scienze della Terra, Università degli Studi di Ferrara, Via Saragat 1, 44122 Ferrara, Italy
[6] INAF, Istituto de Astrofisica e Planetologia Spaziali, Via Fosso del Cavaliere 100, 00133 Rome, Italy
[7] INAF, Viale del Parco Mellini 84, 00136 Rome, Italy

ABSTRACT

A multi-decade theoretical effort has been devoted to finding an efficient mechanism to use the rotational and electrodynamical extractable energy of a Kerr-Newman black hole (BH), to power the most energetic astrophysical sources such as gamma-ray bursts (GRBs) and active galactic nuclei. We show an efficient general relativistic electrodynamical process which occurs in the "inner engine" of a binary driven hypernova. The inner engine is composed of a rotating Kerr BH of mass M and dimensionless spin parameter α, a magnetic field of strength B_0 aligned and parallel to the rotation axis, and a very low-density ionized plasma. Here, we show that the gravitomagnetic interaction between the BH and the magnetic field induces an electric field that accelerates electrons and protons from the environment to ultrarelativistic energies emitting synchrotron radiation. We show that in GRB 190114C the BH of mass $M = 4.4\,M_\odot$, $\alpha = 0.4$, and $B_0 \approx 4 \times 10^{10}$ G can lead to a high-energy ($\gtrsim$GeV) luminosity of 10^{51} erg s^{-1}. The inner engine parameters are determined by requiring (1) that the BH extractable energy explains the GeV and ultrahigh-energy emission energetics, (2) that the emitted photons are not subjected to magnetic-pair production, and (3) that the synchrotron radiation timescale agrees with the observed high-energy timescale. We find for GRB 190114C a clear jetted emission of GeV energies with a semi-aperture angle of approximately 60° with respect to the BH rotation axis.

Key words. black hole physics – magnetic fields – gamma-ray burst: individual: GRB 190114C – gamma-ray burst: general

1. Introduction

Rotating black holes (BHs) have traditionally been described by the Kerr (Kerr 1963) and the Kerr-Newman metrics (Newman et al. 1965) which assume three conditions: (i) they are in a matter vacuum, (ii) they are embedded in an asymptotically flat spacetime, and (iii) they fulfill global stationarity. Under these conditions, BHs are just a sink of energy, namely "dead BHs". The discovery of the reversible and irreversible transformations in both these spacetimes (Christodoulou 1970; Christodoulou & Ruffini 1971) opened the conceptual possibility of extracting both rotational and electromagnetic energy from a Kerr-Newman BH. These results also led to the asymptotic mass-energy formula relating the mass M of a BH to three independent parameters, the irreducible mass M_{irr}, the charge Q, and the angular momentum J, soon confirmed by Hawking (1972). The perspective that up to 50% of the mass-energy of a Kerr-Newman BH could be extracted directed the attention to the alternative view of "alive BHs" whose extractable energy could be used as an astrophysical source (see, e.g., "Introducing the black hole" Ruffini & Wheeler 1971a and "On the energetics of black holes" by R. Ruffini in DeWitt & DeWitt 1973).

Since then an efficient process has been sought that is able to power the most energetic astrophysical sources, gamma-ray bursts (GRBs), and active galactic nuclei (AGNs), using the extractable energy from a BH. The theoretical framework has been constantly evolving (see, e.g., Tursunov & Dadhich 2019, for a review on this topic). As we show in this paper, the recent discovery of the birth of a BH in GRB 130427A (Ruffini et al. 2019a; Rueda & Ruffini 2020) demonstrates that the Kerr BH harbored in the inner engine of this source is indeed an enormous source of giga-electron volt (GeV) energy. The main topic of this article is to reach a deeper understanding of the process of rotational energy extraction by further identifying the astrophysical setting, the boundary conditions, and the basic new physical laws that allow this process to become observable. Specifically, for the case of GRB 190114C, our goal is to infer the values of the independent physical component, the spectral distribution of the high-energy GeV emission, and the geometrical properties of the GeV and ultrahigh-energy emissions.

Our approach is based on the binary-driven hypernova (BdHN) model of long GRBs (Rueda & Ruffini 2012; Fryer et al. 2014; Becerra et al. 2016; Ruffini et al. 2019a). The BdHN progenitor is a binary system composed of a carbon-oxygen (CO) star and a neutron star (NS) companion. The collapse of the iron core of the evolved CO star forms a newborn NS (νNS) at its center and expels the stellar outermost layers, hence leading to a supernova (SN) explosion. The SN ejecta produces a hypercritical accretion process both onto the νNS and onto the NS companion. For very compact binaries (orbital period on the order of 5 min), the NS companion reaches the critical mass rapidly (a few seconds), undergoes gravitational collapse,

and forms a rotating BH. We have called these long GRBs in which there is BH formation, BdHNe of type I (BdHN I). Their isotropic energy release is in the range 10^{53}–10^{54} erg. Numerical simulations of the above process in one, two, and three dimensions have been presented in Fryer et al. (2014), Becerra et al. (2015, 2016, 2019), respectively. Only a fraction of BdHNe form BHs (380 BdHNe I have been identified; see Ruffini et al. 2021). In progenitors with longer binary periods, on the order of hours, no BHs are formed; the outcome is a binary NS with long GRBs in the range 10^{51}–10^{53} erg (Wang et al. 2019). For even longer binary periods, on the order of days, even less energetic long GRBs are encountered, the BdHNe III, for example the case of GRB 060218 (Liang et al., in prep.).

We now return to GRB 190114C. It has already been shown that the collapse of the CO star, which triggers the complete GRB process in the presence of a binary NS companion, leads to a SN creating an additional NS (i.e., the νNS). The SN process is observed earlier at X-ray (up to a few keV) and soft gamma-ray (up to a few MeV) wavelengths, and it has been referred to as "SN-rise" (see, e.g., Wang et al. 2019). For GRB 190114C this occurs in the rest-frame interval $t_{rf} \lesssim 1.99$ s. It carries an energy of $E_{SN\text{-}rise} = 2.82 \times 10^{52}$ erg and is characterized by a blackbody plus cutoff power-law spectrum (Liang et al. 2019). The short duration of the SN-rise finds a natural explanation in the BdHN model. In a BdHN I the companion NS is separated at only 10^{10}–10^{11} cm (i.e., about 1 light-second) from the CO star, implying that only the first spike becomes observable before the expanding SN ejecta triggers the hypercritical accretion process onto the NS companion (see, e.g., Becerra et al. 2019; Wang et al. 2019).

The newborn BH is embedded in the magnetic field inherited from the NS (Rueda et al. 2020), and sits at the center of a cavity of very low density (see Ruffini et al. 2019b, for numerical simulations) of material from the SN ejecta. For GRB 190114C such a density has been estimated to be on the order of 10^{-14} g cm^{-3}. The cavity is carved during the accretion and subsequent gravitational collapse of the NS leading to the BH. The magnetic field remains anchored to material that did not participate in the BH formation (see Rueda et al. 2020 for a detailed discussion on the magnetic field around the newborn Kerr BH in a BdHN I).

The Kerr BH in the cavity is therefore not isolated and acts in conjunction with a test magnetic field of strength B_0, aligned with the BH rotation axis. An additional important feature is that there is no vacuum surrounding the BH. As we show in this article, a fully ionized, very low-density plasma is essential to allow the electrodynamical performance of the energy extraction process by the inner engine, which is necessarily non-stationary.

The operation procedure of the inner engine leads the mass and spin of the BH to decrease as functions of time, while the BH irreducible mass (M_{irr}) remains constant. The electrons accelerate to ultrahigh energies at the expense of the BH extractable energy[1]

$$E_{extr} \equiv (M - M_{irr})c^2, \tag{1}$$

obtainable from the BH mass-energy formula (Christodoulou 1970; Christodoulou & Ruffini 1971; Hawking 1971)

$$M^2 = \frac{c^2}{G^2}\frac{J^2}{4M_{irr}^2} + M_{irr}^2, \tag{2}$$

---

[1] We use cgs-Gaussian units throughout, unless otherwise specified. Careted symbols stand for quantities in geometric units; for example, $\hat{M} \equiv GM/c^2$ denotes geometric mass. See Table 1 for details on the units and conversion factors between the cgs-Gaussian and geometric systems of units.

where J and M are respectively the angular momentum and the mass of the BH.

As we explain in this article, using the mathematical role of the Papapetrou-Wald solution (Papapetrou 1966; Wald 1974), a profound change of paradigm in relativistic astrophysics has been made possible by the inner engine (Ruffini et al. 2019a), namely the introduction of the effective charge given by the product of J and B_0:

$$Q_{eff} = \frac{G}{c^3}2JB_0. \tag{3}$$

This effective charge originates from the gravitomagnetic interaction of the Kerr BH with the surrounding magnetic field, left over by the collapse of the accreting NS to the BH still rooted in the surrounding material (see, e.g., Rueda et al. 2020). The existence of this effective charge finally explains the success of utilizing the concept of a Kerr-Newman BH as a temporary step to approach the analysis of quantum electrodynamical processes in the field of a rotating BH (see, e.g., Damour & Ruffini 1975).

We are now able to elaborate, with the use of quantum electrodynamics and general relativity, a novel and physically more complete treatment of the GRB high-energy engine in a globally neutral system, therefore satisfying Eq. (2). Starting from these general premises, the main focus of this article is the role of the newborn BH in giving origin to the GeV emission observed by *Fermi*-LAT in the context of the inner engine of a BdHN I. In Sect. 2 we mathematically describe the electromagnetic field surrounding the Kerr BH following the Papapetrou-Wald solution of the Einstein-Maxwell equations (Papapetrou 1966; Wald 1974). Section 3 summarizes the operation of the inner engine, including its energy budget and electric potential energy available for the acceleration of charged particles around the BH. The particle motion along the BH rotation axis and its relation to the inner engine contribution to ultrahigh-energy cosmic rays (UHE-CRs) is presented in Sect. 4. In Sect. 5 we estimate the energy loss by synchrotron radiation for electrons moving outside the BH rotation axis. We obtain there the typical electron Lorentz factor, the corresponding pitch angles leading to high-energy ($\gtrsim$GeV) photons, and the radiation timescale. Section 6 presents an estimate of the energy and angular momentum extracted to the Kerr BH in the emission process, in the radiation timescale, implied by the BH mass-energy formula. In Sect. 7 we present our method of inferring the inner engine parameters, namely the BH mass and spin, and the magnetic field strength from the three conditions required (the observed high-energy emission covered by the extractable energy of the BH, the observed high-energy luminosity equal to the synchrotron radiation value, the emitted high-energy photons able to freely escape from the system). In Sect. 8 we apply this framework to the case of GRB 190114C obtaining the corresponding inner engine parameters. Section 9 is dedicated to a comparison of our results with previous literature results. Finally, we outline the conclusions in Sect. 10.

2. Electric and magnetic fields around the BH

Following the considerations presented in Ruffini et al. (2015, 2019a) corresponding to GRB 130427A, we turn to a quantitative estimate of the inner engine via a solution of the Einstein-Maxwell equations of a Kerr BH embedded in a test, asymptotically aligned, uniform magnetic field (Papapetrou 1966; Wald 1974), hereafter the Papapetrou-Wald solution.

Table 1. Units of the relevant physical quantities used in this article in the cgs-Gaussian and geometric system of units.

	cgs-Gaussian	Geometric	cgs to geometric
M	g	cm	$G/c^2 = 7.425 \times 10^{-29}$ cm g^{-1}
Q	cm$^{3/2}$ g$^{1/2}$ s^{-1} (statC)	cm	$G^{1/2}/c^2 = 2.874 \times 10^{-25}$ cm$^{-1/2}$ g$^{-1/2}$ s
J	g cm^2 s^{-1}	cm^2	$G/c^3 = 2.477 \times 10^{-39}$ g^{-1} s
Φ	cm^2 g s^{-2} (erg)	cm	$G/c^4 = 8.261 \times 10^{-50}$ cm^{-1} g^{-1} s^2
ϕ	cm$^{1/2}$ g$^{1/2}$ s^{-1} (statV)	cm^0	$G^{1/2}/c^2 = 2.874 \times 10^{-25}$ cm$^{-1/2}$ g$^{-1/2}$ s
E	cm$^{-1/2}$ g$^{1/2}$ s^{-1} (statV cm^{-1})	cm^{-1}	$G^{1/2}/c^2 = 2.874 \times 10^{-25}$ cm$^{-1/2}$ g$^{-1/2}$ s
B	cm$^{-1/2}$ g$^{1/2}$ s^{-1} (gauss, G)	cm^{-1}	$G^{1/2}/c^2 = 2.874 \times 10^{-25}$ cm$^{-1/2}$ g$^{-1/2}$ s

Notes. M mass, Q charge, J angular momentum, Φ electric potential energy, ϕ electric potential, E electric field, B magnetic field. We use length (cm) as the base unit in the geometric system.

The BH rotation and the aligned magnetic field induce an electric field with the following radial and polar components:

$$E_{\hat{r}} = \frac{B_0 \hat{a} \hat{M}}{\Sigma^2 A^{1/2}} \left[2r^2 \sin^2\theta \, \Sigma - (r^2 + \hat{a}^2)(r^2 - \hat{a}^2\cos^2\theta)(1 + \cos^2\theta) \right], \tag{4a}$$

$$E_{\hat{\theta}} = B_0 \hat{a} \hat{M} \frac{\Delta^{1/2}}{\Sigma^2 A^{1/2}} 2\, r\, \hat{a}^2 \sin\theta \cos\theta \, (1 + \cos^2\theta). \tag{4b}$$

The magnetic field components are

$$B_{\hat{r}} = \frac{B_0 \cos\theta}{\Sigma^2 A^{1/2}} \left\{ (r^2 + \hat{a}^2)\Sigma^2 - 2\hat{M}r\hat{a}^2[2r^2\cos^2\theta + \hat{a}^2(1 + \cos^4\theta)] \right\}, \tag{5a}$$

$$B_{\hat{\theta}} = -\frac{\Delta^{1/2}}{\Sigma^2 A^{1/2}} B_0 \sin\theta \, [\hat{M}\hat{a}^2(r^2 - \hat{a}^2\cos^2\theta)(1 + \cos^2\theta) + r\Sigma^2], \tag{5b}$$

where $\Sigma = r^2 + \hat{a}^2\cos^2\theta$, $\Delta = r^2 - 2\hat{M}r + \hat{a}^2$, $A = (r^2 + \hat{a}^2)^2 - \Delta\hat{a}^2\sin^2\theta$, and $\hat{M} = GM/c^2$ and $\hat{a} = \hat{J}/\hat{M} = (GJ/c^3)/(GM/c^2) = J/(Mc)$ are respectively the geometric mass and specific angular momentum of the BH (see Table 1).

We here use the locally non-rotating observer, also known as zero angular momentum observer (ZAMO; see Bardeen 1970; Bardeen et al. 1972). Therefore, the electromagnetic field components ((4a), (4b) and (5a), (5b)) differ from those presented in Ruffini et al. (2019a), where the Carter's observer was used.

For moderate dimensionless spin values, $\alpha \lesssim 0.7$, where $\alpha \equiv \hat{a}/\hat{M} = cJ/(GM^2)$, the electric and magnetic fields are accurately represented by the first-order expansion ($\alpha \ll 1$ or $\hat{a} \ll \hat{M}$):

$$E_{\hat{r}} \approx -\frac{B_0 \hat{a} \hat{M}}{r^2}(3\cos^2\theta - 1), \quad E_{\hat{\theta}} \approx 0, \tag{6a}$$

$$B_{\hat{r}} \approx B_0 \cos\theta, \quad B_{\hat{\theta}} \approx -B_0 \sqrt{1 - \frac{2\hat{M}}{r}} \sin\theta. \tag{6b}$$

Thus, the electric field is mainly radial and inwardly directed. The electric field decreases with the square of the distance; therefore, it is maximum at the BH horizon, $r_+ = \hat{M}(1 + \sqrt{1 - \alpha^2})$, and on the rotation axis $\theta = 0$, so $E_{\hat{r},\max} = -2B_0\hat{a}/r_+^2 = -\alpha B_0/2$. The electric field vanishes for $3\cos^2\theta_\pm - 1 = 0$. Therefore, it is inwardly directed in the northern hemisphere for spherical polar angles (measured clockwise) $-\theta_\pm < \theta < \theta_\pm$, where $\theta_\pm = \arccos(\sqrt{3}/3) \approx 55°$ (see Eqs. (6a), (6b) and Fig. 1). Because of the equatorial symmetry it also points inward in the southern hemisphere for $\pi - \theta_\pm < \theta < \pi + \theta_\pm$. In these regions, electrons are outwardly accelerated. In the remaining regions the
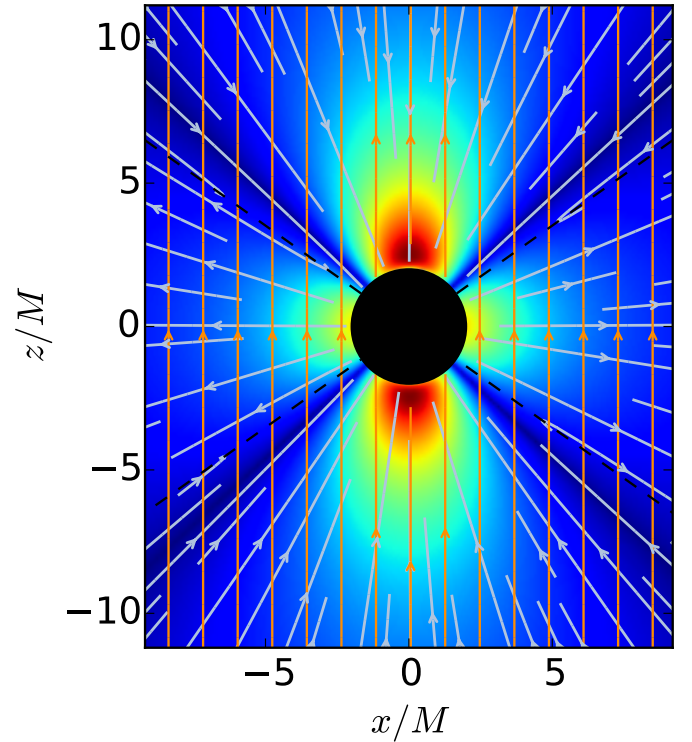
Fig. 1. Electric (blue lines) and magnetic (golden lines) field lines of the Papapetrou-Wald solution in the xz-plane in Cartesian coordinates. The BH spin parameter is set to $a/M = 0.3$ and the magnetic field and the BH spin are aligned and parallel. The background is a density-plot of the electric field energy density which is decreasing from red to blue. The BH horizon is the black disk. Distances are in units of M and the fields in units of B_0. Outward electron acceleration occurs in the region limited by the dashed black lines, i.e., where the electric field is inwardly directed. In the northern hemisphere it covers spherical polar angles (measured clockwise) $-\theta_\pm < \theta < \theta_\pm$, where $\theta_\pm \approx 55°$. By equatorial symmetry, in the southern hemisphere, it covers $\pi - \theta_\pm < \theta < \pi + \theta_\pm$.

electric field reverses sign, becoming outwardly directed (see Fig. 1). The value of $\theta_\pm$ is indeed accurately given by the slow-rotation approximation; for instance, a numerical calculation shows that $\theta_\pm \approx 54.74° - 59.76°$ for $\alpha = 0.01 - 0.99$. We show below in this article that, the electrons located in these northern and southern hemisphere cones of semi-aperture angle of $\approx 60°$, are outwardly accelerated with the appropriate pitch angles leading to GeV photons (see Sect. 5 and Fig. 2 for details). Clearly, being anisotropic, this "jetted" emission is not always visible.

This feature has been crucial for the inference of the morphology of the BdHN I from the high-energy (GeV) data of long GRBs (Ruffini et al. 2021).

It can be also seen that the magnetic field is everywhere nearly aligned with the BH rotation axis; at any distance we have $B_z \gg B_x \sim B_y$, and at distances $r \gg 2\hat{M}$ it is perfectly aligned (i.e., $B_x \to 0$, $B_y \to 0$, and $B_z \to B_0$). All these features can be seen in Fig. 1, which shows the electric and magnetic field lines given by the general expressions given by Eqs. (4a), (4b) and (5a), (5b).

3. Operation of the inner engine

The operation of the inner engine is based on three components naturally present in a BdHN I:

- the Kerr metric that describes the gravitational field produced by the newborn rotating BH;
- an asymptotically uniform magnetic field around the newborn BH fulfilling the Papapetrou-Wald solution (see Sect. 2);
- a very low-density plasma around the newborn BH composed of ions and electrons of 10^{-14} g cm^{-3} (Ruffini et al. 2019b).

The inner engine operation follows these precise steps:

1. The magnetic field and the BH rotation induce an electric field as given by the Papapetrou-Wald solution (see Sect. 2). For an aligned and parallel magnetic field to the BH spin, the electric field is nearly radial and inwardly directed at, and about, the BH rotation axis within an angle $\theta_\pm$ (see Fig. 1).
2. The induced electric field accelerates electrons outwardly. The number of electrons that can be accelerated is set by the energy stored in the electric field Rueda & Ruffini (2020):

$$\mathcal{E} \approx \frac{1}{2} E_{\hat{r}}^2 r_+^3 = \hbar \,\Omega_{\text{eff}}, \tag{7a}$$

$$\Omega_{\text{eff}} = 4 \left(\frac{m_{\text{Pl}}}{m_{\text{n}}} \right)^8 \left(\frac{B_0^2}{\rho_{\text{Pl}}} \right) \alpha \,\Omega_+. \tag{7b}$$

Here $\Omega_+ = c^2 \partial M / \partial J = c \,\alpha / (2 \,r_+)$ is the so-called BH angular velocity; m_{n} the neutron mass; and $\rho_{\text{Pl}} \equiv m_{\text{Pl}} c^2 / \lambda_{\text{Pl}}^3$, $\lambda_{\text{Pl}} = \hbar / (m_{\text{Pl}} c)$, and $m_{\text{Pl}} = \sqrt{\hbar c / G}$ are respectively the Planck energy-density, length, and mass. These expressions evidence the nature of the underlying physical process generating the electric field and the BH horizon: the electrodynamics of the Papapetrou-Wald solution (Ruffini et al. 2019a), the origin of its magnetic field from the binary NS companion (Rueda et al. 2020), and the smooth formation of the BH from the induced gravitational collapse process (Rueda & Ruffini 2012). Additional details on the above formulation are presented in Rueda & Ruffini (2020).

3. The maximum possible electron acceleration and energy is set by the electric potential energy difference from the horizon to infinity can be written as (Rueda & Ruffini 2020)

$$\Delta\Phi = \frac{1}{c} e \, a \, B_0, = \hbar \,\omega_{\text{eff}}, \tag{8a}$$

$$\omega_{\text{eff}} = \frac{G}{c^4} 4 \left(\frac{m_{\text{Pl}}}{m_{\text{n}}} \right)^4 e \, B_0 \,\Omega_+, \tag{8b}$$

where $a = J/M$.

4. Along the polar axis radiation losses are absent (see below in Sect. 4), while at off-axis latitudes (see below in Sect. 5) the accelerated electrons emit synchrotron radiation. The radiation timescale τ_{rad} must fulfill

$$\tau_{\text{rad}} = \frac{\mathcal{E}}{L_{\text{GeV}}}, \tag{9}$$

where L_{GeV} is the observed GeV luminosity.

5. After this, the energy $\mathcal{E}$ has been used and emitted. The process restarts with a new angular momentum $J = J_0 - \Delta J$, being ΔJ the angular momentum extracted to the Kerr BH by the event (see below Eqs. (19a)–(19c) in Sect. 6).

6. The above steps are repeated, with the same efficiency, if the density of plasma is sufficient, namely if the number of particles is enough to cover the new value of the energy $\mathcal{E}$. Therefore, the inner engine evolves in a sequence of elementary processes, each emitting a well-defined, precise amount of energy.

For the sake of example, let us chose fiducial parameters $B_0 = 10^{11}$ G, $M = 3\,M_\odot$, and $\alpha = 0.5$. In this case the available energy is $\mathcal{E} \approx 3.39 \times 10^{37}$ erg, and the maximum energy that an accelerated electron can gain is $\Delta\Phi \approx 1.06 \times 10^7$ erg $= 6.64 \times 10^{18}$ eV.

4. Acceleration on the polar axis: Ultrahigh-energy cosmic rays

Along the polar axis, $\theta = 0$, the electric and magnetic fields only have the z-component and are thus parallel; see Eqs. (4a), (4b) and (5a), (5b), or Eqs. (6a) and (6b). Since the electron is accelerated by the electric field, this implies that the electron pitch angle, which is the angle between the electron's injection velocity (into the magnetic field) and the magnetic field, is zero. Consequently, no radiation losses (by synchrotron emission) occur for motion along the BH rotation axis.

The electrons accelerate outward gaining the total electric potential energy, $\Delta\Phi \sim 10^{18}$ eV. Therefore, the maximum number of electrons that the inner engine can accelerate along the axis is

$$N_{\text{pole}} = \frac{\mathcal{E}}{\Delta\Phi} = \frac{\Omega_{\text{eff}}}{\omega_{\text{eff}}} \sim 10^{31}. \tag{10}$$

These ultrarelativistic electrons contribute to leptonic UHE-CRs. The timescale of this acceleration process along the polar axis is

$$\tau_{\text{pole}} \equiv \frac{\Delta\Phi}{e E_{\hat{r}} \, c} \approx \frac{r_+}{c} = \frac{\alpha}{2\Omega_+} \approx 10^{-5} \text{ s.} \tag{11}$$

This implies that the inner engine can accelerate electrons along the BH rotation axis at a rate

$$\dot{N}_{\text{pole}} \equiv \frac{N_{\text{pole}}}{\tau_{\text{pole}}} \sim 10^{36} \text{ s}^{-1}, \tag{12}$$

leading to a power

$$\dot{\mathcal{E}}_{\text{pole}} = \dot{N}_{\text{pole}} \Delta\Phi = \frac{\mathcal{E}}{\tau_{\text{pole}}} \sim 10^{54} \text{ eV s}^{-1} \approx 10^{42} \text{ erg s}^{-1}. \tag{13}$$

Since the electric and magnetic fields along the rotation axis (and nearly close to it) are parallel (see Fig. 1), the particles in that region are all accelerated (nearly) parallel to the BH rotation axis. Therefore, we do not expect the accelerated particles to have appreciable collisions able to reduce the above estimate of their maximum kinetic energy gain. Therefore, $\dot{\mathcal{E}}_{\text{pole}}$ given by Eq. (13) is the maximum power available for UHECRs.

Table 2. Some astrophysical properties of the inner engine for GRB 190114C and AGN, in the latter adopting as a proxy M 87* (Rueda & Ruffini 2020).

	GRB 190114C	AGN (M 87*-like)
M ($M_\odot$)	4.4	6.0×10^9
α	0.4	0.1
B_0 (G)	4.0×10^{10}	10
$\tau_{\rm pole}$	4.33×10^{-5} s	0.68 d
$\Delta\Phi$ (eV)	3.12×10^{18}	2.66×10^{17}
$\mathcal{E}$ (erg)	7.02×10^{37}	6.96×10^{44}
$\dot{\mathcal{E}}_{\rm pole}$ (erg s^{-1})	1.62×10^{42}	1.18×10^{40}
χ ($^\circ$)	$0.1805-18.05$	$0.0451-4.51$
$t_{\rm c}$ (s)	$1.45 \times 10^{-16}-1.45 \times 10^{-14}$	$0.2939-29.39$
$L_{\rm GeV}$ (erg s^{-1})	$4.83 \times 10^{51}-4.83 \times 10^{53}$	$2.37 \times 10^{43}-2.37 \times 10^{45}$

Notes. The timescale of particle acceleration along the BH rotation axis $\tau_{\rm pole}$ is given by Eq. (11); the maximum energy gained in such acceleration $\Delta\Phi$ is given by Eqs. (8a) and (8b). The energy $\mathcal{E}$ available for acceleration and radiation is given by Eqs. (7a) and (7b). The maximum power available for acceleration (i.e., to power UHECRs) is $\dot{\mathcal{E}}_{\rm pole}$ and is given by Eq. (13). The pitch angle χ is computed from Eq. (16) adopting the photon energy range $0.1-1$ GeV photons; the corresponding synchrotron radiation timescale $t_{\rm c}$ is given by Eq. (18), and an estimate of the associated GeV luminosity, $L_{\rm GeV} \sim \mathcal{E}/t_{\rm c}$, is also shown. In both cases the corresponding inner engine parameters (BH mass M, spin α, and surrounding magnetic field strength B_0) have been fixed to explain the observed high-energy ($\gtrsim$GeV) luminosity (see Sect. 7 for the case of GRB 190114C and Rueda & Ruffini 2020 for M 87*).

The extension of the considerations presented here to very massive BHs and AGN, the role of the accretion disk in these galactic configurations, and the possibility of accelerating protons to produce UHECRs by the BH have started to be addressed (Rueda & Ruffini 2020). We compare and contrast in Table 2 some of the inner engine physical properties applied to the case of GRB 190114C and to M 87*.

5. Acceleration at off-axis latitudes: Synchrotron radiation

For the present electric field, and assuming radial motion, the dynamics of the electrons in the electromagnetic field, for $\gamma \gg 1$, is determined from (de Jager et al. 1996; Ruffini et al. 2019a)

$$m_{\rm e}c^2 \frac{{\rm d}\gamma}{{\rm d}t} = e\frac{1}{2}\alpha B_0\, c - \frac{2}{3}e^4\frac{B_0^2 \sin^2\langle\chi\rangle}{m_{\rm e}^2 c^3}\gamma^2, \tag{14}$$

where e is the elementary charge, γ is the electron Lorentz factor, $\langle\chi\rangle$ is the injection angle between the direction of electron motion and the magnetic field (the pitch angle), and $m_{\rm e}$ is the electron mass. This equation is integrated assuming the electrons are injected near the horizon (where the electric field strength is $\alpha B_0/2$), for selected values of the injection angle $\langle\chi\rangle$, with an initial Lorentz factor $\gamma = 1$ at $t = 0$.

The synchrotron spectrum peaks roughly at the photon critical energy (see, e.g., Landau & Lifshitz 1975)

$$\epsilon_\gamma = \frac{3e\hbar}{2m_{\rm e}\,c}B_0 \sin\langle\chi\rangle\,\gamma^2 = \frac{3}{2}m_{\rm e}c^2\beta\sin\langle\chi\rangle\,\gamma^2, \tag{15}$$

where in the last expression we introduced $\beta = B_0/B_{\rm c}$, with $B_{\rm c} = m_{\rm e}^2 c^2/(e\hbar) \approx 4.41 \times 10^{13}$ G. Therefore, the synchrotron peak energy shifts from lower to higher energies (soft-to-hard spectral evolution) as the electron accelerates. For example, the photon critical energy ϵ_γ, for $\gamma \gtrsim 10^3$, a magnetic field $B_0 = 10^{11}$ G (so $\beta = 0.0023$), and a pitch angle $\chi = 10°$ falls in the GeV regime.

During the acceleration, the Lorentz factor increases linearly with time up to an asymptotic maximum value (see Ruffini et al.

2019a, for details). This maximum value, set by the balance between the energy gain by acceleration in the electric field and energy loss by synchrotron radiation, is (Ruffini et al. 2019a)

$$\gamma_{\rm max} = \frac{1}{2}\left[\frac{3}{e^2/(\hbar c)}\frac{\alpha}{\beta \sin^2\langle\chi\rangle}\right]^{1/2}, \tag{16}$$

which defines the maximum electron energy $\epsilon_{\rm e} = \gamma_{\rm max} m_{\rm e} c^2$. Associated with $\gamma_{\rm max}$, by replacing Eq. (16) into (15) we obtain the maximum peak energy of the spectrum (Ruffini et al. 2019a)

$$\epsilon_{\gamma,\rm max} = \frac{9}{8}\frac{m_{\rm e}c^2}{e^2/\hbar c}\frac{\alpha}{\sin\langle\chi\rangle} \approx \frac{78.76}{\sin\langle\chi\rangle}\alpha\,{\rm MeV}, \tag{17}$$

and the synchrotron cooling timescale $t = t_{\rm c}$ for the above maximum photon critical energy is given by (Ruffini et al. 2019a)

$$t_{\rm c} = \frac{\hbar}{m_{\rm e}c^2}\frac{3}{\sin\langle\chi\rangle}\left(\frac{e^2}{\hbar c}\alpha\beta^3\right)^{-1/2}. \tag{18}$$

For model parameters $\alpha = 0.5$ and $B_0 = 10^{11}$ G, photons of energy $0.1-10$ GeV (typical photon energy range detected by the *Fermi*-LAT) are emitted by electrons with pitch angles $\chi \approx 0.23-23°$, and electron energy $\epsilon_{\rm e} = 1.98 \times 10^8-1.98 \times 10^{10}$ eV, radiating on a timescale of $t_{\rm c} = 2.63 \times 10^{-17}-2.63 \times 10^{-15}$ s. We show in Fig. 2 the pitch angle χ as a function of the maximum photon critical energy (spectrum peak energy) $\epsilon_{\gamma,\rm max}$, obtained from Eq. (17), in the energy range $0.1-10$ GeV, and for three selected values of α. Figure 3 shows the contours of constant χ for electrons moving in the electromagnetic field of the Papapetrou-Wald solution shown in Fig. 1. In particular, we show pitch angles for which electrons emit photons of GeV energies (see also Fig. 2). It can be seen that this high-energy jetted emission occurs within an effective opening angle $\theta_\pm \approx 60°$. This anisotropic emission is essential to infer the BdHN I morphology from the GeV emission data of long GRBs (Ruffini et al. 2021).
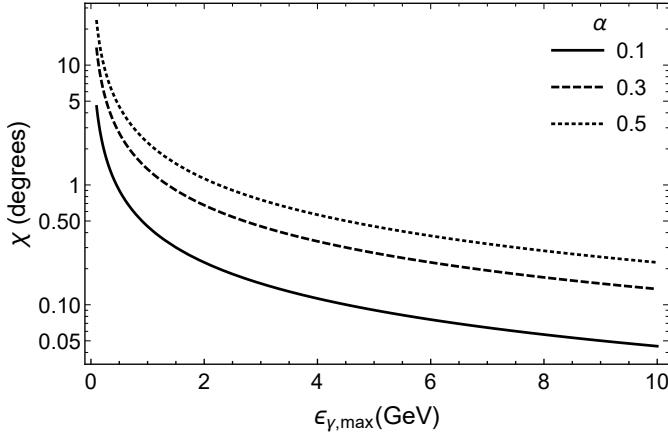
Fig. 2. Pitch angle χ (in units of degrees) as a function of the photon critical energy ϵ_γ (in units of GeV) obtained from Eq. (17). The focus of the plot for photon critical energy is in the range $0.1-10$ GeV. The solid, dashed, and dotted curves correspond to selected values of the BH spin parameter $\alpha = 0.1, 0.3,$ and 0.5, respectively.

6. Energy and angular momentum extraction, golden rule, and duration of the inner engine activity

At the end of every elementary process, all the energy $\mathcal{E}$ has been emitted. The inner engine restarts its operation with the same magnetic field of B_0, but with a new slightly smaller angular momentum $J = J_0 - \Delta J$, being ΔJ the angular momentum extracted by the process. From the BH mass-formula (2), keeping the irreducible mass constant (i.e., $\Delta M_{\rm irr} = 0$, and $\Delta M c^2 = \mathcal{E}$), we obtain a change in the BH angular momentum ΔJ in each event:

$$J_{\rm eff} = I_{\rm eff}\Omega_{\rm eff}, \quad I_{\rm eff} = M\left(\frac{2GM_{\rm irr}}{c^2}\right)^2, \tag{19a}$$

$$\Delta J = \frac{J_{\rm eff}}{J}\hbar, \tag{19b}$$

$$\Delta J = \frac{1}{\bar{\Omega}}\Delta E, \quad \bar{\Omega} \equiv \frac{J}{I_{\rm eff}}, \quad \Delta E \equiv \mathcal{E}. \tag{19c}$$

Here the last equation, a truly golden formula, relates the energy radiated ($\Delta E = \mathcal{E}$) to the angular momentum extracted to the rotating BH (ΔJ).

For the fiducial parameters that we used above, $M = 3\,M_\odot$, $\alpha = 0.5$, and $B_0 = 10^{11}$ G, we have $J \approx 3.96 \times 10^{49}\,{\rm g\,cm^2\,s^{-1}}$, $M_{\rm irr} \approx 2.9\,M_\odot$, and $\Delta J \approx 1.0 \times 10^{33}\,{\rm g\,cm^2\,s^{-1}}$, so a fractional change $\Delta J/J \approx 10^{-16}$, implying that the activity can last for thousands of years or more, providing there is ionized plasma to feed the inner engine.

7. Inference of the BH mass, spin, and surrounding magnetic field

We require three physical and astrophysical conditions to obtain the three inner engine parameters, the BH mass and spin, M and α, and the strength of the magnetic field surrounding the BH, B_0. Following Ruffini et al. (2019a), who show that the use of solely the GeV emission data, after the ultrarelativistic prompt emission (UPE) phase (see Liang et al. 2019), is enough to determine the inner engine parameters (see Fig. 4). In particular, we show that this procedure serves to obtain a lower limit to the mass
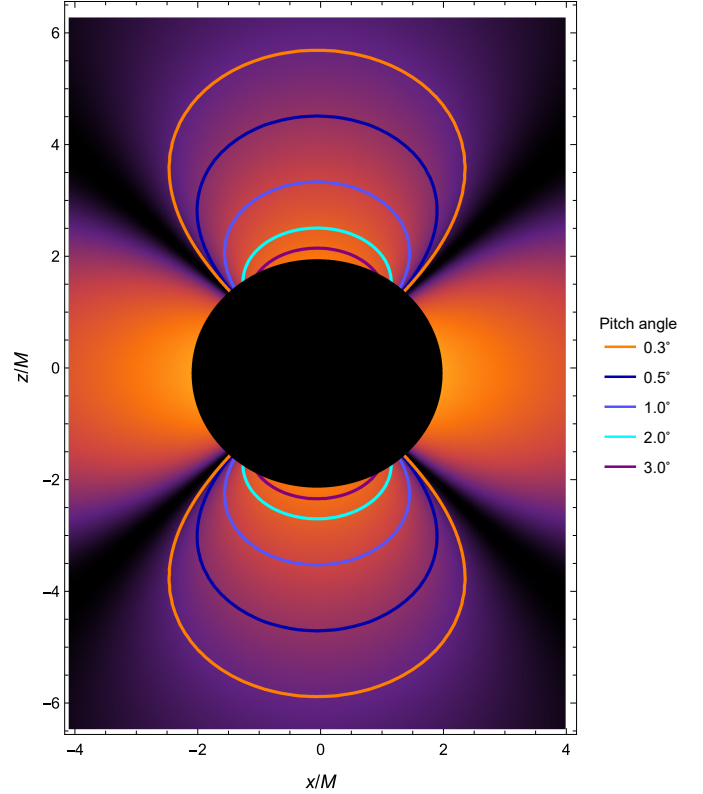
Fig. 3. Contours of constant pitch angle (χ) of electrons moving in the electromagnetic field of the Papapetrou-Wald solution shown in Fig. 1. For the present magnetic dominated case ($|\boldsymbol{E}|/|\boldsymbol{B}| < 1$), charged particles follow the magnetic field lines; therefore, $\sin\chi = |\boldsymbol{B}|^{-1}\sqrt{(\boldsymbol{E}+\boldsymbol{v}\times\boldsymbol{B}/c)^2 - (\boldsymbol{v}\cdot\boldsymbol{E})^2/c^2} \approx \sqrt{|\boldsymbol{E}|^2/|\boldsymbol{B}|^2 - |\boldsymbol{E}_\parallel|^2/|\boldsymbol{B}|^2} \approx |\boldsymbol{E}|/|\boldsymbol{B}|\sin\Psi$ (see, e.g., Kelner et al. 2015), where $\boldsymbol{E}_\parallel$ is the electric field component parallel to the magnetic field, and Ψ is the angle between $\boldsymbol{B}$ and $-\boldsymbol{E}$ (the minus sign is used because we are interested in the pitch angle of electrons). In the slow-rotation regime (see Eqs. (6a) and (6b)), $\sin\Psi \approx \sin\theta/(1-2M\sin^2\theta/r)$, so $\sin\chi \approx |\boldsymbol{E}|/|\boldsymbol{B}|\sin\theta/(1-2M\sin^2\theta/r)$. The BH is indicated by the black disk. The background color map indicates the electric field energy density (lighter colors means more intense).

and spin of the BH. The most important point is that we obtain the value of the irreducible mass of the BH that is kept constant through the energy extraction process. This allows us to determine the time evolution of the BH mass and spin. This can be achieved by fulfilling the three following conditions.

7.1. Condition 1

First, we require that the rotational energy of the BH provides the energy budget for the observed GeV emission energetics,

$$E_{\rm extr} \geq E_{\rm GeV}, \tag{20}$$

which via Eqs. (1) and (2) leads to the following inequality between M, α, and $E_{\rm GeV}$:

$$M \geq \frac{1}{\eta}\frac{E_{\rm GeV}}{c^2}, \quad \eta \equiv 1 - \sqrt{\frac{1+\sqrt{1-\alpha^2}}{2}}. \tag{21}$$

We recall that the maximum value of the efficiency parameter is $\eta_{\rm max} \approx 0.293$, which is attained for a maximally rotating BH, $\alpha_{\rm max} = 1$. It is also important to recall that, by keeping the BH irreducible mass constant in the energy extraction process, we
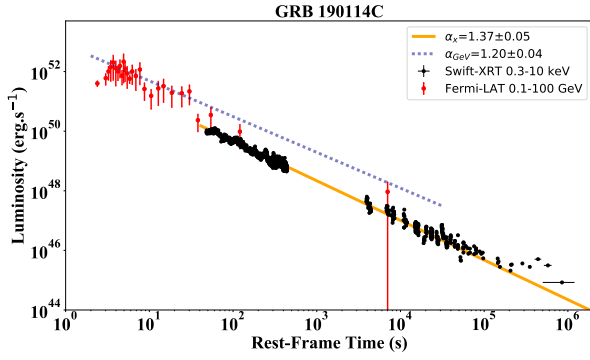
Fig. 4. Red data points: rest-frame $0.1-100$ GeV luminosity light curve of GRB 190114C during and after UPE phase obtained from *Fermi*-LAT. Green dashed line: best fit for power-law behavior of the luminosity following the UPE phase with slope of 1.2 ± 0.04 and amplitude of $7.75 \pm 0.44 \times 10^{52}$ erg s^{-1}. Black data points: rest-frame $0.3-10$ keV luminosity expressed in the rest frame obtained from *Swift*-XRT. It follows a power-law behavior with an amplitude of $A_X = (5.14 \pm 2.03) \times 10^{52}$ erg s^{-1} and a slope of $\alpha_X = 1.37 \pm 0.05$.

are inferring a lower limit to the BH mass. An increasing M_{irr} with time implies a higher BH mass to explain the same GeV energetics.

7.2. Condition 2

We require that the GeV photons must be transparent to the magnetic e^+e^- pair creation process. The attenuation coefficient for this process is (see Daugherty & Harding 1983 and Sect. 5 in Ruffini et al. 2019a)

$$\bar{R} \sim 0.23 \frac{e^2}{\hbar c}\left(\frac{\hbar}{m_e c}\right)^{-1} \beta \sin\langle\chi\rangle \exp\left(-\frac{4/3}{\psi}\right), \qquad (22)$$

where $\psi = \beta \sin\langle\chi\rangle \epsilon_\gamma/(2 m_e c^2)$. Substituting Eq. (17) into Eq. (22), $\bar{R}$ becomes a function of ϵ_γ and the product $\alpha\beta$. For a given ϵ_γ and α, the lower the magnetic field, the larger the mean free path $\bar{R}^{-1}$, as expected. When $\chi \ll 1$, the exponential term dominates, hence $\bar{R}^{-1}$ exponentially increases tending to become infinite. An order-of-magnitude estimate of the magnetic field can be obtained by requiring $\psi \ll 1$,

$$\beta \ll \frac{16}{9} \frac{e^2}{\hbar c} \frac{1}{\alpha} \approx \frac{1.298 \times 10^{-2}}{\alpha}, \quad \text{or} \quad B_0 \ll \frac{5.728 \times 10^{11}}{\alpha} \text{ G}, \qquad (23)$$

which is independent of the photon peak energy. It should be noted that this constraint already restricts the magnetic field to be undercritical ($\beta < 1$), and as we shall see it is sufficient for explaining the GeV emission after the UPE phase. The constraint (23) is analogous to imposing a lower limit on $\bar{R}^{-1}$. For instance, adopting a photon energy of 0.1 GeV, it can be checked that for $\alpha\beta = 1.298 \times 10^{-2}$, the mean free path is $\bar{R}^{-1} = 1.17 \times 10^5$ cm. Lower values of $\alpha\beta$ lead to much larger values of $\bar{R}^{-1}$. It is very interesting that this value is comparable to $GM_\odot/c^2 \approx 1.477 \times 10^5$ cm. Therefore, requesting a value of $\alpha\beta$ lower than the above-mentioned one, implies having a mean free path that is much larger than the BH horizon. Specifically, the high-energy photons are produced in the vicinity of the BH, but they can freely escape from the system. If we adopt as a fiducial value that 0.1 GeV photons have a sufficiently large mean free

path (e.g., $\bar{R}^{-1} \geq 10^{16}$ cm), we obtain (Ruffini et al. 2019a)

$$\beta \leq \frac{3.737 \times 10^{-4}}{\alpha}, \quad \text{or} \quad B_0 \leq \frac{1.649 \times 10^{10}}{\alpha} \text{ G}. \qquad (24)$$

That we are in the exponentially increasing part of the mean free path is evident by the fact that, by requesting a mean free path which is 11 orders of magnitude larger than the one implied by (23), our upper limit to the magnetic field is decreased less than one order of magnitude. Therefore, our estimate of the magnetic field is not sensitive to the choice of the value of $\bar{R}^{-1}$, providing it satisfies $\gtrsim 10^5$ cm. This implies that the magnetic field strength of the inner engine is constrained to have a value, roughly speaking, in the range $10^{10}-10^{11}$ G (see Fig. 5).

7.3. Condition 3

The third condition (i.e., the closure equation) is obtained by requesting that the timescale of the synchrotron radiation, the cooling time t_c given by Eq. (18), be equal to the observed GeV emission timescale (Ruffini et al. 2019a)

$$\tau_{\mathrm{rad},1} = \frac{\mathcal{E}_1}{L_{\mathrm{GeV},1}}, \qquad (25)$$

where $\mathcal{E}$ is the electrostatic energy available for the process (see Eqs. (7a) and (7b)). The subscript "1" refers to quantities evaluated at the beginning of the transparency of the GeV emission (i.e., at the end of the UPE phase) at $t = t_{\mathrm{rf,UPE}}$ (see Sect. 8). We refer to this as the first elementary impulsive event. Therefore, the third equation of the system is

$$t_c\left(\langle\chi\rangle, \alpha, \beta\right) = \tau_{\mathrm{rad},1}\left(\mu, \alpha, \beta, L_{\mathrm{GeV},1}\right), \qquad (26)$$

where $\mu = M/M_\odot$ and $M_\odot$ is the solar mass.

Therefore, having imposed these three conditions, we obtain the three inner engine parameters from the system of Eqs. (21), (24), and (26), as follows:
1. We adopt the equality in Eq. (21), which implies that we will obtain a lower limit to the BH and spin;
2. We replace it into the equality of Eq. (24), which implies that we are adopting the upper limit to the magnetic field strength (for a given α);
3. We obtain the following expression for β as a function of α and of the observables E_{GeV} and L_{GeV} (Ruffini et al. 2019a):

$$\begin{aligned}
\beta &= \beta(\epsilon_\gamma, E_{\mathrm{GeV}}, L_{\mathrm{GeV},1}, \alpha) \\
&= \frac{1}{\alpha}\left(\frac{64}{9}\sqrt{3}\frac{e^2}{\hbar c}\frac{\epsilon_\gamma}{B_c^2 r_+(\mu,\alpha)^3}\frac{L_{\mathrm{GeV},1}}{eB_c c^2}\right)^{2/7},
\end{aligned} \qquad (27)$$

where we have substituted Eq. (17) into Eq. (18) to express t_c as a function of the peak photon energy ϵ_γ, instead of the pitch angle χ.

Therefore, the BH horizon r_+ is a function of μ and α, but in view of Eq. (21) it becomes a function of E_{GeV} and α. Given the observational quantities E_{GeV} (integrated after the UPE phase) and the luminosity $L_{\mathrm{GeV},1}$ (at the end of the UPE phase), Eq. (27) gives a family of solutions of β as a function of α. The solution of this equation together with Eq. (24) gives the values of β and α. With the knowledge of α and E_{GeV}, we obtain μ from Eq. (21).

8. Application to GRB 190114C

We now turn to apply the above procedure to GRB 190114C. For the observational properties of this source we follow the
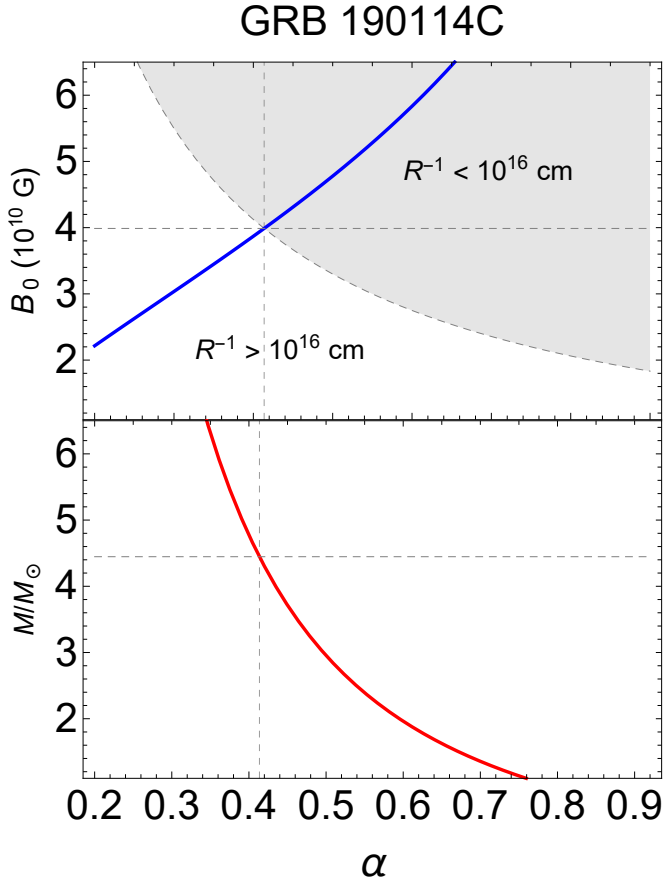
GRB 190114C

Fig. 5. Parameters of the inner engine of GRB 190114C. For this source we have $L_{\text{GeV},1} = 1.47 \times 10^{52}\,\text{erg s}^{-1}$ and $E_{\text{GeV}} = 1.8 \times 10^{53}\,\text{erg}$. *Upper panel*: family of solutions of B_0 as a function of α (blue curve), given by Eq. (27). We use here a photon energy $\epsilon_\gamma = 0.1\,\text{GeV}$ (lower edge of the *Fermi*-LAT energy band). In the gray shaded region the mean free path is $\bar{R}^{-1} < 10^{16}\,\text{cm}$, while in the white shaded region it is $\bar{R}^{-1} \geq 10^{16}\,\text{cm}$. The curve separating the two regions is therefore given by the equality in (24). *Lower panel*: corresponding family of solutions $M(\alpha)$ (red curve), given by Eq. (21).

results of Liang et al. (2019). The UPE phase has been shown in that paper to end at the rest-frame time $t_{\text{rf,UPE}} = 3.99\,\text{s}$, so we limit our analysis to longer times. Therefore, for GRB 190114C, we have $t_{\text{rad},1} = t_{\text{rf,UPE}} = 3.99\,\text{s}$. The $0.1–100\,\text{GeV}$ luminosity observed by *Fermi*-LAT, at $t \geq t_{\text{rf,UPE}}$, is well fitted by a power-law function analogous to the case of GRB 130427A (Ruffini et al. 2019a) (see our Fig. 4):

$$L_{\text{GeV}} = A\,t^{-n} = (7.75 \pm 0.44) \times 10^{52}\,t^{-(1.2\pm0.04)}\,\text{erg s}^{-1}. \quad (28)$$

The associated integrated isotropic energy observed by *Fermi*-LAT, from $t_1 = t_{\text{rf,UPE}} = 3.99\,\text{s}$ to $\sim 10^4\,\text{s}$, is $E_{\text{GeV}} = (1.8 \pm 1.3) \times 10^{53}\,\text{erg}$, and the luminosity at $t = t_{\text{rad},1}$ is $L_{\text{GeV},1} = 1.47 \times 10^{52}\,\text{erg s}^{-1}$ (see Liang et al. 2019).

For the above numbers, and assuming the minimum energy budget requirement, specifically assuming the equality in Eq. (20), the inner engine parameters are (see Fig. 5) magnetic field $B_0 \approx 3.9 \times 10^{10}\,\text{G}$, and spin and BH mass $\alpha = 0.41$ and $M = 4.45\,M_\odot$, respectively. The corresponding BH irreducible mass is $M_{\text{irr}} = 4.35\,M_\odot$. For the above spin value, Eq. (17) leads to a pitch angle for the emission of $0.1\,\text{GeV}$ photons, $\theta \approx \pi/9$.

The inequality (20) implies that the above mass and spin values of the BH must be considered as lower limits. As we show in Sect. 6, the inner engine can be long-lasting so it can continue

to emit and so will eventually radiate more than the observed E_{GeV} that we have used limiting ourselves to the first $10^4\,\text{s}$ of emission. However, in view of the power-law behavior of the GeV luminosity, most of the energy is emitted in this early evolution so the BH parameters do not change significantly if we consider the extrapolation of the energy budget. For example, let us assume that the power-law luminosity (28) extends for 1000 yr. This would increase the total GeV energy radiated by 25%, and recalculating all the parameters we obtain $\alpha = 0.46$, $M = 4.50\,M_\odot$, and $M_{\text{irr}} = 4.38\,M_\odot$.

9. Comparison with previous literature

9.1. Long GRBs in the traditional model

We first recall some key features of the traditional model of long GRBs. To this end, we are facilitated by the book by Bing Zhang (Zhang 2018), which includes an extensive number of references. The traditional GRB model roots can be found in the papers by Rees & Meszaros (1992), Mészáros & Rees (1997), and Woosley (1993). The model proposed by Rees & Meszaros (1992) is based on a single system: GRBs are explained by a single BH from which an ultrarelativistic blastwave originates and whose expansion follows the Blandford–McKee self-similar solution (Blandford & McKee 1976). Woosley (1993) connected the GRB origin to a Kerr BH emitting an ultrarelativistic jet that originates from matter accretion onto the BH. The BH was proposed to form from the direct collapse of a massive star, called a failed SN or a "collapsar", leading to a BH in the mass range $5–10\,M_\odot$.

In these models the afterglows are explained via the kinetic energy of the ultrarelativistic blastwave, which can reach very high bulk Lorentz factors, $\Gamma \sim 1000$, to be released when it interacts with the circumburst medium (Waxman & Piran 1994; Sari & Piran 1995; Wijers et al. 1997; Sari 1997; Sari et al. 1998). The observed spectrum is proposed to be produced by synchrotron and synchrotron self-Compton (SSC) emission from accelerated electrons during the deceleration of the ultrarelativistic blastwave radiating at distances $10^{16}–10^{18}\,\text{cm}$. As pointed out by Zhang (2018), these models based on a ultrarelativistic blastwave radiating at distances $10^{16}–10^{18}\,\text{cm}$ have been applied to jointly explain in the jetted emission several observations:

1. the X-ray afterglow, the steep and shallow decay of the luminosity in the Nousek-Zhang phase (Nousek et al. 2006; Zhang et al. 2006), the X-ray flares and the gamma-ray flares;
2. the emission in the MeV and in the keV observed by the *Neils Gehrels Swift* Observatory, as well as the emission in the optical and in the radio, as well as the emission in the TeV recently observed by MAGIC (Mirzoyan et al. 2019; MAGIC Collaboration 2019a,b);
3. the high-energy (GeV) emission observed in some long GRBs by *Fermi*-LAT.

Within the traditional model, all the above emissions are explained using solely the kinetic energy of the ultrarelativistic blastwave with $\Gamma \sim 10^3$, and radiating at $10^{16}–10^{18}\,\text{cm}$. It becomes clear that, requiring to the single kinetic energy of an ultrarelativistic blastwave to account for the entire energetics of all the observed radiation, at all wavelengths, from the prompt to the afterglow, results in an extreme request to the energy reservoir of the GRB engine.

Within the traditional collapsar-fireball model, the presence of a mildly relativistic expanding component has been introduced in Ramirez-Ruiz et al. (2002), called a cocoon, which

moves sideways to the jet. However, as is clearly elucidated in Nakar & Piran (2017; see also references therein), the emission in the X-rays from this cocoon is too low with respect to be observed X-ray afterglow of long GRBs, unless the cocoon Lorentz factor becomes $\Gamma > 10$. The possibility of a mildly relativistic component in the traditional model is interesting for its implications for the nature of the low-energy sources such as GRB 060218 (see, e.g., Nakar 2015). These sources have energies $10^{49}-10^{51}$ erg, which is the range of energies of BdHNe II and III. However, this is beyond the scope of this article, which is dedicated to BdHNe I, which are characterized by the energy range $10^{52}-10^{54}$ erg. In conclusion, an explanation of the X-ray afterglow in the traditional model needs ultrarelativistic values of the Lorentz factor (see also Zhang 2018, for a review on the subject).

9.2. Long GRBs in the BdHN model

As we note in Sect. 1, the BdHNe have a binary progenitor composed of a CO star and a companion NS. The GRB is composed of independent physical process identified by a time-resolved spectral analysis. Some key results are the following:

1. In the analysis of the data of the XRT detector on board the *Neils Gehrels Swift* satellite of the gamma-ray flare, the X-ray flares, the flare-plateau, and the early afterglow phases (the Nousek-Zhang phase), after the ultrarelativistic prompt radiation phase, showed that the emitter in these phases is in mildly relativistic expansion with $\Gamma \lesssim 5$ (see Ruffini et al. 2018a, for details). A similar upper limit $\Gamma \lesssim 3$ was obtained in the case of GRB 151027A (Ruffini et al. 2018b), and for GRB 130427A the corresponding upper limit on the bulk Lorentz factor is $\Gamma \lesssim 2$ (Ruffini et al. 2018c). Therefore, these stringent upper limits on Γ exclude any ultrarelativistic motion following the UPE phase, contrary to the prediction of traditional GRB models based on the ultrarelativistic blastwave.

2. The high-energy GeV emission follows from the action of the inner engine presented in this work, powered by the BH rotational energy extraction process. In the case of GRB 190114C studied in this work, this corresponds to $t_{rf} \gtrsim 3.99$ s (see Fig. 4 and Liang et al. 2019). It is characterized by an afterglow in the GeV radiation which, when expressed in the rest frame, follows a power-law luminosity (see Eq. (28) and Fig. 4), and it carries an energy of $E_{GeV} = (1.8 \pm 1.3) \times 10^{53}$ erg.

3. In parallel, the X-ray afterglow emission observed by the *Swift* satellite originates from the synchrotron radiation produced in the expanding SN ejecta, threaded by the magnetic field of the νNS, and aided by the injection of particles and the pulsar-like radiation from the νNS into the SN ejecta (Ruffini et al. 2018c; Wang et al. 2019; Rueda et al. 2020). These processes are mainly powered by the rotational energy of the νNS and have led to a significant progress in understanding the origin of the X-ray afterglow emission (see, e.g., the case of GRB 130427A in Ruffini et al. 2018c, and GRB 160509A, GRB 160625B, GRB 180728A, and GRB 190114C in Rueda et al. 2020). In these analyses the spin of the νNS and the strength and structure of its magnetic field have been inferred. In the case of GRB 190114C, the luminosity expressed in the rest frame follows a power-law behavior $L_X = A_X t^{-\alpha_X}$, where $A_X = (5.14 \pm 2.03) \times 10^{52}$ erg s^{-1} and $\alpha_X = 1.37 \pm 0.05$ and carries an energy $E_X = 2.11 \times 10^{52}$ erg; see Fig. 4 (Ruffini et al. 2021; see also Liang et al. 2019). This interpretation of the X-ray afterglow

in the BdHN model conforms with the observational upper limits on the Γ factor of the X-ray afterglow emitter summarized in point 1 above (see Ruffini et al. 2018a, for details). In this way, being the total energetics divided into the different components of the system and their associated different physical phenomena, the energetic request to each emission episode in the BdHN becomes affordable.

9.3. Process of BH energy extraction

Having indicated the main differences between the traditional GRB model and the BdHN model regarding the X-ray and the GeV afterglow emissions, we focus now on the mechanism of the high-energy (GeV) emission, which is intimately related to the physics of the GRB central engine.

There is a vast literature devoted to magnetic fields around BHs and how they may act in a mechanism that could extract the rotational energy of a Kerr BH. An early attempt in the absence of a charge by a matter-dominated magnetized plasma accreting in a disk around a pre-existing Kerr BH was presented in Ruffini & Wilson (1975). The effective potential describing the circular orbit of massive particles around a Kerr BH was adopted (see Ruffini & Wheeler 1971b, in problem 2 of Sect. 104 in Landau & Lifshitz 1975). The infinite conductivity condition, $F_{\mu\nu}u^{\nu} = 0$, where $F_{\mu\nu}$ is the electromagnetic field tensor and u^{ν} the plasma four-velocity, was used there leading to $E \cdot B = 0$. Under these conditions, the acceleration of particles and processes of energy extraction were not possible.

This work was further developed by Blandford & Znajek (1977); in order to overcome the condition $E \cdot B = 0$ in the magnetosphere, they adopted the concepts of gaps and spontaneous e^+e^- pair creation, closely following the seminal ideas of pulsar theory by Sturrock (1971) and Ruderman & Sutherland (1975). They imposed a force-free condition, $F_{\mu\nu}J^{\nu} = 0$, where J^{ν} is the current density, as well as gaps outside the BH horizon. The aim was to produce an ultrarelativistic matter-dominated plasma whose bulk kinetic energy could be used to explain the energetics of a jet at large distances from the BH.

There is also another direction in the literature following the work of MacDonald & Thorne (1982). It extends the work of Blandford & Znajek (1977) and looks at the problem of matter-dominated accretion in presence of a magnetic field anchored to a rotating surrounding disk. Specifically, they proposed an analogy of a rotating BH immersed in a magnetic field with a rotating conductive sphere and/or with the analogy of such a BH and the surrounding magnetosphere as an electric circuit. Independent of the analogies, the underlying physical system remains the same as that proposed by Blandford & Znajek (1977).

The present model is mainly motivated by fitting the GeV emission of GRBs. There is no matter-dominated disk accretion. There is instead a very low-density ionized plasma fulfilling an acceleration electrodynamical process around a newly born BH. We use the Papapetrou-Wald solution in which the electromagnetic field is naturally characterized by regions where $E \cdot B \neq 0$ (see Sect. 2, Fig. 1, and Wald 1974). This feature naturally allows the acceleration of particles without the need of introducing any gaps. There is no ultrarelativistic matter-dominated plasma outflow. The accelerated charged particles emit synchrotron-radiation photons that carry off energy and angular momentum close to the BH. The BH in our scenario is not pre-existing: it is smoothly formed by the hypercritical accretion onto the binary companion NS. The magnetic field, characterizing the Papapetrou-Wald solution, is amplified during the process of gravitational collapse of the binary companion NS

(Rueda et al. 2020). There is no room in this model for the gravitational stable circular orbits around the Kerr BH. The particles are accelerated by an ultrarelativistic electrodynamical process.

Our description is also different with respect to recent GRB literature. For instance, in Metzger et al. (2011), Beniamini et al. (2017), and references therein, the presence of a magnetized wind, outflow, or jet is powered by a central engine. In these works the engine is represented by a NS endowed with an ultrahigh magnetic field, a magnetar, that loses its rotational energy via magnetic-dipole braking, in complete analogy to pulsars. The magnetar powers the outflows that produce the GRB emission at large radii on the order of 10^{15} cm. These models focus on the explanation of the (MeV) GRB prompt and the (X-ray) afterglow emission using the rotational energy of a magnetar, so they do not look either to the physics of BHs, or to the GeV emission that are the topics of the present article.

The understanding of the complex nature of a BdHN requires the knowledge of different episodes, which in some cases are strictly independent, and their description can occur independently of each other.

For instance, the existence of hyper-energetic SN, the SN-rise, radiates off 10^{52} erg in the case of GRB 190114C (Liang et al. 2019). In parallel, the interaction of the SN ejecta with the magnetic field of the νNS and its pulsar-like emission, explain the observed X-ray afterglow (Ruffini et al. 2018c; Wang et al. 2019; Rueda et al. 2020). This emission is produced at distances $10^{12}–10^{16}$ cm from the binary progenitor.

In the present work we address the most energetic GRB component, the GeV emission originating close to the horizon, at distances of 10^6 cm, starting in the case of GRB 190114C at a rest-frame time of 3.99 s after the trigger.

After the clarification of these concepts, we will be ready to describe the optically thick sub-MeV emission in the time interval $1.99–3.99$ s, which comprises the 55% of the energy of GRB 190114C, overcoming the compactness problem using our classic approach of the fireshell model (see Ruffini et al. 1999, 2000; Bianco et al. 2001; Moradi et al., in prep.).

10. Conclusions

The inner engine theory applied in this work to GRB 190114C represents an authentic full paradigm shift from the traditional model of long GRBs based on the emission of an ultrarelativistic blastwave, somehow powered by a Kerr BH. It seems too expensive for nature to accelerate matter in bulk, against the gravitational pull of the BH, to a large distance of $\sim10^{16}–10^{17}$ cm and with $\Gamma \sim 10^3$ to guarantee the transparency of high-energy radiation. For instance, the explanation of the GRB 190114C high-energy emission needs an ultrarelativistic blastwave with a kinetic energy on the order of 10^{55} erg (see, e.g., MAGIC Collaboration 2019a,b). It is clear that such energy cannot be powered by extracting the rotational energy of a Kerr BH of a few $M_\odot$, which will be a few 10^{53} erg (see Eq. (21)).

We have shown that the inner engine can nicely explain the GeV emission by accelerating electrons in the vicinity of the Kerr BH, which radiate their kinetic energy gain via synchrotron emission. The number of particles needed by the inner engine to explain the observed high-energy emission is relatively low. Let us adopt the derived inner engine parameter for GRB 190114C: $M = 4.4\,M_\odot$, $\alpha = 0.4$, and $B_0 = 4 \times 10^{10}$ G. For instance, from Eq. (17) we obtain that for this α a photon peak energy of 10 GeV is obtained for an electron pitch angle $\chi \approx 0.2°$ (see also Fig. 2). Using Eq. (16), this implies an electron Lorentz factor $\gamma \approx 6.76 \times 10^4$, which corresponds to an

electron energy $\epsilon_e = \gamma m_e c^2 \approx 5.53 \times 10^{-2}$ erg $= 3.45 \times 10^{10}$ eV. Therefore, the number of such electrons needed to power the GeV emission of total energy $E_{GeV} = 1.8 \times 10^{53}$ erg $\approx 0.1\,M_\odot c^2$, is $N_e = E_{GeV}/\epsilon_e = 3.25 \times 10^{54}$, which for ionized matter implies a mass of $m_p N_e \approx 2.73 \times 10^{-3}\,M_\odot$, where m_p is the proton mass.

Therefore, the inner engine uses a more efficient electrodynamical process that produces observable high-energy emission in the vicinity of the BH. In fact the acceleration is not based on a bulk-expanding motion. Every single electron is accelerated from its initial velocity up to an asymptotic value defined by the maximum electric potential energy available for their acceleration, which depends only on the external magnetic field strength and the BH spin parameter; see Eqs. (8a) and (8b). These accelerated electrons radiate mainly at high energies in the GeV domain. The radiation of the inner engine (e.g., at keV to MeV energies) is negligible (with respect to the observed values). The observed radiation in the keV to MeV energy domains is explained by a different mechanism in a BdHN I; see (Rueda et al. 2020). The observed luminosity of GeV allows us to estimate the mass and spin of the BH.

We have determined the parameters of the inner engine of GRB 190114C using only the GeV emission data after the UPE phase. We asked the system to satisfy three physical conditions. First, that the GeV energetics is paid by the extractable energy of the BH (see Eq. (21)); second that the system is transparent to GeV photons produced by the synchrotron radiation of the accelerated electrons (see Eq. (24)); and third that the synchrotron radiation timescale explains the observed GeV emission timescale (see Eq. (26)) with the aid of Eq. (18). In order to be fulfilled, this last constraint implies that the GeV emission is emitted from electrons being accelerated with the appropriate pitch angles (see Figs. 2 and 3). These pitch angles occur within a cone of approximately 60° from the BH rotation axis (see Fig. 3), which is a key result for the interpretation of the morphology of the BdHN I (Ruffini et al. 2021).

From this procedure, we have obtained the inner engine parameters of GRB 190114C: $B_0 \approx 3.9 \times 10^{10}$ G, $\alpha \approx 0.41$, and $M = 4.45\,M_\odot$. The corresponding irreducible mass of the BH is $M_{irr} = 4.35\,M_\odot$. It is worth recalling that both M_{irr} and B_0 are kept constant and this should be all over the evolution. The corresponding BH parameters for GRB 130427A are dimensionless spin $\alpha = 0.47$, mass $M = 2.3\,M_\odot$, and irreducible mass $M_{irr} = 2.2\,M_\odot$ (Ruffini et al. 2019a). The above are the first two BH masses derived directly from the GRB observations, and in both cases they are above the theoretical values of the NS critical mass enforcing the validity of the BdHN I model: the BH are formed by smooth hypercritical accretion of the HN ejecta on the NS binary companion.

Since here we only used the GeV emission data, the BH parameters that we have obtained, namely mass and spin, have to be considered as lower limits. Thus, it is clear that even a slightly higher mass (or spin) of the BH can guarantee even larger and longer emission of the inner engine.

Our analysis paves the way to additional research; the data from the different energy bands (e.g., the higher energy bands; MAGIC Collaboration 2019a,b) might provide additional information on the energy distribution of the electrons injected by the electric field into the magnetic field, and on the pitch angle distribution for the synchrotron emission. Figure 3 shows, for the electromagnetic field configuration of the Papapetrou-Wald solution (see Fig. 1), the contours of constant pitch angle and constant electric energy density.

Before concluding, it is worth recalling some crucial aspects of the inner engine here applied to the case of GRB 190114C.

The nature of the emission results from considering the physical process leading to the electric and magnetic fields and the BH formation (see Sect. 3 and Rueda et al. 2020). This is fundamental to show that the emission process leading to the observed luminosity is not continuous, but discrete. The timescale of the emission in GRBs is too short to be probed directly by current observational facilities. Direct evidence of the value and discreteness might come instead from the observation of large BHs of 10^8–$10^{10}\,M_\odot$ in AGN. For instance, in the case of M 87*, for fiducial parameters $M = 6 \times 10^9\,M_\odot$, $\alpha = 0.1$, and $B_0 = 10\,$G, the inner engine theory predicts a high-energy (GeV) emission with a luminosity of a few $10^{43}\,\mathrm{erg\,s}^{-1}$, with a timescale of up to tenths of seconds (see Table 2). Emission at higher energies (e.g., in the TeV band), would be characterized by a lower luminosity and a longer timescale. The timescale for UHECR emission is instead approximately half a day (see Table 2 and Rueda & Ruffini 2020).

We can therefore conclude, in the light of the results of this article and the previous articles in this series, that all BdHN I are powered by three independent sources of energy. The BdHN I is triggered by the SN explosion originating from the collapse of the CO_{core} generating a νNS. The accretion of the SN onto the νNS (see Sect. 9.2 and Ruffini et al. 2018c; Wang et al. 2019; Rueda et al. 2020), gives origin to the X-ray afterglow observed by *Swift*. The hypercritical accretion of the SN onto the binary companion NS gives origin to the BH as soon as the NS reaches the critical mass. This smooth accretion process is alternative to the direct gravitational collapse of a massive star. This happens in GRB 190114C at $t_{rf} = 1.99\,$s. The further accretion of the SN ejecta onto the newly born BH generates the prompt gamma-ray radiation observed in GRB 190114C between 1.99 s and 3.99 s (Moradi et al., in prep.). The further accretion of the SN ejecta onto the newly born BH leads to a process of energy extraction from the inner engine that generates the jetted high-energy ($\gtrsim$GeV) emission. This radiation, as is shown in this article using the Papapetrou-Wald solution (see Sect. 2), is emitted close to the BH horizon and within an angle of nearly 60° from the BH rotation axis (see Sect. 5 and Fig. 3).

References

Bardeen, J. M. 1970, ApJ, 162, 71
Bardeen, J. M., Press, W. H., & Teukolsky, S. A. 1972, ApJ, 178, 347
Becerra, L., Cipolletta, F., Fryer, C. L., Rueda, J. A., & Ruffini, R. 2015, ApJ, 812, 100
Becerra, L., Bianco, C. L., Fryer, C. L., Rueda, J. A., & Ruffini, R. 2016, ApJ, 833, 107
Becerra, L., Ellinger, C. L., Fryer, C. L., Rueda, J. A., & Ruffini, R. 2019, ApJ, 871, 14
Beniamini, P., Giannios, D., & Metzger, B. D. 2017, MNRAS, 472, 3058
Bianco, C. L., Ruffini, R., & Xue, S.-S. 2001, A&A, 368, 377
Blandford, R. D., & McKee, C. F. 1976, Phys. Fluids, 19, 1130
Blandford, R. D., & Znajek, R. L. 1977, MNRAS, 179, 433
Christodoulou, D. 1970, Phys. Rev. Lett., 25, 1596
Christodoulou, D., & Ruffini, R. 1971, Phys. Rev. D, 4, 3552
Damour, T., & Ruffini, R. 1975, Phys. Rev. Lett., 35, 463
Daugherty, J. K., & Harding, A. K. 1983, ApJ, 273, 761
de Jager, O. C., Harding, A. K., Michelson, P. F., et al. 1996, ApJ, 457, 253
DeWitt, C., & DeWitt, B. S. 1973, in Proceedings, Ecole d'Eté de Physique Théorique: Les Astres Occlus (New York, NY: Gordon and Breach), Les Houches Summer School, 23
Fryer, C. L., Rueda, J. A., & Ruffini, R. 2014, ApJ, 793, L36
Hawking, S. W. 1971, Phys. Rev. Lett., 26, 1344
Hawking, S. W. 1972, Commun. Math. Phys., 25, 152
Kelner, S. R., Prosekin, A. Y., & Aharonian, F. A. 2015, AJ, 149, 33
Kerr, R. P. 1963, Phys. Rev. Lett., 11, 237
Landau, L. D., & Lifshitz, E. M. 1975, The Classical Theory of Fields (Oxford: Pergamon Press)
Liang, L., Ruffini, R., Rueda, J. A., et al. 2019, ArXiv e-prints [arXiv:1910.12615]
MacDonald, D., & Thorne, K. S. 1982, MNRAS, 198, 345
MAGIC Collaboration (Acciari, V. A., et al.) 2019a, Nature, 575, 455
MAGIC Collaboration (Acciari, V. A., et al.) 2019b, Nature, 575, 459
Mészáros, P., & Rees, M. J. 1997, ApJ, 482, L29
Metzger, B. D., Giannios, D., Thompson, T. A., Bucciantini, N., & Quataert, E. 2011, MNRAS, 413, 2031
Mirzoyan, R., Noda, K., Moretti, E., et al. 2019, GCN Circ., 23701, 1
Nakar, E. 2015, ApJ, 807, 172
Nakar, E., & Piran, T. 2017, ApJ, 834, 28
Newman, E. T., Couch, E., Chinnapared, K., et al. 1965, J. Math. Phys., 6, 918
Nousek, J. A., Kouveliotou, C., Grupe, D., et al. 2006, ApJ, 642, 389
Papapetrou, A. 1966, Annales de L'Institut Henri Poincare Section (A) Physique Theorique, 4, 83
Ramirez-Ruiz, E., Celotti, A., & Rees, M. J. 2002, MNRAS, 337, 1349
Rees, M. J., & Meszaros, P. 1992, MNRAS, 258, 41P
Ruderman, M. A., & Sutherland, P. G. 1975, ApJ, 196, 51
Rueda, J. A., & Ruffini, R. 2012, ApJ, 758, L7
Rueda, J. A., & Ruffini, R. 2020, Eur. Phys. J. C, 80, 300
Rueda, J. A., Ruffini, R., Karlica, M., Moradi, R., & Wang, Y. 2020, ApJ, 893, 148
Ruffini, R., & Wheeler, J. A. 1971a, Phys. Today, 24, 30
Ruffini, R., & Wheeler, J. A. 1971b, ESRO, 52, 45
Ruffini, R., & Wilson, J. R. 1975, Phys. Rev. D, 12, 2959
Ruffini, R., Salmonson, J. D., Wilson, J. R., & Xue, S.-S. 1999, A&AS, 138, 511
Ruffini, R., Salmonson, J. D., Wilson, J. R., & Xue, S.-S. 2000, A&A, 359, 855
Ruffini, R., Wang, Y., Enderli, M., et al. 2015, ApJ, 798, 10
Ruffini, R., Wang, Y., Aimuratov, Y., et al. 2018a, ApJ, 852, 53
Ruffini, R., Becerra, L., Bianco, C. L., et al. 2018b, ApJ, 869, 151
Ruffini, R., Karlica, M., Sahakyan, N., et al. 2018c, ApJ, 869, 101
Ruffini, R., Moradi, R., Rueda, J. A., et al. 2019a, ApJ, 886, 82
Ruffini, R., Melon Fuksman, J. D., & Vereshchagin, G. V. 2019b, ApJ, 883, 191
Ruffini, R., Moradi, R., Rueda, J. A., et al. 2021, MNRAS, in press [arXiv:2103.09142]
Sari, R. 1997, ApJ, 489, L37
Sari, R., & Piran, T. 1995, ApJ, 455, L143
Sari, R., Piran, T., & Narayan, R. 1998, ApJ, 497, L17
Sturrock, P. A. 1971, ApJ, 164, 529
Tursunov, A., & Dadhich, N. 2019, Universe, 5, 125
Wald, R. M. 1974, Phys. Rev. D, 10, 1680
Wang, Y., Rueda, J. A., Ruffini, R., et al. 2019, ApJ, 874, 39
Waxman, E., & Piran, T. 1994, ApJ, 433, L85
Wijers, R. A. M. J., Rees, M. J., & Meszaros, P. 1997, MNRAS, 288, L51
Woosley, S. E. 1993, ApJ, 405, 273
Zhang, B. 2018, The Physics of Gamma-ray Bursts (Cambridge: Cambridge University Press)
Zhang, B., Fan, Y. Z., Dyks, J., et al. 2006, ApJ, 642, 354

Neutrino Oscillations in Neutrino-Dominated Accretion Around Rotating Black Holes

Juan David Uribe [1,2,†] , Eduar Antonio Becerra-Vergara [1,2,3,†] and Jorge Armando Rueda [2,4,5,6,*,†]

1 Dipartimento di Fisica, Sapienza Università di Roma, P.le Aldo Moro 5, 00185 Rome, Italy; juandavid.uribe@uniroma1.it (J.D.U.); eduar.becerra@icranet.org (E.A.B.-V.)
2 ICRANet, Piazza della Repubblica 10, 65122 Pescara, Italy
3 Grupo de Investigación en Relatividad y Gravitación, Escuela de Física, Universidad Industrial de Santander, A. A. 678, Bucaramanga 680002, Colombia
4 ICRANet-Ferrara, Dipartimento di Fisica e Scienze della Terra, Università degli Studi di Ferrara, Via Saragat 1, 44122 Ferrara, Italy
5 Dipartimento di Fisica e Scienze della Terra, Università degli Studi di Ferrara, Via Saragat 1, 44122 Ferrara, Italy
6 INAF, Istituto di Astrofisica e Planetologia Spaziali, Via Fosso del Cavaliere 100, 00133 Rome, Italy
* Correspondence: jorge.rueda@icra.it
† These authors contributed equally to this work.

Abstract: In the binary-driven hypernova model of long gamma-ray bursts, a carbon–oxygen star explodes as a supernova in the presence of a neutron star binary companion in close orbit. Hypercritical (i.e., highly super-Eddington) accretion of the ejecta matter onto the neutron star sets in, making it reach the critical mass with consequent formation of a Kerr black hole. We have recently shown that, during the accretion process onto the neutron star, fast neutrino flavor oscillations occur. Numerical simulations of the above system show that a part of the ejecta stays bound to the newborn Kerr black hole, leading to a new process of hypercritical accretion. We address herein, also for this phase of the binary-driven hypernova, the occurrence of neutrino flavor oscillations given the extreme conditions of high density (up to 10^{12} g cm^{-3}) and temperatures (up to tens of MeV) inside this disk. We estimate the behavior of the electronic and non-electronic neutrino content within the two-flavor formalism ($\nu_e\nu_x$) under the action of neutrino collective effects by neutrino self-interactions. We find that in the case of inverted mass hierarchy, neutrino oscillations inside the disk have frequencies between $\sim(10^5$–$10^9)$ s^{-1}, leading the disk to achieve flavor equipartition. This implies that the energy deposition rate by neutrino annihilation ($\nu + \bar{\nu} \rightarrow e^- + e^+$) in the vicinity of the Kerr black hole is smaller than previous estimates in the literature not accounting for flavor oscillations inside the disk. The exact value of the reduction factor depends on the ν_e and ν_x optical depths but it can be as high as $\sim$5. The results of this work are a first step toward the analysis of neutrino oscillations in a novel astrophysical context, and as such, deserve further attention.

Keywords: accretion disk; neutrino physics; gamma-ray bursts; black hole physics

1. Introduction

Neutrino flavor oscillations are now an experimental fact [1], and in recent years, their study based only on Mikheyev–Smirnov–Wolfenstein (MSW) effects [2,3] has been transformed by the insight that refractive effects of neutrinos on themselves due to the neutrino self-interaction potential are essential. Their behavior in a vacuum, in matter or by neutrino self-interactions has been studied in the context of early universe evolution [4–15], solar and atmospheric neutrino anomalies [16–24] and core-collapse supernovae (SN) ([25–51] and references therein). We are interested in astrophysical situations when neutrino self-interactions become more relevant than the matter potential. This implies systems in which a high density of neutrinos is present and in fact most of the literature on neutrino self-interaction dominance is concentrated on supernova neutrinos. It has

been shown how collective effects, such as synchronized and bipolar oscillations, change the flavor content of the emitted neutrinos when compared with the original content deep inside the exploding star.

This article aims to explore the problem of neutrino flavor oscillations in the case of long gamma-ray bursts (GRBs), in particular in the context of the binary-driven hypernova (BdHN) scenario. Long GRBs are the most energetic and powerful cosmological transients so far observed, releasing energies of up to a few 10^{54} erg in just a few seconds. Most of the energy is emitted in the prompt gamma-ray emission and in the X-ray afterglow. We refer the reader to [52] for an excellent review on GRBs and its observational properties.

The GRB progenitor in the BdHN model is a binary system composed of a carbon–oxygen star (CO_{core}) and a companion neutron star (NS) in tight orbit with orbital periods in the order of a few minutes [53–58]. These binaries are expected to occur in the final stages of the evolutionary path of a binary system of two main-sequence stars of masses in the order of 10–15 $M_\odot$, after passing from X-ray binary phase and possibly multiple common-envelope phases (see [57,59] and references therein).

The CO_{core} explodes as SN, creating at its center a newborn NS (νNS), and ejecting the matter from its outermost layers. Part of the ejected matter falls back and accretes onto the νNS, while the rest continues its expansion leading to a hypercritical accretion (i.e., highly super-Eddington) process onto the NS companion. The NS companion reaches the critical mass for gravitational collapse, hence forming a rotating black hole (BH). The class of BdHN in which a BH is formed has been called type I, i.e., BdHN I [60].

One of the most important aspects of the BdHN model of long GRBs is that different GRB observables in different energy bands of the electromagnetic spectrum are explained by different components and physical ingredients of the system. This is summarized in Table 1, taken from [61]. For a review on the BdHN model and all the physical phenomena at work, we refer the reader to [62].

Table 1. Summary of the gamma-ray burst (GRB) observables associated with each BdHN I component and physical phenomenon. Adapted from Table 1 in [61] with the permission of the authors. References in the table: [a] [60], [b] [57,62,63], [c] [64], [d] [65,66], [e] [67], [f] [60,68].

BdHN Component/Phenomena	GRB Observable				
	X-Ray Precursor	Prompt (MeV)	GeV-TeV Emission	X-Ray Flares Early Afterglow	X-Ray Plateau and Late Afterglow
SN breakout [a]	⊗				
Hypercrit. acc. onto the NS [b]	⊗				
e^+e^-: transparency in low baryon load region [c]		⊗			
Inner engine: BH + *B* + matter [d]			⊗		
e^+e^-: transparency in high baryon load region [e]				⊗	
Synchrotron by νNS injected particles on SN ejecta [f]					⊗
νNS pulsar-like emission [f]					⊗

The emission of neutrinos is a crucial ingredient, since they act as the main cooling process that allows the accretion onto the NS to proceed at very high rates of up to 1 $M_\odot$ s^{-1} [57,59,63,69,70]. In [71], we studied the neutrino flavor oscillations in this hypercritical accretion process onto the NS, all the way to BH formation. We showed that the density of neutrinos on top the NS in the accreting "atmosphere" is such that neutrino self-interactions dominate the flavor evolution, leading to collective effects. The latter induce in this system quick flavor conversions with short oscillation lengths as small as

(0.05–1) km. Far from the NS surface, the neutrino density decreases, and so the matter potential and MSW resonances dominate the flavor oscillations. The main result has been that the neutrino flavor content emerging on top of the accretion zone was completely different compared to the one created at the bottom of it. In the BdHN scenario, part of the SN ejecta stays bound to the newborn Kerr BH, forming an accretion disk onto it. In this context, the study of accretion disks and their nuances related to neutrinos is of paramount importance to shed light on this aspect of the GRB central engine. In most cases, the mass that is exchanged in close binaries has enough angular momentum so that it cannot fall radially. As a consequence, the gas will start rotating around the star or BH, forming a disk. At this point, it is worth digressing to mention the case of short GRBs. They are widely thought to be the product of mergers of compact-object binaries, e.g., NS–NS and/or NS–BH binaries (see, e.g., the pioneering works [72–75]). It is then clear that, especially in NS–NS mergers, matter can be kept bound and circularize around the new central remnant. Additionally, in such a case, an accretion disk will form around the more massive NS or the newborn BH (if the new central object overcomes the critical mass), and therefore the results of this work become relevant for such physical systems.

The magneto-hydrodynamics that describe the behavior of accretion disks are too complex to be solved analytically and full numerical analysis is time-consuming and costly. To bypass this difficulty, different models make approximations that allow casting the physics of an accretion disk as a two-dimensional or even one-dimensional problem. These approximations can be can be pigeonholed into four categories: symmetry, temporal evolution, viscosity and dynamics. Almost all analytic models are axially symmetric. This is a sensible assumption for any physical system that rotates. Similarly, most models are time-independent, although this is a more complicated matter. A disk can evolve in time in several ways. For example, the accretion rate $\dot{M}$ depends on the external source of material which need not be constant, and at the same time, the infalling material increases the mass and angular momentum of the central object, constantly changing the gravitational potential. Additionally, strong winds and outflows can continually change the mass of the disk. Nonetheless, $\dot{M}(\boldsymbol{x}, t) = \dot{M} = $ constant is assumed. Viscosity is another problematic approximation. For the gas to spiral down, its angular momentum needs to be reduced by shear stresses. These come from the turbulence driven by differential rotation and the electromagnetic properties of the disk [76–79], but again, to avoid magneto-hydrodynamical calculations, the turbulence is accounted for using a phenomenological viscosity $\alpha = $ constant, such that the kinematical viscosity takes the form $\nu \approx \alpha H c_s$, where c_s is the local isothermal sound speed of the gas and H is the height of the disk measured from the plane of rotation (or half-thickness). This idea was first put forward by [80] and even though there is disagreement about the value and behavior of the viscosity constant, and it has been criticized as inadequate [81–84], several thriving models use this prescription. Finally, the assumptions concerning the dynamics of the disk are related to what terms are dominant in the energy conservation equation and the Navier–Stokes equation that describe the fluid (apart from the ones related to symmetry and time independence). In particular, it amounts to deciding what cooling mechanisms are important, what external potentials should be considered and what are the characteristics of the internal forces in the fluid. The specific tuning of these terms breeds one of the known models: thin disks, slim disks, advection-dominated accretion flows (ADAFs), thick disks, neutrino-dominated accretion flows (NDAFs), convection-dominated accretion flows (CDAFs), luminous hot accretion flows (LHAFs), advection-dominated inflow-outflow solutions (ADIOS) and magnetized tori. The options are numerous and each model is full of subtleties, making accretion flows around a given object an extremely rich area of research. For useful reviews and important articles with a wide range of subjects related to accretion disks, see [85–99] and references therein.

NDAFs are of special interest for GRBs. They are hyperaccreting slim disks, optically thick to radiation that can reach high densities $\rho \approx 10^{10}$–10^{13} g cm^{-3} and high temperatures $T \approx 10^{10}$–10^{11} K around the inner edge. Under these conditions, the main cooling

mechanism is neutrino emission since copious amounts of (mainly electron) neutrinos and antineutrinos are created by electron–positron pair annihilation, URCA and nucleon–nucleon bremsstrahlung processes, and later emitted from the disk surface. These $\nu\bar{\nu}$ pairs might then annihilate above the disk producing an e^-e^+ dominated outflow. NDAFs were proposed as a feasible central engine for GRBs in [100] and have been studied extensively since [101–112]. In [103] and later in [107], it was found that the inner regions of the disk can be optically thick to $\nu_e\bar{\nu}_e$, trapping them inside the disk, hinting that NDAFs may be unable to power GRBs. However, the system involves neutrinos propagating through dense media, and consequently, an analysis of neutrino oscillations, missing in the above literature, must be performed. Figure 1 represents the standard situation of the physical system of interest. The dominance of the self-interaction potential induces collective effects or decoherence. In either case, the neutrino flavor content of the disk changes. Some recent articles are starting to recognize their role in accretion disks and spherical accretion [71,113–117]. In particular, refs. [113,117] calculated the flavor evolution of neutrinos once they are emitted from the disk, but did not take into account the oscillation behavior inside the disk. The energy deposition rate above a disk by neutrino-pair annihilation as a powering mechanism of GRBs in NDAFs can be affected by neutrino oscillation in two ways. The neutrino spectrum emitted at the disk surface depends not only on the disk temperature and density but also on the neutrino flavor transformations inside the disk. Additionally, once the neutrinos are emitted, they undergo flavor transformations before being annihilated.
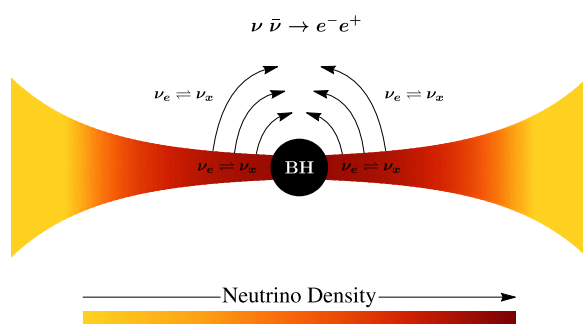
Figure 1. Schematic representation of the physical system. Due to conditions of high temperature and density, neutrinos are produced in copious amounts inside the disk. Since they have very low cross-sectional areas, neutrinos are free to escape but not before experiencing collective effects due to the several oscillation potentials. The energy deposition rate of the process $\nu + \bar{\nu} \rightarrow e^- + e^+$ depends on the local distribution of electronic and non-electronic (anti)neutrinos, which is affected by the flavor oscillation dynamics.

Our main objective is to propose a simple model to study neutrino oscillations inside an accretion disk and analyze its consequences. Applying the formalism of neutrino oscillations to non-symmetrical systems is difficult, so we chose a steady-state, α-disk as a first step in the development of such a model. The generalizations to more sophisticated accretion disks (see, e.g., [118–121]) can be subjects of future research.

This article is organized as follows. We outline the features of NDAFs and discuss in detail the assumptions needed to derive the disk equations in Section 2. Then, in Section 3, we discuss the general characteristics of the equation that drive the evolution of neutrino oscillations. We use the comprehensive exposition of the accretion disk of the previous section to build a simple model that adds neutrino oscillations to NDAFs, while emphasizing how the thin disk approximation can simplify the equations of flavor evolution. In Section 4 we set the parameters of the physical system and give some details on the initial conditions needed to solve the equations of accretion disks and neutrino oscillations. In Section 5 we discuss the main results of our calculations and analyze the phenomenology of neutrino oscillations in accretion disks. Finally, we present in Section 6 the conclusions of this work. Additional technical details are presented in a series of appendices at the end.

2. Hydrodynamics

2.1. Units, Velocities and Averaging

Throughout this article, we use Planck units $c = G = \hbar = k_B = k_e = 1$. To describe the spacetime around a Kerr BH of mass M, we use the metric $g_{\mu\nu}$ in Boyer–Lindquist coordinates, with a space-like signature, and with a dimensionless spin parameter $a = J/M^2$, which can be written as:

$$ds^2 = \left(g_{tt} - \omega^2 g_{\phi\phi}\right)dt^2 + g_{\phi\phi}(d\phi - \omega\, dt)^2 + g_{rr}\, dr^2 + g_{\theta\theta}\, d\theta^2, \tag{1}$$

in coordinates (t, r, θ, ϕ). The covariant components $(\boldsymbol{g})_{\mu\nu}$ of the metric are

$$\begin{aligned} g_{tt} &= -\left(1 - \frac{2\,M\,r}{\Sigma}\right), \quad g_{rr} = \frac{\Sigma}{\Delta}, \quad g_{\theta\theta} = \Sigma, \\ g_{\phi\phi} &= \left(r^2 + M^2 a^2 + \frac{2\,M^3 a^2 r}{\Sigma}\sin^2\theta\right)\sin^2\theta, \quad g_{t\phi} = -\frac{2\,M^2\,a\,r}{\Sigma}\sin^2\theta, \end{aligned} \tag{2}$$

and its determinant is $g = -\Sigma^2 \sin^2\theta$, with the well known functions $\Sigma = r^2 + M^2 a^2 \cos^2\theta$ and $\Delta = r^2 - 2Mr + M^2 a^2$. We denote the coordinate frame by CF. Note that these coordinates can be used by an observer on an asymptotic rest frame. The angular velocity of the locally non-rotating frame (LNRF) is

$$\omega = -\frac{g_{t\phi}}{g_{\phi\phi}} = \frac{2\,a\,M^2}{(r^3 + M^2 a^2 r + 2M^3 a^2)}, \tag{3}$$

and in Equation (2) it can be seen explicitly that if an observer has an angular velocity $\omega = d\phi/dt$, it would not measure any differences between the $\pm\phi$ directions. The LNRF is defined by orthonormality and the coordinate change $\phi_{\text{LNRF}} = \tilde{\phi} = \phi - \omega\,t$ [122,123]. We assume that the disk lies on the equatorial plane of the BH ($\theta = \pi/2$). This way we represent the average movement of the fluid by geodesic circular orbits with angular velocity $\Omega = d\phi/dt = u^\phi/u^t$ plus a radial velocity so that the local rest frame (LRF) of the fluid is obtained by performing, first, an azimuthal Lorentz boost with velocity $\beta^{\hat{\phi}}$ to a co-rotating frame (CRF) [124], and then a radial Lorentz boost with velocity $\beta^{\tilde{r}}$. Clearly, the metric on the LNRF, CRF and LRF is $\text{diag}(-1, 1, 1, 1)$. The expression for the angular velocity of circular orbits is obtained by setting $\dot{r} = \ddot{r} = 0$ in the r-component of the geodesic equation

$$\Omega^\pm = \pm\frac{\sqrt{M}}{(r^{3/2} \pm M^{3/2}a)}, \tag{4}$$

where $(+)$ is for prograde orbits and $(-)$ is for retrograde orbits. We will limit our calculations to prograde movement with $0 \le a \le 1$, but extension to retrograde orbits is straightforward. Finally, we can get the components of the 4-velocity of the fluid by transforming $\boldsymbol{u}_{\text{LRF}} = (1, 0, 0, 0)$ back to the CF

$$u^\mu = \left(\frac{\gamma_{\tilde{r}}\gamma_{\hat{\phi}}}{\sqrt{\omega^2 g_{\phi\phi} - g_{tt}}}, \frac{\gamma_{\tilde{r}}\beta^{\tilde{r}}}{\sqrt{g_{rr}}}, 0, \frac{\gamma_{\tilde{r}}\gamma_{\hat{\phi}}\Omega}{\sqrt{\omega^2 g_{\phi\phi} - g_{tt}}}\right), \tag{5}$$

leaving $\beta^{\tilde{r}}$ to be determined by the conservation laws. In Equation (5) we have replaced $\beta^{\hat{\phi}}$ with Equation (A3). A discussion on the explicit form of the transformations and some miscellaneous results are given in Appendix A. We will also assume that the disk is in a steady-state. This statement requires some analysis. There are two main ways in which it can be false:

First, as matter falls into the BH, its values M and a change [125,126], effectively changing the spacetime around it. For the spacetime to remain the same (i.e., for M and a to stay constant) we require $\Omega^{-1} \ll t_{\mathrm{acc}} = \Delta M_0 / \dot{M}_{\mathrm{acc}}$, where ΔM_0 is the total mass of the disk and $\dot{M}_{\mathrm{acc}}$ is the accretion rate. The characteristic accretion time must be bigger than the dynamical time of the disk so that flow changes due to flow dynamics are more important than flow changes due to spacetime changes. Equivalent versions of this condition that appear throughout disk accretion articles are $t_{\mathrm{dym}} \ll t_{\mathrm{visc}}$ and

$$\beta^r \ll \beta^\phi < 1, \tag{6}$$

where it is understood that the accretion rate obeys $\dot{M}_{\mathrm{acc}} \approx \Delta M_0 / t_{\mathrm{acc}}$. To put these numbers into perspective, consider a solar mass BH ($M = 1 M_\odot$) and a disk with mass between $\Delta M_0 = (1 - 10) M_\odot$. For accretion rates up to $\dot{M}_{\mathrm{acc}} = 1 M_\odot / \mathrm{s}$ the characteristic accretion time is $t_{\mathrm{acc}} \lesssim (1 - 10)$ s, while $\Omega^{-1} \sim (10^{-5} - 10^{-1})$ s between $r = r_{\mathrm{ISCO}}$ and $r = 2000 M_\odot$. Consequently, a wide range of astrophysical systems satisfy this condition, and it is equivalent to claiming that both ∂_t and ∂_ϕ are killing fields.

Second, at any point inside the disk, any field $\boldsymbol{\psi}(t, r, \theta, \phi)$ that reports a property of the gas may variate in time due to the turbulent motion of the flow. Thus, to assume that any field is time-independent and smooth enough in r for its flow to be described by Equation (5) means replacing such field by its average over an appropriate spacetime volume. The same process allows one to choose a natural set of variables that split the hydrodynamics into r-component equations and θ-component equations. The averaging process has been explained in [124,127,128]. We include the analysis here and try to explain it in a self-consistent manner. The turbulent motion is characterized by the eddies. The azimuthal extension of the largest eddies can be 2π, like waves crashing around an island, but their linear measure cannot be larger than the thickness of the disk, and as measured by an observer on the CRF, their velocity is in the order of $\beta^{\tilde{r}}$ so that their period along the r component is $\Delta \tilde{t} \approx (\mathrm{Thickness}) / \beta^{\tilde{r}}$ (e.g., §33, [129]). If we denote by H the average half-thickness of the disk as measured by this observer at r over the time $\Delta \tilde{t}$, then the appropriate volume $\mathcal{V}$ is composed by the points (t, r, θ, ϕ) such that $t \in [t^* - \Delta t/2, t^* + \Delta t/2]$, $\theta \in [\theta_{\min}, \theta_{\max}]$ and $\phi \in [0, 2\pi)$, where we have transformed $\Delta \tilde{t}$ and $\Delta \tilde{r}$ back to the CF using Equation (A4) as approximations. The values $\theta_{\min}$ and $\theta_{\max}$ correspond to the upper and lower faces of the disk, respectively. Then, the average takes the form

$$\boldsymbol{\psi}(t, r, \theta, \phi) \mapsto \boldsymbol{\psi}(r, \theta) = \langle \boldsymbol{\psi}(t, r, \theta, \phi) \rangle = \frac{\int_{t^* - \Delta t/2}^{t^* + \Delta t/2} \int_0^{2\pi} \boldsymbol{\psi}(r, t, \theta, \phi) \sqrt{\frac{-g}{g_{rr} g_{\theta\theta}}} dt d\phi}{\int_{t^* - \Delta t/2}^{t^* + \Delta t/2} \int_0^{2\pi} \sqrt{\frac{-g}{g_{rr} g_{\theta\theta}}} dt d\phi}. \tag{7}$$

The steady-state condition is achieved by requiring that the Lie derivative of the averaged quantity along the killing field ∂_t vanishes: $\mathcal{L}_{\partial_t} \langle \boldsymbol{\psi} \rangle = 0$. Note that the thickness measurement performed by the observer already has an error $\sim M^2 a^2 H^3 / 6 r^4$ since it extends the Lorentz frame beyond the local neighborhood, but if we assume that the disk is thin ($H/r \ll 1$), and we do, this error remains small. At the same time, we can take all metric components evaluated at the equator and use Equation (5) as the representative average velocity. Under these conditions, we have $\theta_{\max} - \theta_{\min} \approx 2H/r$, and the term $\sqrt{-g/g_{rr}}$ in Equation (7) cancels out. It becomes clear that an extra θ integral is what separates the radial and polar variables. In other words, the r-component variables are the vertically integrated fields

$$\boldsymbol{\psi}(r, \theta) \mapsto \boldsymbol{\psi}(r) = \int_{\theta_{\min}}^{\theta_{\max}} \boldsymbol{\psi}(r, \theta) \sqrt{g_{\theta\theta}} d\theta. \tag{8}$$

The vertical equations of motion can be obtained by setting up Newtonian (with relativistic corrections) equations for the field $\boldsymbol{\psi}(r, \theta)$ at each value of r (see, e.g., [99,127,130,131]).

2.2. Conservation Laws

The equations of evolution of the fluid are contained in the conservation laws $\nabla_\mu T^{\mu\nu} = 0$ and $\nabla_\mu(\rho u^\mu) = 0$. The most general stress–energy tensor for a Navier–Stokes viscous fluid with heat transfer is [132,133]

$$T = \overbrace{(\rho + U + P)\boldsymbol{u} \otimes \boldsymbol{u} + P\boldsymbol{g}}^{\text{Ideal Fluid}} + \overbrace{(-2\eta\sigma - \zeta(\boldsymbol{\nabla} \cdot \boldsymbol{u})\boldsymbol{P})}^{\text{Viscous Stress}} + \overbrace{\boldsymbol{q} \otimes \boldsymbol{u} + \boldsymbol{u} \otimes \boldsymbol{q}}^{\text{Heat flux}}, \qquad (9)$$

where ρ, P, U, ζ, η, $\boldsymbol{q}$, $\boldsymbol{P}$ and σ are the rest-mass energy density, pressure, internal energy density, dynamic viscosity, bulk viscosity, heat-flux 4-vector, projection tensor and shear tensor, respectively, and thermodynamic quantities are measured on the LRF. We do not consider electromagnetic contributions and ignore the causality problems associated with the equations derived from this stress–energy tensor, since we are not interested in phenomena close to the horizon [124]. Before deriving the equations of motion and to add a simple model of neutrino oscillations to the dynamics of disk accretion, we must make some extra assumptions. We will assume that the θ integral in Equation (8) can be approximated by

$$\int_{\theta_{\min}}^{\theta_{\max}} \boldsymbol{\psi}\sqrt{g_{\theta\theta}}d\theta \approx \boldsymbol{\psi}r(\theta_{\max} - \theta_{\min}) \approx 2H\boldsymbol{\psi}, \qquad (10)$$

for any field $\boldsymbol{\psi}$. Additionally, we use Stokes' hypothesis ($\zeta = 0$). Since we are treating the disk as a thin fluid in differential rotation, we will assume that, on average, the only non-zero component of the shearing stress on the CRF is $\sigma_{\tilde{r}\tilde{\phi}}$ (there are torques only on the ϕ direction), and $q_{\tilde{\theta}}$ is the only non-zero component of the energy flux (on average the flux is vertical). By $u^\mu \sigma_{\mu\nu} = 0$ and Equation (A7) we have

$$\sigma_{r\phi} = \frac{\gamma_{\tilde{\phi}}^3}{2} \frac{g_{\phi\phi}}{\sqrt{\omega^2 g_{\phi\phi} - g_{tt}}} \partial_r\Omega, \quad \sigma_{rt} = -\Omega\sigma_{r\phi}. \qquad (11)$$

Finally, the turbulent viscosity is estimated to be $\sim l\Delta u$ where l is the size of the turbulent eddies and Δu is the average velocity difference between points in the disk separated by a distance l. By the same arguments in (§33, [129]) and in Section 2.2, l can be at most equal to $2H$ and Δu can be at most equal to the isothermal sound speed $c_s = \sqrt{\partial P/\partial\rho}$ or else the flow would develop shocks [89]. The particular form of c_s can be calculated from Equation (15). This way we get

$$\eta = \Pi\nu_{\text{turb}} = 2\alpha\Pi H c_s, \qquad (12)$$

with $\alpha \leq 1$ and $\Pi = \rho + U + P$. In a nutshell, this is the popular α-prescription put forward by [80]. As we mentioned at the end of Section 2.1, on the CRF for a fixed value of r, the polar equation takes the form of Euler's equation for a fluid at rest where the acceleration is given by the tidal gravitational acceleration. Namely, the θ component of the fluid's path-lines relative acceleration in the θ direction is

$$\frac{1}{r}\partial_\theta P \approx \rho r \cos\theta \left[\boldsymbol{R}(\boldsymbol{u}, \partial_{\tilde{\theta}}, \boldsymbol{u}) \cdot \partial_{\tilde{\theta}}\right]_{\theta=\pi/2}, \qquad (13)$$

with $\boldsymbol{R}$ being the Riemann curvature tensor. With $u^{\tilde{\mu}} \approx (1,0,0,0)$, Equations (10) and (A8) and assuming that there is no significant compression of the fluid under the action of the tidal force, integration of this equation yields the relation up to second order in $\pi/2 - \theta$:

$$P = \frac{1}{2}\rho R^{\tilde{\theta}}{}_{\tilde{t}\tilde{\theta}\tilde{t}}\Big|_{\theta=\pi/2}\left(H^2 - r^2\left(\frac{\pi}{2} - \theta\right)^2\right), \qquad (14)$$

where we used the condition $P = 0$ at the disk's surface. Hence, the average pressure inside the disk is (cf. [99,107,131])

$$P = \frac{1}{3}\rho H^2 R^{\tilde{\theta}}{}_{\tilde{t}\tilde{\theta}\tilde{t}}\Big|_{\theta=\pi/2}. \tag{15}$$

The equation of mass conservation is obtained by directly inserting into Equation (A13) the averaged density and integrating vertically to obtain

$$2Hr\rho u^r = \text{constant} = -\frac{\dot{M}}{2\pi}, \tag{16}$$

where the term $2Hr\rho u^r$ is identified as the average inward mass flux through a cylindrical surface of radius r per unit of azimuthal angle, and thus must be equal to the accretion rate divided by 2π. The same process applied to Equation (A12) yields the energy conservation equation:

$$u^r\left[\partial_r(HU) - \frac{U+P}{\rho}\partial_r(H\rho)\right] = 2\eta H\sigma^{r\phi}\sigma_{r\phi} - H\epsilon, \tag{17}$$

where factors proportional to H/r are ignored and we assume $\Pi \approx \rho$ to integrate the second term on the left-hand side. ϵ is the average energy density measured on the LRF (see the discussion around Equation (A16)). The first term on the right-hand side is the viscous heating rate F_{heat} and the second term is the cooling rate F_{cool}. The last constitutive equation is obtained by applying the zero torque at the last stable orbit condition. These relations are calculated in Appendix A. We just replace the density in Equation (16) using Equation (A21), obtaining

$$u^r = -\frac{4\alpha H c_s \sigma^r_\phi}{M f(x, x^*)}. \tag{18}$$

2.3. Equations of State

We consider that the main contribution to the rest-mass energy density of the disk is made up of neutrons, protons and ions. This way $\rho = \rho_B = n_B m_B$ with baryon number density n_B and baryon mass m_B equal to the atomic unit mass. The disk's baryonic mass obeys Maxwell–Boltzmann statistics, and its precise composition is determined by the nuclear statistical equilibrium (NSE). We denote the mass fraction of an ion i by $X_i = \rho_i/\rho_B$ (if $i = p$ or n then we are referring to proton or neutrons) and it can be calculated by the Saha equation [134,135]

$$X_i = \frac{A_i m_B}{\rho} G_i \left(\frac{TA_i m_B}{2\pi}\right)^{3/2} \exp\left(\frac{Z_i\left(\mu_p + \mu_p^C\right) + N_i\mu_n - \mu_i^C + B_i}{T}\right), \tag{19}$$

with the constraints:

$$\sum_i X_i = 1, \quad \sum_i Z_i Y_i = Y_e. \tag{20}$$

In these equations, T, A_i, N_i, Z_i, Y_e, Y_i, G_i, μ_i and B_i are the temperature, atomic number, neutron number, proton number, electron fraction (electron abundance per baryon), ion abundance per baryon, nuclear partition function, chemical potential (including the nuclear rest-mass energy) and ion binding energy. The μ_i^C are the Coulomb corrections for the NSE state in a dense plasma (see Appendix C). The binding energy data for a large collection of nuclei can be found in [136] and the temperature-dependent partition functions are found in [137,138]. Even though we take into account Coulomb corrections in NSE, we assume that the baryonic mass can be described by an ideal gas[1,2] and

$$P_B = \sum_i P_i = n_B T \sum_i \frac{X_i}{A_i}, \quad U_B = \frac{3}{2}P_B. \tag{21}$$

---

[1] Since bulk viscosity effects appear as a consequence of correlations between ion velocities due to Coulomb interactions and of large relaxation times to reach local equilibrium, the NSE and ideal gas assumptions imply that imposing Stokes' hypothesis becomes de rigueur [133,139,140]

[2] We will consider accretion rates of up to $1M_\odot \text{ s}^{-1}$. These disks reach densities of 10^{13} g cm^{-3}. Baryons can be lightly degenerate at these densities but we will still assume that the baryonic mass can be described by an ideal gas.

The disk also contains photons, electrons, positrons, neutrinos and antineutrinos. As is usual in neutrino oscillations analysis, we distinguish only between electron (anti)neutrinos $\nu_e, (\bar{\nu}_e)$ and x (anti)neutrinos $\nu_x(\bar{\nu}_x)$, where $x = \mu + \tau$ is the superposition of muon neutrinos and tau neutrinos. Photons obey the usual relations

$$P_\gamma = \frac{\pi^2 T^4}{45}, \quad U_\gamma = 3P_\gamma, \tag{22}$$

while, for electrons and positrons we have

$$n_{e^\pm} = \frac{\sqrt{2}}{\pi^2} \xi^{3/2} [\mathcal{F}_{1/2,0}(\xi, \eta_{e^\pm}) + \xi \mathcal{F}_{3/2,0}(\xi, \eta_{e^\pm})], \tag{23a}$$

$$U_{e^\pm} = \frac{\sqrt{2}}{\pi^2} \xi^{5/2} [\mathcal{F}_{3/2,0}(\xi, \eta_{e^\pm}) + \xi \mathcal{F}_{5/2,0}(\xi, \eta_{e^\pm})], \tag{23b}$$

$$P_{e^\pm} = \frac{2\sqrt{2}}{3\pi^2} \xi^{5/2} \left[\mathcal{F}_{3/2,0}(\xi, \eta_{e^\pm}) + \frac{\xi}{2} \mathcal{F}_{5/2,0}(\xi, \eta_{e^\pm}) \right], \tag{23c}$$

with $\xi = T/m_e$ and written in terms of the generalized Fermi functions

$$\mathcal{F}_{k,\ell}(y, \eta) = \int_\ell^\infty \frac{x^k \sqrt{1 + xy/2}}{\exp(x - \eta) + 1} dx. \tag{24}$$

In these equations $\eta_{e^\pm} = (\mu_{e^\pm} - m_e)/T$ is the electron (positron) degeneracy parameter without rest-mass contributions (not to be confused with η in Section 2.2). Since electrons and positrons are in equilibrium with photons due to the pair creation and annihilation processes $(e^- + e^+ \to 2\gamma)$, we know that their chemical potentials are related by $\mu_{e^+} = -\mu_{e^-}$, which implies $\eta_{e^+} = -\eta_{e^-} - 2/\xi$ from the charge neutrality condition, and we obtain

$$n_B Y_e = n_{e^-} - n_{e^+}. \tag{25}$$

For neutrinos, the story is more complicated. In the absence of oscillations and if the disk is hot and dense enough for neutrinos to be trapped within it and in thermal equilibrium, n_ν, U_ν, P_ν can be calculated with Fermi–Dirac statistics using the same temperature T

$$n_{\nu(\bar{\nu})}^{\text{trapped}} = \frac{T^3}{\pi^2} \mathcal{F}_{2,0}\left(\eta_{\nu(\bar{\nu})}\right), \tag{26a}$$

$$U_{\nu(\bar{\nu})}^{\text{trapped}} = \frac{T^4}{\pi^2} \mathcal{F}_{3,0}\left(\eta_{\nu(\bar{\nu})}\right), \tag{26b}$$

$$P_{\nu(\bar{\nu})}^{\text{trapped}} = \frac{U_{\nu(\bar{\nu})}^{\text{trapped}}}{3}, \tag{26c}$$

where it is understood that $\mathcal{F}(\eta) = \mathcal{F}(y = 0, \eta)$ with $\eta_{\nu(\bar{\nu})} = \mu_{\nu(\bar{\nu})}/T$ and the ultra-relativistic approximation $m_\nu \ll 1$ for any neutrino flavor is used. If thermal equilibrium is has not been achieved, Equation (26) cannot be used. Nevertheless, at any point in the disk and for given values of T and ρ, (anti)neutrinos are being created through several processes. The processes we take into account are pair annihilation $e^- + e^+ \to \nu + \bar{\nu}$, electron or positron capture by nucleons $p + e^- \to n + \nu_e$ or $n + e^+ \to p + \bar{\nu}_e$, electron capture by ions $A + e^- \to A' + \nu_e$, plasmon decay $\tilde{\gamma} \to \nu + \bar{\nu}$ and nucleon-nucleon bremsstrahlung $n_1 + n_2 \to n_3 + n_4 + \nu + \bar{\nu}$. The emission rates can be found in Appendix D. The chemical equilibria for these processes determine the values of $\eta_{\nu(\bar{\nu})}$. In particular,

$$\eta_{\nu_e} = \eta_{e^-} + \ln\left(\frac{X_p}{X_n}\right) + \frac{1 - \mathbb{Q}}{\varsigma}, \tag{27a}$$

$$\eta_{\bar{\nu}_e} = -\eta_{\nu_e}, \tag{27b}$$

$$\eta_{\nu_x} = \eta_{\bar{\nu}_x} = 0, \tag{27c}$$

satisfy all equations. Here, $\mathbb{Q} = (m_n - m_p)/m_e \approx 2.531$. Once the (anti)neutrino number and energy emission rates (R_i, Q_i) are calculated for each process i, the (anti)neutrino thermodynamic quantities are given by

$$n_{\nu(\bar{\nu})}^{\text{free}} = H \sum_i R_{i,\nu(\bar{\nu})}, \tag{28a}$$

$$U_{\nu(\bar{\nu})}^{\text{free}} = H \sum_i Q_{i,\nu(\bar{\nu})}, \tag{28b}$$

$$P_{\nu(\bar{\nu})}^{\text{free}} = \frac{U_{\nu(\bar{\nu})}^{\text{free}}}{3}. \tag{28c}$$

Remember we are using Planck units, so in these expressions there should be an H/c instead of just an H. The transition for each (anti)neutrino flavor between both regimes occurs when Equations (26b) and (28b) are equal, and it can be simulated by defining the parameter

$$w_{\nu(\bar{\nu})} = \frac{U_{\nu(\bar{\nu})}^{\text{free}}}{U_{\nu(\bar{\nu})}^{\text{free}} + U_{\nu(\bar{\nu})}^{\text{trapped}}}. \tag{29}$$

With this equation, the (anti)neutrino average energy can be defined as

$$\langle E_{\nu(\bar{\nu})} \rangle = \left(1 - w_{\nu(\bar{\nu})}\right) \frac{U_{\nu(\bar{\nu})}^{\text{free}}}{n_{\nu(\bar{\nu})}^{\text{free}}} + w_{\nu(\bar{\nu})} \frac{U_{\nu(\bar{\nu})}^{\text{trapped}}}{n_{\nu(\bar{\nu})}^{\text{trapped}}}. \tag{30}$$

and the approximated number and energy density are

$$n_{\nu(\bar{\nu})} = \begin{cases} n_{\nu(\bar{\nu})}^{\text{free}}, & \text{if } w_{\nu(\bar{\nu})} < 1/2. \\ n_{\nu(\bar{\nu})}^{\text{trapped}}, & \text{if } w_{\nu(\bar{\nu})} \geq 1/2. \end{cases} \tag{31a}$$

$$U_{\nu(\bar{\nu})} = \begin{cases} U_{\nu(\bar{\nu})}^{\text{free}}, & \text{if } w_{\nu(\bar{\nu})} < 1/2. \\ U_{\nu(\bar{\nu})}^{\text{trapped}}, & \text{if } w_{\nu(\bar{\nu})} \geq 1/2. \end{cases} \tag{31b}$$

$$P_{\nu(\bar{\nu})} = \frac{U_{\nu(\bar{\nu})}}{3}. \tag{31c}$$

Note that both Equations (28c) and (31c) are approximations since they are derived from equilibrium distributions, but they help make the transition smooth. Besides, the neutrino pressure before thermal equilibrium is negligible. This method was presented in [107] where it was used only for electron (anti)neutrinos. The total (anti)neutrino number and energy flux through one the disk's faces can be approximated by

$$\dot{n}_{\nu_j(\bar{\nu}_j)} = \sum_{j \in \{e,x\}} \frac{n_{\nu_j(\bar{\nu}_j)}}{1 + \tau_{\nu_j(\bar{\nu}_j)}}, \tag{32a}$$

$$F_{\nu_j(\bar{\nu}_j)} = \sum_{j \in \{e,x\}} \frac{U_{\nu_j(\bar{\nu}_j)}}{1 + \tau_{\nu_j(\bar{\nu}_j)}}, \tag{32b}$$

where τ_{ν_i} is the total optical depth for the (anti)neutrino $\nu_i(\bar{\nu}_i)$. By collecting all the expressions, we write the total internal energy and total pressure as

$$U = \sum_{j \in \{e,x\}} \left(U_{\nu_j} + U_{\bar{\nu}_j} \right) + U_B + U_{e^-} + U_{e^+} + U_\gamma \ , \tag{33a}$$

$$P = \sum_{j \in \{e,x\}} \left(P_{\nu_j} + P_{\bar{\nu}_j} \right) + P_B + P_{e^-} + P_{e^+} + P_\gamma \ . \tag{33b}$$

The (anti)neutrino energy flux through the disk faces contributes to the cooling term in the energy conservation equation, but it is not the only one. Another important energy sink is photodisintegration of ions. To calculate it we proceed as follows. The energy spent to knocking off a nucleon of an ion i is equal to the binding energy per nucleon B_i/A_i. Now, consider a fluid element of volume V whose moving walls are attached to the fluid so that no baryons flow in or out. The total energy of photodisintegration contained within this volume is the sum over i of (energy per nucleon of ion i)$\times$(# of freed nucleons of ion i inside V). This can be written as $\sum_i (B_i/A_i) n_{f,i} V$, or, alternatively, $n_B V \sum_i (B_i/A_i) X_{f,i}$. If we approximate B_i/A_i by the average binding energy per nucleon $\bar{B}$ (which is a good approximation save for a couple of light ions) the expression becomes $n_B V \bar{B} \sum_i X_{f,i} = n_B V \bar{B} X_f = n_B V \bar{B} (X_p + X_n)$. We place the value of $\bar{B}$ in Section 4.

The rate of change of this energy on the LRF, denoting the proper time by λ, is

$$\frac{d}{d\lambda} \left[n_B V \bar{B} (X_p + X_n) \right] = n_B V \bar{B} \frac{d}{d\lambda} (X_p + X_n). \tag{34}$$

The derivative of $n_B V$ vanishes by baryon conservation. Transforming back to CF and taking the average we find the energy density per unit time used in disintegration of ions

$$\epsilon_{\text{ions}} = n_B \bar{B} u^r H \partial_r (X_p + X_n). \tag{35}$$

The average energy density measured on the LRF ϵ appearing in Equation (17) is

$$\epsilon = \epsilon_{\text{ions}} + \frac{1}{H} \sum_{i \in \{e,x\}} (F_{\nu_i} + F_{\bar{\nu}_i}). \tag{36}$$

Finally, a similar argument allows us to obtain the equation of lepton number conservation. For any lepton ℓ, the total lepton number density is $\sum_{\ell \in \{e,\mu,\tau\}} (n_\ell - n_{\bar{\ell}} + n_{\nu_\ell} - n_{\bar{\nu}_\ell})$. Thus, with Equation (25), calculating the rate of change as before, using Gauss's theorem and taking the average, we get

$$u^r H \left[n_B \partial_r Y_e + \partial_r \sum_{\ell \in \{e,x\}} (n_{\nu_\ell} - n_{\bar{\nu}_\ell}) \right] = \sum_{\ell \in \{e,x\}} (\dot{n}_{\bar{\nu}_\ell} - \dot{n}_{\nu_\ell}), \tag{37}$$

where the right-hand side represents the flux of lepton number through the disk's surface.

3. Neutrino Oscillations

To study the flavor evolution of neutrinos within a particular system, a Hamiltonian governing neutrino oscillation must be set up. The relative strengths of the potentials appearing in such a Hamiltonian depend on four elements: geometry, mass content, neutrino content and neutrino mass hierarchy. Geometry refers to the nature of net neutrino fluxes and possible gravitational effects. Mass and neutrino contents refer to respective distributions of leptons of each flavor (e, μ, τ) present in the medium. Finally, mass hierarchy refers to the relative values of the masses m_1, m_2, m_3 for each neutrino mass eigenstates (see Table 2). We dedicate this section to a detailed derivation of the equations of flavor evolution for a neutrino dominated accretion disk. To maintain consistency with the traditional literature of neutrino oscillations, we will reuse some symbols appearing in

previous sections. To avoid confusion, we point out that the symbols in this section are independent of the previous sections unless we explicitly draw a comparison.

Table 2. Mixing and squared mass differences as they appear in [141]. Error values in parentheses are shown in 3σ interval. The squared mass difference is defined as $\Delta m^2 = m_3^2 - \left(m_2^2 + m_1^2\right)/2$ and its sign depends on the hierarchy $m_1 < m_2 < m_3$ or $m_3 < m_1 < m_2$.

$\Delta m_{21}^2 = 7.37\,(6.93 - 7.96) \times 10^{-5}\ \text{eV}^2$
$|\Delta m^2| = 2.56\,(2.45 - 2.69) \times 10^{-3}\ \text{eV}^2$ Normal Hierarchy
$|\Delta m^2| = 2.54\,(2.42 - 2.66) \times 10^{-3}\ \text{eV}^2$ Inverted Hierarchy
$\sin^2\theta_{12} = 0.297\,(0.250 - 0.354)$
$\sin^2\theta_{23}(\Delta m^2 > 0) = 0.425\,(0.381 - 0.615)$
$\sin^2\theta_{23}(\Delta m^2 < 0) = 0.589\,(0.383 - 0.637)$
$\sin^2\theta_{13}(\Delta m^2 > 0) = 0.0215\,(0.0190 - 0.0240)$
$\sin^2\theta_{13}(\Delta m^2 < 0) = 0.0216\,(0.0190 - 0.0242)$

3.1. Equations of Oscillation

The equations that govern the evolution of an ensemble of mixed neutrinos are the Boltzmann collision equations

$$i\dot{\rho}_{\mathbf{p},t} = C\left(\rho_{\mathbf{p},t}\right), \tag{38a}$$
$$i\dot{\bar{\rho}}_{\mathbf{p},t} = C\left(\bar{\rho}_{\mathbf{p},t}\right). \tag{38b}$$

The collision terms should include the vacuum oscillation plus all possible scattering interactions that neutrinos undergo through their propagation. For free streaming neutrinos, only the vacuum term and the forward-scattering interactions are taken into account so that the equations become

$$i\dot{\rho}_{\mathbf{p},t} = \left[\mathsf{H}_{\mathbf{p},t}, \rho_{\mathbf{p},t}\right], \tag{39a}$$
$$i\dot{\bar{\rho}}_{\mathbf{p},t} = \left[\bar{\mathsf{H}}_{\mathbf{p},t}, \bar{\rho}_{\mathbf{p},t}\right]. \tag{39b}$$

Here, $\mathsf{H}_{\mathbf{p},t}$ ($\bar{\mathsf{H}}_{\mathbf{p},t}$) is the oscillation Hamiltonian for (anti)neutrinos and $\rho_{\mathbf{p},t}$ ($\bar{\rho}_{\mathbf{p},t}$) is the matrix of occupation numbers: $(\rho_{\mathbf{p},t})_{ij} = \langle a_j^\dagger a_i \rangle_{\mathbf{p},t}$ for neutrinos and $((\bar{\rho}_{\mathbf{p},t})_{ij} = \langle \bar{a}_i^\dagger \bar{a}_j \rangle_{\mathbf{p},t}$ for antineutrinos), for each momentum $\mathbf{p}$ and flavors i, j. The diagonal elements are the distribution functions $f_{\nu_i(\bar{\nu}_i)}(\mathbf{p})$ such that their integration over the momentum space gives the neutrino number density n_{ν_i} of a determined flavor i at time t. The off-diagonal elements provide information about the overlapping between the two neutrino flavors. Taking into account the current–current nature of the weak interaction in the standard model, the Hamiltonian for each equation is [142–144]

$$\mathsf{H}_{\mathbf{p},t} = \Omega_{\mathbf{p},t} + \sqrt{2}G_F \int \left(l_{\mathbf{q},t} - \bar{l}_{\mathbf{q},t}\right)\left(1 - \mathbf{v}_{\mathbf{q},t} \cdot \mathbf{v}_{\mathbf{p},t}\right)\frac{d^3\mathbf{q}}{(2\pi)^3} + \sqrt{2}G_F \int \left(\rho_{\mathbf{q},t} - \bar{\rho}_{\mathbf{q},t}\right)\left(1 - \mathbf{v}_{\mathbf{q},t} \cdot \mathbf{v}_{\mathbf{p},t}\right)\frac{d^3\mathbf{q}}{(2\pi)^3}, \tag{40a}$$

$$\bar{\mathsf{H}}_{\mathbf{p},t} = -\Omega_{\mathbf{p},t} + \sqrt{2}G_F \int \left(l_{\mathbf{q},t} - \bar{l}_{\mathbf{q},t}\right)\left(1 - \mathbf{v}_{\mathbf{q},t} \cdot \mathbf{v}_{\mathbf{p},t}\right)\frac{d^3\mathbf{q}}{(2\pi)^3} + \sqrt{2}G_F \int \left(\rho_{\mathbf{q},t} - \bar{\rho}_{\mathbf{q},t}\right)\left(1 - \mathbf{v}_{\mathbf{q},t} \cdot \mathbf{v}_{\mathbf{p},t}\right)\frac{d^3\mathbf{q}}{(2\pi)^3}. \tag{40b}$$

where G_F is the Fermi coupling constant, $\Omega_{\mathbf{p},t}$ is the matrix of vacuum oscillation frequencies, $l_{\mathbf{p},t}$ and $\bar{l}_{\mathbf{p},t}$ are matrices of occupation numbers for charged leptons built in a similar way to the neutrino matrices, and $\mathbf{v}_{\mathbf{p},t} = \mathbf{p}/p$ is the velocity of a particle with momentum $\mathbf{p}$ (either neutrino or charged lepton). As stated before, we will only consider two neutrino flavors: e and $x = \mu + \tau$. Three-flavor oscillations can be approximated by two-flavor oscillations as a result of the strong hierarchy of the squared mass differences $|\Delta m_{13}^2| \approx |\Delta m_{23}^2| \gg |\Delta m_{12}^2|$. In this case, only the smallest mixing angle θ_{13} is considered. We will drop the suffix for the rest of the discussion. Consequently, the relevant oscillations

are $\nu_e \rightleftharpoons \nu_x$ and $\bar{\nu}_e \rightleftharpoons \bar{\nu}_x$, and each term in the Hamiltonian governing oscillations becomes a 2×2 Hermitian matrix. Now, consider an observer on the LRF (which is almost identical to the CRF due to Equation (6) at a point r. In its spatial local frame, the unit vectors $\hat{x}, \hat{y}, \hat{z}$ are parallel to the unit vectors $\hat{r}, \hat{\theta}, \hat{\phi}$ of the CF, respectively. Solving Equation (39) in this coordinate system would yield matrices $\rho, \bar{\rho}$ as functions of time t. However, in our specific physical system, both the matter density and the neutrino density vary with the radial distance from the BH. This means that the equations of oscillations must be written in a way that makes explicit the spatial dependence, i.e., in terms of the coordinates x, y, z. For a collimated ray of neutrinos, the expression $dt = dr$ would be good enough, but for radiating extended sources or neutrino gases the situation is more complicated.

In Equation (39) we must replace the matrices of occupation numbers by the space-dependent Wigner functions $\rho_{\mathbf{p},\mathbf{x},t}$ (and $\bar{\rho}_{\mathbf{p},\mathbf{x},t}$) and the total time derivative by the Liouville operator [145,146]:

$$
\dot{\rho}_{\mathbf{p},\mathbf{x},t} = \overbrace{\frac{\partial \rho_{\mathbf{p},\mathbf{x},t}}{\partial t}}^{\text{Explicit Time}} + \overbrace{\mathbf{v}_\mathbf{p} \cdot \nabla_\mathbf{x} \rho_{\mathbf{p},\mathbf{x},t}}^{\text{Drift}} + \overbrace{\dot{\mathbf{p}} \cdot \nabla_\mathbf{p} \rho_{\mathbf{p},\mathbf{x},t}}^{\text{External Forces}} .
\tag{41}
$$

In this context, $\mathbf{x}$ represents a vector in the LRF. In the most general case, finding $\rho_{\mathbf{p},\mathbf{x},t}$ and $\bar{\rho}_{\mathbf{p},\mathbf{x},t}$ means solving a 7D neutrino transport problem in the variables $x, y, z, p_x, p_y, p_z, t$. Since our objective is to construct a simple model of neutrino oscillations inside the disk, to obtain the specific form of Equation (39) we must simplify the equations by imposing on it conditions that are consistent with the assumptions made in Section 2.

- Due to axial symmetry, the neutrino density is constant along the **z** direction. Moreover, since neutrinos follow null geodesics, we can set $\dot{p}_z \approx \dot{p}_\phi = 0$.
- Within the thin disk approximation (as represented by Equation (10)) the neutrino and matter densities are constant along the **y** direction and the momentum change due to curvature along this direction can be neglected, that is, $\dot{p}_y \approx 0$.
- In the LRF, the normalized radial momentum of a neutrino can be written as $p_x = \pm r / \sqrt{r^2 - 2Mr + M^2 a^2}$. Hence, the typical scale of the change of momentum with radius is $\Delta r_{p_x,\text{eff}} = |d \ln p_x / dr|^{-1} = (r/M)(r^2 - 2Mr + M^2 a^2)/(Ma^2 - r)$, which obeys $\Delta r_{p_x,\text{eff}} > r_s$ for $r > 2 r_{\text{in}}$. This means we can assume $\dot{p}_x \approx 0$ up to regions very close to the inner edge of the disk.
- We define an effective distance $\Delta r_{\rho,\text{eff}} = |d \ln (Y_e n_B) / dr|^{-1}$. For all the systems we evaluated, we found that it is comparable to the height of the disk ($\Delta r_{\rho,\text{eff}} \sim 2 - 5\, r_s$). This means that at any point of the disk we can calculate neutrino oscillations in a small regions assuming that both the electron density and neutrino densities are constant.
- We neglect energy and momentum transport between different regions of the disk by neutrinos that are recaptured by the disk due to curvature. This assumption is reasonable except for regions very close to the BH but is consistent with the thin disk model (see, e.g., [128]). We also assume initially that the neutrino content of neighboring regions of the disk (different values of r) do not affect each other. As a consequence of the results discussed above, we assume that at any point inside the disk and at any instant of time an observer can describe both the charged leptons and neutrinos as isotropic gases around small enough regions of the disk. This assumption is considerably restrictive but we will generalize it in Section 5.

The purpose of these approximations is twofold. On one hand, we can reduce the problem considerably, since they allow us to add the neutrino oscillations to a steady-state disk model by simply studying the behavior of neutrinos at each point of the disk using the constant values of density and temperature at that point. We will see in Section 5, that this assumption would correspond to a transient state of an accretion disk, since very fast neighboring regions of the disk start interacting. On the other hand, the approximations allow us to simplify the equations of oscillation considering that all but the first term in Equation (41) vanish, leaving only a time derivative. In addition, both terms of the form

$\mathbf{v_{q},t} \cdot \mathbf{v_{p},t}$ in Equation (40) average to zero so that $\rho_{\mathbf{p},\mathbf{x},t} = \rho_{p,t}$ and $\bar{\rho}_{\mathbf{p},\mathbf{x},t} = \bar{\rho}_{p,t}$. We are now in a position to derive the simplified equations of oscillation for this particular model. Let us first present the relevant equations for neutrinos. Due to the similarity between $H_{p,t}$ and $\bar{H}_{p,t}$, the corresponding equations for antineutrinos can be obtained analogously. For simplicity, we will drop the suffix t since the time dependence is now obvious. In the two-flavor approximation, ρ_p is a 2×2 Hermitian matrix and can be expanded in terms of the Pauli matrices σ_i and a polarization vector $\mathsf{P}_p = (\mathsf{P}^x, \mathsf{P}^y, \mathsf{P}^z)$ in the neutrino flavor space, such that

$$\rho_p = \begin{pmatrix} \rho_{ee} & \rho_{ex} \\ \rho_{xe} & \rho_{xx} \end{pmatrix} = \frac{1}{2} (f_p \mathbf{1} + \mathsf{P}_p \cdot \vec{\sigma}), \tag{42}$$

where $f_p = \mathrm{Tr}[\rho_p] = f_{\nu_e}(p) + f_{\nu_x}(p)$ is the sum of the distribution functions for ν_e and ν_x. Note that the z component of the polarization vector obeys

$$\mathsf{P}_p^z = f_{\nu_e}(p) - f_{\nu_x}(p). \tag{43}$$

Hence, this component tracks the fractional flavor composition of the system. Appropriately normalizing ρ_p allows one to define a survival and mixing probability

$$P_{p,\nu_e \to \nu_e} = \frac{1}{2}\left(1 + \mathsf{P}_p^z\right), \tag{44a}$$

$$P_{p,\nu_e \to \nu_x} = \frac{1}{2}\left(1 - \mathsf{P}_p^z\right). \tag{44b}$$

The Hamiltonian can be written as a sum of three interaction terms:

$$\mathsf{H} = \mathsf{H}_{\text{vacuum}} + \mathsf{H}_{\text{matter}} + \mathsf{H}_{\nu\nu}. \tag{45}$$

The first term is the Hamiltonian in vacuum [27]:

$$\mathsf{H}_{\text{vacuum}} = \frac{\omega_p}{2} \begin{pmatrix} -\cos 2\theta & \sin 2\theta \\ \sin 2\theta & \cos 2\theta \end{pmatrix} = \frac{\omega_p}{2} \mathbf{B} \cdot \vec{\sigma}, \tag{46}$$

where $\omega_p = \Delta m^2/2p$, $\mathbf{B} = (\sin 2\theta, 0, -\cos 2\theta)$ and θ is the smallest neutrino mixing angle in vacuum. The other two terms in Equation (40) are special since they make the evolution equations non-linear. Since we are considering that the electrons inside the form an isotropic gas, the vector $\mathbf{v_q}$ in the first integral is distributed uniformly on the unit sphere and the factor $\mathbf{v_q} \cdot \mathbf{v}_p$ averages to zero. After integrating the matter Hamiltonian is given by

$$\mathsf{H}_{\text{matter}} = \frac{\lambda}{2} \begin{pmatrix} 1 & 0 \\ 0 & -1 \end{pmatrix} = \frac{\lambda}{2} \mathbf{L} \cdot \vec{\sigma}, \tag{47}$$

where $\lambda = \sqrt{2}G_F(n_{e^-} - n_{e^+})$ is the charged current matter potential and $\mathbf{L} = (0,0,1)$. Similarly, the same product disappears in the last term and after integrating we get

$$\mathsf{H}_{\nu\nu} = \sqrt{2}G_F[\mathsf{P} - \bar{\mathsf{P}}] \cdot \vec{\sigma}. \tag{48}$$

Clearly, $\mathsf{P} = \int \mathsf{P}_p \, d\mathbf{p}/(2\pi)^3$. Introducing every Hamiltonian term in Equation (39), and using the commutation relations of the Pauli matrices, we find the equations of oscillation for neutrinos and antineutrinos for each momentum mode p:

$$\dot{\mathsf{P}}_p = \left[\omega_p \mathbf{B} + \lambda \mathbf{L} + \sqrt{2}G_F(\mathsf{P} - \bar{\mathsf{P}})\right] \times \mathsf{P}_p, \tag{49a}$$

$$\dot{\bar{\mathsf{P}}}_p = \left[-\omega_p \mathbf{B} + \lambda \mathbf{L} + \sqrt{2}G_F(\mathsf{P} - \bar{\mathsf{P}})\right] \times \bar{\mathsf{P}}_p, \tag{49b}$$

where we have assumed that the total neutrino distribution remains constant, $\dot{f}_p = 0$. This shows how the polarization vectors can be normalized. By performing the transformations $\mathsf{P}_p / f_p \mapsto \mathsf{P}_p$ and $\bar{\mathsf{P}}_p / \bar{f}_p \mapsto \bar{\mathsf{P}}_p$, and multiplying and dividing the last term by the total neutrino density Equation (49), we get

$$\dot{\mathsf{P}}_p = \left[\omega_p \mathbf{B} + \lambda \mathbf{L} + \mu \mathbf{D} \right] \times \mathsf{P}_p, \tag{50a}$$

$$\dot{\bar{\mathsf{P}}}_p = \left[-\omega_p \mathbf{B} + \lambda \mathbf{L} + \mu \mathbf{D} \right] \times \bar{\mathsf{P}}_p, \tag{50b}$$

$$\mathbf{D} = \frac{1}{n_{\nu_e} + n_{\nu_x}} \int \left(f_q \mathsf{P}_q - \bar{f}_q \bar{\mathsf{P}}_q \right) \frac{d\mathbf{q}}{(2\pi)^3}. \tag{50c}$$

These are the traditional forms of the equations in terms of the vacuum, matter and self-interaction potentials ω_p, λ and μ with

$$\mu = \sqrt{2} G_F \sum_{i \in \{e, x\}} n_{\nu_i}. \tag{51}$$

Different normalization schemes are possible (see, e.g., [36,49,144,147]). Assuming that we can solve the equations of oscillation with constant potentials λ and μ simplifies the problem even further. Following [29], with the vector transformation (a rotation around the z axis of flavor space)

$$R_z = \begin{pmatrix} \cos(\lambda t) & \sin(\lambda t) & 0 \\ -\sin(\lambda t) & \cos(\lambda t) & 0 \\ 0 & 0 & 1 \end{pmatrix}, \tag{52}$$

Equation (50) becomes

$$\dot{\mathsf{P}}_p = \left[\omega_p \mathbf{B} + \mu \mathbf{D} \right] \times \mathsf{P}_p, \tag{53a}$$

$$\dot{\bar{\mathsf{P}}}_p = \left[-\omega_p \mathbf{B} + \mu \mathbf{D} \right] \times \bar{\mathsf{P}}_p, \tag{53b}$$

eliminating the λ potential, but making **B** time dependent. By defining the vector $\mathbf{S}_p = \mathsf{P}_p + \bar{\mathsf{P}}_p$, and adding and subtracting Equations (53a) and (53b) we get

$$\dot{\mathbf{S}}_p = \omega_p \mathbf{B} \times \mathbf{D}_p + \mu \mathbf{D} \times \mathbf{S}_p \approx \mu \mathbf{D} \times \mathbf{S}_p, \tag{54a}$$

$$\dot{\mathbf{D}}_p = \omega_p \mathbf{B} \times \mathbf{S}_p + \mu \mathbf{D} \times \mathbf{D}_p \approx \mu \mathbf{D} \times \mathbf{D}_p. \tag{54b}$$

The last approximation is true if we assume that the self-interaction potential is larger than the vacuum potential $\omega_p / \mu \ll 1$. We will show in Section 5 that this is the case for thin disks. The first equation implies that all the vectors $\mathbf{S}_p$ and their integral **S** evolve in the same way, suggesting the relation $\mathbf{S}_p = (f_p + \bar{f}_p) \mathbf{S}$. By replacing in Equation (54b) and integrating

$$\dot{\mathbf{S}} = \mu \mathbf{D} \times \mathbf{S}, \tag{55a}$$

$$\dot{\mathbf{D}} = \langle \omega \rangle \mathbf{B} \times \mathbf{S}. \tag{55b}$$

where $\langle \omega \rangle = \int \omega_p (f_p + \bar{f}_p) d\mathbf{p} / (2\pi)^3$ is the average vacuum oscillation potential. The fact that in our model the equations of oscillations can be written in this way has an important consequence. Usually, as it is done in supernovae neutrino oscillations, to solve Equation (50) we would need the neutrino distributions throughout the disk. If neutrinos are trapped, their distribution is given by Equation (26). If neutrinos are free, their temperature is not the same as the disk's temperature. Nonetheless, we can approximate the neutrino distribution in this regime by a Fermi–Dirac distribution with the same chemical potential as defined by Equation (27) but with an effective temperature T_ν^{eff}. This tempera-

ture can be obtained by solving the equation $\langle E_\nu \rangle = U\left(T_\nu^{\text{eff}}, \eta_\nu\right) / n\left(T_\nu^{\text{eff}}, \eta_\nu\right)$ which gives

$$T_{\nu_x, \bar{\nu}_x}^{\text{eff}} = \langle E_{\nu_x, \bar{\nu}_x} \rangle \frac{180\, \zeta(3)}{7\pi^4}, \tag{56a}$$

$$T_{\nu_e, \bar{\nu}_e}^{\text{eff}} = \frac{\langle E_{\nu_e, \bar{\nu}_e} \rangle}{3} \frac{\text{Li}_3(-\exp(\eta_{\nu_e, \bar{\nu}_e}))}{\text{Li}_4(-\exp(\eta_{\nu_e, \bar{\nu}_e}))}, \tag{56b}$$

where $\zeta(3)$ is Apéry's constant (ζ is the Riemann zeta function) and $\text{Li}_s(z)$ is Jonquière's function. For convenience and considering the range of values that the degeneracy parameter reaches (see Section 6), we approximate the effective temperature of electron neutrinos and antineutrinos with the expressions

$$T_{\nu_e}^{\text{eff}} = \frac{\langle E_{\nu_e} \rangle}{3} \left(a \eta_{\nu_e}^2 + b \eta_{\nu_e} + c \right), \tag{57a}$$

$$T_{\bar{\nu}_e}^{\text{eff}} = \frac{\langle E_{\bar{\nu}_e} \rangle}{3}. \tag{57b}$$

with constants $a = 0.0024$, $b = -0.085$, $c = 0.97$. However, Equation (55) allows us to consider just one momentum mode, and the rest of the spectrum behaves in the same way.

4. Initial Conditions and Integration

In the absence of oscillations, we can use Equations (15), (17) and (37) to solve for the set of functions $\eta_{e^-}(r)$, $\xi(r)$ and $Y_e(r)$ using as input parameters the accretion rate $\dot{M}$, the dimensionless spin parameter a, the viscosity parameter α and the BH mass M. From [99,107] we learn that neutrino dominated disks require accretion between $0.01\ M_\odot\ \text{s}^{-1}$ and $1\ M_\odot\ \text{s}^{-1}$ (this accretion rate range varies depending on the value of α). For accretion rates smaller than the lower value, the neutrino cooling is not efficient, and for rates larger than the upper value, the neutrinos are trapped within the flow. We also limit ourselves to the above accretion rate range, since it is consistent with the one expected to occur in a BdHN (see, e.g., [57,63,70]). We also know that s high spin parameter, high accretion rate, high BH mass and low viscosity parameter produce disks with higher density and higher temperature. This can be explained using the fact that several variables of the disk, such as pressure, density and height, are proportional to a positive power of M and a positive power of the quotient $\dot{M}/\alpha$. To avoid this semi-degeneracy in the system, we reduce the parameter space, and considering that we want to focus on the study of the oscillation dynamics inside the disk, we fix the BH mass at $M = 3 M_\odot$, the viscosity parameter at $\alpha = 0.01$ and the spin parameter at $a = 0.95$ while changing the accretion rate. These values also allow us to compare our results with earlier disk models. Equations (17) and (37) are first-order ordinary differential equations, and since we perform the integration from an external (far away) radius r_{out} up to the innermost stable circular orbit r_{in}, we must provide two boundary conditions at r_{out}. Following the induced gravitational collapse (IGC) paradigm of GRBs associated with type Ib/c supernovae we assume that at the external edge of the disk, the infalling matter is composed mainly by the ions present in the material ejected from an explosion of a carbon–oxygen core, that is, mainly oxygen and electrons. This fixes the electron fraction $Y_e(r_{\text{out}}) = 0.5$. We can also calculate the average binding energy per nucleon that appears in Equation (34) using the data in [136]. To establish the NSE we consider H2, H3, HE3, HE4, LI6, LI7, BE7, BE9, BE10, B10, B11, C11, C12, C13, C14, N13, N14, N15, O14, O15, O16, O17 and O18, and obtain the value of the average binding energy per nucleon $\bar{B} = 6.35$ MeV. The second boundary condition can be obtained by the relation $(T\eta + m_B)\sqrt{g_{tt}} = \text{constant}$ [148–150], with η being the degeneracy parameter of the fluid. If we require the potentials to vanish at infinity and invoke Euler's theorem, we arrive at the relation in the weak field limit

$$\frac{M}{r_{\text{out}}} = \left. \frac{\rho + U + P - TS}{\rho} \right|_{r=r_{\text{out}}}. \tag{58}$$

For a classical gas composed of ions and electrons, this relation becomes

$$\frac{M}{r_{\text{out}}} \lesssim \left.\frac{U}{\rho}\right|_{r=r_{\text{out}}}. \tag{59}$$

That is, the virial specific energy must be smaller or comparable to the energy per baryon. Equation (59) can be used together with Equations (15) and (33) to solve for $\eta_{e^-}(r_{\text{out}})$, $\xi(r_{\text{out}})$. The value of r_{out} is chosen to be at most the circularization radius of the accreting material as described in [63,69]. We can estimate this radius by solving for r in the expression of the angular momentum per unit mass for a equatorial circular orbits. Hence, using Equation (5) we need to solve

$$u_\phi = M \frac{x^2 - 2x + a^2}{x^{3/2}\sqrt{x^3 - 3x + 2a}} \sim 3 \times 10^7 \text{ cm}, \tag{60}$$

where $x = \sqrt{r/M}$ which yields $r_{\text{out}} \sim 1800 r_s$ and the expression is in geometric units. Finally, for the initial conditions to be accepted, they are evaluated by the gravitational instability condition [151]:

$$\sqrt{\left. R^{\tilde{\theta}}_{\tilde{t}\tilde{\theta}\tilde{t}}\right|_{\theta=\pi/2}}\,\Omega \geq 2\sqrt{3}\pi\rho. \tag{61}$$

Integration of the equations proceeds as follows: With the initial conditions we solve Equation (37) to obtain the electron fraction in the next integration point. With the new value of the electron fraction we solve the differential algebraic system of Equations (15) and (17) at this new point. This process continues until the innermost stable circular orbit r_{in} is reached.

To add the dynamics of neutrino oscillations we proceed the same as before, but at each point of integration, once the values of Y_e, η and ξ are found, we solve Equation (50) for the average momentum mode to obtain the survival probabilities as a function of time. We then calculate the new neutrino and antineutrino distributions with the conservation of total number density and the relations

$$n_{\nu_e}^{\text{new}}(t) = P_{\nu_e \to \nu_e}(t)n_{\nu_e} + [1 - P_{\nu_e \to \nu_e}(t)]n_{\nu_x}, \tag{62a}$$

$$n_{\nu_x}^{\text{new}}(t) = P_{\nu_x \to \nu_x}(t)n_{\nu_x} + [1 - P_{\nu_x \to \nu_x}(t)]n_{\nu_e}. \tag{62b}$$

Since the disk is assumed to be in a steady-state, we then perform a time average of Equation (62) as discussed in Section 2. With the new distributions, we can calculate the new neutrino and antineutrino average energies and use them to re-integrate the disk equations.

Neutrino emission within neutrino-cooled disks is dominated by electron and positron capture, which only produces electron (anti)neutrinos. The second most important process is electron–positron annihilation, but it is several orders of magnitude smaller. In Figure 2 we show the total number emissivity for these two processes for an accretion rate of $\dot{M} = 0.1 M_\odot$ s $^{-1}$. Other cases behave similarly. Moreover, although the degeneracy parameter suppresses the positron density, a high degeneracy limit does not occur in the disk and the degeneracy is kept low at values between about 0.2 and 3, as shown in Figure 3. The reason for this is the effect of high degeneracy on neutrino cooling. Higher degeneracy leads to a lower density of positrons, which suppresses the neutrino production and emission, which in turn leads to a lower cooling rate, higher temperature, lower degeneracy and higher positron density. This equilibrium leads, via the lepton number conservation Equation (37), to a balance between electronic and non-electronic neutrino densities within the inner regions of the disk. Given this fact, to solve the equations of oscillations, we can approximate the initial conditions of the polarization vectors with

$$\mathsf{P} = \bar{\mathsf{P}} \approx (0, 0, 1). \tag{63}$$
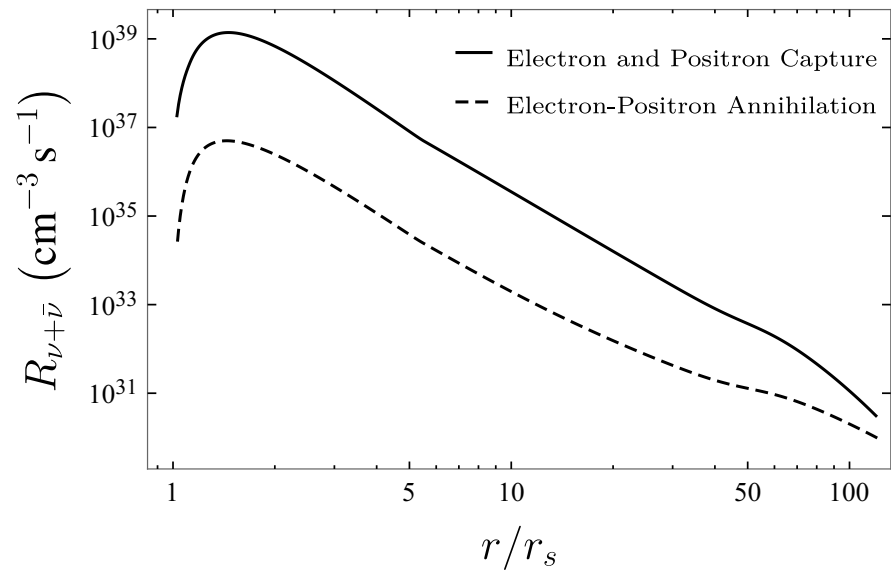
Figure 2. Total number emissivity for electron and positron capture ($p + e^- \rightarrow n + \nu_e$, $n + e^+ \rightarrow p + \bar{\nu}_e$) and electron–positron annihilation ($e^- + e^+ \rightarrow \nu + \bar{\nu}$) for accretion disks with $\dot{M} = 0.1 M_\odot \; \mathrm{s}^{-1}$ between the inner radius and the ignition radius.

(**a**)

(**b**)

(**c**)

(**d**)
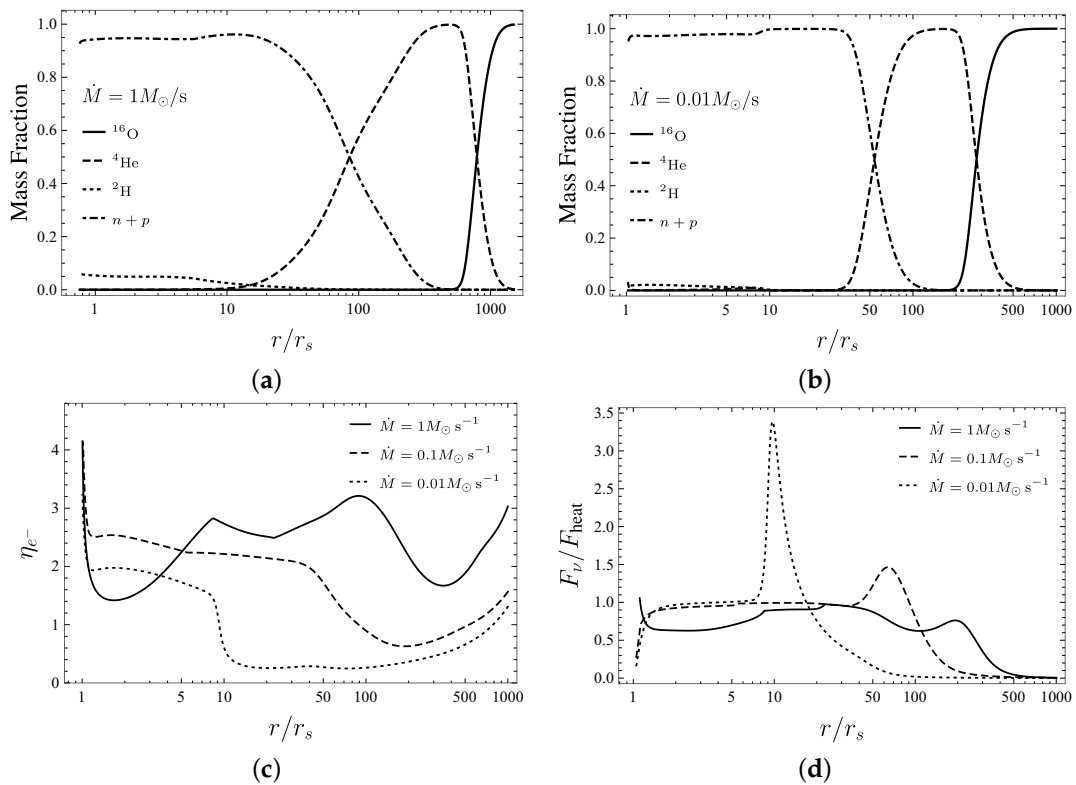
Figure 3. *Cont.*
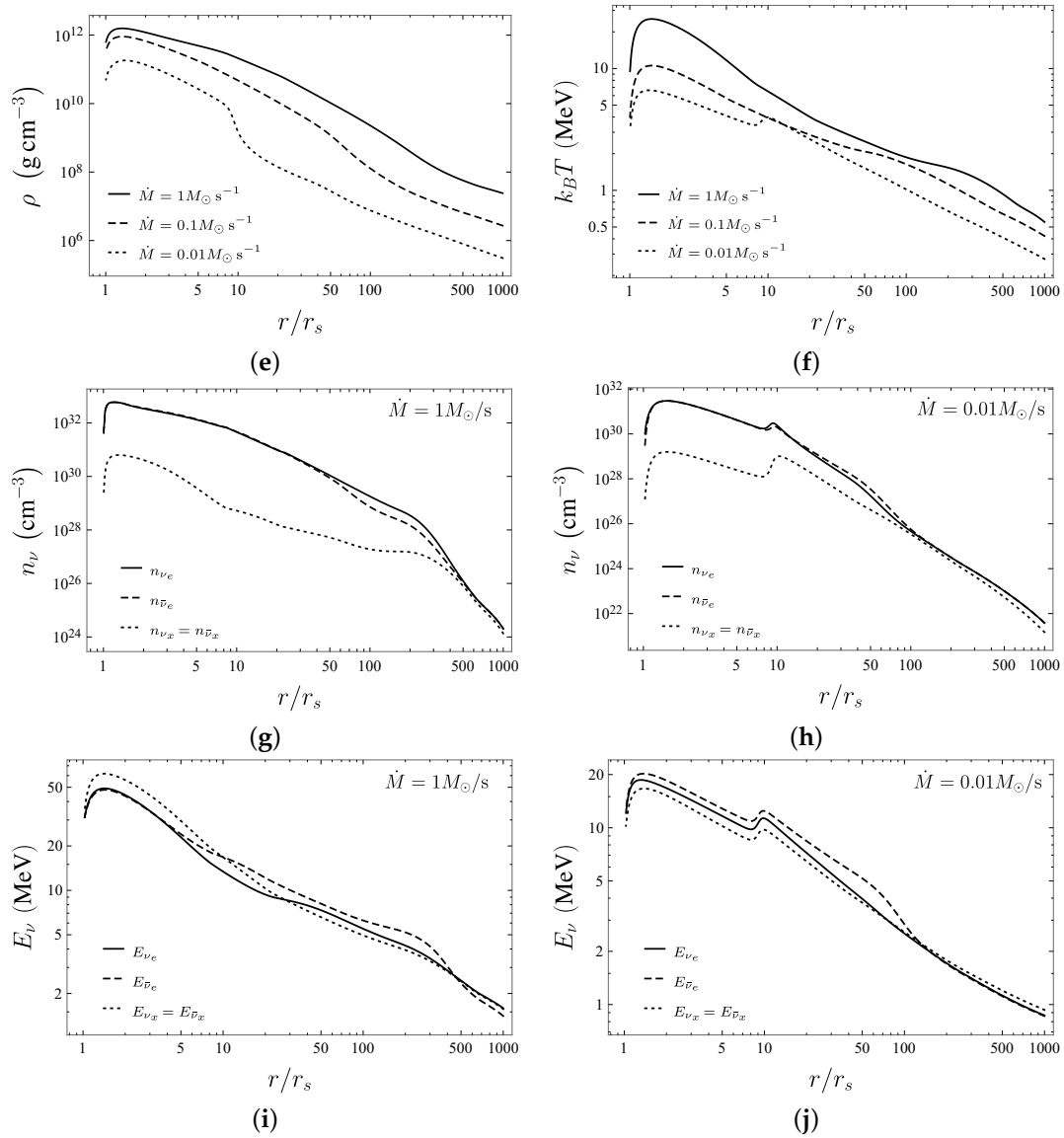
Figure 3. Properties of accretion disks in the absence of oscillations with $M = 3M_{\odot}$, $\alpha = 0.01$, $a = 0.95$. (**a**,**b**) The mass fraction inside the disk. We have plotted only the ones that appreciably change. (**c**) The electron degeneracy parameter. (**d**) The comparison between the neutrino cooling flux F_{ν} and the viscous heating F_{heat}. (**e**) The baryon density. (**f**) The temperature. (**g**,**h**) The neutrino number density. (**i**,**j**) The average neutrino energies.

5. Results and Analysis

In Figures 3 and 4, we present the main features of accretion disks for the parameters $M = 3M_{\odot}$; $\alpha = 0.01$; $a = 0.95$; and two selected accretion rates, $\dot{M} = 1M_{\odot}$ s^{-1} and $\dot{M} = 0.01M_{\odot}$ s^{-1}. It exhibits the usual properties of thin accretions disks. High accretion rate disks have higher density, temperature and electron degeneracy. Additionally, for high accretion rates, the cooling due to photodisintegration and neutrino emission kicks in at larger radii. For all cases, as the disk heats up, the number of free nucleons starts to increase enabling the photodisintegration cooling at $r \sim (100–300)r_s$. Only the disintegration of alpha particles is important, and the nucleon content of the infalling matter is of little consequence for the dynamics of the disk. When the disk reaches temperatures $\sim$1.3 MeV, the electron capture switches on, the neutrino emission becomes significant and the physics of the disk is dictated by the energy equilibrium between F_{heat} and F_{ν}. The radius at which neutrino cooling becomes significant (called ignition radius r_{ign}) is defined by the condition $F_{\nu} \sim F_{\text{heat}}/2$. For the low accretion rate $\dot{M} = 0.01M_{\odot}$ s^{-1}, the photodisintegration cooling finishes before the neutrino cooling becomes significant; this leads to fast heating of the

disk. Then the increase in temperature triggers a strong neutrino emission that carries away the excess heat generating a sharp spike in F_ν surpassing F_{heat} by a factor of $\sim$3.5. This behavior is also present in the systems studied in [107], but there it appears for fixed accretion rates and high viscosity ($\alpha = 0.1$). This demonstrates the semi-degeneracy mentioned in Section 5. The evolution of the fluid can be tracked accurately through the degeneracy parameter. At the outer radius, η_{e^-} starts to decrease as the temperature of the fluid rises. Once neutrino cooling becomes significant, it starts to increase until the disk reaches the local balance between heating and cooling. At this point, η_{e^-} stops rising and is maintained (approximately) at a constant value. Very close to r_{in}, the zero torque condition of the disk becomes important and the viscous heating is reduced drastically. This is reflected in a sharp decrease in the fluid's temperature and increase in the degeneracy parameter. For the high accretion rate, an additional effect has to be taken into account. Due to high ν_e optical depth, neutrino cooling is less efficient, leading to an increase in temperature and a second dip in the degeneracy parameter. This dip is not observed in low accretion rates because τ_{ν_e} does not reach significant values.
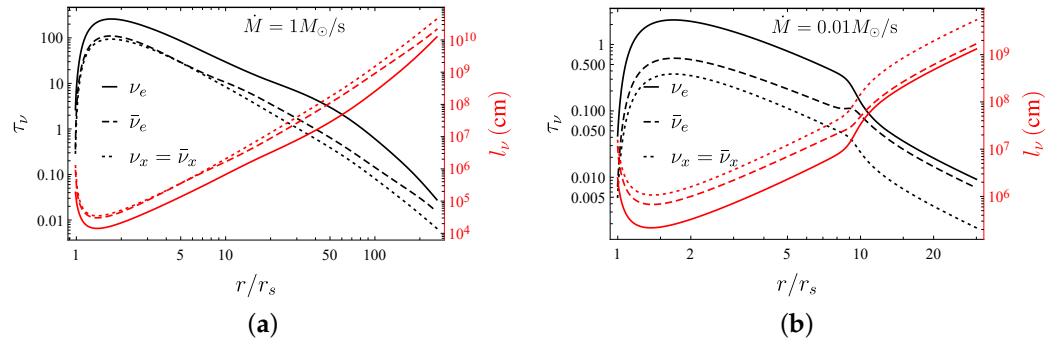
Figure 4. Total optical depth (left scale) and mean free path (right scale) for neutrinos and antineutrinos of both flavors between the inner radius and the ignition radius for accretion disks with (**a**) $\dot{M} = 1 M_\odot$ s^{-1} and (**b**) $0.01 M_\odot$ s^{-1}.

With the information in Figure 3 we can obtain the oscillation potentials which we plot in Figure 5. Since the physics of the disk for $r < r_{\text{ign}}$ are independent of the initial conditions at the external radius and for $r > r_{\text{ign}}$ the neutrino emission is negligible, the impact of neutrino oscillations is important only inside r_{ign}.
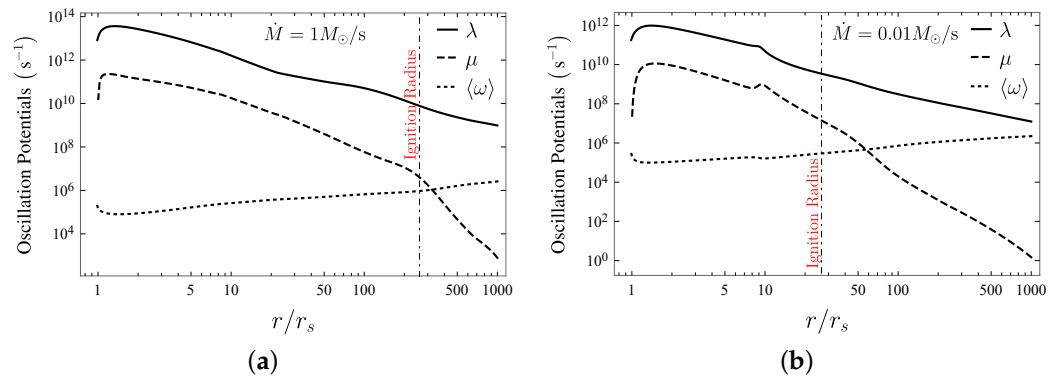
Figure 5. Oscillation potentials as functions of r with $M = 3 M_\odot$, $\alpha = 0.01$, $a = 0.95$ for accretion rates (**a**) $\dot{M} = 1 M_\odot$ s^{-1} and (**b**) $\dot{M} = 0.01 M_\odot$ s^{-1}, respectively. The vertical line represents the position of the ignition radius.

We can see that the discussion at the end of Section 3.1 is justified since, for $r_{\text{in}} < r < r_{\text{ign}}$, the potentials obey the relation

$$\langle \omega \rangle \ll \mu \ll \lambda. \tag{64}$$

Generally, the full dynamics of neutrino oscillations are a rather complex interplay between the three potentials, yet it is possible to understand the neutrino response in the disk using some numerical and algebraic results obtained in [33,36,144] and references therein. Specifically, we know that if $\mu \gg \langle \omega \rangle$, as long as the MSW condition $\lambda \simeq \langle \omega \rangle$ is not met (precisely our case), collective effects should dominate the neutrino evolution even if $\lambda \gg \mu$. On the other hand, if $\mu \lesssim \langle \omega \rangle$, the neutrino evolution is driven by the relative values between the matter and vacuum potentials (not our case). With Equation (55) we can build a very useful analogy. These equations are analogous to the equations of motion of a simple mechanical pendulum with a vector position given by **S**, precessing around with angular momentum **D**, subjected to a gravitational force $\langle \omega \rangle \mu \mathbf{B}$ with mass μ^{-1}. Using Equation (63) obtains the expression $|\mathbf{S}| = S \approx 2 + O(\langle \omega \rangle / \mu)$. Calculating $\partial_t (\mathbf{S} \cdot \mathbf{S})$, it can be checked that this value is conserved up to fluctuations of order $\langle \omega \rangle / \mu$. The analogous angular momentum is $\mathbf{D} = \mathsf{P} - \bar{\mathsf{P}} = 0$. Thus, the pendulum moves initially in a plane defined by **B** and the z-axis, i.e., the plane xz. Then, it is possible to define an angle φ between **S** and the z-axis such that

$$\mathbf{S} = S(\sin \varphi, 0, \cos \varphi). \tag{65}$$

The only non-zero component of **D** is the y-component. From Equation (55) we find

$$\dot{\varphi} = \mu D, \tag{66a}$$
$$\dot{D} = -\langle \omega \rangle S \cos(\varphi + 2\theta). \tag{66b}$$

These equations can be equivalently written as

$$\ddot{\varphi} = -k^2 \sin(2\theta + \varphi), \tag{67}$$

where we have introduced the inverse characteristic time k by

$$k^2 = \langle \omega \rangle \mu S, \tag{68}$$

which is related to the anharmonic oscillations of the pendulum. The role of the matter potential λ is to logarithmically extend the oscillation length by the relation [144]

$$\tau = -k^{-1} \ln \left[\frac{k}{\theta (k^2 + \lambda^2)^{1/2}} \left(1 + \frac{\langle \omega \rangle}{S\mu} \right) \right]. \tag{69}$$

The total oscillation time can then be approximated by the period of an harmonic pendulum plus the logarithmic extension

$$t_{\mathrm{osc}} = \frac{2\pi}{k} + \tau. \tag{70}$$

The initial conditions of Equation (63) imply

$$\varphi(t = 0) = \arcsin \left(\frac{\langle \omega \rangle}{S\mu} \sin 2\theta \right), \tag{71}$$

so that φ is a small angle. The potential energy for a simple pendulum is

$$V(\varphi) = k^2 [1 - \cos(\varphi + 2\theta)] \approx k^2 (\varphi + 2\theta)^2. \tag{72}$$

If $k^2 > 0$, which is true for the normal hierarchy $\Delta m^2 > 0$, we expect small oscillations around the initial position since the system begins in a stable position of the potential. The magnitude of flavor conversions is in the order $\sim \langle \omega \rangle / S\mu \ll 1$. We stress that normal hierarchy does not mean an absence of oscillations but rather imperceptible oscillations in P_z. No strong flavor oscillations are expected. On the contrary, for the inverted hierarchy $\Delta m^2 < 0$, $k^2 < 0$ and the initial φ indicates that the system begins in an unstable position and we expect very large anharmonic oscillations. P^z (and $\bar{\mathsf{P}}^z$) oscillates between two

different maxima, passing through a minimum $-P^z$ ($-\bar{P}^z$) several times. This implies total flavor conversion: all electronic neutrinos (antineutrinos) are converted into non-electronic neutrinos (antineutrinos) and vice versa. This has been called bipolar oscillation in the literature [44]. If the initial conditions are not symmetric as in Equation (63), the asymmetry is measured by a constant $\varsigma = \bar{P}^z/P^z$ if $\bar{P}^z < P^z$ or $\varsigma = P^z/\bar{P}^z$ if $\bar{P}^z > P^z$ so that $0 < \varsigma < 1$. Bipolar oscillations are present in an asymmetric system as long as the relation

$$\frac{\mu}{|\langle\omega\rangle|} < 4\frac{1+\varsigma}{(1-\varsigma)^2}, \tag{73}$$

is obeyed [144]. If this condition is not met, instead of bipolar oscillation we get synchronized oscillations. Since we are considering constant potentials, synchronized oscillations are equivalent to the normal hierarchy case. From Figure 5 we can conclude that in the normal hierarchy case, neutrino oscillations have no effects on neutrino-cooled disks under the assumptions we have made. On the other hand, in the inverted hierarchy case, we expect extremely fast flavor conversions with periods of order $t_{\text{osc}} \sim (10^{-9}\text{–}10^{-5})$ s for high accretion rates and $t_{\text{osc}} \sim (10^{-8}\text{–}10^{-5})$ s for low accretion rates, between the respective r_{in} and r_{ign}.

For the purpose of illustration we solve the equations of oscillations for the $\dot{M} = 0.1 M_\odot$ s^{-1} case at $r = 10 r_s$. The electronic (anti)neutrino survival probability at this point is shown in Figure 6 for inverted hierarchy and normal hierarchy, respectively. On both plots, there is no difference between the neutrino and antineutrino survival probabilities. This should be expected, since for these values of r, the matter and self-interaction potentials are much larger than the vacuum potential, and there is virtually no difference between Equations (50a) and (50b). Additionally, as mentioned before, note that the (anti)neutrino flavor proportions remain virtually unchanged for normal hierarchy, while the neutrino flavor proportions change drastically for the inverted hierarchy case. The characteristic oscillation time of the survival probability in inverted hierarchy found on the plot is

$$t_{\text{osc}} \approx 8.4 \times 10^{-7}\text{ s}, \tag{74}$$

which agrees with the ones given by Equation (70) up to a factor of order one. Such a small value suggests extremely quick $\nu_e \bar{\nu}_e \to \nu_x \bar{\nu}_x$ oscillations. A similar effect occurs for regions of the disk inside the ignition radius for all three accretion rates. In this example, the time average of the survival probabilities yields the values $\langle P_{\nu_e \to \nu_e}\rangle = \langle P_{\bar{\nu}_e \to \bar{\nu}_e}\rangle = 0.92$. With this number and Equations (62) and (57), the (anti)neutrino spectrum for both flavors can be constructed. However, more importantly, this means that the local observer at that point in the disk measures, on average, an electron (anti)neutrino loss of around 8%, which is represented by an excess of non-electronic (anti)neutrinos.
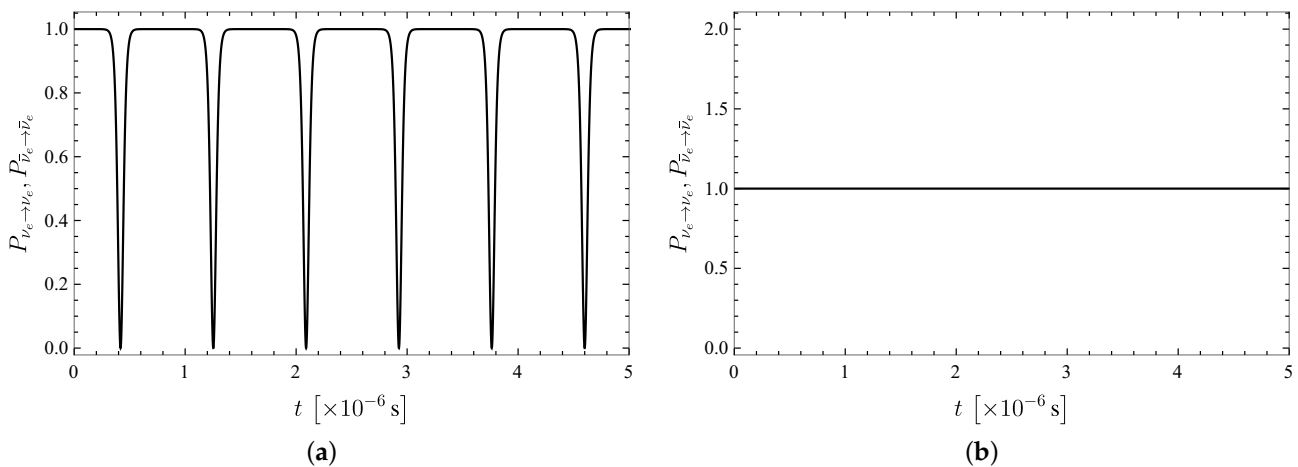
Figure 6. Survival provability for electron neutrinos and antineutrinos for the accretion disk with $\dot{M} = 0.1 M_\odot$ s^{-1} at $r = 10 r_s$. The survival probabilities for neutrinos and antineutrinos in both plots coincide. (**a**) Inverted hierarchy and (**b**) normal hierarchy.

In Section 3.1 we proposed to calculate neutrino oscillations assuming that small neighboring regions of the disk are independent and that neutrinos can be viewed as isotropic gases in those regions. However, this cannot be considered a steady-state of the disk. To see this, consider Figure 4. The maximum value of the neutrino optical depth is in the order of 10^3 for the highest accretion rate, meaning that the time that takes neutrinos to travel a distance of one Schwarzschild inside the disk radius obeys

$$t_{r_s} \ll \text{Max}(\tau_\nu) r_s \approx 10^{-2} \, \text{s}, \tag{75}$$

which is lower than the accretion time of the disk as discussed in Section 2 but higher than the oscillation time. Different sections of the disk are not independent, since they very quickly share (anti)neutrinos created with a non-vanishing momentum along the radial direction. Furthermore, the oscillation patterns between neighboring regions of the disk are not identical. In Figure 7 we show the survival probability as a function of time for different (but close) values of r for $\dot{M} = 0.1 M_\odot \, \text{s}^{-1}$. The superposition between neutrinos with different oscillation histories has several consequences: (1) It breaks the isotropy of the gas because close to the BH, neutrinos are more energetic and their density is higher, producing a radially directed net flux, meaning that the factor $\mathbf{v}_{\mathbf{q},t} \cdot \mathbf{v}_{\mathbf{p},t}$ does not average to zero. This implies that realistic equations of oscillations include a multi-angle term and a radially decaying neutrino flux similar to the situation in SN neutrinos. (2) It constantly changes the neutrino content at any value of r independently of the neutrino collective evolution given by the values of the oscillation potentials at that point. This picture plus the asymmetry that electron and non-electron neutrinos experience through the matter environment (electron (anti)neutrinos can interact through $n + \nu_e \to p + e^-$ and $p + \bar{\nu}_e \to n + e^+$), suggests that the disk achieves complete flavor equipartitioning (decoherence). We can identify two competing causes, namely, quantum decoherence and kinematic decoherence.
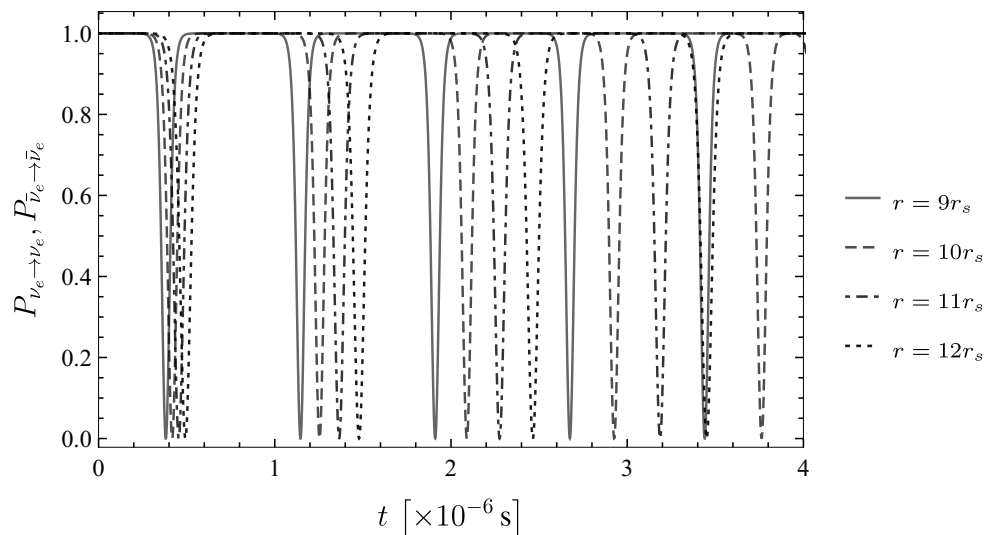
Figure 7. Survival provability for electron neutrinos and antineutrinos for the accretion disk with $\dot{M} = 0.1 M_\odot \, \text{s}^{-1}$ at $r = 9r_s, 10r_s, 11r_s, 12r_s$.

Quantum decoherence is the product of collisions among the neutrinos or with a thermal background medium can be understood as follows [152]. From Appendix D.2 we know that different (anti)neutrino flavors posses different cross-sections and scattering rates $\Gamma_{\nu_i, \bar{\nu}_i}$. In particular, we have $\Gamma_{\nu_x} \approx \Gamma_{\bar{\nu}_x} < \Gamma_{\bar{\nu}_e} < \Gamma_{\nu_e}$. An initial electron (anti)neutrino created at a point r will begin to oscillate into $\nu_x(\bar{\nu}_x)$. The probability of finding it in one of the two flavors evolves as previously discussed. However, in each interaction $n + \nu_e \to p + e^-$, the electron neutrino component of the superposition is absorbed, while the ν_x component remains unaffected. Thus, after the interaction the two flavors can no longer interfere. This allows the remaining ν_x to oscillate and develop a new coherent ν_e component which

is made incoherent in the next interaction. The process will come to equilibrium only when there are equal numbers of electronic and non-electronic neutrinos. That is, the continuous emission and absorption of electronic (anti)neutrinos generate non-electronic (anti)neutrinos with an average probability of $\langle P_{\nu_e \to \nu_e} \rangle$ in each interaction, and once the densities of flavors are equal, the oscillation dynamic stops. An initial system composed of $\nu_e, \bar{\nu}_e$ turns into an equal mixture of $\nu_e, \bar{\nu}_e$ and $\nu_x, \bar{\nu}_x$, reflected as an exponential damping of oscillations. For the particular case in which non-electronic neutrinos can be considered as sterile (do not interact with the medium), the relaxation time of this process can be approximated as [153,154]

$$t_Q = \frac{1}{2 l_{\nu\bar{\nu}} \langle \omega \rangle^2 \sin^2 2\theta} + \frac{2 l_{\nu\bar{\nu}} \lambda^2}{\langle \omega \rangle^2 \sin^2 2\theta}, \tag{76}$$

where $l_{\nu\bar{\nu}}$ represents the (anti)neutrino mean free path.

Kinematic decoherence is the result of a non-vanishing flux term such that at any point, (anti)neutrinos traveling in different directions do not experience the same self-interaction potential due to the multi-angle term in the integral of Equation (40). Different trajectories do not oscillate in the same way, leading to a de-phasing and a decay of the average $\langle P_{\nu \to \nu} \rangle$, and thus to the equipartitioning of the overall flavor content. The phenomenon is similar to an ensemble of spins in an inhomogeneous magnetic field. In [35] it is shown that for asymmetric $\nu\bar{\nu}$ gas, even an infinitesimal anisotropy triggers an exponential evolution towards equipartitioning, and in [36] it was shown that if the symmetry between neutrinos and antineutrinos is not broken beyond the limit of 25%, kinematic decoherence is still the main effect of neutrino oscillations. As a direct consequence of the $\nu\bar{\nu}$ symmetry present within the ignition radius of accretion disks (see Figure 3), an equipartition among different neutrino flavors is expected. This multi-angle term keeps the order of the characteristic time t_{osc} of Equation (70) unchanged, and kinematic decoherence happens within a few oscillation cycles. The oscillation time gets smaller closer to the BH due to the $1/\mu^{1/2}$ dependence. Therefore, we expect that neutrinos emitted within the ignition radius will be equally distributed among both flavors in about few microseconds. Once the neutrinos reach this maximally mixed state, no further changes are expected. We emphasize that kinematic decoherence does not mean quantum decoherence. Figures 6 and 7 clearly show the typical oscillation pattern which happens only if quantum coherence is still acting on the neutrino system. Kinematic decoherence, differently to quantum decoherence, is just the result of averaging over the neutrino intensities resulting from quick flavor conversion. Therefore, neutrinos are yet able to quantum oscillate if appropriate conditions are satisfied.

Simple inspection of Equations (70) and (76) with Figure 4 yields $t_{\mathrm{osc}} \ll t_Q$. Clearly the equipartition time is dominated by kinematic decoherence. These two effects are independent of the neutrino mass hierarchy, and neutrino flavor equipartitioning is achieved for both hierarchies. Within the disk dynamic, this is equivalent to imposing the condition $\langle P_{\nu_e \to \nu_e} \rangle = \langle P_{\bar{\nu}_e \to \bar{\nu}_e} \rangle = 0.5$.

Figure 8 shows a comparison between disks with and without neutrino flavor equipartition for the three accretion rates considered. The roles of an equipartition are to increase the disk's density, reduce the temperature and electron fraction and further stabilize the electron degeneracy for regions inside the ignition radius. The effect is mild for low accretion rates and very pronounced for high accretion rates. This result is in agreement with our understanding of the dynamics of the disk and can be explained in the following way. In low accretion systems the neutrino optical depth for all flavors is $\tau_{\nu\bar{\nu}} \lesssim 1$, and the differences between the cooling fluxes, as given by Equation (32) are small. Hence, when the initial (mainly electron flavor) is redistributed among both flavors, the total neutrino cooling remains virtually unchanged and the disk evolves as if equipartition had never occurred save the new emission flavor content. On the other hand, when accretion rates are high, the optical depth obeys $\tau_{\nu_x} \approx \tau_{\bar{\nu}_x} \lesssim \tau_{\bar{\nu}_e} < \tau_{\nu_e} \sim 10^3$. The ν_e cooling is heavily suppressed—the other factors, less so. When flavors are redistributed, the new ν_x particles are free to escape, enhancing the total cooling and reducing the temperature. As

the temperature decreases, so do the electron and positron densities, leading to a lower electron fraction. The net impact of a flavor equipartition is to make the disk evolution less sensitive to ν_e opacity, and thus, increase the total cooling efficiency. As a consequence, once the fluid reaches a balance between F^+ and F_ν, this state is kept without being affected by high optical depths and η_{e^-} stays at a constant value until the fluid reaches the zero torque condition close to $r_{\rm in}$. Note that for every case, inside the ignition radius, we find $\tau_{\nu_x} \approx \tau_{\bar{\nu}_x} \lesssim \tau_{\bar{\nu}_e} < \tau_{\nu_e}$ so that the equipartition enhances, mainly, neutrino cooling F_ν (and not antineutrino cooling $F_{\bar\nu}$). The quotient between neutrino cooling with and without an equipartition can be estimated with

$$\frac{F_\nu^{\rm eq}}{F_\nu} \approx \frac{1}{2}\left(1 + \frac{\langle E_{\nu_x}\rangle}{\langle E_{\nu_e}\rangle}\frac{1 + \tau_{\nu_e}}{1 + \tau_{\nu_x}}\right). \tag{77}$$
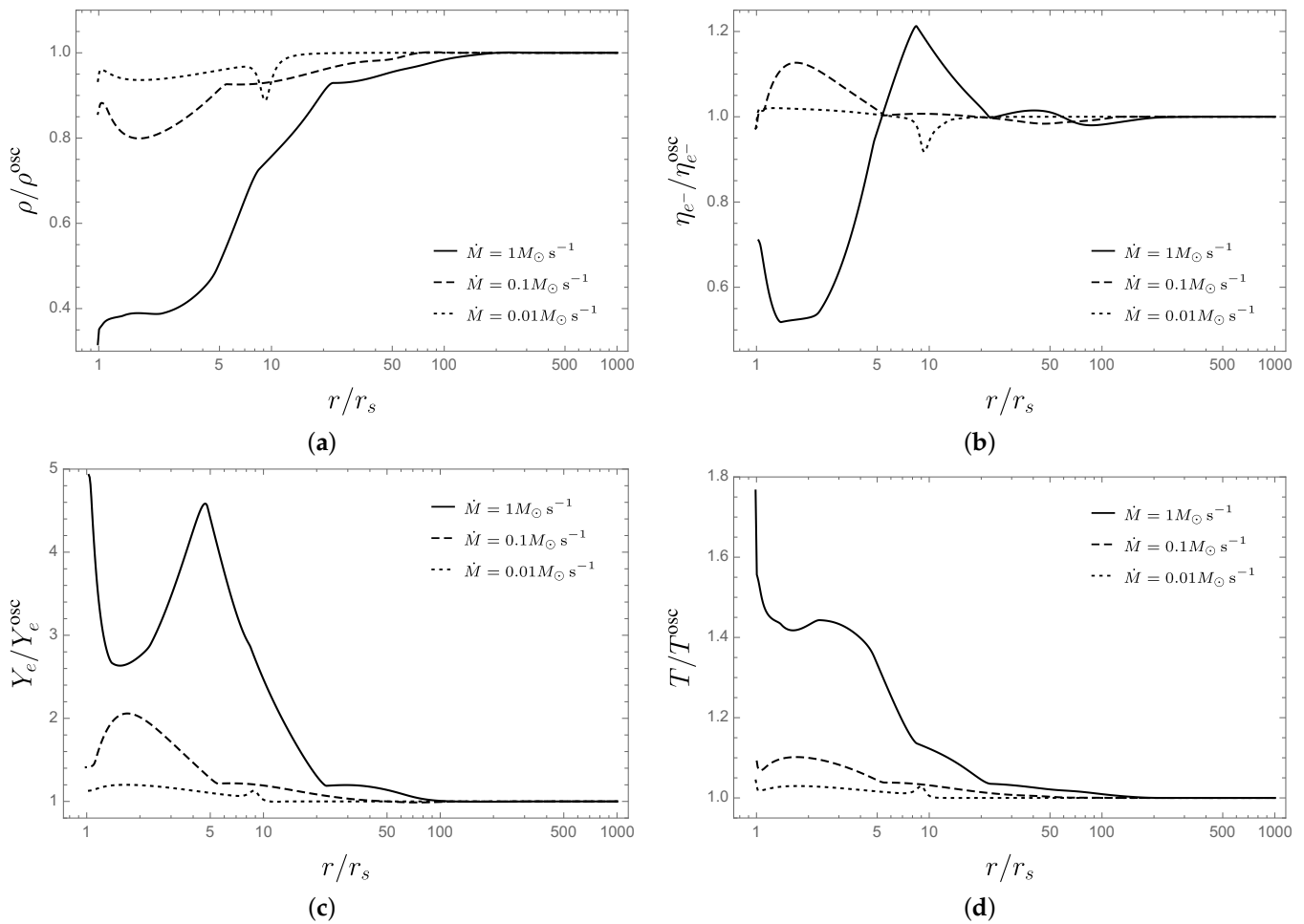
Figure 8. Comparison between the main variables describing thin disks with and without a neutrino flavor equipartition for each accretion rate considered. Here $\rho^{\rm osc}, \eta_{e^-}^{\rm osc}, Y_e^{\rm osc}, T^{\rm osc}$ are the density, electron degeneracy, electron fraction and temperature of a disk with a flavor equipartition. Together with Figure 3, these plots completely describe the profile of a disk under a flavor equipartition. (**a**) The ratio between baryon densities. (**b**) The ratio between degeneracy parameters. (**c**) The ratio between electron fractions. (**d**) The ratio between temperatures.

This relation exhibits the right limits. From Figure 3 we see that $\langle E_{\nu_e}\rangle \approx \langle E_{\nu_x}\rangle$. Hence, If $1 \gg \tau_{\nu_e} > \tau_{\nu_x}$, then $F_\nu^{\rm eq} = F_\nu$ and the equipartition is unnoticeable. However, if $1 < \tau_{\nu_x} < \tau_{\nu_e}$ then $F_\nu^{\rm eq}/F_\nu > 1$. In our simulations, this fraction reaches values of 1.9 for $\dot{M} = 1 M_\odot\,{\rm s}^{-1}$ to 2.5 for $\dot{M} = 0.01 M_\odot\,{\rm s}^{-1}$.

The disk variables at each point do not change beyond a factor of order five in the most obvious case. However, these changes can be important for cumulative quantities,

e.g., the total neutrino luminosity and the total energy deposition rate into electron–positron pairs due to neutrino antineutrino annihilation. To see this we perform a Newtonian calculation of these luminosities following [99,100,112,155–158], and references therein. The neutrino luminosity is calculated by integrating the neutrino cooling flux throughout both faces of the disk:

$$L_{\nu_i} = 4\pi \int_{r_{\text{in}}}^{r_{\text{out}}} C_{\text{cap}} F_{\nu_i} r dr. \tag{78}$$

The factor $0 < C_{\text{cap}} < 1$ is a function of the radius (called capture function in [126]) that accounts for the proportion of neutrinos that are re-captured by the BH, and thus, do not contribute to the total luminosity. For a BH with $M = 3M_\odot$ and $a = 0.95$, the numerical value of the capture function as a function of the dimensionless distance $x = r/r_s$ is well fitted by

$$C_{\text{cap}}(x) = \left(1 + \frac{0.3348}{x^{3/2}}\right)^{-1}, \tag{79}$$

with a relative error smaller than 0.02%. To calculate the energy deposition rate, the disk is modeled as a grid of cells in the equatorial plane. Each cell k has a specific value of differential neutrino luminosity $\Delta\ell_{\nu_i}^k = F_{\nu_i}^k r_k \Delta r_k \Delta\phi_k$ and average neutrino energy $\langle E_{\nu_i}\rangle^k$. If a neutrino of flavor i is emitted from the cell k and an antineutrino is emitted from the cell k', and before interacting at a point $\mathbf{r}$ above the disk, each travels a distance r_k and $r_{k'}$, then their contribution to the energy deposition rate at $\mathbf{r}$ is (see Appendix D.3 for details)

$$
\begin{aligned}
\Delta Q_{\nu_i \bar{\nu}_i k k'} &= A_{1,i} \frac{\Delta\ell_{\nu_i}^k}{r_k^2} \frac{\Delta\ell_{\bar{\nu}_i}^{k'}}{r_{k'}^2} \left(\langle E_{\nu_i}\rangle^k + \langle E_{\bar{\nu}_i}\rangle^{k'}\right) \left(1 - \frac{\mathbf{r}_k \cdot \mathbf{r}_{k'}}{r_k r_{k'}}\right)^2 \\
&+ A_{2,i} \frac{\Delta\ell_{\nu_i}^k}{r_k^2} \frac{\Delta\ell_{\bar{\nu}_i}^{k'}}{r_{k'}^2} \left(\frac{\langle E_{\nu_i}\rangle^k + \langle E_{\bar{\nu}_i}\rangle^{k'}}{\langle E_{\nu_i}\rangle^k \langle E_{\bar{\nu}_i}\rangle^{k'}}\right) \left(1 - \frac{\mathbf{r}_k \cdot \mathbf{r}_{k'}}{r_k r_{k'}}\right).
\end{aligned}
\tag{80}
$$

The total neutrino annihilation luminosity is the sum over all pairs of cells integrated in space

$$L_{\nu_i \bar{\nu}_i} = 4\pi \int_{\mathcal{A}} \sum_{k,k'} \Delta Q_{\nu_i \bar{\nu}_i k k'} d^3 \mathbf{r}, \tag{81}$$

where $\mathcal{A}$ is the entire space above (or below) the disk.

In Table 3 we show the neutrino luminosities and the neutrino annihilation luminosities for disks with and without neutrino collective effects. In each case, the flavor equipartition induces a loss in L_{ν_e} by a factor of ~ 3, and a loss in $L_{\bar{\nu}_e}$ luminosity by a factor of ~ 2. At the same time, L_{ν_x} and $L_{\bar{\nu}_e}$ are increased by a factor ~ 10. This translates into a reduction of the energy deposition rate due to electron neutrino annihilation by a factor of ~ 7, while the energy deposition rate due to non-electronic neutrinos goes from being negligible to be of the same order of the electronic energy deposition rate. The net effect is to reduce the total energy deposition rate of neutrino annihilation by a factor of ~ 3–5 for the accretion rates considered. In particular, we obtain factors of 3.03 and 3.66 for $\dot{M} = 1\ M_\odot\ \text{s}^{-1}$ and $\dot{M} = 0.01\ M_\odot\ \text{s}^{-1}$, respectively, and a factor of 4.73 for $\dot{M} = 0.1\ M_\odot\ \text{s}^{-1}$. The highest value corresponds to an intermediate value of the accretion rate because, for this case, there is a ν_e cooling suppression ($\tau_{\nu_e} > 1$) and the quotient $\tau_{\nu_e}/\tau_{\nu_x}$ is maximal. By Equation (77), the difference between the respective cooling terms is also maximal. In Figure 9 we show the energy deposition rate per unit volume around the BH for each flavor with accretion rates $\dot{M} = 1\ M_\odot\ \text{s}^{-1}$ and $\dot{M} = 0.1\ M_\odot\ \text{s}^{-1}$. There we can see the drastic enhancement of the non-electronic neutrino energy deposition rate and the reduction of the electronic deposition rate. Due to the double peak in the neutrino density for $\dot{M} = 0.01\ M_\odot\ \text{s}^{-1}$ case (see Figure 3), the deposition rate per unit volume also shows two peaks—one at $r_s < r < 2r_s$ and the other at $10\,r_s < r < 11\,r_s$. Even so, the behavior is similar to the other cases.
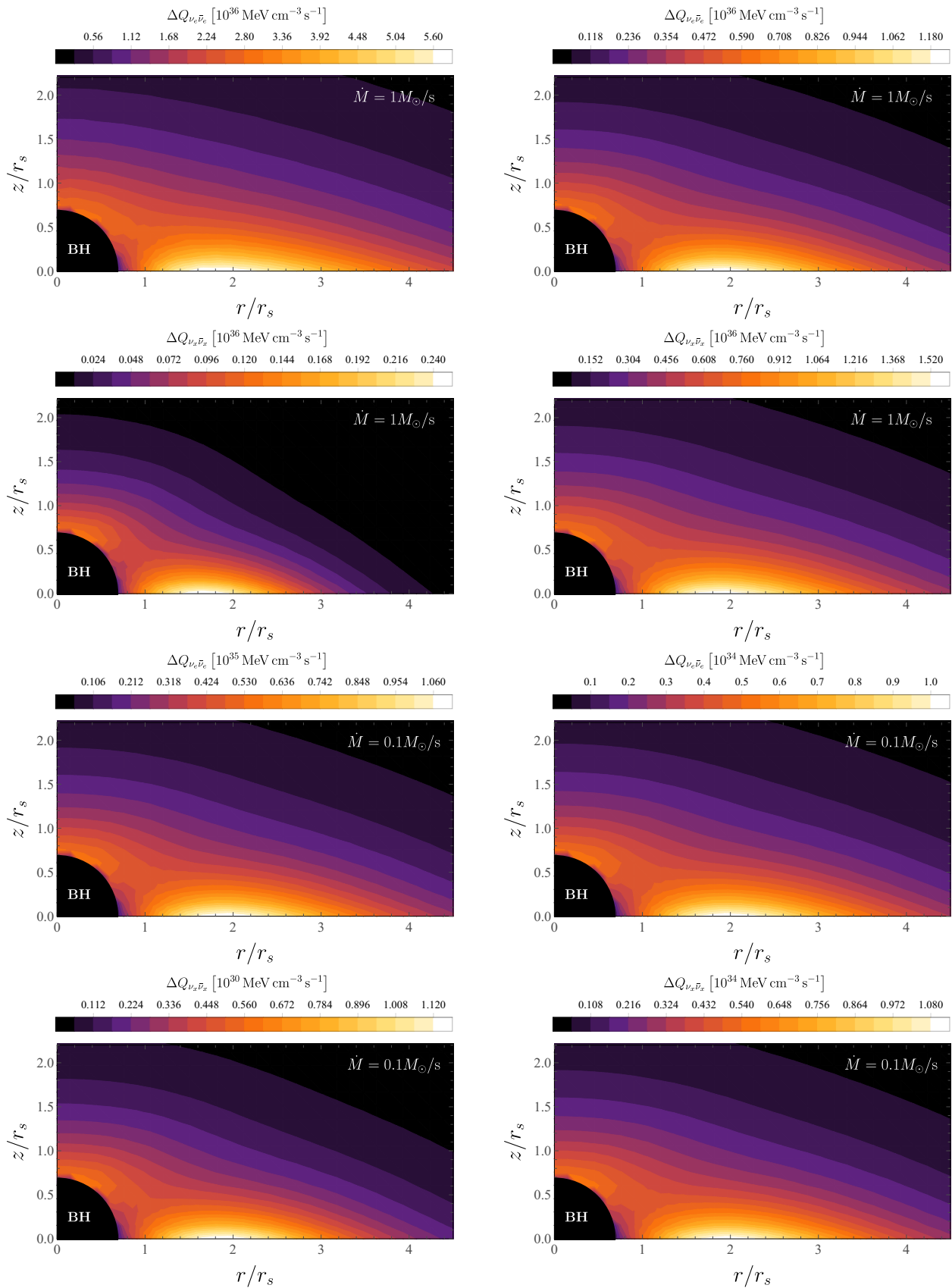
Figure 9. Comparison of the neutrino annihilation luminosity per unit volume $\Delta Q_{\nu_i \bar{\nu}_i} = \sum_{k,k'} \Delta Q_{\nu_i \bar{\nu}_i kk'}$ between disk without (**left** column) and with (**right** column) flavor equipartitioning for accretion rates $\dot{M} = 1 M_\odot$ s^{-1} and $\dot{M} = 0.01 M_\odot$ s^{-1}.

Table 3. Comparison of total neutrino luminosities L_ν and annihilation luminosities $L_{\nu\bar\nu}$ between disks with and without flavor equipartitions. All luminosities are reported in MeV s^{-1}.

	Without Oscillations						With Oscillations (Flavor Equipartition)					
	L_{ν_e}	$L_{\bar\nu_e}$	L_{ν_x}	$L_{\bar\nu_x}$	$L_{\nu_e\bar\nu_e}$	$L_{\nu_x\bar\nu_x}$	L_{ν_e}	$L_{\bar\nu_e}$	L_{ν_x}	$L_{\bar\nu_x}$	$L_{\nu_e\bar\nu_e}$	$L_{\nu_x\bar\nu_x}$
1 $M_\odot$ s^{-1}	6.46×10^{58}	7.33×10^{58}	1.17×10^{58}	1.17×10^{58}	1.25×10^{57}	1.05×10^{55}	1.87×10^{58}	4.37×10^{58}	7.55×10^{58}	5.44×10^{58}	1.85×10^{56}	2.31×10^{56}
0.1 $M_\odot$ s^{-1}	9.19×10^{57}	1.08×10^{58}	8.06×10^{55}	8.06×10^{55}	1.62×10^{55}	1.27×10^{50}	2.47×10^{57}	4.89×10^{57}	7.75×10^{57}	5.27×10^{57}	1.78×10^{54}	1.64×10^{54}
0.01 $M_\odot$ s^{-1}	1.05×10^{57}	1.12×10^{57}	2.43×10^{55}	2.43×10^{55}	1.78×10^{53}	8.68×10^{48}	4.29×10^{56}	5.48×10^{56}	6.71×10^{56}	5.70×10^{56}	3.53×10^{52}	1.23×10^{52}

6. Discussion

The generation of a seed, energetic e^-e^+ plasma, seems to be a general prerequisite of GRB theoretical models for the explanation of the prompt (MeV) gamma-ray emission. The e^-e^+ pair annihilation produces photons leading to an opaque pair-photon plasma that self-accelerates, expanding to ultrarelativistic Lorentz factors in the order of 10^2–10^3 (see, e.g., [159–161]). The reaching of transparency of MeV-photons at large Lorentz factor and corresponding large radii is requested to solve the so-called compactness problem posed by the observed non-thermal spectrum in the prompt emission [162–164]. There is a vast literature on this subject, and we refer the reader to [165–170] and references therein for further details.

Neutrino-cooled accretion disks onto rotating BHs have been proposed as a possible way of producing the above-mentioned e^-e^+ plasma. The reason is that such disks emit a large amount of neutrino and antineutrinos that can undergo pair annihilation near the BH [100–112]. The viability of this scenario clearly depends on the energy deposition rate of neutrino-antineutrinos into e^-e^+ and so on the local (anti)neutrino density and energy.

We have here shown that, inside these hyperaccreting disks, a rich neutrino oscillation phenomenology is present due to the high neutrino density. Consequently, the neutrino/antineutrino emission and the corresponding pair annihilation process around the BH leading to electron–positron pairs, are affected by neutrino flavor conversion. Using the thin disk and α-viscosity approximations, we have built a simple stationary model of general relativistic neutrino-cooled accretion disks around a Kerr BH that takes into account not only a wide range of neutrino emission processes and nucleosynthesis, but also the dynamics of flavor oscillations. The main assumption relies on considering the neutrino oscillation behavior within small neighboring regions of the disk as independent from each other. This, albeit being a first approximation to a more detailed picture, has allowed us to set the main framework to analyze the neutrino oscillations phenomenology in inside neutrino-cooled disks.

In the absence of oscillations, a variety of neutrino-cooled accretion disks onto Kerr BHs, without neutrino flavor oscillations, have been modeled in the literature (see, e.g., [99,100,107,112,124] for a recent review). The physical setting of our disk model follows closely the ones considered in [107], but with some extensions and differences in some aspects:

1. The equation of vertical hydrostatic equilibrium, Equation (15), can be derived in several ways [124,127,131]. We followed a particular approach consistent with the assumptions in [127], in which we took the vertical average of a hydrostatic Euler equation in polar coordinates. The result is an equation that leads to smaller values of the disk pressure when compared with other models. It is expected that the pressure at the center of the disk is smaller than the average density multiplied by the local tidal acceleration at the equatorial plane. Still, the choice between the assortment of pressure relations is tantamount to the fine-tuning of the model. Within the thin disk approximation, all these approaches are equivalent, since they all assume vertical equilibrium and neglect self-gravity.

2. Following the BdHN scenario for the explanation of GRBs associated with Type Ic SNe (see Section 2), we considered a gas composed of ^{16}O at the outermost radius of the disk and followed the evolution of the ion content using the Saha equation to fix the local NSE. In [107], only ^{4}He is present, and in [112], ions up to ^{56}Fe are introduced.

The affinity between these cases implies that this particular model of disk accretion is insensible to the initial mass fraction distribution. This is explained by the fact that the average binding energy for most ions is very similar; hence, any cooling or heating due to a redistribution of nucleons, given by the NSE, is negligible when compared to the energy consumed by direct photodisintegration of alpha particles. Additionally, once most ions are dissociated, the main cooling mechanism is neutrino emission, which is similar for all models; the modulo includes the supplementary neutrino emission processes included in addition to electron and positron capture. However, during our numerical calculations, we noticed that the inclusion of non-electron neutrino emission processes can reduce the electron fraction by up to $\sim$8%. This effect was observed again during the simulation of flavor equipartition alluding to the need for detailed calculations of neutrino emissivities when establishing NSE state. We obtained similar results to [107] (see Figure 3), but by varying the accretion rate and fixing the viscosity parameter. This suggests that a more natural differentiating set of variables in the hydrodynamic equations of an α-viscosity disk is the combination of the quotient $\dot{M}/\alpha$ and either $\dot{M}$ or α. This result is already evident in, for example, Figures 11 and 12 of [107], but was not mentioned there.

Concerning neutrino oscillations, we showed that for the conditions inside the ignition radius, the oscillation potentials follow the relation $\langle \omega \rangle \ll \mu \ll \lambda$, as is illustrated by Figure 5. We also showed that within this region the number densities of electron neutrinos and antineutrinos are very similar. As a consequence of this particular environment, very fast pair conversions $\nu_e \bar{\nu}_e \rightleftharpoons \nu_x \bar{\nu}_x$, induced by bipolar oscillations, are obtained for the inverted mass hierarchy case with oscillation frequencies between 10^9 s^{-1} and 10^5 s^{-1}. For the normal hierarchy case, no flavor changes were observed (see Figures 6 and 7). Bearing in mind the magnitudes of these frequencies and the low neutrino travel times through the disk, we conclude that an accretion disk under our main assumption cannot represent a steady-state. However, using numerical and algebraic results obtained in [33,35,36] and references therein, we were able to generalize our model to a more realistic picture of neutrino oscillations. The main consequence of the interactions between neighboring regions of the disk is the onset of kinematic decoherence in a timescale in the order of the oscillation times. Kinematic decoherence induces a fast flavor equipartition among electronic and non-electronic neutrinos throughout the disk. Therefore, the neutrino content emerging from the disk is very different from the one that is usually assumed (see, e.g., [113,117,171]). The comparison between disks with and without flavor equipartition is summarized in Figure 8 and Table 3. We found that the flavor equipartition, while leaving antineutrino cooling practically unchanged, it enhances neutrino cooling by allowing the energy contained (and partially trapped inside the disk due to high opacity) within the ν_e gas to escape in the form of ν_x, rendering the disk insensible to the electron neutrino opacity. We give in Equation (77) a relation to estimate the change in F_ν as a function of $\tau_{\nu_e}\tau_{\nu_x}$ that describes correctly the behavior of the disk under the flavor equipartition. The variation of the flavor content in the emission flux implies a loss in L_{ν_e} and an increase in L_{ν_x} and $L_{\bar{\nu}_e}$. As a consequence, the total energy deposition rate of the process $\nu + \bar{\nu} \rightarrow e^- + e^+$ is reduced. We showed that this reduction can be as high 80% and is maximal whenever the quotient $\tau_{\nu_e}/\tau_{\nu_x}$ is also maximal and the condition $\tau_{\nu_e} > 1$ is obtained.

At this point, we can identify several issues which must still to be investigated in view of the results we have presented:

First, throughout the accretion disk literature, several fits of the neutrino and neutrino annihilation luminosity can be found (see, e.g., [99] and references therein). However, all these fits were calculated without taking into account neutrino oscillations. Since we have shown that oscillations directly impact luminosity, these results need to be extended.

Second, the calculations of the neutrino and antineutrino annihilation luminosities we have performed ignore general relativistic effects, save for the correction given by the capture function, and the possible neutrino oscillations from the disk surface to the

annihilation point. In [172], it has been shown that general relativistic effects can enhance the neutrino annihilation luminosity in a neutron star binary merger by a factor of 10. In [100], however, it is argued that in BHs this effect has to be mild since the energy gained by falling into the gravitational potential is lost by the electron–positron pairs when they climb back up. Nonetheless, this argument ignores the bending of neutrino trajectories and neutrino capture by the BH which can be significant for $r \lesssim 10 r_s$. In [173], the increment is calculated to be no more than a factor of 2 and can be less depending on the geometry of the emitting surface. However, as before, these calculations assume a purely $\nu_e \bar{\nu}_e$ emission and ignore oscillations after the emission. Simultaneously, the literature on neutrino oscillation above accretion disks (see, e.g., [113,117]) does not take int account oscillations inside the disk and assume only $\nu_e \bar{\nu}_e$ emission. A similar situation occurs in works studying the effect of neutrino emission on r-process nucleosynthesis in hot outflows (wind) ejected from the disk (see, e.g., [174]).

It is still unclear how the complete picture (oscillations inside the disk → oscillations above the disk + relativistic effects) affects the final energy deposition. We are currently working on the numerical calculation of the annihilation energy deposition rate using a ray tracing code and including neutrino oscillations from the point of their creation until they are annihilated—i.e., within the accretion disk and after its emission from the surface of the disk and during its trajectory until reaching the annihilation point. These results and their consequences for the energy deposition annihilation rate will be the subject of a future publication.

The knowledge of the final behavior of a neutrino-dominated accretion disk with neutrino oscillations requires time-dependent, multi-dimensional, neutrino-transport simulations coupled with the evolution of the disk. These simulations are computationally costly even for systems with a high degree of symmetry, therefore a first approximation is needed to identify key theoretical and numerical features involved in the study of neutrino oscillations in neutrino-cooled accretion disks. This work serves as a platform for such a first approximation. Considering that kinematic decoherence is a general feature of anisotropic neutrino gases, with the simplified model presented here, we were able to obtain an analytical result that agrees with the physics understanding of accretion disks.

In [171] it is pointed out that for a total energy in $\bar{\nu}_e$ of 10^{52} erg and an average neutrino energy $\langle E_{\nu,\bar{\nu}} \rangle \sim 20$ MeV, the Hyper-Kamiokande neutrino-horizon is in the order of 1 Mpc. If we take a total energy carried out by $\bar{\nu}_e$ in the order of the gravitational gain by accretion ($E_g \sim 10^{52}$–10^{53} erg) in the more energetic case of binary-driven hypernovae and the neutrino energies in Figure 3, we should expect the neutrino-horizon distance to be also in the order of 1 Mpc. However, if we adopt the local binary-driven hypernovae rate ~ 1 Gpc^{-3} yr^{-1} [175], it is clear that the direct detection of this neutrino signal is quite unlikely. However, we have shown that neutrino oscillation can have an effect on $e^- e^+$ plasma production above BHs in GRB models. Additionally, the unique conditions inside the disk and its geometry lend themselves to a variety of neutrino oscillations that can have impacts on other astrophysical phenomena, not only in plasma production, but also in r-process nucleosynthesis in disk winds. This, in particular, is the subject of a future publication. As such, this topic deserves appropriate attention, since it paves the way for new, additional astrophysical scenarios for testing neutrino physics.

Abbreviations

The following abbreviations are used in this manuscript:

BdHN	Binary-Driven Hypernova
BH	Black Hole
CF	Coordinate Frame
CO_{core}	Carbon–Oxygen Star
CRF	Co-rotating Frame
GRB	Gamma-ray Burst
IGC	Induced Gravitational Collapse
ISCO	Innermost Stable Circular Orbit
LNRF	Locally Non-Rotating Frame
MSW	Mikheyev–Smirnov–Wolfenstein
NDAF	Neutrino-Dominated Accretion Flows
NS	Neutron Star
NSE	Nuclear Statistical Equilibrium
SN	Supernova

Appendix A. Transformations and Christoffel Symbols

For the sake of completeness, here we give the explicitly the transformation used in Equation (5) and the Christoffel symbols used during calculations. The coordinate transformation matrices between the CF and the LNRF on the tangent vector space is [123]

$$
e_{\hat{v}}{}^{\mu} = \begin{pmatrix} \frac{1}{\sqrt{\omega^2 g_{\phi\phi} - g_{tt}}} & 0 & 0 & 0 \\ 0 & \frac{1}{\sqrt{g_{rr}}} & 0 & 0 \\ 0 & 0 & \frac{1}{\sqrt{g_{\theta\theta}}} & 0 \\ \frac{\omega}{\sqrt{\omega^2 g_{\phi\phi} - g_{tt}}} & 0 & 0 & \frac{1}{\sqrt{g_{\phi\phi}}} \end{pmatrix}, \quad e^{\hat{v}}{}_{\mu} = \begin{pmatrix} \sqrt{\omega^2 g_{\phi\phi} - g_{tt}} & 0 & 0 & 0 \\ 0 & \sqrt{g_{rr}} & 0 & 0 \\ 0 & 0 & \sqrt{g_{\theta\theta}} & 0 \\ -\omega\sqrt{g_{\phi\phi}} & 0 & 0 & \sqrt{g_{\phi\phi}} \end{pmatrix}, \quad (A1)
$$

so that the basis vectors transform as $\partial_{\hat{v}} = e^{\mu}{}_{\tilde{v}} \partial_{\mu}$, that is, with e^T. For clarity, coordinates on the LNRF have a caret $(x^{\hat{\mu}})$, coordinates on the CRF have a tilde $(x^{\tilde{\mu}})$ and coordinates on the LRF have two $(x^{\tilde{\hat{\mu}}})$. An observer on the LNRF sees the fluid elements move with an azimuthal velocity $\beta^{\hat{\phi}}$. This observer then can perform a Lorentz boost $L_{\beta^{\hat{\phi}}}$ to a new frame. On this new frame an observer sees the fluid elements falling radially with velocity $\beta^{\tilde{r}}$, so it can perform another Lorentz boost $L_{\beta^{\tilde{r}}}$ to the LRF. Finally, the transformation between the the LRF and the CF coordinates $x^{\mu} = e_{\hat{\rho}}{}^{\mu} (L_{\beta^{\hat{\phi}}})_{\tilde{\alpha}}{}^{\hat{\rho}} (L_{\beta^{\tilde{r}}})_{\tilde{v}}{}^{\tilde{\alpha}} x^{\tilde{v}} = A_{\tilde{v}}{}^{\mu} x^{\tilde{v}}$, where the components of A are

$$
A^{\tilde{v}}{}_{\mu} = \begin{pmatrix} \gamma_{\tilde{r}} \gamma_{\hat{\phi}} \left(\sqrt{\omega^2 g_{\phi\phi} - g_{tt}} + \beta^{\hat{\phi}} \omega \sqrt{g_{\phi\phi}} \right) & -\gamma_{\tilde{r}} \beta^{\tilde{r}} \sqrt{g_{rr}} & 0 & -\gamma_{\tilde{r}} \gamma_{\hat{\phi}} \beta^{\hat{\phi}} \sqrt{g_{\phi\phi}} \\ -\gamma_{\hat{\phi}} \gamma_{\tilde{r}} \beta^{\tilde{r}} \left(\sqrt{\omega^2 g_{\phi\phi} - g_{tt}} + \beta^{\hat{\phi}} \omega \sqrt{g_{\phi\phi}} \right) & \gamma_{\tilde{r}} \sqrt{g_{rr}} & 0 & \gamma_{\tilde{r}} \gamma_{\hat{\phi}} \beta^{\tilde{r}} \beta^{\hat{\phi}} \sqrt{g_{\phi\phi}} \\ 0 & 0 & \sqrt{g_{\theta\theta}} & 0 \\ -\gamma_{\hat{\phi}} \left(\beta^{\hat{\phi}} \sqrt{\omega^2 g_{\phi\phi} - g_{tt}} + \omega \sqrt{g_{\phi\phi}} \right) & 0 & 0 & \gamma_{\hat{\phi}} \sqrt{g_{\phi\phi}} \end{pmatrix}. \quad (A2)
$$

Since Lorentz transformations do not commute, the transformation A raises the question: what happens if we invert the order? In this case, we would not consider a co-rotating frame but a cofalling frame on which observers see fluid elements, not falling, but rotating. The new transformation velocities $\beta^{r'}$, $\beta^{\phi'}$ are subject to the conditions $\beta^{\phi'} = \gamma_{r'} \beta^{\hat{\phi}}$,

$\beta^{r'} = \beta^{\tilde{r}}/\gamma_{\hat{\phi}}$ and $\gamma_{r'}\gamma_{\phi'} = \gamma_{\tilde{r}}\gamma_{\hat{\phi}}$. Although both approaches are valid, considering that the radial velocity is an unknown, the first approach is clearly cleaner. To obtain the coordinate transformation between the CF and the CRF $A_{\tilde{\nu}}{}^{\mu}$ and $A^{\tilde{\nu}}{}_{\mu}$ we can simply set $\beta^{\tilde{r}} = 0$ in Equation (A2). With this, we can calculate

$$\frac{d\hat{\phi}}{d\hat{t}} = \beta^{\hat{\phi}} = \frac{u^{\mu}e^{\hat{\phi}}{}_{\mu}}{u^{\nu}e^{\hat{t}}{}_{\nu}} = \sqrt{\frac{g_{\phi\phi}}{\omega^2 g_{\phi\phi} - g_{tt}}}(\Omega - \omega), \tag{A3}$$

and

$$d\tilde{r} = \sqrt{g_{rr}}dr, \quad d\tilde{t} = \frac{\gamma_{\hat{\phi}}}{\sqrt{\omega^2 g_{\phi\phi} - g_{tt}}}dt = \frac{1}{\sqrt{-g_{tt} - 2\Omega g_{t\phi} - \Omega^2 g_{\phi\phi}}}dt, \quad d\tilde{\theta} = \sqrt{g_{\theta\theta}}d\theta. \tag{A4}$$

The non-vanishing Christoffel symbols are

$$
\begin{aligned}
&\Gamma^{t}{}_{tr} = \frac{M(r^2 - M^2 a^2 \cos^2\theta)(r^2 + M^2 a^2)}{\Sigma^2 \Delta}, \quad \Gamma^{t}{}_{t\theta} = -\frac{M^3 a^2 r \sin 2\theta}{\Sigma^2}, \\
&\Gamma^{t}{}_{r\phi} = -\frac{M^2 a(3r^4 + M^2 a^2 r^2 + M^2 a^2 \cos^2\theta(r^2 - M^2 a^2))\sin^2\theta}{\Sigma^2 \Delta}, \\
&\Gamma^{t}{}_{\theta\phi} = \frac{2M^4 a^3 r \cos\theta \sin^3\theta}{\Sigma^2}, \quad \Gamma^{r}{}_{tt} = \frac{M\Delta(r^2 - M^2 a^2 \cos^2\theta)}{\Sigma^3}, \\
&\Gamma^{r}{}_{t\phi} = -\frac{M^2 a\Delta(r^2 - M^2 a^2 \cos^2\theta)\sin^2\theta}{\Sigma^3}, \\
&\Gamma^{r}{}_{rr} = \frac{r}{\Sigma} + \frac{M - r}{\Delta}, \quad \Gamma^{r}{}_{r\theta} = -\frac{M^2 a^2 \sin\theta}{M^2 a^2 \cos\theta + r^2 \tan\theta}, \quad \Gamma^{r}{}_{\theta\theta} = -\frac{r\Delta}{\Sigma}, \\
&\Gamma^{r}{}_{\phi\phi} = \left(Ma\Gamma^{r}{}_{t\phi} - \Gamma^{r}{}_{\theta\theta}\right)\sin^2\theta, \quad \Gamma^{\theta}{}_{tt} = -\Gamma^{t}{}_{\theta\theta}\frac{\csc^2\theta}{Ma\Sigma}, \quad \Gamma^{\theta}{}_{t\phi} = \frac{M^2 ar(r^2 + M^2 a^2)\sin 2\theta}{\Sigma^3}, \\
&\Gamma^{\theta}{}_{rr} = \frac{M^2 a^2 \sin\theta\cos\theta}{\Sigma\Delta}, \quad \Gamma^{\theta}{}_{t\theta} = \frac{r}{\Sigma}, \quad \Gamma^{\theta}{}_{\theta\theta} = \Gamma^{r}{}_{r\theta}, \\
&\Gamma^{\theta}{}_{\phi\phi} = \left(\frac{\Delta}{\Sigma} + \frac{2Mr(r^2 + M^2 a^2)^2}{\Sigma^3}\right)\sin\theta\cos\theta, \quad \Gamma^{\phi}{}_{tr} = -\frac{M^2 a(r^2 - M^2 a^2 \cos^2\theta)}{\Sigma^2 \Delta}, \\
&\Gamma^{\phi}{}_{t\theta} = -\frac{2M^2 ar \cot\theta}{\Sigma^2}, \quad \Gamma^{\phi}{}_{r\phi} = \frac{r(\Sigma - 2Mr)}{\Sigma\Delta} + \frac{Ma\Sigma}{\Delta^2}\Gamma^{r}{}_{t\phi}, \quad \Gamma^{\phi}{}_{\theta\phi} = \cot\theta - \Gamma^{t}{}_{t\theta}.
\end{aligned}
\tag{A5}
$$

Using the connection coefficients and the metric, both evaluated at the equatorial plane we can collect several equations for averaged quantities. The expansion of the fluid world lines is

$$\boldsymbol{\theta} = \nabla_{\mu}u^{\mu} = \frac{2}{r}u^r + \partial_r u^r. \tag{A6}$$

There are several ways to obtain an approximate version of the shear tensor (e.g., [124,176,177]) but by far the simplest one is proposed by [127]. On the CRF the fluid four-velocity can be approximated by $u^{\tilde{\mu}} = (1,0,0,0)$ by Equation (6). Both the fluid four-acceleration $a_{\nu} = u^{\mu}\nabla_{\mu}u_{\nu}$ and expansion parameter, Equation (A6), vanish so that the shear tensor reduces to $2\sigma_{\tilde{\mu}\tilde{\nu}} = \nabla_{\tilde{\mu}}u_{\tilde{\nu}} + \nabla_{\tilde{\nu}}u_{\tilde{\mu}}$. In particular, the r-ϕ component is

$$\sigma_{\tilde{r}\tilde{\phi}} = -\frac{1}{2}\left(\Gamma^{\tilde{t}}{}_{\tilde{\phi}\tilde{r}} + \Gamma^{\tilde{t}}{}_{\tilde{r}\tilde{\phi}}\right) = -\frac{1}{4}\left(2c_{\tilde{t}\tilde{\phi}}{}^{\tilde{r}} + 2c_{\tilde{t}\tilde{r}}{}^{\tilde{\phi}}\right) = \frac{1}{2}c_{\tilde{r}\tilde{t}}{}^{\tilde{\phi}} = \frac{\gamma_{\hat{\phi}}^2}{2}\frac{\sqrt{g_{\phi\phi}}}{\sqrt{\omega^2 g_{\phi\phi} - g_{tt}}\sqrt{g_{rr}}}\partial_r\Omega, \tag{A7}$$

where $c_{\tilde{\mu}\tilde{\nu}}{}^{\tilde{\alpha}}$ are the commutation coefficients for the CRF. Finally, of particular interest is the $\tilde{\theta}$ component of the Riemann curvature tensor

$$R^{\tilde{\theta}}{}_{\tilde{t}\tilde{\theta}\tilde{t}}\bigg|_{\theta=\pi/2} = \frac{M}{r^3}\frac{r^2 - 4aM^{3/2}r^{1/2} + 3M^2 a^2}{r^2 - 3Mr + 2aM^{3/2}r^{1/2}}, \tag{A8}$$

which gives a measurement of the relative acceleration in the $\tilde{\theta}$ direction of nearly equatorial geodesics.

Appendix B. Stress–Energy Tensor

Here we present some equations related to the stress–energy that we used in this paper. Equation (9) for a zero bulk viscosity fluid in components is

$$T_{\nu}^{\mu} = \Pi u^{\mu} u_{\nu} + P \delta_{\nu}^{\mu} - 2\eta \sigma_{\nu}^{\mu} + q^{\mu} u_{\nu} + q_{\nu} u^{\mu}, \tag{A9}$$

whose (vanishing) covariant derivative is

$$
\begin{aligned}
\nabla_{\mu} T_{\nu}^{\mu} &= u^{\mu} u_{\nu} \partial_{\mu} \Pi + \Pi \theta u_{\nu} + \Pi a_{\nu} + \partial_{\nu} P - 2\eta \nabla_{\mu} \sigma_{\nu}^{\mu} + q^{\mu} \nabla_{\mu} u_{\nu} + u_{\nu} \nabla_{\mu} q^{\mu} + q_{\nu} \theta + u^{\mu} \nabla_{\mu} q_{\nu} \\
&= u^{\mu} \left[u_{\nu} \left(\partial_{\mu} \Pi - \frac{\Pi}{\rho} \partial_{\mu} \rho \right) - \frac{q_{\nu}}{\rho} \partial_{\mu} \rho \right] + \Pi a_{\nu} + \partial_{\nu} P - 2\eta \nabla_{\mu} \sigma_{\nu}^{\mu} + q^{\mu} \nabla_{\mu} u_{\nu} + u_{\nu} \nabla_{\mu} q^{\mu} + u^{\mu} \nabla_{\mu} q_{\nu},
\end{aligned} \tag{A10}
$$

where baryon conservation is used $\rho\theta = -u^{\mu}\partial_{\mu}\rho$. To get an equation of motion for the fluid, we project along the direction perpendicular to u_{ν}

$$
\begin{aligned}
P_{\beta}^{\nu} \nabla_{\mu} T_{\nu}^{\mu} &= u^{\mu} \left[u_{\beta} \left(\partial_{\mu} \Pi - \frac{\Pi}{\rho} \partial_{\mu} \rho \right) - \frac{q_{\beta}}{\rho} \partial_{\mu} \rho \right] + \Pi a_{\beta} + \partial_{\beta} P - 2\eta \nabla_{\mu} \sigma_{\beta}^{\mu} + q^{\mu} \nabla_{\mu} u_{\beta} + u_{\beta} \nabla_{\mu} q^{\mu} \\
&\quad + u^{\mu} \nabla_{\mu} q_{\beta} - u^{\mu} u_{\beta} \left[\partial_{\mu} \Pi - \frac{\Pi}{\rho} \partial_{\mu} \rho \right] + u^{\nu} u_{\beta} \partial_{\nu} P - 2\eta u^{\nu} u_{\beta} \nabla_{\mu} \sigma_{\nu}^{\mu} - u_{\beta} \nabla_{\mu} q^{\mu} + u^{\nu} u_{\beta} u^{\mu} \nabla_{\mu} q_{\nu} \\
&= -\frac{q_{\beta}}{\rho} u^{\mu} \partial_{\mu} \rho + \Pi a_{\beta} + \partial_{\beta} P - 2\eta \nabla_{\mu} \sigma_{\beta}^{\mu} + q^{\mu} \nabla_{\mu} u_{\beta} + u^{\mu} \nabla_{\mu} q_{\beta} + u_{\beta} u^{\nu} \partial_{\nu} P - 2\eta u^{\nu} u_{\beta} \nabla_{\mu} \sigma_{\nu}^{\mu} + u^{\nu} u_{\beta} u^{\mu} \nabla_{\mu} q_{\nu} \\
&= -\frac{q_{\beta}}{\rho} u^{\mu} \partial_{\mu} \rho + \Pi a_{\beta} + \partial_{\beta} P - 2\eta \nabla_{\mu} \sigma_{\beta}^{\mu} + q^{\mu} \nabla_{\mu} u_{\beta} + u^{\mu} \nabla_{\mu} q_{\beta} + u_{\beta} \left(u^{\nu} \partial_{\nu} P + 2\eta \sigma^{\mu\nu} \sigma_{\mu\nu} - q_{\nu} a^{\nu} \right),
\end{aligned} \tag{A11}
$$

where the identities $q_{\mu} u^{\mu} = u^{\mu} a_{\mu} = \sigma^{\mu\nu} u_{\nu} = 0$, $u_{\mu} u^{\nu} = -1$, $\sigma^{\mu\nu} \sigma_{\mu\nu} = \sigma^{\mu\nu} \nabla_{\mu} u_{\nu}$ are used. Combining the Equations (A10) and (A11) we get

$$u^{\mu} \left[\partial_{\mu} U - \frac{U + P}{\rho} \partial_{\mu} \rho \right] = 2\eta \sigma^{\mu\nu} \sigma_{\mu\nu} - q_{\mu} a^{\mu} - \nabla_{\mu} q^{\mu}. \tag{A12}$$

With Equation (A6) we can obtain an equation for mass conservation

$$
\begin{aligned}
0 &= \nabla_{\mu} (\rho u^{\mu}) = u^{\mu} \partial_{\mu} \rho + \rho \theta = u^{\mu} \partial_{\mu} \rho + \rho \left(\frac{2}{r} u^{r} + \partial_{r} u^{r} \right), \\
&\Rightarrow \partial_{r} \left(r^{2} \rho u^{r} \right) + r^{2} u^{j} \partial_{j} \rho = 0, \quad \text{for } j \in \{t, \theta, \phi\}.
\end{aligned} \tag{A13}
$$

Finally, we reproduce the zero torque at the innermost stable circular orbit condition that appears in [128]. Using the killing vector fields ∂_{ϕ}, ∂_{t} and the approximation $\Pi \approx \rho$, we can calculate

$$
\begin{aligned}
0 &= \boldsymbol{\nabla} \cdot (\boldsymbol{T} \cdot \partial_{\phi}) = \nabla_{\mu} T_{\phi}^{\mu} = \frac{1}{\sqrt{-g}} \partial_{\mu} \left(\sqrt{-g} T_{\phi}^{\mu} \right) \approx \frac{1}{r^{2}} \partial_{r} \left(\rho u^{r} u_{\phi} r^{2} - 2\eta \sigma_{\phi}^{r} r^{2} \right) + u_{\phi} \partial_{\theta} q^{\theta}, \\
&\Rightarrow \partial_{r} \left(\rho u^{r} u_{\phi} r^{2} - 2\eta \sigma_{\phi}^{r} r^{2} \right) = -r^{2} u_{\phi} \partial_{\theta} q^{\theta}, \\
&\Rightarrow \partial_{r} \left(\frac{\dot{M}}{2\pi} u_{\phi} + 4 r H \eta \sigma_{\phi}^{r} \right) = 2 H u_{\phi} \epsilon,
\end{aligned} \tag{A14}
$$

where we integrated vertically and used Equation (16). Analogously, using Equation (11) we obtain

$$\partial_{r} \left(\frac{\dot{M}}{2\pi} u_{t} - 4 r H \Omega \eta \sigma_{\phi}^{r} \right) = 2 H u_{t} \epsilon. \tag{A15}$$

The vertical integration of the divergence of the heat flux is as follows: Since, on average, $\boldsymbol{q} = q^{\theta}\boldsymbol{\partial}_{\theta}$, we have $\nabla_{\mu}q^{\mu} = \partial_{\theta}q^{\theta}$ and by Equation (A2), $q^{\theta} = rq^{\hat{\theta}}$. Vertically integrating yields

$$\int_{\theta_{\min}}^{\theta_{\max}} \partial_{\theta}q^{\theta} rd\theta = rq^{\theta}\Big|_{\theta_{\min}}^{\theta_{\max}} = 2q^{\tilde{\hat{\theta}}} = 2H\epsilon, \tag{A16}$$

where $q^{\tilde{\hat{\theta}}}$ is the averaged energy flux radiating out of a face of the disk, as measured by an observer on the LRF, which we approximate as the half-thickness of the disk H times the average energy density per unit proper time ϵ lost by the disk. With the variable change $z = 8\pi r H \eta \sigma^r_{\phi}/\dot{M}$ and $y = 4\pi H \epsilon/\dot{M}$ the equations reduce to

$$\partial_r(u_{\phi} + z) = yu_{\phi}, \tag{A17a}$$
$$\partial_r(u_t - \Omega z) = yu_t. \tag{A17b}$$

Using the relation $\partial_r u_t = -\Omega\partial_r u_{\phi}$ (see Equation (10.7.29) in [178]) and $\partial_r(u_t + \Omega u_{\phi}) = u_{\phi}\partial_r\Omega$ we can combine the previous equations to obtain

$$z = -\frac{y(u_t + \Omega u_{\phi})}{\partial_r\Omega}, \tag{A18a}$$

$$\partial_r\left(AB^2\right) = B\partial_r u_{\phi}, \tag{A18b}$$

with $A = y/\partial_r\Omega$ and $B = u_t + \Omega u_{\phi}$. To integrate these equations we use the zero torque condition $z(r = r^*) = 0$ where r^* is the radius of the innermost stable circular orbit, which gives the relation

$$y = \frac{\partial_r\Omega}{(u_t + \Omega u_{\phi})^2}\int_{r^*}^r(u_t + \Omega u_{\phi})\partial_r u_{\phi}dr = \frac{\partial_r\Omega}{(u_t + \Omega u_{\phi})^2}\left(u_t u_{\phi}\Big|_{r^*}^r - 2\int_{r^*}^r u_{\phi}\partial_r u_t dr\right), \tag{A19}$$

or, equivalently,

$$8\pi H r \rho \nu_{\text{turb}}\sigma^r_{\phi} \approx 8\pi H r \Pi \nu_{\text{turb}}\sigma^r_{\phi} = -\frac{\dot{M}}{(u_t + \Omega u_{\phi})}\left(u_t u_{\phi}\Big|_{r^*}^r - 2\int_{r^*}^r u_{\phi}\partial_r u_t dr\right). \tag{A20}$$

Using Equation (5), the approximation $\gamma_{\tilde{r}} \approx 1$ and the variable change $r = xM^2$ the integral can be easily evaluated by partial fractions

$$8\pi H r \rho \nu_{\text{turb}}\sigma^r_{\phi} = \dot{M}Mf(x, x^*), \tag{A21a}$$

$$f(x, x^*) = \frac{x^3 + a}{x^{3/2}\sqrt{x^3 - 3x + 2a}}\left[x - x^* - \frac{3}{2}a\ln\left(\frac{x}{x^*}\right) + \frac{1}{2}\sum_{i=1}^3 \frac{ax_i^2 - 2x_i + a}{x_i^2 - 1}\ln\left(\frac{x - x_i}{x^* - x_i}\right)\right], \tag{A21b}$$

where x_1, x_2, x_3 are the roots of the polynomial $x^3 - 3x + 2a$.

Appendix C. Nuclear Statistical Equilibrium

The results in this section appear in [179]. We include them here since they are necessary to solve Equation (19). Neutrino dominated accretion disks reach densities above $\sim 10^7$ g cm^{-3} and temperatures above $\sim 5 \times 10^9$ K. For these temperatures, forward and reverse nuclear reactions are balanced and the abundances in the plasma are determined by the condition $\mu_i = Z_i\mu_p + N_i\mu_n$, that is, the Nuclear Statistical Equilibrium. However, for densities above 10^6 g cm^{-3}, the electron screening of charged particle reactions can affect the nuclear reaction rates. For this reason, to obtain an accurate NSE state it is necessary to include Coulomb corrections to the ion chemical potential. The Coulomb correction to the *i*-th chemical potential is given by

$$\frac{\mu_i^C}{T} = K_1 \left[\Gamma_i \sqrt{\Gamma_i + K_2} - K_2 \ln\left(\sqrt{\frac{\Gamma_i}{K_2}} + \sqrt{1 + \frac{\Gamma_i}{K_2}} \right) \right]$$

$$+ 2K_3 \left[\sqrt{\Gamma_i} - \arctan\sqrt{\Gamma_i} \right] + Z_1 \left[\Gamma_i - Z_2 \ln\left(1 + \frac{\Gamma_i}{Z_1}\right) \right] + \frac{Z_3}{2} \ln\left(1 + \frac{\Gamma_i^2}{Z_4}\right), \quad \text{(A22)}$$

and the ion coupling parameter in terms of the electron coupling parameter is $\Gamma_i = \Gamma_e Z_i^{5/3}$ with

$$\Gamma_e = \frac{e^2}{T} \left(\frac{4\pi Y_e n_B}{3} \right)^{1/3}. \quad \text{(A23)}$$

where e is the electron charge. The parameters K_i, C_i are given in Table A1.

Table A1. Constants appearing in Equation (A22). See [179].

K_1	K_2	K_3	Z_1	Z_2	Z_3	Z_4
-0.907347	0.62849	0.278497	4.50×10^{-3}	170.0	-8.4×10^{-5}	3.70×10^{-3}

Appendix D. Neutrino Interactions and Cross-Sections

In this appendix we include the neutrino emission rates and neutrino cross-sections used in the accretion disk model. These expressions have been covered in [180–186]. We also include the expression energy emission rate for $\nu\bar{\nu}$ annihilation into electron–positron pairs. Whenever possible we write the rates in terms of generalized Fermi functions since some numerical calculations were done following [187]. We list in Table A2 some useful expressions and constants in Planck units. The numerical values can be found in [141].

Table A2. Constants used throughout this appendix to calculate emissivities and cross-sections. All quantities are reported in Planck units.

Symbol	Value	Name
M_w	6.584×10^{-18}	W boson mass
g_w	0.653	Weak coupling constant
g_a	1.26	Axial-vector coupling constant
α^*	$\frac{1}{137}$	Fine structure constant
$\sin^2\theta_W$	0.231	Weinberg angle
$\cos^2\theta_c$	0.947	Cabibbo angle
G_F	1.738×10^{33}	Fermi coupling constant
$C_{v,e}$	$2\sin^2\theta_W + 1/2$	Weak interaction vector constant for ν_e
$C_{a,e}$	$1/2$	Weak interaction axial-vector constant for ν_e
$C_{v,e}$	$C_{v,e} - 1$	Weak interaction vector constant for ν_x
$C_{a,e}$	$C_{a,e} - 1$	Weak interaction axial-vector constant for ν_x
σ_0	6.546×10^{21}	Weak interaction cross-section

Appendix D.1. Neutrino Emissivities

- Pair annihilation: $e^- + e^+ \to \nu + \bar{\nu}$

This process generates neutrinos of all flavors but around 70% are electron neutrinos [71]. This is due to the fact that the only charged leptons in the accretion systems we study are electrons and positrons, so creation of electron neutrinos occurs via either charged or neutral electroweak currents while creation of non-electronic neutrinos can only

occur through neutral currents. Using the electron or positron four-momentum $p = (E, \boldsymbol{p})$, the Dicus cross-section for a particular flavor i is [180]

$$\sigma_{D,i} = \frac{G_F^2}{12\pi E_{e^-} E_{e^+}} \left[C_{+,i} \left(m_e^4 + 3m_e^2 p_{e^-} \cdot p_{e^+} + 2(p_{e^-} \cdot p_{e^+})^2 \right) + 3C_{-,i} \left(m_e^4 + m_e^2 p_{e^-} \cdot p_{e^+} \right) \right]. \quad \text{(A24)}$$

The factors $C_{\pm,i}$, are written in terms of the weak interaction vector and axial-vector constants: $C_{\pm,i} = C_{v,i}^2 \pm C_{a,i}^2$ [141]. Representing the Fermi–Dirac distribution for electrons (positrons) as f_{e^-} (f_{e^+}) with $\eta_{e^\mp}$ the electron (positron) degeneracy parameter including its rest mass. The number and energy emission rates can be calculated by replacing $\Lambda = 2$ and $\Lambda = E_{e^-} + E_{e^+}$ in the integral [184]:

$$\frac{4}{(2\pi)^6} \int \Lambda \sigma_D f_{e^-} f_{e^+} d^3\boldsymbol{p}_{e^-} d^3\boldsymbol{p}_{e^+}, \quad \text{(A25)}$$

giving the expressions

$$R_{\nu_i + \bar{\nu}_i} = \frac{G_F^2 m_e^8}{18\pi} [C_{+,i}(8\mathbb{U}_1 \mathbb{V}_1 + 5\mathbb{U}_{-1}\mathbb{V}_{-1} + 9\mathbb{U}_0\mathbb{V}_0 - 2\mathbb{U}_{-1}\mathbb{V}_1 - 2\mathbb{U}_1\mathbb{V}_{-1})$$

$$+ 9C_{-,i}(\mathbb{U}_{-1}\mathbb{V}_{-1} + \mathbb{U}_0\mathbb{V}_0)], \quad \text{(A26a)}$$

$$Q_{\nu_i + \bar{\nu}_i} = \frac{G_F^2 m_e^9}{36\pi} [C_{+,i}(8(\mathbb{U}_2\mathbb{V}_1 + \mathbb{U}_1\mathbb{V}_2) + 7(\mathbb{U}_1\mathbb{V}_0 + \mathbb{U}_0\mathbb{V}_1) + 5(\mathbb{U}_{-1}\mathbb{V}_0 + \mathbb{U}_0\mathbb{V}_{-1})$$

$$- 2(\mathbb{U}_2\mathbb{V}_{-1} + \mathbb{U}_{-1}\mathbb{V}_2)) + 9C_{-,i}(\mathbb{U}_0(\mathbb{V}_1 + \mathbb{V}_{-1}) + \mathbb{V}_0(\mathbb{U}_1 + \mathbb{U}_{-1}))]. \quad \text{(A26b)}$$

The functions $\mathbb{U}, \mathbb{V}$ can be written in terms of generalized Fermi functions

$$\mathbb{U}_j = \sqrt{2}\xi^{3/2} \sum_{k=0}^{j+1} \binom{j+1}{k} \xi^k \mathcal{F}_{k+1/2,0}(\xi, \eta_{e^-}), \quad \text{(A27a)}$$

$$\mathbb{V}_j = \sqrt{2}\xi^{3/2} \sum_{k=0}^{j+1} \binom{j+1}{k} \xi^k \mathcal{F}_{k+1/2,0}(\xi, \eta_{e^+}). \quad \text{(A27b)}$$

It is often useful to define the functions

$$\varepsilon_i^m = \frac{2G_F^2 (m_e)^4}{3(2\pi)^7} \int f_{e^-} f_{e^+} \left(E_{e^-}^m + E_{e^+}^m \right) \sigma_{D,i} \, d^3\boldsymbol{p}_{e^-} d^3\boldsymbol{p}_{e^+}. \quad \text{(A28)}$$

For $m = 0$ and $m = 1$ Equation (A28) gives the neutrino and antineutrino number emissivity (neutrino production rate), and the neutrino and antineutrino energy emissivity (energy per unit volume per unit time) for a certain flavor i, respectively (that is, Equation (A26)). Hence, not only we are able to calculate the total number and energy emissivity, but we can also calculate the neutrino or antineutrino energy moments with

$$\langle E_{\nu_i(\bar{\nu}_i)}^m \rangle = \frac{\varepsilon_i^m}{\varepsilon_i^0}, \quad \text{for } m \geq 1. \quad \text{(A29)}$$

- Electron capture and positron capture: $p + e^- \to n + \nu_e$, $n + e^+ \to p + \bar{\nu}_e$ and $A + e^- \to A' + \nu_e$

  Due to lepton number conservation this process generated only electron (anti)neutrinos. The number and energy emission rates for electron and positron capture by nucleons are

$$R_{\nu_e} = \frac{m_e^5 G_F^2 \cos^2\theta_c}{\sqrt{2}\pi^3}\left(1 + 3g_A^2\right)\Delta_{np}\xi^{3/2}\Big[\xi^3 \mathcal{F}_{7/2,\chi}(\xi,\eta_{e^-})$$
$$+ (3 - 2\mathbb{Q})\xi^2 \mathcal{F}_{5/2,\chi}(\xi,\eta_{e^-}) + (1 - \mathbb{Q})(3 - \mathbb{Q})\xi \mathcal{F}_{3/2,\chi}(\xi,\eta_{e^-}) + (1 - \mathbb{Q})^2 \mathcal{F}_{1/2,\chi}(\xi,\eta_{e^-})\Big], \quad \text{(A30a)}$$

$$Q_{\nu_e} = \frac{m_e^6 G_F^2 \cos^2\theta_c}{\sqrt{2}\pi^3}\left(1 + 3g_A^2\right)\Delta_{np}\xi^{3/2}\Big[\xi^4 \mathcal{F}_{9/2,\chi}(\xi,\eta_{e^-})$$
$$+ \xi^3(4 - 3\mathbb{Q})\mathcal{F}_{7/2,\chi}(\xi,\eta_{e^-}) + 3(\mathbb{Q} - 1)(\mathbb{Q} - 2)\xi^2 \mathcal{F}_{5/2,\chi}(\xi,\eta_{e^-})$$
$$+ (1 - \mathbb{Q})^2(4 - \mathbb{Q})\xi \mathcal{F}_{3/2,\chi}(\xi,\eta_{e^-}) + (1 - \mathbb{Q})^3 \mathcal{F}_{1/2,\chi}(\xi,\eta_{e^-})\Big], \quad \text{(A30b)}$$

$$R_{\bar{\nu}_e} = \frac{m_e^5 G_F^2 \cos^2\theta_c}{\sqrt{2}\pi^3}\left(1 + 3g_A^2\right)\Delta_{pn}\xi^{3/2}\Big[\xi^3 \mathcal{F}_{7/2,0}(\xi,\eta_{e^+})$$
$$+ (3 + 2\mathbb{Q})\xi^2 \mathcal{F}_{5/2,0}(\xi,\eta_{e^+}) + (1 + \mathbb{Q})(3 + \mathbb{Q})\xi \mathcal{F}_{3/2,0}(\xi,\eta_{e^+}) + (1 + \mathbb{Q})^2 \mathcal{F}_{1/2,0}(\xi,\eta_{e^+})\Big], \quad \text{(A30c)}$$

$$Q_{\bar{\nu}_e} = \frac{m_e^6 G_F^2 \cos^2\theta_c}{\sqrt{2}\pi^3}\left(1 + 3g_A^2\right)\Delta_{np}\xi^{3/2}\Big[\xi^4 \mathcal{F}_{9/2,0}(\xi,\eta_{e^+})$$
$$+ \xi^3(4 + 3\mathbb{Q})\mathcal{F}_{7/2,0}(\xi,\eta_{e^+}) + 3(\mathbb{Q} + 1)(\mathbb{Q} + 2)\xi^2 \mathcal{F}_{5/2,0}(\xi,\eta_{e^+})$$
$$+ (1 + \mathbb{Q})^2(4 + \mathbb{Q})\xi \mathcal{F}_{3/2,0}(\xi,\eta_{e^+}) + (1 + \mathbb{Q})^3 \mathcal{F}_{1/2,0}(\xi,\eta_{e^+})\Big], \quad \text{(A30d)}$$

where $\Delta_{ij} = (n_i - n_j)/\left(\exp(\eta_i - \eta_j) - 1\right)$, $i, j \in \{p, n\}$ are the Fermi blocking factors in the nucleon phase spaces and $\mathbb{Q} = (m_n - m_p)m_e \approx 2.531$ is the nucleon mass difference. The number and energy emission rates for electron capture by an ion i are

$$R_{\nu_e,i} = \frac{\sqrt{2}m_e^5 G_F^2 \cos^2\theta_c}{7\pi^3}g_A^2 n_i \kappa_{Z_i}\kappa_{N_i}\xi^{3/2}\Big[\xi^3 \mathcal{F}_{7/2,\tilde{\chi}}(\xi,\eta_{e^-})$$
$$+ (3 - 2\mathbb{Q})\xi^2 \mathcal{F}_{5/2,\tilde{\chi}}(\xi,\eta_{e^-}) + (1 - \mathbb{Q})(3 - \mathbb{Q})\xi \mathcal{F}_{3/2,\tilde{\chi}}(\xi,\eta_{e^-})(1 - \mathbb{Q})^2 \mathcal{F}_{1/2,\tilde{\chi}}(\xi,\eta_{e^-})\Big], \quad \text{(A31a)}$$

$$Q_{\nu_e,i} = \frac{\sqrt{2}m_e^6 G_F^2 \cos^2\theta_c}{7\pi^3}g_A^2 n_i \kappa_{Z_i}\kappa_{N_i}\xi^{3/2}\Big[\xi^4 \mathcal{F}_{9/2,\tilde{\chi}}(\xi,\eta_{e^-}) + \xi^3(4 - 3\mathbb{Q})\mathcal{F}_{7/2,\tilde{\chi}}(\xi,\eta_{e^-})$$
$$+ 3(\mathbb{Q} - 1)(\mathbb{Q} - 2)\xi^2 \mathcal{F}_{5/2,\tilde{\chi}}(\xi,\eta_{e^-}) + (1 - \mathbb{Q})^2(4 - \mathbb{Q})\xi \mathcal{F}_{3/2,\tilde{\chi}}(\xi,\eta_{e^-}) + (1 - \mathbb{Q})^3 \mathcal{F}_{1/2,\tilde{\chi}}(\xi,\eta_{e^-})\Big]. \quad \text{(A31b)}$$

The lower integration limits in these expressions are given by $\chi = (\mathbb{Q} - 1)/\xi$ and $\bar{\chi} = (\mu_n - \mu_p + \Delta)/T - 1/\xi$ where $\Delta \approx 2.457 \times 10^{-22}$ is the energy of the neutron $1f_{5/2}$ state above the ground state. The functions $\kappa_{Z_i}, \kappa_{N_i}$ are

$$\kappa_{Z_i} = \begin{cases} 0 & \text{if } Z_i \leq 20. \\ Z_i - 20 & \text{if } 20 < Z_i \leq 28., \\ 8 & \text{if } Z_i > 28. \end{cases} \quad \kappa_{N_i} = \begin{cases} 6 & \text{if } N_i \leq 34. \\ 40 - N_i & \text{if } 34 < N_i \leq 40. \\ 0 & \text{if } N_i > 40. \end{cases} \quad \text{(A32)}$$

- Plasmon decay: $\tilde{\gamma} \to \nu + \bar{\nu}$.

$$R_{\nu_e + \bar{\nu}_e} = \frac{C_{v,e}\sigma_0 T^8}{96\pi^3 m_e^2 \alpha^*}\tilde{\gamma}^6(\tilde{\gamma} + 1)\exp(-\tilde{\gamma}), \quad \text{(A33a)}$$

$$Q_{\nu_e + \bar{\nu}_e} = \frac{C_{v,e}\sigma_0 T^9}{192\pi^3 m_e^2 \alpha^*}\tilde{\gamma}^6\left(\tilde{\gamma}^2 + 2\tilde{\gamma} + 2\right)\exp(-\tilde{\gamma}), \quad \text{(A33b)}$$

$$R_{\nu_x + \bar{\nu}_x} = \frac{C_{v,x}\sigma_0 T^8}{48\pi^3 m_e^2 \alpha^*}\tilde{\gamma}^6(\tilde{\gamma} + 1)\exp(-\tilde{\gamma}), \quad \text{(A33c)}$$

$$Q_{\nu_x + \bar{\nu}_x} = \frac{C_{v,x}\sigma_0 T^9}{96\pi^3 m_e^2 \alpha^*}\tilde{\gamma}^6\left(\tilde{\gamma}^2 + 2\tilde{\gamma} + 2\right)\exp(-\tilde{\gamma}), \quad \text{(A33d)}$$

where $\tilde{\gamma} = \tilde{\gamma}_0\sqrt{\left(\pi^2 + 3(\eta_{e^-} + 1/\xi)^2\right)/3}$ and $\tilde{\gamma}_0 = 2\sqrt{\frac{\alpha^*}{3\pi}} \approx 5.565 \times 10^{-2}$.

- Nucleon-nucleon bremsstrahlung $n_1 + n_2 \to n_3 + n_4 + \nu + \bar{\nu}$.

The nucleon-nucleon bremsstrahlung produces the same amount of neutrinos of all three flavors. The number and energy emission rates can be approximated by (see, e.g., [186])

$$R_{\nu_i + \bar{\nu}_i} = \left(2.59 \times 10^{13}\right)\left(X_p^2 + X_n^2 + \frac{28}{3}X_p X_n\right)n_B^2 \xi^{9/2}, \tag{A34a}$$

$$Q_{\nu_i + \bar{\nu}_i} = \left(4.71 \times 10^{-9}\right)\left(X_p^2 + X_n^2 + \frac{28}{3}X_p X_n\right)n_B^2 \xi^{10/2}. \tag{A34b}$$

Appendix D.2. Cross-Sections

We consider four interactions to describe the (anti)neutrino total cross-section.

- Neutrino annihilation: $(\nu + \bar{\nu} \rightarrow e^- + e^+)$.

$$\sigma_{\nu_e \bar{\nu}_e} = \frac{4}{3}K_{\nu_e \bar{\nu}_e}\sigma_0 \frac{\langle E_{\nu_e}\rangle \langle E_{\bar{\nu}_e}\rangle}{m_e^2} \quad \text{with} \quad K_{\nu_e \bar{\nu}_e} = \frac{1 + 4\sin^2\theta_W + 8\sin^4\theta_W}{12}, \tag{A35a}$$

$$\sigma_{\nu_x \bar{\nu}_x} = \frac{4}{3}K_{\nu_x \bar{\nu}_x}\sigma_0 \frac{\langle E_{\nu_x}\rangle \langle E_{\bar{\nu}_x}\rangle}{m_e^2} \quad \text{with} \quad K_{\nu_x \bar{\nu}_x} = \frac{1 - 4\sin^2\theta_W + 8\sin^4\theta_W}{12}, \tag{A35b}$$

- Electron (anti)neutrino absorption by nucleons: $(\nu_e + n \rightarrow e^- + p$ and $\bar{\nu}_e + p \rightarrow e^+ + n)$.

$$\sigma_{\nu_e n} = \sigma_0 \left(\frac{1 + 3g_a^2}{4}\right)\left(\frac{\langle E_{\nu_e}\rangle}{m_e} + \mathbb{Q}\right)^2 \sqrt{1 - \frac{1}{\left(\frac{\langle E_{\nu_e}\rangle}{m_e} + \mathbb{Q}\right)^2}}, \tag{A36a}$$

$$\sigma_{\bar{\nu}_e p} = 3.83 \times 10^{22} \left(\frac{\wp\langle E_{\bar{\nu}_e}\rangle}{m_e} - \mathbb{Q}\right)^2 \sqrt{1 - \frac{1}{\left(\frac{\wp\langle E_{\bar{\nu}_e}\rangle}{m_e} - \mathbb{Q}\right)^2}}\left(\frac{\wp\langle E_{\bar{\nu}_e}\rangle}{m_e}\right)^{g(E_{\bar{\nu}_e})}, \tag{A36b}$$

$$g(E_{\bar{\nu}_e}) = -0.07056 + 0.02018\ln\left(\frac{\wp\langle E_{\bar{\nu}_e}\rangle}{m_e}\right) - 0.001953\ln^3\left(\frac{\wp\langle E_{\bar{\nu}_e}\rangle}{m_e}\right). \tag{A36c}$$

where $\wp = 0.511$.

- (anti)neutrino scattering by baryons: $(\nu + A_i \rightarrow \nu + A_i$ and $\bar{\nu} + A_i \rightarrow \bar{\nu} + A_i)$.

$$\sigma_p = \frac{\sigma_0 \langle E\rangle^2}{4m_e^2}\left(4\sin^4\theta_W - 2\sin^2\theta_W + \frac{1 + 3g_a^2}{4}\right), \tag{A37a}$$

$$\sigma_n = \frac{\sigma_0 \langle E\rangle^2}{4m_e^2}\frac{1 + 3g_a^2}{4}, \tag{A37b}$$

$$\sigma_{A_i} = \frac{\sigma_0 A_i^2 \langle E\rangle^2}{16m_e^2}\left[\left(4\sin^2\theta_W - 1\right)\frac{Z_i}{A_i} + 1 - \frac{Z_i}{A_i}\right]. \tag{A37c}$$

- (anti)neutrino scattering by electrons or positrons: $(\nu + e^\pm \rightarrow \nu + e^\pm$ and $\bar{\nu} + e^\pm \rightarrow \bar{\nu} + e^\pm)$.

$$\sigma_e = \frac{3}{8}\sigma_0 \xi \frac{\langle E\rangle}{m_e}\left(1 + \frac{\eta_e + 1/\xi}{4}\right)\left[(C_{v,i} + n_\ell C_{a,i})^2 + \frac{1}{3}(C_{v,i} - n_\ell C_{a,i})^2\right]. \tag{A38}$$

Here, n_ℓ is the (anti)neutrino lepton number (that is, 1 for neutrinos and -1 for antineutrinos, depending on the cross-section to be calculated), and in the last four expressions, $\langle E\rangle$ is replaced by the average (anti)neutrino energy of the corresponding flavor. With these expressions, the total opacity for neutrinos or antineutrinos is

$$\kappa_{\nu_i(\bar{\nu}_i)} = \frac{\sum_i \sigma_i n_i}{\rho}, \tag{A39}$$

where n_i is the number density of the target particle associated with the process corresponding to the cross-section σ_i. The (anti)neutrino optical depth appearing in Equation (32) can then be approximated as

$$\tau_{\nu_i(\bar{\nu}_i)} = \int \kappa_{\nu_i(\bar{\nu}_i)} \rho d\theta \approx \kappa_{\nu_i(\bar{\nu}_i)} \rho H. \tag{A40}$$

Appendix D.3. Neutrino-Antineutrino Pair Annihilation

Since the main interaction between $\nu\bar{\nu}$ is the annihilation into e^-e^+, this process above neutrino-cooled disks has been proposed as the origin of the energetic plasma involved in the production of GRBs. Once the (anti)neutrino energy emissivity and average energies are calculated it is possible to calculate the energy deposition rate of the process $\nu_i + \bar{\nu}_i \to e^- + e^+$ for each flavor i. Ignoring Pauli blocking effects in the phase spaces of electron and positrons, the local energy deposition rate at a position **r** by $\nu\bar{\nu}$ annihilation can be written in terms of the neutrino and antineutrino distributions $f_{\nu_i} = f_{\nu_i}(\mathbf{r}, E_\nu), f_{\bar{\nu}_i} = f_{\bar{\nu}_i}(\mathbf{r}, E_{\bar{\nu}})$ as [155]

$$\begin{aligned}
Q_{\nu_i\bar{\nu}_i} &= A_{1,i} \int_0^\infty dE_{\nu_i} \int_0^\infty dE_{\bar{\nu}_i} E_{\nu_i}^3 E_{\bar{\nu}_i}^3 (E_{\nu_i} + E_{\bar{\nu}_i}) \int_{S_2} d\Omega_{\nu_i} \int_{S_2} d\Omega_{\bar{\nu}_i} f_{\nu_i} f_{\bar{\nu}_i} (1 - \cos\theta)^2, \\
&+ A_{2,i} \int_0^\infty dE_{\nu_i} \int_0^\infty dE_{\bar{\nu}_i} E_{\nu_i}^2 E_{\bar{\nu}_i}^2 (E_{\nu_i} + E_{\bar{\nu}_i}) \int_{S_2} d\Omega_{\nu_i} \int_{S_2} d\Omega_{\bar{\nu}_i} f_{\nu_i} f_{\bar{\nu}_i} (1 - \cos\theta),
\end{aligned} \tag{A41}$$

where we have introduced the constants appearing in Equation (80)

$$\begin{aligned}
A_{1,i} &= \frac{\sigma_0 \left[(C_{v,i} - C_{a,i})^2 + (C_{v,i} + C_{a,i})^2 \right]}{12\pi^2 m_e^2}, \\
A_{2,i} &= \frac{\sigma_0 \left[2C_{v,i}^2 - C_{a,i}^2 \right]}{6\pi^2 m_e^2}.
\end{aligned} \tag{A42}$$

In Equation (A41), θ is the angle between the neutrino and antineutrino momentum and $d\Omega$ is the differential solid angle of the incident (anti)neutrino at **r**. The integral can be re-written in terms of the total intensity (energy integrated intensity) $I_\nu = \int E_\nu^3 f_\nu dE_\nu$ as [156]

$$\begin{aligned}
Q_{\nu_i\bar{\nu}_i} &= A_{1,i} \int_{S_2} d\Omega_{\nu_i} I_{\nu_i} \int_{S_2} d\Omega_{\bar{\nu}_i} I_{\bar{\nu}_i} (\langle E_{\nu_i} \rangle + \langle E_{\bar{\nu}_i} \rangle)(1 - \cos\theta)^2 \\
&+ A_{2,i} \int_{S_2} d\Omega_{\nu_i} I_{\nu_i} \int_{S_2} d\Omega_{\bar{\nu}_i} I_{\bar{\nu}_i} \frac{\langle E_{\nu_i} \rangle + \langle E_{\bar{\nu}_i} \rangle}{\langle E_{\nu_i} \rangle \langle E_{\bar{\nu}_i} \rangle}(1 - \cos\theta).
\end{aligned} \tag{A43}$$

The incident radiation intensity passing through the solid differential angle $d\Omega$ at **r** is the intensity $I_{\mathbf{r}_d,\nu}$ emitted from the point on the disk $\mathbf{r}_d$ diluted by the inverse square distance $r_k = |\mathbf{r} - \mathbf{r}_d|$ between both points. Finally, assuming that each point $\mathbf{r}_d$ on the disk's surface acts as a half-isotropic radiator of (anti)neutrinos, the total flux emitted at $\mathbf{r}_d$ is $F_{\mathbf{r}_d,\nu} = \int_0^{\pi/2} \int_0^{2\pi} I_{\mathbf{r}_d,\nu} \cos\theta' \sin\theta' d\theta' d\phi' = \pi I_{\mathbf{r}_d,\nu}$, with θ', ϕ' the direction angles at $\mathbf{r}_d$. Collecting all obtains

$$\begin{aligned}
Q_{\nu_i\bar{\nu}_i} &= A_{1,i} \int_{\mathbf{r}_{d,\nu_i} \in \text{disk}} d\mathbf{r}_{d,\nu_i} \int_{\mathbf{r}_{d,\bar{\nu}_i} \in \text{disk}} d\mathbf{r}_{d,\bar{\nu}_i} \frac{F_{\mathbf{r}_d,\nu_i}}{r_{k,\nu_i}^2} \frac{F_{\mathbf{r}_d,\bar{\nu}_i}}{r_{k,\bar{\nu}_i}^2} (\langle E_{\nu_i} \rangle + \langle E_{\bar{\nu}_i} \rangle)(1 - \cos\theta)^2 \\
&+ A_{2,i} \int_{\mathbf{r}_{d,\nu_i} \in \text{disk}} d\mathbf{r}_{d,\nu_i} \int_{\mathbf{r}_{d,\bar{\nu}_i} \in \text{disk}} d\mathbf{r}_{d,\bar{\nu}_i} \frac{F_{\mathbf{r}_d,\nu_i}}{r_{k,\nu_i}^2} \frac{F_{\mathbf{r}_d,\bar{\nu}_i}}{r_{k,\bar{\nu}_i}^2} \frac{\langle E_{\nu_i} \rangle + \langle E_{\bar{\nu}_i} \rangle}{\langle E_{\nu_i} \rangle \langle E_{\bar{\nu}_i} \rangle}(1 - \cos\theta).
\end{aligned} \tag{A44}$$

References

1. De Salas, P.F.; Forero, D.V.; Ternes, C.A.; Tortola, M.; Valle, J.W.F. Status of neutrino oscillations 2018: 3σ hint for normal mass ordering and improved CP sensitivity. *Phys. Lett. B* **2018**, *782*, 633–640. [CrossRef]
2. Wolfenstein, L. Neutrino Oscillations in Matter. *Phys. Rev. D* **1978**, *17*, 2369–2374. [CrossRef]
3. Mikheyev, S.P.; Smirnov, A.Y. Resonant amplification of ν oscillations in matter and solar-neutrino spectroscopy. *Il Nuovo Cimento C* **1986**, *9*, 17–26. [CrossRef]
4. Barbieri, R.; Dolgov, A. Neutrino oscillations in the early universe. *Nucl. Phys. B* **1991**, *349*, 743–753. [CrossRef]
5. Enqvist, K.; Kainulainen, K.; Maalampi, J. Refraction and Oscillations of Neutrinos in the Early Universe. *Nucl. Phys. B* **1991**, *349*, 754–790. [CrossRef]
6. Savage, M.J.; Malaney, R.A.; Fuller, G.M. Neutrino Oscillations and the Leptonic Charge of the Universe. *Astrophys. J.* **1991**, *368*, 1–11. [CrossRef]
7. Kostelecky, V.A.; Samuel, S. Neutrino oscillations in the early universe with an inverted neutrino mass hierarchy. *Phys. Lett. B* **1993**, *318*, 127–133. [CrossRef]
8. Kostelecky, V.A.; Samuel, S. Nonlinear neutrino oscillations in the expanding universe. *Phys. Rev. D* **1994**, *49*, 1740–1757. [CrossRef]
9. Kostelecký, V.; Pantaleone, J.; Samuel, S. Neutrino oscillations in the early universe. *Phys. Lett. B* **1993**, *315*, 46–50. [CrossRef]
10. McKellar, B.H.J.; Thomson, M.J. Oscillating doublet neutrinos in the early universe. *Phys. Rev. D* **1994**, *49*, 2710–2728. [CrossRef]
11. Lunardini, C.; Smirnov, A.Y. High-energy neutrino conversion and the lepton asymmetry in the universe. *Phys. Rev. D* **2001**, *64*, 73006. [CrossRef]
12. Dolgov, A.D.; Hansen, S.H.; Pastor, S.; Petcov, S.T.; Raffelt, G.G.; Semikoz, D.V. Cosmological bounds on neutrino degeneracy improved by flavor oscillations. *Nucl. Phys. B* **2002**, *632*, 363–382. [CrossRef]
13. Wong, Y.Y. Analytical treatment of neutrino asymmetry equilibration from flavor oscillations in the early universe. *Phys. Rev. D* **2002**, *66*, 25015. [CrossRef]
14. Abazajian, K.N.; Beacom, J.F.; Bell, N.F. Stringent constraints on cosmological neutrino-antineutrino asymmetries from synchronized flavor transformation. *Phys. Rev. D* **2002**, *66*, 13008. [CrossRef]
15. Kirilova, D.P. Neutrino oscillations and the early universe. *Cent. Eur. J. Phys.* **2004**, *2*, 467–491. [CrossRef]
16. Bahcall, J.N.; Concepcion Gonzalez-Garcia, M.; na-Garay, C.P. Solar Neutrinos Before and After KamLAND. *J. High Energy Phys.* **2003**, *2003*, 09. [CrossRef]
17. Balantekin, A.B.; Yuksel, H. Global Analysis of Solar Neutrino and KamLAND Data. *J. Phys. G Nucl. Part. Phys.* **2003**, *29*, 665. [CrossRef]
18. Fogli, G.L.; Lisi, E.; Marrone, A.; Montanino, D.; Palazzo, A.; Rotunno, A.M. Neutrino Oscillations: A Global Analysis. *arXiv* **2003**, arXiv:0310012.
19. de Holanda, P.C.; Smirnov, A.Y. Solar neutrinos: The SNO salt phase results and physics of conversion. *Astropart. Phys.* **2004**, *21*, 287–301. [CrossRef]
20. Giunti, C. Status of neutrino masses and mixing. *Eur. Phys. J. C* **2004**, *33*, 852–856. [CrossRef]
21. Maltoni, M.; Schwetz, T.; Tórtola, M.A.; Valle, J.W. Status of three-neutrino oscillations after the SNO-salt data. *Phys. Rev. D* **2003**, *68*, 113010. [CrossRef]
22. Dighe, A. Supernova neutrino oscillations: What do we understand? *J. Phys. Conf. Ser.* **2010**, *203*, 012015. [CrossRef]
23. Haxton, W.C.; Hamish Robertson, R.G.; Serenelli, A.M. Solar Neutrinos: Status and Prospects. *Annu. Rev. Astron. Astrophys.* **2013**, *51*, 21–61. [CrossRef]
24. Vissani, F. Solar neutrino physics on the beginning of 2017. *Nucl. Phys. At. Energy* **2017**, *18*, 5–12. [CrossRef]
25. Notzold, D.; Raffelt, G. Neutrino Dispersion at Finite Temperature and Density. *Nucl. Phys. B* **1988**, *307*, 924–936. [CrossRef]
26. Pantaleone, J. Neutrino oscillations at high densities. *Phys. Lett. B* **1992**, *287*, 128–132. [CrossRef]
27. Qian, Y.Z.; Fuller, G.M. Neutrino-neutrino scattering and matter enhanced neutrino flavor transformation in Supernovae. *Phys. Rev. D* **1995**, *51*, 1479–1494. [CrossRef] [PubMed]
28. Pastor, S.; Raffelt, G. Flavor oscillations in the supernova hot bubble region: Nonlinear effects of neutrino background. *Phys. Rev. Lett.* **2002**, *89*, 191101. [CrossRef]
29. Duan, H.; Fuller, G.M.; Qian, Y.Z. Collective neutrino flavor transformation in supernovae. *Phys. Rev. D* **2006**, *74*, 123004. [CrossRef]
30. Sawyer, R.F. Speed-up of neutrino transformations in a supernova environment. *Phys. Rev. D* **2005**, *72*, 45003. [CrossRef]
31. Fuller, G.M.; Qian, Y.Z. Simultaneous flavor transformation of neutrinos and antineutrinos with dominant potentials from neutrino-neutrino forward scattering. *Phys. Rev. D* **2006**, *73*, 23004. [CrossRef]
32. Duan, H.; Fuller, G.M.; Carlson, J.; Qian, Y.Z. Coherent Development of Neutrino Flavor in the Supernova Environment. *Phys. Rev. Lett.* **2006**, *97*, 241101. [CrossRef] [PubMed]
33. Fogli, G.L.; Lisi, E.; Marrone, A.; Mirizzi, A. Collective neutrino flavor transitions in supernovae and the role of trajectory averaging. *JCAP* **2007**, *0712*, 10. [CrossRef]
34. Duan, H.; Fuller, G.M.; Qian, Y.Z. A Simple Picture for Neutrino Flavor Transformation in Supernovae. *Phys. Rev. D* **2007**, *76*, 85013. [CrossRef]
35. Raffelt, G.G.; Sigl, G. Self-induced decoherence in dense neutrino gases. *Phys. Rev. D* **2007**, *75*, 83002. [CrossRef]
36. Esteban-Pretel, A.; Pastor, S.; Tomas, R.; Raffelt, G.G.; Sigl, G. Decoherence in supernova neutrino transformations suppressed by deleptonization. *Phys. Rev. D* **2007**, *76*, 125018. [CrossRef]

37. Esteban-Pretel, A.; Pastor, S.; Tomas, R.; Raffelt, G.G.; Sigl, G. Mu-tau neutrino refraction and collective three-flavor transformations in supernovae. *Phys. Rev. D* **2008**, *77*, 65024. [CrossRef]

38. Chakraborty, S.; Choubey, S.; Dasgupta, B.; Kar, K. Effect of Collective Flavor Oscillations on the Diffuse Supernova Neutrino Background. *JCAP* **2008**, *0809*, 13. [CrossRef]

39. Duan, H.; Fuller, G.M.; Carlson, J.; Qian, Y.Z. Flavor Evolution of the Neutronization Neutrino Burst from an O-Ne-Mg Core-Collapse Supernova. *Phys. Rev. Lett.* **2008**, *100*, 21101. [CrossRef]

40. Duan, H.; Fuller, G.M.; Carlson, J. Simulating nonlinear neutrino flavor evolution. *Comput. Sci. Dis.* **2008**, *1*, 015007. [CrossRef]

41. Dasgupta, B.; Dighe, A.; Mirizzi, A. Identifying neutrino mass hierarchy at extremely small theta(13) through Earth matter effects in a supernova signal. *Phys. Rev. Lett.* **2008**, *101*, 171801. [CrossRef] [PubMed]

42. Dasgupta, B.; Dighe, A. Collective three-flavor oscillations of supernova neutrinos. *Phys. Rev. D* **2008**, *77*, 113002. [CrossRef]

43. Sawyer, R.F. The multi-angle instability in dense neutrino systems. *Phys. Rev. D* **2009**, *79*, 105003. [CrossRef]

44. Duan, H.; Fuller, G.M.; Qian, Y.Z. Collective Neutrino Oscillations. *Ann. Rev. Nucl. Part. Sci.* **2010**, *60*, 569–594. [CrossRef]

45. Wu, M.R.; Qian, Y.Z. Resonances Driven by a Neutrino Gyroscope and Collective Neutrino Oscillations in Supernovae. *Phys. Rev. D* **2011**, *84*, 45009. [CrossRef]

46. Bilenky, S.M. Neutrino oscillations: Brief history and present status. *arXiv* **2014**, arXiv:1408.2864.

47. Kneller, J.P. The Physics Of Supernova Neutrino Oscillations. In Proceedings of the 12th Conference on the Intersections of Particle and Nuclear Physics (CIPANP 2015), Vail, CO, USA, 19–24 May 2015.

48. Volpe, C. Theoretical developments in supernova neutrino physics: Mass corrections and pairing correlators. *J. Phys. Conf. Ser.* **2016**, *718*, 62068. [CrossRef]

49. Mirizzi, A.; Tamborra, I.; Janka, H.T.; Saviano, N.; Scholberg, K.; Bollig, R.; Hüdepohl, L.; Chakraborty, S. Supernova neutrinos: production, oscillations and detection. *Nuovo Cimento Riv. Ser.* **2016**, *39*, 1–112. [CrossRef]

50. Horiuchi, S.; Kneller, J.P. What can be learned from a future supernova neutrino detection? *J. Phys. G Nucl. Phys.* **2018**, *45*, 43002. [CrossRef]

51. Zaizen, M.; Yoshida, T.; Sumiyoshi, K.; Umeda, H. Collective neutrino oscillations and detectabilities in failed supernovae. *Phys. Rev. D* **2018**, *98*, 103020. [CrossRef]

52. Zhang, B. *The Physics of Gamma-ray Bursts*; Cambridge University Press: Cambridge, UK, 2018. [CrossRef]

53. Ruffini, R.; Bernardini, M.G.; Bianco, C.L.; Vitagliano, L.; Xue, S.S.; Chardonnet, P.; Fraschetti, F.; Gurzadyan, V. Black Hole Physics and Astrophysics: The GRB-Supernova Connection and URCA-1 - URCA-2. In *The Tenth Marcel Grossmann Meeting, Proceedings of the MG10 Meeting Held at Brazilian Center for Research in Physics (CBPF), Rio de Janeiro, Brazil, 20–26 July 2003*; Novello, M., Bergliaffa, S.P., Ruffini, R., Eds.; World Scientific Publishing: Singapore, 2006; Volumes 3, p. 369. [CrossRef]

54. Ruffini, R.; Bernardini, M.G.; Bianco, C.L.; Caito, L.; Chardonnet, P.; Cherubini, C.; Dainotti, M.G.; Fraschetti, F.; Geralico, A.; Guida, R.; et al. On Gamma-ray Bursts. In *The Eleventh Marcel Grossmann Meeting On Recent Developments in Theoretical and Experimental General Relativity, Gravitation and Relativistic Field Theories*; Kleinert, H., Jantzen, R.T., Ruffini, R., Eds.; World Scientific: Singapore, 2008; pp. 368–505. [CrossRef]

55. Izzo, L.; Rueda, J.A.; Ruffini, R. GRB 090618: A candidate for a neutron star gravitational collapse onto a black hole induced by a type Ib/c supernova. *Astron. Astrophys.* **2012**, *548*, L5. [CrossRef]

56. Rueda, J.A.; Ruffini, R. On the Induced Gravitational Collapse of a Neutron Star to a Black Hole by a Type Ib/c Supernova. *Astrophys. J.* **2012**, *758*, L7. [CrossRef]

57. Fryer, C.L.; Rueda, J.A.; Ruffini, R. Hypercritical Accretion, Induced Gravitational Collapse, and Binary-Driven Hypernovae. *Astrophys. J.* **2014**, *793*, L36. [CrossRef]

58. Ruffini, R.; Wang, Y.; Enderli, M.; Muccino, M.; Kovacevic, M.; Bianco, C.L.; Penacchioni, A.V.; Pisani, G.B.; Rueda, J.A. GRB 130427A and SN 2013cq: A Multi-wavelength Analysis of An Induced Gravitational Collapse Event. *Astrophys. J.* **2015**, *798*, 10. [CrossRef]

59. Fryer, C.L.; Oliveira, F.G.; Rueda, J.A.; Ruffini, R. Neutron-Star-Black-Hole Binaries Produced by Binary-Driven Hypernovae. *Phys. Rev. Lett.* **2015**, *115*, 231102. [CrossRef]

60. Wang, Y.; Rueda, J.A.; Ruffini, R.; Becerra, L.; Bianco, C.; Becerra, L.; Li, L.; Karlica, M. Two Predictions of Supernova: GRB 130427A/SN 2013cq and GRB 180728A/SN 2018fip. *Astrophys. J.* **2019**, *874*, 39. [CrossRef]

61. Rueda, J.A.; Ruffini, R.; Karlica, M.; Moradi, R.; Wang, Y. Magnetic Fields and Afterglows of BdHNe: Inferences from GRB 130427A, GRB 160509A, GRB 160625B, GRB 180728A, and GRB 190114C. *Astrophys. J.* **2020**, *893*, 148. [CrossRef]

62. Rueda, J.A.; Ruffini, R.; Wang, Y. Induced Gravitational Collapse, Binary-Driven Hypernovae, Long Gramma-ray Bursts and Their Connection with Short Gamma-ray Bursts. *Universe* **2019**, *5*, 110. [CrossRef]

63. Becerra, L.; Bianco, C.L.; Fryer, C.L.; Rueda, J.A.; Ruffini, R. On the Induced Gravitational Collapse Scenario of Gamma-ray Bursts Associated with Supernovae. *Astrophys. J.* **2016**, *833*, 107. [CrossRef]

64. Bianco, C.L.; Ruffini, R.; Xue, S. The elementary spike produced by a pure e^+e^- pair-electromagnetic pulse from a Black Hole: The PEM Pulse. *Astron. Astrophys.* **2001**, *368*, 377–390. [CrossRef]

65. Ruffini, R.; Moradi, R.; Rueda, J.A.; Becerra, L.; Bianco, C.L.; Cherubini, C.; Filippi, S.; Chen, Y.C.; Karlica, M.; Sahakyan, N.; et al. On the GeV Emission of the Type I BdHN GRB 130427A. *Astrophys. J.* **2019**, *886*, 82. [CrossRef]

66. Ruffini, R.; Melon Fuksman, J.D.; Vereshchagin, G.V. On the Role of a Cavity in the Hypernova Ejecta of GRB 190114C. *Astrophys. J.* **2019**, *883*, 191. [CrossRef]

67. Ruffini, R.; Wang, Y.; Aimuratov, Y.; Barres de Almeida, U.; Becerra, L.; Bianco, C.L.; Chen, Y.C.; Karlica, M.; Kovacevic, M.; Li, L.; et al. Early X-ray Flares in GRBs. *Astrophys. J.* **2018**, *852*, 53. [CrossRef]

68. Ruffini, R.; Karlica, M.; Sahakyan, N.; Rueda, J.A.; Wang, Y.; Mathews, G.J.; Bianco, C.L.; Muccino, M. A GRB Afterglow Model Consistent with Hypernova Observations. *Astrophys. J.* **2018**, *869*, 101. [CrossRef]

69. Becerra, L.; Cipolletta, F.; Fryer, C.L.; Rueda, J.A.; Ruffini, R. Angular Momentum Role in the Hypercritical Accretion of Binary-driven Hypernovae. *Astrophys. J.* **2015**, *812*, 100. [CrossRef]

70. Becerra, L.; Ellinger, C.L.; Fryer, C.L.; Rueda, J.A.; Ruffini, R. SPH Simulations of the Induced Gravitational Collapse Scenario of Long Gamma-ray Bursts Associated with Supernovae. *Astrophys. J.* **2019**, *871*, 14. [CrossRef]

71. Becerra, L.; Guzzo, M.M.; Rossi-Torres, F.; Rueda, J.A.; Ruffini, R.; Uribe, J.D. Neutrino Oscillations within the Induced Gravitational Collapse Paradigm of Long Gamma-ray Bursts. *Astrophys. J.* **2018**, *852*, 120. [CrossRef]

72. Goodman, J. Are gamma-ray bursts optically thick? *Astrophys. J.* **1986**, *308*, L47–L50. [CrossRef]

73. Paczynski, B. Gamma-ray bursters at cosmological distances. *Astrophys. J.* **1986**, *308*, L43–L46. [CrossRef]

74. Eichler, D.; Livio, M.; Piran, T.; Schramm, D.N. Nucleosynthesis, neutrino bursts and gamma-rays from coalescing neutron stars. *Nature* **1989**, *340*, 126–128. [CrossRef]

75. Narayan, R.; Piran, T.; Shemi, A. Neutron star and black hole binaries in the Galaxy. *Astrophys. J.* **1991**, *379*, L17–L20. [CrossRef]

76. Balbus, S.A.; Hawley, J.F. A powerful local shear instability in weakly magnetized disks. I—Linear analysis. II—Nonlinear evolution. *Astrophys. J.* **1991**, *376*, 214–233. [CrossRef]

77. Hawley, J.F.; Balbus, S.A. A Powerful Local Shear Instability in Weakly Magnetized Disks. II. Nonlinear Evolution. *Astrophys. J.* **1991**, *376*, 223. [CrossRef]

78. Balbus, S.A.; Hawley, J.F. Instability, turbulence, and enhanced transport in accretion disks. *Rev. Mod. Phys.* **1998**, *70*, 1–53. [CrossRef]

79. Balbus, S.A. Enhanced Angular Momentum Transport in Accretion Disks. *Annu. Rev. Astron. Astrophys.* **2003**, *41*, 555–597. [CrossRef]

80. Shakura, N.I.; Sunyaev, R.A. Black holes in binary systems. Observational appearance. *Astron. Astrophys.* **1973**, *24*, 337–355.

81. King, A.R.; Pringle, J.E.; Livio, M. Accretion disc viscosity: How big is alpha? *Mon. Not. R. Astron. Soc.* **2007**, *376*, 1740–1746. [CrossRef]

82. Pessah, M.E.; Chan, C.K.; Psaltis, D. The fundamental difference between shear alpha viscosity and turbulent magnetorotational stresses. *Mon. Not. R. Astron. Soc.* **2008**, *383*, 683–690. [CrossRef]

83. King, A. Accretion disc theory since Shakura and Sunyaev. *Mem. Soc. Astron. Ital.* **2012**, *83*, 466.

84. Kotko, I.; Lasota, J.P. The viscosity parameter α and the properties of accretion disc outbursts in close binaries. *Astron. Astrophys.* **2012**, *545*, A115. [CrossRef]

85. Pringle, J.E. Accretion discs in astrophysics. *Annu. Rev. Astron. Astrophys.* **1981**, *19*, 137–162. [CrossRef]

86. Krolik, J.H. *Active Galactic Nuclei: From the Central Black Hole to the Galactic Environment*; Princeton University Press: Princeton, NJ, USA, 1999.

87. Abramowicz, M.A.; Björnsson, G.; Pringle, J.E. *Theory of Black Hole Accretion Discs*; Cambridge University Press: Cambridge, UK, 1999; p. 309.

88. Manmoto, T. Advection-dominated Accretion Flow around a Kerr Black Hole. *Astrophys. J.* **2000**, *534*, 734–746. [CrossRef]

89. Frank, J.; King, A.; Raine, D.J. *Accretion Power in Astrophysics*, 3rd ed.; Cambridge University Press: Cambridge, UK, 2002; p. 398.

90. Blaes, O.M. Course 3: Physics Fundamentals of Luminous Accretion Disks around Black Holes. In *Accretion Discs, Jets and High Energy Phenomena in Astrophysics*; Beskin, V., Henri, G., Menard, F., Pelletier, G., Dalibard, J., Eds.; Springer: Berlin/Heidelberg, Germany, 2004; pp. 137–185.

91. Narayan, R.; McClintock, J.E. Advection-dominated accretion and the black hole event horizon. *New Astron. Rev.* **2008**, *51*, 733–751. [CrossRef]

92. Kato, S.; Fukue, J.; Mineshige, S. *Black-Hole Accretion Disks—Towards a New Paradigm—*; Kyoto University Press: Kyoto, Japan, 2008.

93. Qian, L.; Abramowicz, M.A.; Fragile, P.C.; Horák, J.; Machida, M.; Straub, O. The Polish doughnuts revisited. I. The angular momentum distribution and equipressure surfaces. *Astron. Astrophys.* **2009**, *498*, 471–477. [CrossRef]

94. Montesinos, M. Review: Accretion Disk Theory. *arXiv* **2012**, arXiv:1203.6851.

95. Abramowicz, M.A.; Fragile, P.C. Foundations of Black Hole Accretion Disk Theory. *Living Rev. Relativ.* **2013**, *16*, 1. [CrossRef] [PubMed]

96. Yuan, F.; Narayan, R. Hot Accretion Flows Around Black Holes. *Annu. Rev. Astron. Astrophys.* **2014**, *52*, 529–588. [CrossRef]

97. Blaes, O. General Overview of Black Hole Accretion Theory. *Space Sci. Rev.* **2014**, *183*, 21–41. [CrossRef]

98. Lasota, J.P. Black Hole Accretion Discs. *Astrophysics of Black Holes: From Fundamental Aspects to Latest Developments*; Bambi, C., Ed.; Astrophysics and Space Science Library; Springer: Berlin/Heidelberg, Germany, 2016; Volume 440, p. 1. [CrossRef]

99. Liu, T.; Gu, W.M.; Zhang, B. Neutrino-dominated accretion flows as the central engine of gamma-ray bursts. *New Astron. Rev.* **2017**, *79*, 1–25. [CrossRef]

100. Popham, R.; Woosley, S.E.; Fryer, C. Hyperaccreting Black Holes and Gamma-ray Bursts. *Astrophys. J.* **1999**, *518*, 356–374. [CrossRef]

101. Narayan, R.; Piran, T.; Kumar, P. Accretion Models of Gamma-ray Bursts. *Astrophys. J.* **2001**, *557*, 949–957. [CrossRef]

102. Kohri, K.; Mineshige, S. Can Neutrino-cooled Accretion Disks Be an Origin of Gamma-ray Bursts? *Astrophys. J.* **2002**, *577*, 311–321. [CrossRef]
103. Di Matteo, T.; Perna, R.; Narayan, R. Neutrino Trapping and Accretion Models for Gamma-ray Bursts. *Astrophys. J.* **2002**, *579*, 706–715. [CrossRef]
104. Kohri, K.; Narayan, R.; Piran, T. Neutrino-dominated Accretion and Supernovae. *Astrophys. J.* **2005**, *629*, 341–361. [CrossRef]
105. Lee, W.H.; Ramirez-Ruiz, E.; Page, D. Dynamical Evolution of Neutrino-cooled Accretion Disks: Detailed Microphysics, Lepton-driven Convection, and Global Energetics. *Astrophys. J.* **2005**, *632*, 421–437. [CrossRef]
106. Gu, W.M.; Liu, T.; Lu, J.F. Neutrino-dominated Accretion Models for Gamma-ray Bursts: Effects of General Relativity and Neutrino Opacity. *Astrophys. J.* **2006**, *643*, L87–L90. [CrossRef]
107. Chen, W.X.; Beloborodov, A.M. Neutrino-cooled Accretion Disks around Spinning Black Holes. *Astrophys. J.* **2007**, *657*, 383–399. [CrossRef]
108. Kawanaka, N.; Mineshige, S. Neutrino-cooled Accretion Disk and Its Stability. *Astrophys. J.* **2007**, *662*, 1156–1166. [CrossRef]
109. Janiuk, A.; Yuan, Y.F. The role of black hole spin and magnetic field threading the unstable neutrino disk in gamma ray bursts. *Astron. Astrophys.* **2010**, *509*, A55. [CrossRef]
110. Kawanaka, N.; Piran, T.; Krolik, J.H. Jet Luminosity from Neutrino-dominated Accretion Flows in Gamma-ray Bursts. *Astrophys. J.* **2013**, *766*, 31. [CrossRef]
111. Luo, S.; Yuan, F. Global neutrino heating in hyperaccretion flows. *Mon. Not. R. Astron. Soc.* **2013**, *431*, 2362–2370. [CrossRef]
112. Xue, L.; Liu, T.; Gu, W.M.; Lu, J.F. Relativistic Global Solutions of Neutrino-dominated Accretion Flows. *Astrophys. J. Suppl. Ser.* **2013**, *207*, 23. [CrossRef]
113. Malkus, A.; Kneller, J.P.; McLaughlin, G.C.; Surman, R. Neutrino oscillations above black hole accretion disks: Disks with electron-flavor emission. *Phys. Rev. D* **2012**, *86*, 85015. [CrossRef]
114. Frensel, M.; Wu, M.R.; Volpe, C.; Perego, A. Neutrino flavor evolution in binary neutron star merger remnants. *Phys. Rev. D* **2017**, *95*, 23011. [CrossRef]
115. Tian, J.Y.; Patwardhan, A.V.; Fuller, G.M. Neutrino flavor evolution in neutron star mergers. *Phys. Rev. D* **2017**, *96*, 43001. [CrossRef]
116. Wu, M.R.; Tamborra, I. Fast neutrino conversions: Ubiquitous in compact binary merger remnants. *Phys. Rev. D* **2017**, *95*, 103007. [CrossRef]
117. Padilla-Gay, I.; Shalgar, S.; Tamborra, I. Multi-Dimensional Solution of Fast Neutrino Conversions in Binary Neutron Star Merger Remnants. *arXiv* **2020**, arXiv:2009.01843.
118. Janiuk, A.; Mioduszewski, P.; Moscibrodzka, M. Accretion and outflow from a magnetized, neutrino cooled torus around the gamma-ray burst central engine. *Astrophys. J.* **2013**, *776*, 105. [CrossRef]
119. Janiuk, A. Microphysics in the Gamma-ray Burst Central Engine. *Astrophys. J.* **2017**, *837*, 39. [CrossRef]
120. Janiuk, A.; Sapountzis, K.; Mortier, J.; Janiuk, I. Numerical Simulations of Black Hole Accretion Flows. *arXiv* **2018**, arXiv:1805.11305.
121. Janiuk, A. The r-process Nucleosynthesis in the Outflows from Short GRB Accretion Disks. *Astrophys. J.* **2019**, *882*, 163. [CrossRef]
122. Bardeen, J.M. A Variational Principle for Rotating Stars in General Relativity. *Astrophys. J.* **1970**, *162*, 71. [CrossRef]
123. Bardeen, J.M.; Press, W.H.; Teukolsky, S.A. Rotating Black Holes: Locally Nonrotating Frames, Energy Extraction, and Scalar Synchrotron Radiation. *Astrophys. J.* **1972**, *178*, 347–370. [CrossRef]
124. Gammie, C.F.; Popham, R. Advection-dominated Accretion Flows in the Kerr Metric. I. Basic Equations. *Astrophys. J.* **1998**, *498*, 313–326. [CrossRef]
125. Bardeen, J.M. Kerr Metric Black Holes. *Nature* **1970**, *226*, 64–65. [CrossRef]
126. Thorne, K.S. Disk-Accretion onto a Black Hole. II. Evolution of the Hole. *Astrophys. J.* **1974**, *191*, 507–520. [CrossRef]
127. Novikov, I.D.; Thorne, K.S. Astrophysics of black holes. In *Black Holes (Les Astres Occlus)*; Dewitt, C., Dewitt, B.S., Eds.; Gordon and Breach Science Publishers Inc.: New York, NY, USA, 1973; pp. 343–450.
128. Page, D.N.; Thorne, K.S. Disk-Accretion onto a Black Hole. Time-Averaged Structure of Accretion Disk. *Astrophys. J.* **1974**, *191*, 499–506. [CrossRef]
129. Landau, L.D.; Lifshitz, E.M. *Fluid Mechanics*; Pergamon Press: Oxford, UK, 1959.
130. Abramowicz, M.A.; Chen, X.M.; Granath, M.; Lasota, J.P. Advection-Dominated Accretion Flows Around Kerr Black Holes. *Astrophys. J.* **1996**, *471*, 762–773. [CrossRef]
131. Abramowicz, M.A.; Lanza, A.; Percival, M.J. Accretion Disks around Kerr Black Holes: Vertical Equilibrium Revisited. *Astrophys. J.* **1997**, *479*, 179–183. [CrossRef]
132. Misner, C.W.; Thorne, K.S.; Wheeler, J.A. *Gravitation*; Princeton University Press: Princeton, NJ, USA, 1973.
133. Mihalas, D.; Mihalas, B.W. *Foundations of Radiation Hydrodynamics*; Oxford University Press: Oxford, UK, 1984.
134. Clifford, F.E.; Tayler, R.J. The equilibrium distribution of nuclides in matter at high temperatures. *Mon. Not. R. Astron. Soc.* **1965**, *69*, 21. [CrossRef]
135. Calder, A.C.; Townsley, D.M.; Seitenzahl, I.R.; Peng, F.; Messer, O.E.B.; Vladimirova, N.; Brown, E.F.; Truran, J.W.; Lamb, D.Q. Capturing the Fire: Flame Energetics and Neutronization for Type Ia Supernova Simulations. *Astrophys. J.* **2007**, *656*, 313–332. [CrossRef]

136. Mavrodiev, S.C.; Deliyergiyev, M.A. Modification of the nuclear landscape in the inverse problem framework using the generalized Bethe-Weizsäcker mass formula. *Int. J. Mod. Phys. E* **2018**, *27*, 1850015. [CrossRef]
137. Rauscher, T.; Thielemann, F.K. Astrophysical Reaction Rates From Statistical Model Calculations. *At. Data Nucl. Data Tables* **2000**, *75*, 1–351.
138. Rauscher, T. Nuclear Partition Functions at Temperatures Exceeding 10^{10} K. *Astrophys. J. Suppl. Ser.* **2003**, *147*, 403–408. [CrossRef]
139. Vincenti, W.G.; Kruger, C.H. *Introduction to Physical Gas Dynamics*; Krieger Pub Co (June 1, 1975); John Wlley & Sons: Hoboken, NJ, USA, 1965.
140. Buresti, G. A note on Stokes' hypothesis. *Acta Mech.* **2015**, *226*, 3555–3559. [CrossRef]
141. Particle Data Group. Review of Particle Physics. *Phys. Rev. D* **2018**, *98*, 30001. [CrossRef]
142. Dolgov, A.D. Neutrinos in the Early Universe. *Sov. J. Nucl. Phys.* **1981**, *33*, 700–706.
143. Sigl, G.; Raffelt, G. General kinetic description of relativistic mixed neutrinos. *Nucl. Phys. B* **1993**, *406*, 423–451. [CrossRef]
144. Hannestad, S.; Raffelt, G.G.; Sigl, G.; Wong, Y.Y.Y. Self-induced conversion in dense neutrino gases: Pendulum in flavour space. *Phys. Rev. D* **2006**, *74*, 105010. Erratum in **2007**, *76*, 029901, doi:10.1103/PhysRevD.76.029901. [CrossRef]
145. Cardall, C.Y. Liouville equations for neutrino distribution matrices. *Phys. Rev. D* **2008**, *78*, 85017. [CrossRef]
146. Strack, P.; Burrows, A. Generalized Boltzmann formalism for oscillating neutrinos. *Phys. Rev. D* **2005**, *71*, 93004. [CrossRef]
147. Dasgupta, B.; Dighe, A.; Mirizzi, A.; Raffelt, G.G. Collective neutrino oscillations in non-spherical geometry. *Phys. Rev. D* **2008**, *78*, 33014. [CrossRef]
148. Tolman, R.C. *Relativity, Thermodynamics, and Cosmology*; Clarendon Press: Oxford, UK, 1934.
149. Klein, O. On the statistical derivation of the laws of chemical equilibrium. *Il Nuovo Cimento (1943–1954)* **1949**, *6*, 171–180. [CrossRef]
150. Klein, O. On the Thermodynamical Equilibrium of Fluids in Gravitational Fields. *Rev. Mod. Phys.* **1949**, *21*, 531–533. [CrossRef]
151. Paczynski, B. A model of selfgravitating accretion disk. *Acta Astron.* **1978**, *28*, 91–109.
152. Raffelt, G.G. *Stars as Laboratories for Fundamental Physics*; University of Chicago Press: Chicago, IL, USA, 1996.
153. Harris, R.A.; Stodolsky, L. Two state systems in media and "Turing's paradox". *Phys. Lett. B* **1982**, *116*, 464–468. [CrossRef]
154. Stodolsky, L. Treatment of neutrino oscillations in a thermal environment. *Phys. Rev. D* **1987**, *36*, 2273–2277. [CrossRef] [PubMed]
155. Janka, H.T. Implications of detailed neutrino transport for the heating by neutrino-antineutrino annihilation in supernova explosions. *Astron. Astrophys.* **1991**, *244*, 378–382.
156. Ruffert, M.; Janka, H.T.; Takahashi, K.; Schaefer, G. Coalescing neutron stars - a step towards physical models. II. Neutrino emission, neutron tori, and gamma-ray bursts. *Astron. Astrophys.* **1997**, *319*, 122–153.
157. Rosswog, S.; Ramirez-Ruiz, E.; Davies, M.B. High-resolution calculations of merging neutron stars—III. Gamma-ray bursts. *Mon. Not. R. Astron. Soc.* **2003**, *345*, 1077–1090. [CrossRef]
158. Kawanaka, N.; Kohri, K. A possible origin of the rapid variability of gamma-ray bursts due to convective energy transfer in hyperaccretion discs. *Mon. Not. R. Astron. Soc.* **2012**, *419*, 713–717. [CrossRef]
159. Preparata, G.; Ruffini, R.; Xue, S.S. The dyadosphere of black holes and gamma-ray bursts. *Astron. Astrophys.* **1998**, *338*, L87–L90.
160. Ruffini, R.; Salmonson, J.D.; Wilson, J.R.; Xue, S.S. On evolution of the pair-electromagnetic pulse of a charged black hole. *A&As* **1999**, *138*, 511–512. [CrossRef]
161. Ruffini, R.; Salmonson, J.D.; Wilson, J.R.; Xue, S.S. On the pair-electromagnetic pulse from an electromagnetic black hole surrounded by a baryonic remnant. *Astron. Astrophys.* **2000**, *359*, 855–864.
162. Shemi, A.; Piran, T. The appearance of cosmic fireballs. *Astrophys. J.* **1990**, *365*, L55–L58. [CrossRef]
163. Piran, T.; Shemi, A.; Narayan, R. Hydrodynamics of Relativistic Fireballs. *Mon. Not. R. Astron. Soc.* **1993**, *263*, 861. [CrossRef]
164. Meszaros, P.; Laguna, P.; Rees, M.J. Gasdynamics of relativistically expanding gamma-ray burst sources - Kinematics, energetics, magnetic fields, and efficiency. *Astrophys. J.* **1993**, *415*, 181–190. [CrossRef]
165. Piran, T. Gamma-ray bursts and the fireball model. *Phys. Rep.* **1999**, *314*, 575–667. [CrossRef]
166. Piran, T. The physics of gamma-ray bursts. *Rev. Mod. Phys.* **2004**, *76*, 1143–1210. [CrossRef]
167. Mészáros, P. Theories of Gamma-ray Bursts. *Annu. Rev. Astron. Astrophys.* **2002**, *40*, 137. [CrossRef]
168. Mészáros, P. Gamma-ray bursts. *Rep. Prog. Phys.* **2006**, *69*, 2259–2321. [CrossRef]
169. Berger, E. Short-Duration Gamma-ray Bursts. *Annu. Rev. Astron. Astrophys.* **2014**, *52*, 43–105. [CrossRef]
170. Kumar, P.; Zhang, B. The physics of gamma-ray bursts and relativistic jets. *Phys. Rep.* **2015**, *561*, 1–109. [CrossRef]
171. Liu, T.; Zhang, B.; Li, Y.; Ma, R.Y.; Xue, L. Detectable MeV neutrinos from black hole neutrino-dominated accretion flows. *Phys. Rev. D* **2016**, *93*, 123004. [CrossRef]
172. Salmonson, J.D.; Wilson, J.R. General Relativistic Augmentation of Neutrino Pair Annihilation Energy Deposition near Neutron Stars. *Astrophys. J.* **1999**, *517*, 859–865. [CrossRef]
173. Birkl, R.; Aloy, M.A.; Janka, H.T.; Müller, E. Neutrino pair annihilation near accreting, stellar-mass black holes. *Astron. Astrophys.* **2007**, *463*, 51–67. [CrossRef]
174. Caballero, O.L.; McLaughlin, G.C.; Surman, R. Neutrino Spectra from Accretion Disks: Neutrino General Relativistic Effects and the Consequences for Nucleosynthesis. *Astrophys. J.* **2012**, *745*, 170. [CrossRef]
175. Ruffini, R.; Rueda, J.A.; Muccino, M.; Aimuratov, Y.; Becerra, L.M.; Bianco, C.L.; Kovacevic, M.; Moradi, R.; Oliveira, F.G.; Pisani, G.B.; Wang, Y. On the Classification of GRBs and Their Occurrence Rates. *Astrophys. J.* **2016**, *832*, 136. [CrossRef]

176. Moghaddas, M.; Ghanbari, J.; Ghodsi, A. Shear Tensor and Dynamics of Relativistic Accretion Disks around Rotating Black Holes. *Publ. Astron. Soc. Jpn.* **2012**, *64*. [CrossRef]
177. Moeen, M. Calculation of the relativistic bulk tensor and shear tensor of relativistic accretion flows in the Kerr metric. *Iran. J. Astron. Astrophys.* **2017**, *4*, 205–221. [CrossRef]
178. Zeldovich, Y.B.; Novikov, I.D. *Relativistic Astrophysics. Volume 1: Stars and Relativity*; University of Chicago Press: Chicago, IL, USA, 1971.
179. Potekhin, A.Y.; Chabrier, G. Equation of state of fully ionized electron-ion plasmas. II. Extension to relativistic densities and to the solid phase. *Phys. Rev. E* **2000**, *62*, 8554–8563. [CrossRef] [PubMed]
180. Dicus, D.A. Stellar energy-loss rates in a convergent theory of weak and electromagnetic interactions. *Phys. Rev. D* **1972**, *6*, 941–949. [CrossRef]
181. Tubbs, D.L.; Schramm, D.N. Neutrino Opacities at High Temperatures and Densities. *Astrophys. J.* **1975**, *201*, 467–488. [CrossRef]
182. Bruenn, S.W. Stellar core collapse—Numerical model and infall epoch. *Astrophys. J. Suppl. Ser.* **1985**, *58*, 771–841. [CrossRef]
183. Ruffert, M.; Janka, H.T.; Schaefer, G. Coalescing neutron stars—A step towards physical models. I. Hydrodynamic evolution and gravitational-wave emission. *Astron. Astrophys.* **1996**, *311*, 532–566.
184. Yakovlev, D.G.; Kaminker, A.D.; Gnedin, O.Y.; Haensel, P. Neutrino emission from neutron stars. *Phys. Rep.* **2001**, *354*, 1–155. [CrossRef]
185. Burrows, A.; Thompson, T.A. *Neutrino-Matter Interaction Rates in Supernovae*; Fryer, C.L., Ed.; Astrophysics and Space Science Library; Springer: Dordrecht, The Netherlands, 2004; Volume 302, pp. 133–174. [CrossRef]
186. Burrows, A.; Reddy, S.; Thompson, T.A. Neutrino opacities in nuclear matter. *Nucl. Phys. A* **2006**, *777*, 356–394. [CrossRef]
187. Aparicio, J.M. A Simple and Accurate Method for the Calculation of Generalized Fermi Functions. *Astrophys. J. Suppl. Ser.* **1998**, *117*, 627–632. [CrossRef]

On the Magnetic Field Screening
in Strong Crossed Electromagnetic Fields[1]

S. Campion[a, b, *], J. A. Rueda[a, b, c, d, e, **], S. S. Xue[a, b, *], and R. Ruffini[a, b, f, g, h, ****]**

[a] *International Center for Relativistic Astrophysics Network, Pescara, I-65122 Italy*

[b] *ICRA, Dipartimento di Fisica, Sapienza Università di Roma, Rome, 00185 Italy*

[c] *ICRA Net-Ferrara, Dipartimento di Fisica e Scienze della Terra, Università degli Studi di Ferrara, Ferrara, I-44122 Italy*

[d] *Dipartimento di Fisica e Scienze della Terra, Universit`a degli Studi di Ferrara, Ferrara, I-44122 Italy*

[e] *INAF, Istituto di Astrofisica e Planetologia Spaziali, Rome, 00133 Italy*

[f] *Université de Nice Sophia Antipolis, CEDEX 2, Grand Château Parc Valrose, Nice, France*

[g] *ICRANet-Rio, Centro Brasileiro de Pesquisas Físicas, Rio de Janeiro, 22290-180 Brazil*

[h] *INAF, Rome, 00136 Italy*

* *e-mail: stefano.campion@icranet.org*

** *e-mail: jorge.rueda@icra.it*

*** *e-mail: xue@icra.it*

**** *e-mail: ruffini@icra.it*

Abstract—It has been shown that a rotating Black Hole (BH hereafter) immersed in a test background magnetic field, of initial strength B_0 and aligned parallel to the BH rotation axis, generates an induced electric field, which strength is proportional to the background magnetic field. We consider the configuration of crossed fields: $\mathbf{B} = B\hat{z}$ and $\mathbf{E} = E\hat{y}$. In this system, a huge number of e^+e^- pairs can be emitted and start to be accelerated to high energies, by means of the induced electric field, and emit synchrotron photons. These photons interact with the magnetic field via the magnetic pair production process (MPP hereafter), $\gamma + B \rightarrow e^+ + e^-$. The motion of all these pairs around the magnetic field lines generates also an induced magnetic field oriented in the opposite direction to the background one. This implies a reduction of the background magnetic field. The purpose of this study is to show if this reduction occurs, which implies a decreases the MPP efficiency and, consequently, the enhancement of the probability for the synchrotron photons to escape from the region and be detected.

1. INTRODUCTION

The process of screening of a strong electric field by means of the creation of electron-positron pairs by QED vacuum polarization process, and consequent particles showers, has been studied for many years. One of the last studies about this argument was presented in [1], where they shown that an electric field as high as $E \sim \alpha_f E_{cr}$, where α_f is the fine structure constant and $E_{cr} = m_e^2 c^3/e\hbar$ the critical field, cannot be maintained because the creation of particles showers depletes the field.

Until now, no any conclusion has been reached about the screening of a magnetic field. The main topic of this paper is to build a simple model to analyze the screening process of a magnetic field, performed by the motion of electrons and positrons inside a region filled by magnetic $\mathbf{B}$ and electric $\mathbf{E}$ fields. The basic idea of the screening process is the following:

(1) An initial number of $e^{\pm}$ pairs are injected in this region, e.g., via vacuum polarization process.

(2) These particles are accelerated by the electric field and emit radiation via the curvature, synchrotron or synchro-curvature processes, due to the presence of both fields.

(3) Some of these photons create a new pair via the MPP process.

(4) These new pairs start to be accelerated, emit radiation, and circularize around the magnetic field

---

lines generating an induced magnetic field, B_{ind}, oriented in the opposite direction with respect to the particles motion. This B_{ind} decreases the background magnetic field B_0.

The final purpose of this article is to apply this model in order to study the emission from a BH in GRBs [2]. Indeed, if the screening process occurs, and then a reduction of the background magnetic field is present, the optical depth for pairs synchrotron emitted photons decreases and photons are free to escape from the region near the BH and could be observed.

This is a preliminary study of this problem. Indeed, we have built the set of equations which describes the whole mechanism as a one-particle equations. The consequences of this assumption are that all the particles are governed by the same equations and, then, are all emitted in the same direction, have the same energy and velocity and follow the same path. In order to directly apply this model to the GRBs case, one needs to modify both some assumptions and equations of the model as: adding a distribution function for the positions and velocities of the particles; go beyond the approximation of a Minkoskian space-time for long integration time. These improvements will be studied in the nearly future. In the next section we describe the set of equations that we have built and integrated.[2]

2. SYSTEM OF EQUATIONS

Here we summarize the set of equations that we need to integrate to solve our problem. With the considered configuration for the fields, the equations for the particle velocity become [3]:

$$
\begin{cases}
\dfrac{d\beta_x}{d\tilde{t}} = \beta_y \gamma^{-1} [\tilde{B}_{\text{tot}} - \beta_x \tilde{E}_{\text{tot}}], \\[2mm]
\dfrac{d\beta_y}{d\tilde{t}} = [\tilde{E}_{\text{tot}}(1 - \beta_y^2) - \beta_x \tilde{B}_{\text{tot}}]\gamma^{-1}, \\[2mm]
\dfrac{d\beta_z}{d\tilde{t}} = -\tilde{E}_{\text{tot}}\beta_z\beta_y\gamma^{-1},
\end{cases} \quad (1)
$$

where $B_{\text{tot}} = B_0 - B_{\text{ind}}$ and $E_{\text{tot}} = \Upsilon B_{\text{tot}}$. We remind that $\mathbf{B} = B\hat{z}$ and $\mathbf{E} = E\hat{y}$. The equations for the posi-

---

[2] All the following equations are written in a dimensionless way, normalized with these criteria: the temporal variables, as t and $1/\omega_0$, becomes $\tilde{t} = t/\tau_c$ and $\tilde{\omega}_0 = \omega_0\tau_c$, with τ_c the Compton time $\tau_c = \hbar/mc^2 = 1.29 \times 10^{-21}$ s; the length becomes $(\tilde{x}, \tilde{y}, \tilde{z}) = (x, y, z)/\lambdabar_c$, with $\lambdabar_c$ the Compton length $\lambdabar_c = \hbar/mc = 3.86 \times 10^{-11}$ cm; we can normalize the magnetic field as $\tilde{B} = B/B_{\text{cr}}$ and the electric field as $\tilde{E} = E/E_{\text{cr}}$, where the critical electric/magnetic field $E_{\text{cr}} = B_{\text{cr}} = m_e^2 c^3/e = 4.41 \times 10^{13}$ Gauss. All the energies, as the photon energy ε_γ, are normalized with the electrons rest mass energy $m_e c^2 = 0.511$ MeV.

---

tions of the particles can be written as $d\tilde{\mathbf{r}}/d\tilde{t} = \beta(t)$. The equation for the particle Lorentz factor is

$$
\frac{d\gamma}{d\tilde{t}} = \beta_y \tilde{E}_{\text{tot}} - \frac{1}{\sqrt{3}\pi}\alpha_f \bar{H}(\chi), \quad (2)
$$

with $\bar{H}(\chi)$ given by (see Eq. (B6) in [4]):

$$
\bar{H}(\chi) \approx \frac{8\pi\sqrt{3}}{27} \frac{\chi^2}{\left(1 + \frac{3}{4}\frac{(2\chi)^{2/3}}{\sqrt{\Gamma(2/3)}}\right)^2} \\
\times \left[1 + \frac{0.52\sqrt{\chi}(1 + 3\sqrt{\chi} - 3.2\chi)}{1 + 0.3\sqrt{\chi} + 17\chi + 11\chi^2}\right]. \quad (3)
$$

With Eq. (3) the pairs energy loss I can be written as:

$$
I \equiv \left|-\frac{dE}{dt}\right| = \frac{e^2 m^2 c^3}{\sqrt{3}\hbar^2 2\pi}\bar{H}(\chi). \quad (4)
$$

The variable χ is defined as $\chi = \varepsilon_\gamma/2\varepsilon_e = \tilde{\varepsilon}_\gamma/2\gamma$ (if we normalize the photons energies to the electron rest mass energy). The photon energy is given by

$$
\tilde{\varepsilon}_\gamma = \frac{3}{2}\gamma^2\sqrt{\beta_y^2(\tilde{B}_{\text{tot}}^2 - \tilde{E}_{\text{tot}}^2) + (\tilde{E}_{\text{tot}} - \beta_x\tilde{B}_{\text{tot}})^2}. \quad (5)
$$

The equation for the number of created photons is

$$
\frac{dN_\gamma(\tilde{t})}{d\tilde{t}} = N_\pm(t, \phi)\frac{I(t)}{\varepsilon_\gamma(t)} = \frac{2}{3\pi\sqrt{3}}\alpha_f \frac{N_\pm(\tilde{t})}{\gamma^2} \\
\times \frac{\bar{H}(\tilde{\chi})}{\sqrt{\beta_y^2(\tilde{B}_{\text{tot}}^2 - \tilde{E}_{\text{tot}}^2) + (\tilde{E}_{\text{tot}} - \beta_x\tilde{B}_{\text{tot}})^2}}, \quad (6)
$$

while the equation for the number of pairs is

$$
\frac{dN_\pm(\tilde{t})}{d\tilde{t}} = N_\gamma(t)R_A^e(t, \phi)c = N_\gamma(\tilde{t})\tilde{\zeta}(\tilde{t}). \quad (7)
$$

The pair production rate (via MPP process) $\zeta(t)$ is given by (see Eq. (9) in [5]):

$$
\tilde{\zeta} = 0.23\alpha_f\tilde{B}_z\left(1 - \frac{\tilde{E}_y^2}{\tilde{B}_z^2}\right)\frac{\sqrt{\eta_y^2\left(1 - \frac{\tilde{E}_y^2}{\tilde{B}_z^2}\right) + \left(\eta_x - \frac{\tilde{E}_y}{\tilde{B}_z}\right)^2}}{1 - \frac{\tilde{E}_y}{\tilde{B}_z}\eta_x} \\
\times \exp\left[-\frac{8}{3}\frac{\left[\eta_y^2\left(1 - \frac{E_y^2}{B_z^2}\right) + \left(\eta_x - \frac{E_y}{B_z}\right)^2\right]^{-1/2}}{\tilde{\varepsilon}_\gamma\tilde{B}_z}\right]. \quad (8)
$$

The photons momentum director cosines η can be written as a function of the pair velocity β, the azi-
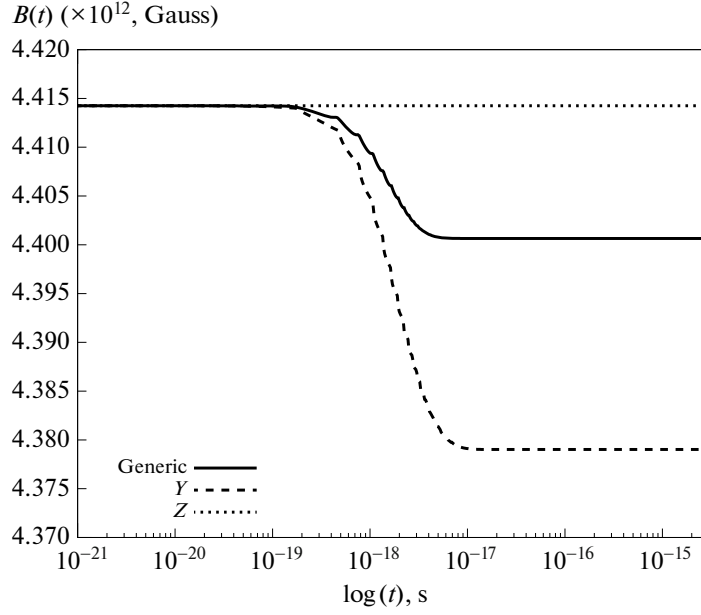
Fig. 1. Magnetic field decrease (with $\Upsilon = 1/5$ and $B_0 = 0.1B_{\mathrm{cr}}$) operated by an initial number of particles, $N_{\pm,0} = 10^{10}$, emitted initially along the directions "*generic*" ($\gamma_0 = 4.18$), $\hat{y}$ ($\gamma_0 = 3.71$), and $\hat{z}$ ($\gamma_0 = 22.66$).

muthal Φ, and polar Θ angles of emission (in the comoving particle frame) [6]:

$$
\begin{cases}
\eta_x = \left\{ \sin(\Theta)\cos(\Phi) + \beta_x \left[\gamma + \dfrac{(\gamma-1)}{\beta^2} v \right] \right\} \\
\quad \times [\gamma(1+v)]^{-1}, \\
\eta_y = \left\{ \sin(\Theta)\sin(\Phi) + \beta_y \left[\gamma + \dfrac{(\gamma-1)}{\beta^2} v \right] \right\} \\
\quad \times [\gamma(1+v)]^{-1}, \\
\eta_z = \left\{ \cos(\Theta) + \beta_z \left[\gamma + \dfrac{(\gamma-1)}{\beta^2} v \right] \right\} \\
\quad \times [\gamma(1+v)]^{-1},
\end{cases}
\tag{9}
$$

with

$$
\begin{aligned}
v = {} & \beta_x \sin(\Theta)\cos(\Phi) + \beta_y \sin(\Theta)\sin(\Phi) \\
& + \beta_z \cos(\Theta).
\end{aligned}
\tag{10}
$$

The evolution of the magnetic field is described by the following equation (in normalized form) (see [6]):

$$
\begin{aligned}
\frac{d\tilde{B}_{\mathrm{tot}}}{d\tilde{t}} = {} & -\alpha_f \frac{\sqrt{\beta_x^2 + \beta_y^2}}{\gamma^2} \frac{dN_\pm}{d\tilde{t}} [\beta_y^2(\tilde{B}_{\mathrm{tot}}^2 - \tilde{E}_{\mathrm{tot}}^2) \\
& + (\tilde{E}_{\mathrm{tot}} - \beta_x \tilde{B}_{\mathrm{tot}})^2].
\end{aligned}
\tag{11}
$$

3. RESULTS

In this section we report the results obtained by the integrations of the set of equations described in the

previous section. In our calculations we assume a proportionality relation between the components of the electric and magnetic field

$$
E(t) = \frac{1}{2}\Upsilon B(t),
\tag{12}
$$

where the parameter Υ should be $\Upsilon \leq 1$. We made integrations selecting three values $\Upsilon = 1, 1/5,$ and $1/50$. This proportionality implies that when $B(t)$ changes, also the $E(t)$ changes consistently and this affects the particles motion and all the successive processes.

In order to integrate the set of equations, we need to choose some initial conditions. Firstly, we select three specific emission directions for the particles: (1) along the $\hat{y}$-axis (parallel to electric field); (2) along the $\hat{z}$-axis (parallel to magnetic field); (3) with a polar and azimuthal angle of $\theta = 75°$ and $\phi = 30°$, respectively (we call it as "*generic*"). For each direction and for each value of the parameter Υ, we have chosen specific initial value of the magnetic field B_0 and the particles Lorentz factor γ_0. We have integrated the system of equations given in Section 2 varying the initial number of emitted particles, $N_{\pm,0}$ and photons, $N_{\gamma,0}$.[3] We have chosen the following values: $N_{\pm,0} = 1, 10^3, 10^6, 10^{10},$ with $N_{\gamma,0} = 0$. In Fig. 1 we

---

[3] All the numerical integrations stop when the Lorentz factor of the particle becomes equal to 1, namely when the particle loses all of its energy due the emission of radiation. We start the integrations at $t_0 = 10^{-21}$ s and the previous condition is reached at $t_f \sim 10^{-18}\text{--}10^{-15}$ s, depending on the specific initial conditions.
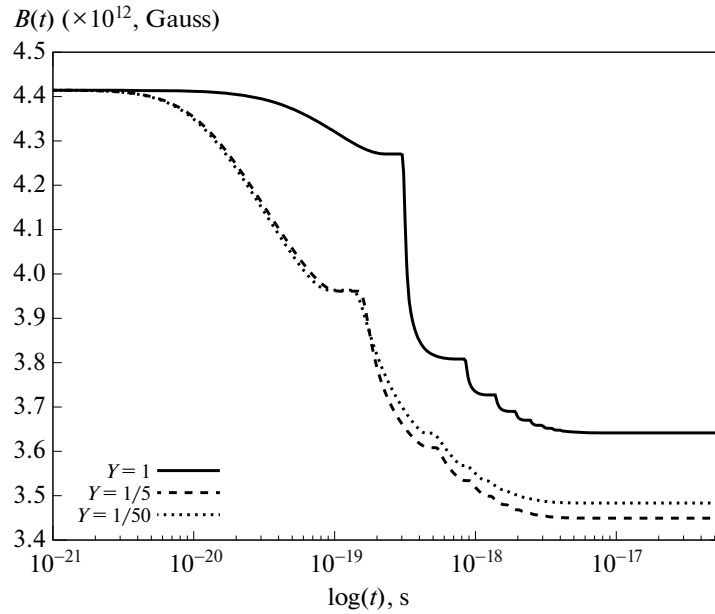
Fig. 2. Magnetic field decrease, with $N_{\pm,0} = 10^{15}$ and $B_0 = 0.1B_{cr}$, emitted initially along the *generic* direction, for $\Upsilon = 1, 1/5, 1/50$, with Lorentz factor $\gamma_0 = 6.48, 4.18, 3.81$, respectively. This plot has been taken from \cite{CampionMFS-PLB}.
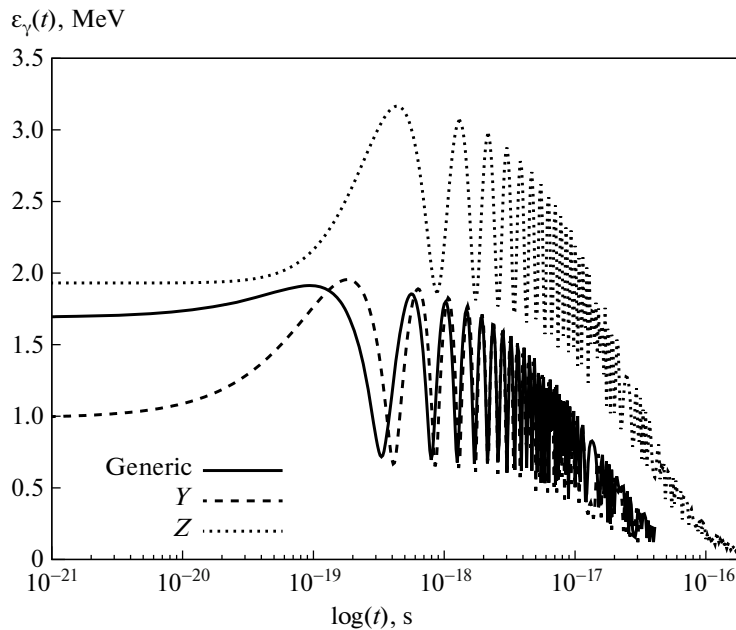
Fig. 3. Emitted photons energy in (MeV) as a function of time, with initial conditions: $N_{\pm,0} = 10^{10}$, emitted initially along the directions "*generic*" (with $\gamma_0 = 6.48$), $\hat{y}$ (with $\gamma_0 = 3.66$), and $\hat{z}$ (with $\gamma_0 = 7.098$). In this case $\Upsilon = 1$ and $B_0 = 0.1B_{cr}$. Plot presented in \cite{CampionMFS-PLB}.

show the reduction of the magnetic field for initial conditions: $\Upsilon = 1/5$, $B_0 = 0.1B_{cr}$, $N_{\pm,0} = 10^{10}$ emitted initially along the three directions, with different γ_0. In Fig. 2 the same is shown for initial conditions: $\Upsilon = (1, 1/5, 1/50)$, $B_0 = 0.1B_{cr}$, $N_{\pm,0} = 10^{15}$ emitted along the *generic* direction.

From these integrations we got some interesting results. Firstly, we see that the model is strictly cor-
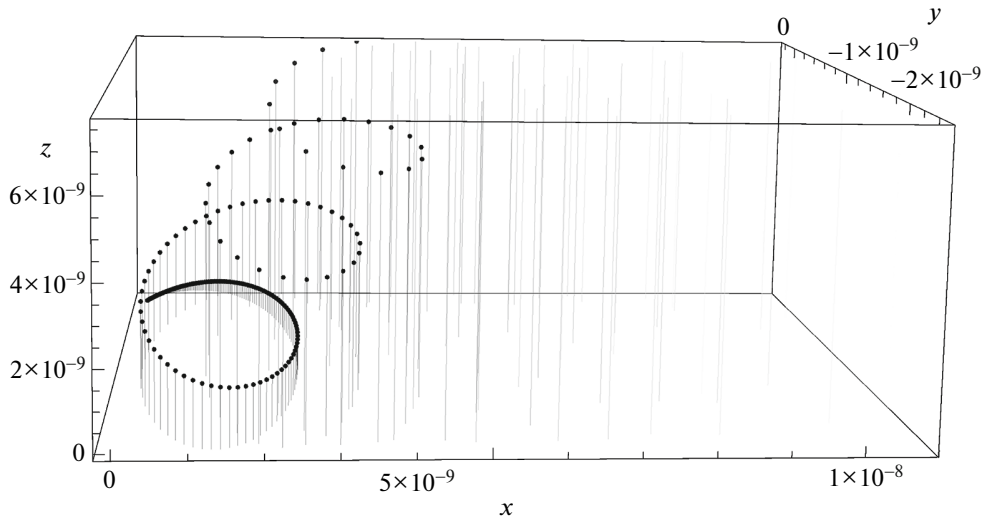
Fig. 4. Coils produced by particles emitted initially along the *generic* direction, with $B_0 = 0.1 B_{cr}$, $N_{\pm,0} = 10^6$, and $\Upsilon = 1/5$.

related to the initial emission direction of particles and to the strength of the background magnetic field. A sufficient decrease of **B** is operated principally when we start the integration with a high initial number of particles $N_{\pm,0} \gtrsim 10^6$. Moreover, we see that the decrease presents a steps behaviour. This corresponds to the oscillatory motion of the particles around the magnetic field lines (which have a circular trajectory), as can be seen in Figs. 3 and 4, where the photon energy $\tilde{\varepsilon}_\gamma(t)$ and the particles trajectory are shown, respectively. When $\tilde{\varepsilon}_\gamma$ is maximum the field decreases, while when it is minimum the field remains constant.

4. CONCLUSIONS

In this paper we have built a simple and schematic model to study the magnetic field screening effect. The basic idea of this model is that, when an initial number of particles are injected in a region where both magnetic and electric field are presents (perpendicular to each other), the oscillatory motion of these particle creates, by the well known Biot−Savart law, an induced magnetic field, oriented in opposite direction with respect to the background one, which decreases the background magnetic field.

The principal result is that the screening of the magnetic field can occur, but with different efficiency depending on the set of initial conditions. A consistently reduction of the magnetic field occurs if a high number of pairs $N_{\pm,0}$ ($10^6 < N_{\pm,0} \leq 10^{15}$) is injected. This effect depends also on the initial direction of emission of the particles. Indeed, we note that the major effect is obtained when the particles are emitted

in the *generic* and $\hat{y}$ direction. Indeed, as can be seen in Eq. (11), the screening is produced by the particle velocity orthogonal component (with respect to the $\hat{z}$-axis), that is dominant if the particles are emitted in the *generic* or $\hat{y}$ direction.

A further dependence of the effect is the one related to the parameter Υ. We can see that a decrease of Υ leads to the decrease of the efficiency of the screening. This can be understood, qualitatively, looking at equations in Section 2 and, principally, to Eq. (11). Indeed, from these equations, if one decreases the strength of **E** also the screening effect is less efficient, since the variation of the fields has consequences also on the particles dynamic and on the emitted energy.

More details about the work presented here can be found in [6] (see also \cite{CampionMFS-PLB}).

REFERENCES

1. A. M. Fedotov, N. B. Narozhny, G. Mourou, and G. Korn, Phys. Rev. Lett. **105**, 080402 (2010); arXiv: 1004.5398.

2. R. Ruffini, J. A. Rueda, M. Muccino, Y. Aimuratov, L. M. Becerra, C. L. Bianco, M. Kovacević, R. Moradi, F. G. Oliveira, G. B. Pisani, et al., Astrophys. J. **832**, 136 (2016).

3. J. D. Jackson, *Classical Electrodynamics* (Am. Assoc. Phys. Teachers, 1999).

4. S. R. Kelner, A. Y. Prosekin, and F. A. Aharonian, Astron. J. **149**, 33 (2015); arXiv: 1501.04994.

5. J. K. Daugherty and I. Lerche, Astrophys. Space Sci. **38**, 437 (1975).

6. S. Campion, PhD Thesis (Rome, Italy, 2021).

7. S. Campion, J. A. Rueda, R. Ruffini, S.-S. Xue, Physics Letters B **820**, 136562 (2021).

An Update of the Binary-Driven Hypernovae Scenario of Long Gamma-Ray Bursts[1]

J. A. Rueda[a, b, c, d, e], *

[a]ICRANet, Pescara, I-65122 Italy
[b]ICRA, Dipartimento di Fisica, Sapienza Università di Roma, Rome, I-00185 Italy
[c]ICRANet-Ferrara, Dipartimento di Fisica e Scienze della Terra, Università degli Studi di Ferrara, Ferrara, I-44122 Italy
[d]Dipartimento di Fisica e Scienze della Terra, Università degli Studi di Ferrara, Ferrara, I-44122 Italy
[e]INAF, Istituto di Astrofisica e Planetologia Spaziali, Rome, 00133 Italy
*e-mail: jorge.rueda@icra.it

Abstract—I discuss some most recent theoretical and observational results on the *inner engine* of the high-energy (GeV) emission of long gamma-ray bursts (GRBs), within the context of the *binary-driven hypernova* (BdHN) model.

1. INTRODUCTION

The BdHN occurs in the latest evolutionary stages of a massive binary. Specifically, when it has evolved into a binary composed of a carbon-oxygen (CO) star and a neutron star (NS) companion in compact orbit [1, 2]. The gravitational collapse of the iron core of the CO star leads to (1) a newborn NS (ν NS) at its center, and (2) a SN explosion which expels the outermost layers of the CO star. The SN explosion, in turn, triggers a hypercritical (i.e., highly super-Eddington) accretion process onto the NS companion [3] as well as onto the ν NS [4]. For orbital periods of the order of, or shorter than, five minutes, the NS companion gains sufficient mass and angular momentum to reach the point of gravitational instability (the NS critical mass) [5−7], hence forming a Kerr BH. The BdHNe forming a Kerr BH have been called of type I, i.e., BdHN I [8, 9]. I here focus on these systems.

Numerical simulations of the BdHN scenario have been performed in one-dimension [3], two-dimensions [6], and three-dimensions [4, 7]. These works simulate the SN explosion, the hypercritical accretion onto the ν NS and the NS, the neutrino emission in the accretion process, and follow the gravitational and rotational evolution of the ν NS and the NS to the point of gravitational collapse with the consequent formation of the Kerr BH.

1.1. Afterglow Phase: X-Rays (keV) Emission

The GRB afterglow in the BdHN originates from synchrotron emission produced by relativistic electrons in the SN ejecta, powered both by the hypercritical accretion of the SN onto the ν NS and by its pulsar-like emission [8−10]. In fact, the modeling of the decaying X-ray luminosity observed by *Swift*-XRT [11] has been used to estimate the spin of the ν NS, as well as the strength and structure of its magnetic field in specific BdHN I and BdHN II [8−10]. Clearly, this emission occurs at distances $\gtrsim 10^{12}$ cm, the location of the expanding SN ejecta.

This description of the afterglow in the BdHN model agrees with existing constraints on the bulk Lorentz factor Γ. Data of the XRT detector on board the Neils Gehrels *Swift* Observatory on the X-ray flares in the afterglow, following the ultrarelativistic prompt emission (UPE) phase, have been analyzed in [12]. The time-evolution of the observed thermal component in the flares has revealed the emitter is in a mildly-relativistic expansion: $\Gamma \lesssim 5$. Further confirmation of this result has come from the upper limit $\Gamma \lesssim 3$ obtained for GRB 151027A [13], and $\Gamma \lesssim 2$ for GRB 130427A [10]. This mildly-relativistic expansion is well far from the $\Gamma \sim 10^3$ needed by the ultrarelativistic blast wave of traditional GRB models. The reader is referred to the comprehensive review [14], for a detailed discussion on the traditional model of GRBs.

1.2. Ultrarelativistic Prompt Phase: Gamma-Rays (MeV) Emission

In the *ultrarelativistic prompt emission* (UPE) phase gamma-rays in the MeV regime are emitted. It comprises most of the GRB observed emission. In the BdHN theory, the UPE is explained by the transition from the optically thick to the optically thin phase of the e^+e^- plasma generated near the BH. The dynamics and reaching of transparency of this plasma is described through the traditional *fireshell* approach [15−17].

In [12], it has been shown that the expansion of the expansion of the e^+e^- plasma along different directions around the BH site leads to different observables. The UPE is produced along the direction of poor baryon contamination, which allows the plasma to reach high values of the Lorentz factor. Along the directions of higher density, the e^+e^--baryon loaded plasma reaches transparency at the right time, and with the right peak luminosity, which explains the features of the observed X-ray flares in the afterglow.

1.3. Inner Engine Phase: High-Energy ($\gtrsim$ GeV) Emission

The high-energy (GeV) emission observed in long GRBs follows a power-law, rest-frame luminosity: $L_{\mathrm{GeV}} = At^{-\alpha}$ (see, e.g., [18]). The observed luminosity of GRB 130427A by *Fermi*-LAT, in the 0.1−100 GeV energy band, obeys $A = (2.05 \pm 0.23) \times 10^{52}$ erg s^{-1}, and $\alpha = 1.2 \pm 0.04$ [18]. In the case of GRB 190114C, $A = (7.75 \pm 0.44) \times 10^{52}$ erg s^{-1} and $\alpha = 1.2 \pm 0.04$ [19, 20]. It is important to recall that GRB 190114C radiated photons of even TeV energies as they were detected by the MAGIC [21, 22].

In [18], we introduced the "*inner engine*" of such high-energy emission in BdHN I. It uses the rotational energy of the newborn BH as energy reservoir which is extracted via the presence of a surrounding magnetic field. The process is driven by the gravitomagnetic interaction of the Kerr BH with such a magnetic field. Associated with the *inner engine*, we introduced in [23] the concept of *blackholic quantum*. Both concepts are treated in Section 2.

Thus, a most important difference with respect to the traditional model is that, in the BdHN scenario, different emissions, at different energies, at different times, are explained by different physical processes occurring in the different BdHN components. A summary of all these processes and the corresponding observables can be found in [9]. In the following, I summarize recent results on the high-energy (GeV) emission component of BdN I, which originates close to the BH horizon, hence at distances of the order of 10^6 cm.

2. THE *INNER ENGINE* AND *BLACKHOLIC QUANTUM* CONCEPTS

The *inner engine* is composed of [18]: (1) the newborn Kerr BH originated in the NS gravitational collapse, (2) the surrounding magnetic field inherited from the collapsed NS, and (3) the very-low-density ionized plasma of the SN ejecta left around the BH site. From the gravitomagnetic interaction of the Kerr BH with the magnetic field it appears an electric field. For the mathematical modeling of this astrophysical situation, it has been used the Papapetrou−Wald solution [24, 25] of the Einstein−Maxwell equations of a Kerr BH immersed in an asymptotically uniform magnetic field. From it, we obtain the electromagnetic field driving the dynamics of the charged particles around the BH.

The radiation from the accelerated particles in these electromagnetic fields has been shown to be able to power the observed high-energy (GeV) emission in GRBs [18]. Obviously, the *inner engine* is non-stationary, the process of the BH energy extraction leads to decreasing mass and spin of the BH. The BH irreducible mass, M_{irr} [26, 27], remains constant in this process.

The energy that can be radiated off necessarily comes from the BH extractable energy:

$$E_{\mathrm{extr}} \equiv (M - M_{\mathrm{irr}})c^2, \qquad (1)$$

as given by the BH mass-energy formula [26−28]

$$M^2 = \frac{c^2 J^2}{4G^2 M_{\mathrm{irr}}^2} + M_{\mathrm{irr}}^2, \qquad (2)$$

where J, M, are, respectively, the angular momentum and the mass of the BH.

The *inner engine* is not separated from the BdHN model, on the contrary, it is naturally forms in BdHN I. The Kerr BH originates from the NS companion gravitational collapse and it is embedded in the magnetic field inherited from the NS from which it comes from [9]. The BH is formed at the center of a "*cavity*" of very-low density matter: numerical simulations for the case of GRB 190114C indicate that the density can be as low as 10^{-14} g cm^{-3} [29]. Clearly, the cavity forms in the accretion process and following collapse of the NS. I refer the reader to [9] for a discussion on the properties of the magnetic field around the newborn BH in a BdHN I.

The *inner engine* operates step-wise:

(1) The interaction of the magnetic field with the *gravitomagnetic* field of the Kerr BH induces an electric field, as it is given by the Papapetrou−Wald solution. For an aligned, parallel magnetic field to the BH spin axis, the electric field is nearly radial and inwardly directed within an angle $\theta_\pm \approx 60°$ from the BH spin axis.

(2) This induced electric field accelerates electrons outwardly. The number of electrons that can be accelerated is set by the available electric energy. For the latter, it has been coined the name "*blackholic quantum*" [23]. Indeed, once the underlying physical process generating the electric field and the BH are taken into consideration, the final equation for the available electric energy acquires the following quantum form [23]:

$$\mathscr{E} \approx \frac{1}{2} E_{\hat{r}}^2 r_+^3 = \hbar \Omega_{\text{eff}}, \quad \Omega_{\text{eff}} = 4 \left(\frac{m_{\text{Pl}}}{m_n} \right)^8 \left(\frac{B_0^2}{\rho_{\text{Pl}}} \right) \alpha \Omega_+, \quad (3)$$

where $\alpha = ca/(GM)$ is the dimensionless BH angular momentum parameter, with $a = J/M$ the angular momentum per unit mass, $\Omega_+ = c^2 \partial M / \partial J = c\alpha/(2r_+)$ is the BH angular velocity, m_n the neutron mass, and $\rho_{\text{Pl}} \equiv m_{\text{Pl}} c^2 / \lambda_{\text{Pl}}^3$, $\lambda_{\text{Pl}} = \hbar/(m_{\text{Pl}} c)$ and $m_{\text{Pl}} = \sqrt{\hbar c / G}$ are, respectively, the Planck energy-density, length, and mass.

(3) The maximum possible electron acceleration/energy is set by the electric potential energy difference from the horizon to infinity which, consistently with the concept of *blackholic quantum*, can be also written in quantum-form [23]:

$$\Delta \Phi = \frac{1}{c} ea B_0 = \hbar \omega_{\text{eff}}, \quad \omega_{\text{eff}} = \frac{4G}{c^4} \left(\frac{m_{\text{Pl}}}{m_n} \right)^4 e B_0 \Omega_+. \quad (4)$$

(4) The potential energy difference $\Delta \Phi$ given by Eq. (4) is attainable only for particles moving along the BH rotation axis, i.e., along the polar axis $\theta = 0$, where radiation losses are negligible [18].

(5) At different latitudes the accelerated electrons radiate via curvature and synchrotron mechanisms. For this radiation to be able to explain the observed luminosity, L_{GeV}, the radiation timescale, τ_{rad}, must fulfill [18]:

$$\tau_{\text{rad}} = \frac{\mathscr{E}}{L_{\text{GeV}}}, \quad (5)$$

which turns to be of the order of 10^{-14} s for $\mathscr{E} \sim 10^{37}$ erg and $L_{\text{GeV}} \sim 10^{51}$ erg s^{-1} (see quantitative example below).

(6) The above steps are repeated over and over providing there are sufficient particles around the BH to cover the energy of the *blackholic quantum*.

3. CONCLUDING REMARKS

I would like to conclude with a quantitative example for fiducial *inner engine* parameters $M = 3M_\odot$, $B_0 = 10^{11}$ G, and $\alpha = 0.5$. This choice is consistent with the one derived in [18] for GRB 130427A. For these parameters, the *blackholic quantum* of energy is $\mathscr{E} \approx 3.39 \times 10^{37}$ erg, and the maximum energy that an

accelerated electron can gain is $\epsilon_e = \Delta \Phi \approx 2.72 \times 10^{18}$ eV. The luminosity produced by the *inner engine* is set by the timescale at which the energy $\mathscr{E}$ is emitted. The radiation losses are dominated by synchrotron emission with the timescale [18]:

$$\tau_{\text{rad}} = \frac{\hbar}{m_e c^2} \frac{3}{\sin \chi} \left[\frac{e^2}{\hbar c} \left(\frac{B_0}{B_c} \right)^3 \alpha \right]^{-1/2}, \quad (6)$$

where m_e is the electron mass, χ is the electron pitch angle, and $B_c = m_e^2 c^3 / (e\hbar) \approx 4.41 \times 10^{13}$ G. For the appropriate values of α, B_0, and χ, this timescale is in agreement with the request set by Eq. (5), for photons emitted at GeV energies.

The emission of charged particles along the polar axis is also of great interest. Radiation losses are therein negligible since the electric and magnetic fields are parallel along that axis, allowing the particles to reach the maximum possible energy which can be as large as a few 10^{18} eV. The contribution of these accelerated particles to the ultrahigh-energy cosmic rays (UHECRs) is under current scrutiny and will be the subject of forthcoming works.

The above theory has been applied to the case of long GRBs. However, rotating BHs immersed in ambient magnetic fields are expected to be at the center of active galaxies, namely in active galactic nuclei (AGN). It becomes clear, as shown in [23], that all the above can be automatically extended to that case. For doing that, we must increase the BH mass by at least a factor 10^8, and the magnetic field must be decreased by nearly the same factor. Therefore, the application of this theory with all its consequences in the case of AGN, including the production of UHECRs, remains as well a most interesting topic to be deepened in forthcoming publications.

REFERENCES

1. J. A. Rueda and R. Ruffini, Astrophys. J. Lett. **758**, L7 (2012); arXiv: 1206.1684.
2. C. L. Fryer, F. G. Oliveira, J. A. Rueda, and R. Ruffini, Phys. Rev. Lett. **115**, 231102 (2015); arXiv: 1505.02809.
3. C. L. Fryer, J. A. Rueda, and R. Ruffini, Astrophys. J. Lett. **793**, L36 (2014); arXiv: 1409.1473.
4. L. Becerra, C. L. Ellinger, C. L. Fryer, J. A. Rueda, and R. Ruffini, Astrophys. J. **871,** 14 (2019); arXiv: 1803.04356.
5. F. Cipolletta, C. Cherubini, S. Filippi, J. A. Rueda, and R. Ruffini, Phys. Rev. D **92**, 023007 (2015); arXiv: 1506.05926.
6. L. Becerra, F. Cipolletta, C. L. Fryer, J. A. Rueda, and R. Ruffini, Astrophys. J. **812**, 100 (2015); arXiv: 1505.07580.
7. L. Becerra, C. L. Bianco, C. L. Fryer, J. A. Rueda, and R. Ruffini, Astrophys. J. **833**, 107 (2016); arXiv: 1606.02523.

8. Y. Wang, J. A. Rueda, R. Ruffini, L. Becerra, C. Bianco, L. Becerra, L. Li, and M. Karlica, Astrophys. J. **874**, 39 (2019); arXiv: 1811.05433.

9. J. A. Rueda, R. Ruffini, M. Karlica, R. Moradi, and Y. Wang, Astrophys. J. **893**, 148 (2020); arXiv: 1905.11339.

10. R. Ruffini, M. Karlica, N. Sahakyan, J. A. Rueda, Y. Wang, G. J. Mathews, C. L. Bianco, and M. Muccino, Astrophys. J. **869**, 101 (2018); arXiv: 1712.05000.

11. G. B. Pisani, R. Ruffini, Y. Aimuratov, C. L. Bianco, M. Kovacevic, R. Moradi, M. Muccino, A. V. Penacchioni, J. A. Rueda, S. Shakeri, et al., Astrophys. J. **833**, 159 (2016); arXiv: 1610.05619.

12. R. Ruffini, Y. Wang, Y. Aimuratov, U. Barres de Almeida, L. Becerra, C. L. Bianco, Y. C. Chen, M. Karlica, M. Kovacevic, L. Li, et al., Astrophys. J. **852**, 53 (2018); arXiv: 1704.03821.

13. R. Ruffini, L. Becerra, C. L. Bianco, Y. C. Chen, M. Karlica, M. Kovačević, J. D. Melon Fuksman, R. Moradi, M. Muccino, G. B. Pisani, et al., Astrophys. J. **869**, 151 (2018); arXiv: 1712.05001.

14. B. Zhang, *The Physics of Gamma-Ray Bursts* (Cambridge Univ. Press, Cambridge, 2018).

15. R. Ruffini, J. D. Salmonson, J. R. Wilson, and S.-S. Xue, Astron. Astrophys. Suppl. **138**, 511 (1999); astro-ph/9905021.

16. R. Ruffini, J. D. Salmonson, J. R. Wilson, and S.-S. Xue, Astron. Astrophys. **359**, 855 (2000); astro-ph/0004257.

17. C. L. Bianco, R. Ruffini, and S.-S. Xue, Astron. Astrophys. **368**, 377 (2001); astro-ph/0102060.

18. R. Ruffini, R. Moradi, J. A. Rueda, L. Becerra, C. L. Bianco, C. Cherubini, S. Filippi, Y. C. Chen, M. Karlica, N. Sahakyan, et al., Astrophys. J. **886**, 82 (2019).

19. L. Liang, R. Ruffini, J. A. Rueda, R. Moradi, Y. Wang, and S. S. Xue, arXiv: 1910.12615 (2019).

20. R. Moradi, J. A. Rueda, R. Ruffini, and Y. Wang, Astron. Astrophys. **649**, A75 (2021); arXiv: 1911.07552.

21. V. A. Acciari, S. Ansoldi, L. A. Antonelli, A. Arbet Engels, D. Baack, A. Babić, B. Banerjee, U. Barres de Almeida, J. A. Barrio, et al. (MAGIC Collab.), Nature (London, U.K.) **575**, 455 (2019).

22. V. A. Acciari, S. Ansoldi, L. A. Antonelli, A. A. Engels, D. Baack, A. Babić, B. Banerjee, U. Barres de Almeida, J. A. Barrio, et al. (MAGIC Collab.), Nature (London, U.K.) **575**, 459 (2019).

23. J. A. Rueda and R. Ruffini, Eur. Phys. J. C **80**, 300 (2020); arXiv: 1907.08066.

24. A. Papapetrou, Ann. Inst. Henri Poincare, Sect. A **4**, 83 (1966).

25. R. M. Wald, Phys. Rev. D **10**, 1680 (1974).

26. D. Christodoulou, Phys. Rev. Lett. **25**, 1596 (1970).

27. D. Christodoulou and R. Ruffini, Phys. Rev. D **4**, 3552 (1971).

28. S. W. Hawking, Phys. Rev. Lett. **26**, 1344 (1971).

29. R. Ruffini, J. D. Melon Fuksman, and G. V. Vereshchagin, Astrophys. J. **883**, 191 (2019).

World Scientific
www.worldscientific.com

A brief review of binary-driven hypernova*

Jorge A. Rueda[†,‡,§,¶,‖,‡‡], Remo Ruffini[‡,§,**,§§],
Rahim Moradi[†,§,††] and Yu Wang[†,§,††,¶¶]

[†]*ICRA and Dipartimento di Fisica,
Università di Roma "La Sapienza",
Piazzale Aldo Moro 5, I-00185 Roma, Italy*

[‡]*ICRANet, Piazza della Repubblica 10,
I-65122 Pescara, Italy*

[§]*ICRANet-Ferrara, Dipartimento
di Fisica e Scienze della Terra,
Università degli Studi di Ferrara,
Via Saragat 1, I–44122 Ferrara, Italy*

[¶]*Dipartimento di Fisica e Scienze della Terra,
Università degli Studi di Ferrara,
Via Saragat 1, I–44122 Ferrara, Italy*

[‖]*INAF, Istituto di Astrofisica e Planetologia Spaziali,
Via Fosso del Cavaliere 100, 00133 Rome, Italy*

[**]*INAF,Viale del Parco Mellini 84,
00136 Rome, Italy*

[††]*INAF – Osservatorio Astronomico d'Abruzzo,
Via M. Maggini snc, I-64100, Teramo, Italy*
[‡‡]*jorge.rueda@icra.it*
[§§]*ruffini@icra.it*
[¶¶]*yu.wang@inaf.it*

Binary-driven hypernova (BdHN) models long gamma-ray burst (GRB) as occurring in the binary systems involving a carbon–oxygen core (CO_{core}) and a companion neutron star (NS) or a black hole (BH). This model, first proposed in 2012, succeeds and improves upon the fireshell model and the induced gravitational collapse (IGC) paradigm. After nearly a decade of development, the BdHN model has reached a nearly complete structure, giving explanation to all the observables of long bursts into its theoretical framework, and has given a refined classification of long GRB according to the original properties of the progenitors. In this paper, we present a summary of the BdHN model and

*Based on talk presented at the Fifteenth Marcel Grossmann Meeting on General Relativity, Rome, July 2018.

the physical processes at work in each of the envisaged Episodes during its occurrence and lifetime, duly contextualized in the framework of GRB observations.

Keywords: MG15 proceedings; high-energy astrophysics; gamma-ray burst; binary-driven hypernova.

1. Introduction

GRB occur in binary systems of two main classes, binary-driven hypernovae (BdHNe) and binary mergers (BMs), observationally corresponding to long and short GRB. In BdHNe, the long GRB is generated by a type Ic SN explosion of an evolved star occurring in presence of a close-by NS or BH companion. This paper is dedicated to the BdHN systems. In BMs, the short GRB is generated from the merger of two compact stars, mostly from the NS-NS systems, and for low energetic short GRB, the binary white dwarfs could be the progenitors, see Refs. 1 and 2 and references therein.

The progenitor of a BdHN is a binary system composed of a carbon–oxygen core (CO_{core}) and a magnetized neutron star (NS) companion in a tight orbit (period of the order of a few minutes). In some cases, the companion might be a stellar-mass BH (see below). We focus here on the more frequent case of an NS companion. At the end of its thermonuclear evolution, the iron core of the pre-SN star (the CO_{core}) undergoes gravitational collapse, forming a new NS (hereafter νNS) at the SN centre. In the νNS formation process, a strong shockwave of kinetic energy $\sim 10^{51}$ erg expands outward and when it emerges (SN breakout) expels the CO_{core} outer layers as the SN ejecta. Part of the ejecta is subsequently accreted onto the companion NS and also onto the νNS by fallback. There are different possible fates for the NS due to the hypercritical accretion process.[3–5] For short binary periods ($\lesssim 5$ min), the NS reaches the critical mass for gravitational collapse and forms a BH. We call this subclass BdHN of type I (BdHN I). Thus, a BdHN I leads to a new binary composed of a νNS originated by the SN, and a BH originated by the collapse of the NS companion. For longer binary periods, the hypercritical accretion onto the NS is not sufficient to bring it to the critical mass, and a more massive NS (MNS) is formed. This subclass is named BdHN of type II (BdHN II). A BdHN II

Table 1. Summary of the BdHN subclasses. Values are taken from[36–38] with some updates. The "number" is the GRB with known redshift identified of each subclass till the end of 2016 (bracket indicates the lower limit). The "in-state" and "out-state" represent the progenitors and outcomes. We also present the peak energy $E_{p,i}$, the isotropic gamma-ray energy, E_{iso} of 1 keV to 10 MeV energy range, and the isotropic ultra-high energy $E_{iso,Gev}$ of 0.1–100 GeV energy range. This table is reproduced from.[15]

Class	Type	Number	In-state	Out-state	$E_{p,i}$ (MeV)	E_{iso} (erg)	$E_{iso,Gev}$ (erg)
Binary driven	I	329	CO_{core}-NS	νNS-BH	~ 0.2–2	$\sim 10^{52}$–10^{54}	$\gtrsim 10^{52}$
hypernova	II	(30)	CO_{core}-NS	νNS-NS	~ 0.01–0.2	$\sim 10^{50}$–10^{52}	—
(BdHN)	III	(19)	CO_{core}-NS	νNS-NS	~ 0.01	$\sim 10^{48}$–10^{50}	—
	IV	5	CO_{core}-BH	νNS-BH	$\gtrsim 2$	$> 10^{54}$	$\gtrsim 10^{53}$

leads to a new binary composed of a νNS and a massive NS. For very long binary
periods, the accretion energy is significantly lower than the above types, and only
the hypernova is observed. We call this subclass of sources of type III (BdHN III).
In addition, we have BdHN type IV (BdHN IV) for the progenitors of a CO_{core} and
a companion BH, and it leads to a new binary of NS and BH.

Having given the physical picture and the classifications of BdHNe, we will
present in the following sections the theory and associated observables of the
BdHNe. The BdHN starts from the final evolution of the binary stars, including the
SN and the accretion of the SN ejecta onto the companion star, to the formation
of BH and the particle acceleration mechanisms processing therein, then to the
generated relativistic outflow propagates and interacts with the SN ejecta and the
interstellar medium (ISM) giving rise to the emissions.

2. Binary Accretion

For the binary accretion and the forming of BH, we refer to the theoretical work of
Refs. 3–10 and the observational papers of Refs. 11–15.

Reference 10 has been the first paper to consider accretion of SN ejecta onto a
very close-by companion star of the binary period of minutes, and it gave the phys-
ical picture and the theoretical architectures of a simple one-dimensional model
that calculates the Bondi–Hoyle–Lyttleton hypercritical accretion rate. Reference 9
numerically simulated for the first time the BdHN hypercritical accretion. Follow-
ing the collapse of the CO_{core} of forming an SN, of which the ejecta falling onto the
Bondi–Hoyle surface of the companion with an accretion rate $> 10^{-2} M_\odot$ s^{-1}, these
one-dimensional numerical simulations give the density and the velocity profiles till
the NS reaches the critical mass of BH in tens or hundreds of seconds. Reference 4
went one step further performing two-dimensional numerical simulations and incor-
porating angular momentum transport from the SN ejecta to the NS of hypercritical
accretion. Those simulations show that under some conditions outflow is necessar-
ily formed because of the excess of angular momentum. Reference 8 demonstrated
that most BdHN with tight orbits (i.e. BdHN I) remain bound after the explosion
and accretion, even when a large fraction of mass (over half of the total binary
mass) is lost, and a large kick velocity is induced. Reference 3 performed the first
three-dimensional numerical simulations of the BdHNe process, which were further
upgraded and improved in Ref. 6 via smoothed-particle-hydrodynamics (SPH) sim-
ulations, see, e.g. in Fig. 1. A wide selection of initial parameters and several NS
equations of state have been there tested. It was there evaluated the outcome of
the NS and the νNS after the hypercritical accretion, namely, whether they reach
or not the mass-shedding limit, or gravitationally collapses to a BH, or become
a more massive and fast-spinning NS. The development of accretion theory and
simulations has led to clarifying the physical processes below the Bondi radius: the
dominant pressure is supported by the random pressure of the infalling matter, the
magnetic pressure is negligible. Such a pressure provides a very high temperature
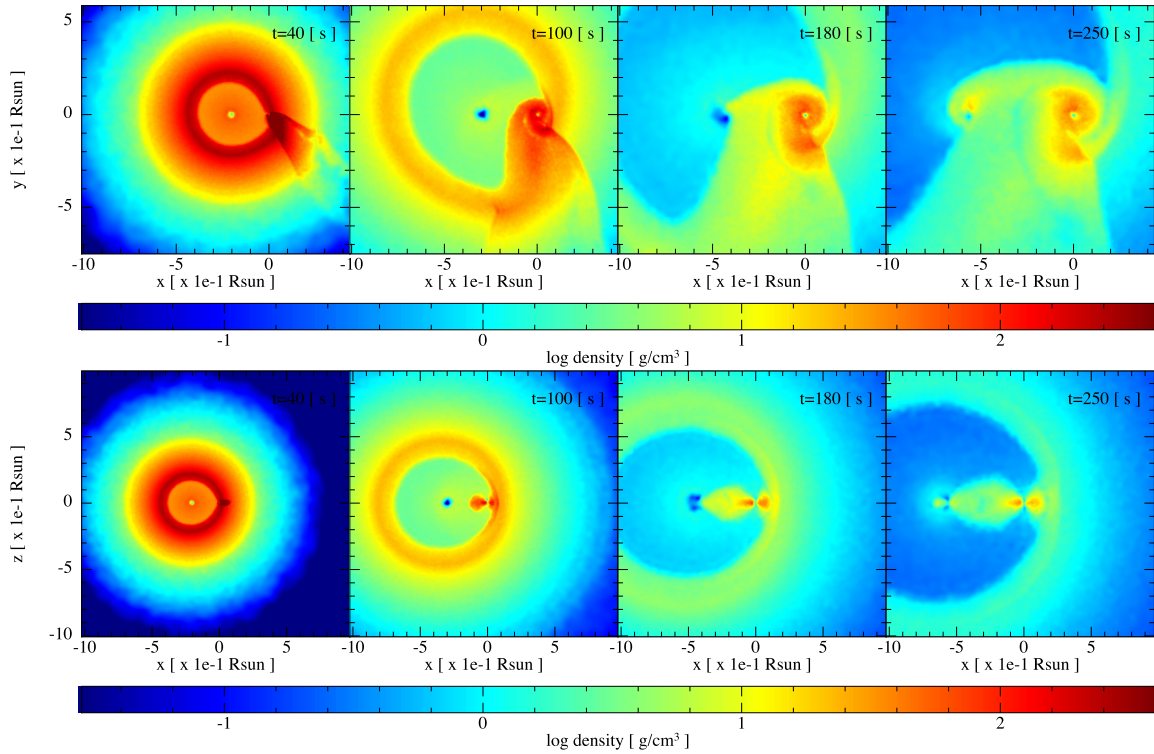
Fig. 1.   Snapshot of the SPH simulation of the binary accretion. The initial binary system consists of a $CO_{\rm rmcore}$ ($M_{\rm rmzams} = 25 M_\odot$) and an NS ($2M_\odot$) with an initial orbital period of about 5 min. The upper panel shows the mass density on the equatorial plane of the binary at different times of the simulation, while the lower panel corresponds to the plane orthogonal to the equator. At $t = 40\,$s, particles captured by NS can be seen forming a kind of tail behind them, then these particles form a circle around NS, and at $t = 100\,$s a thick disk is observed. At $t = 180\,$s, NS starts to accrete the surrounding matters. After about one initial orbital period, at $t = 250\,$s, a disk-like structure has formed around the two stars. This figure is cited from Ref. 6.

of 1–10 MeV, generating a large abundance of neutrinos and photons. The photons are trapped within the inflowing material, as its diffusion velocity is slower than the inflow velocity. The escape of neutrinos takes away most gravitational energy from the accreted flow, allowing the hypercritical accretion to continue for a given period of time. Reference 5 further investigated the neutrino flavour oscillations that occur during the propagation of neutrinos emitted from the surface of a neutron star. The final neutrino flow is composed of $\sim 55\%$ ($\sim 62\%$) of $\sim$ MeV electronic neutrinos for the normal (inverted) neutrino mass hierarchy. In addition, Ref. 7 present the numerical calculation and give useful fitting formulas for the location, binding energy and angular momentum of the last stable orbit of test particles around rotating NSs in full general relativity. The results of this work allow us to estimate in full general relativity the amount of energy and angular transferred by the accreting matter to an accreting, rotating NS.

Let us now dive into one specific example. GRB 180728A well demonstrates the binary accretion scenario by its two pulses in the prompt emission,[15] see Fig. 2. At a given time, the $CO_{\rm core}$ collapses, forms a νNS, and produces an SN explosion.
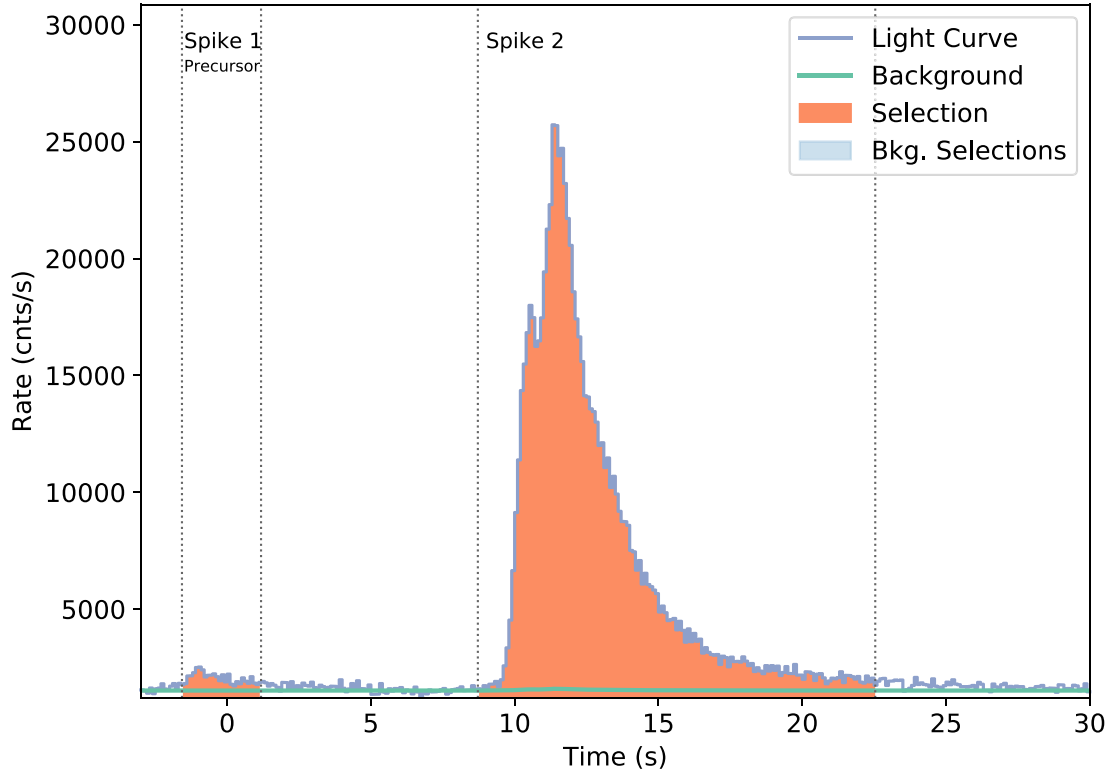
Fig. 2. Light curve of prompt emission of GRB 180728A observed by Fermi-GBM. It contains two pulses. The first pulse ranges from $-1.57\,$s to$1.18\,$s. The second pulse rises at $8.72\,$s, peaks at $11.50\,$s, and fades at $22.54\,$s. This figure is quoted from Ref. 15.

A powerful shockwave is generated and emerges from the SN ejecta. A typical SN shockwave carries $\sim 10^{51}$ erg of kinetic energy, which is partially converted into electromagnetic radiation with an efficiency of $\sim 10\%$. Thus, the energy of $\sim 10^{50}$ erg is consistent with the total energy of the first pulse, which lasts $\sim 2\,$s and contains $\sim 8 \times 10^{49}$ erg in keV-MeV photons. The second pulse rises at $\sim 10\,$s and subsides at $\sim 10\,$s, with a luminosity $\sim 2 \times 51$ erg s^{-1}. The distance of the binary separation can be estimated by the delay time between these two pulses, i.e. $\sim 10\,$s. Because of the SN ejecta front shell moves at $\sim 0.1c$, we estimate the distance of the binary separation to be about 3×10^{10} cm. By given the binary separation and some typical initial parameters, our simulation shows the total mass accreted is $\sim 10^{-2}\ M_\odot$, most of the mass is accreted in $\sim 10\,$s with an accretion rate of $\sim 10^{-3}\ M_\odot\,$s^{-1}. These results are consistent with the second pulse whose total energy is $\sim 10^{51}$ erg, considering an increase in efficiency of $\sim 10\%$, and the luminosity of $\sim 10^{50}$ erg s^{-1} in 10 s duration. The spectrum of the second pulse contains a thermal component which again hints the action of the accretion process. A time-resolved analysis of the thermal component suggests that a mildly relativistic source is expanding and radiating. This radiation is interpreted as an adiabatic expansion heat outflow from the accretion region. The Rayleigh–Taylor convective instability plays a role in the initial accretion phase, driving matter out of the accreting NS with a final velocity of the order of the speed of light. As the matter expands and cools, the temperature

evolution from the theory is again consistent with the observations. This kind of thermal emission of BdHN was first found in Refs. 11 and 12. GRB 180728A offers a good example of BdHN II, and for BdHN I, which has a tighter binary separation, see also the case of GRB 130427A as an example Refs. 13 and 15.

3. The Inner Engine and the GeV Emission

We have introduced the inner engine theory for the explanation of the GRB high-energy (GeV) emission observed in some BdHN I after the prompt emission phase. We here summarize the inner engine properties following the calculations presented in Refs. 16–19; see also Refs. 20–24.

Once the NS reaches the critical mass, a fast-rotating BH forms which contains sufficient rotational energy ($> 10^{54}$ erg) to power a GRB. Reference 19 proposed an efficient way to extract energy from the newborn, Kerr BH.

The inner engine is composed of this newborn rotating BH, surrounded by the magnetic field inherited from the collapsed NS,[25] and the ionized very low density of matter ($\sim 10^{-14} \, \mathrm{g \, cm^{-3}}$) of the SN ejecta.[26] For an aligned magnetic field with the
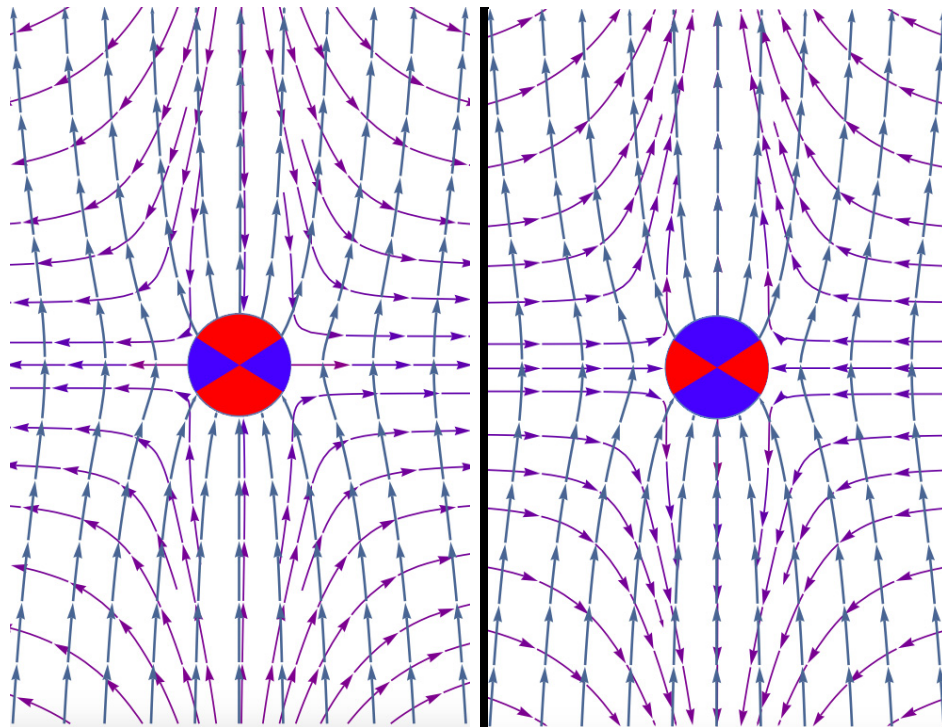
Fig. 3. (Color online) The electromagnetic field lines of Wald solution. The blue lines indicate the magnetic field lines, and the purple lines indicate the electric field lines. **Left:** The magnetic field is parallel to the spin of the Kerr BH, so parallel to the rotation axis. The electric field lines are inward for the polar angle $\theta <\sim \pi/3$, so the electrons are accelerated away from the BH. For $\theta > \pi/3$, the electric field lines are outward, so the protons are accelerated away from the BH. **Right:** The magnetic field is antiparallel to the rotational axis of the Kerr BH. The electric field lines are outward for the polar angle $\theta <\sim \pi/3$, so the protons will be accelerated away from the BH. The electric field lines are inward for $\theta > \pi/3$, so the electrons will be accelerated away from the BH. This figure is quoted from Ref. 19.
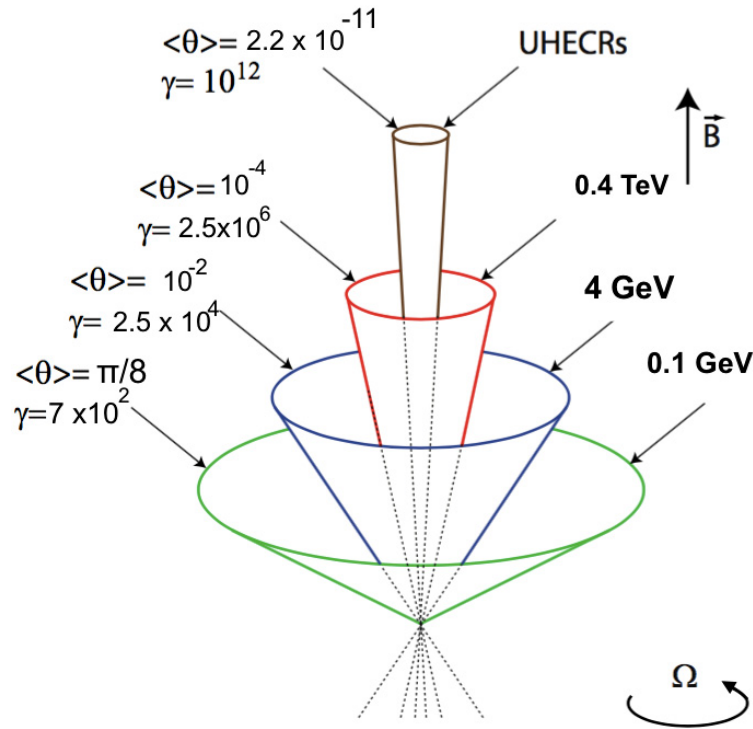
Fig. 4. The radiation emitted by the synchrotron emission of accelerated electrons in the different bands (0.1 GeV to 0.4 TeV) from different angles. In the narrow polar cone, the UHECRs are produced. Arrows indicate the BH rotational direction and the external magnetic field direction. This figure is quoted from Ref. 19.

angular momentum of the Kerr BH, an electric field is induced by gravitomagnetic interaction as described by the Wald solution[27]; see Fig. 3. The medium around the BH provides a sufficient amount of ionized particles that are accelerated to ultra-relativistic energies by the induced electric field, thereby emitting synchrotron and curvature radiation at expenses of the BH rotation energy.

The synchrotron radiation emitted from the accelerated charged particles has been calculated for different polar angles, see Fig. 4. Along the polar axis, the electric and magnetic fields are aligned, so there are no radiation losses and electrons can reach energies as large as $\sim 10^{18}$ eV, becoming a source of ultrahigh-energy cosmic rays (UHECRs). At larger angles, where electrons propagate across the magnetic lines producing synchrotron photons in the GeV energy domain.

The parameters of the inner engine, namely the BH mass and spin, and the surrounding magnetic field strength have been inferred from the following conditions: (1) the Kerr BH extractable energy accounts for the observed GeV radiation energetics in BdHN I, (2) the synchrotron radiation luminosity explains the observed GeV luminosity, and (3) the emitted GeV photons can indeed scape from the system without suffering from magnetic pair production. The case of GRB 130427A has been analyzed in Ref. 19 and GRB 190114C in Ref. 17. For instance, in GRB 190114C, the accelerated electrons radiate 1.8×10^{53} erg in GeV photons via the

synchrotron mechanism, and this procedure lasts for years following a power-law decay of light-curve with power-law index -1.2.

The mass and spin of the BHs came precisely what expected from the gravitational collapse of the fast rotating NS by accretion, and the strength of the magnetic field surrounding the BH turns out to be a few 10^{10} G. Therefore, the intensity of the induced accelerating electric field is undercritical in this BdHN I episode. The above magnetic field strength lower than expected to be inherited from the NS, and that could be the result from a screening process during the GRB prompt emission by electron-positron pairs; see Sec. 4 and Ref. 16 for details on this interesting physical process. In a recent comprehensive analysis of all the up-to-know identified BdHN I and the GeV emission observed in some of them, it has been inferred that the GeV emission must be emitted within an angle of $60°$ from the BH rotation axis; see Ref. 14 for details. This result is in agreement with the theoretical expectation; see Ref. 17.

Another discovery of this inner engine model is that this energetic emission from GRB is not continuous but proceeds in a repetitive sequence of discrete impulse events. Since the inner engine repeats the procedure of charge (BH spin and magnetic field induce electric field) and discharge (electric field accelerates the charged particle that escape from the system), the repetition time grows slowly along with the loss of BH rotational energy. Along the emission of these discrete events the magnetic field keeps constant, but the BH spin decreases after each event by a well-defined amount given by the concept of *blackholic quantum* described in Ref. 18. The blackholic quanta explaining the GeV emission are characterized by an energy $\Delta E_q \sim 10^{38}$ erg, emitted over a timescale $\tau_q \sim 10^{-15}$ s. The fraction of BH angular momentum extracted after each event is $\Delta J_q/J \sim 10^{-16}$, i.e. $\Delta J_q \sim 10^{33}$ g cm^2 s^{-1},[17] where J is the Kerr BH angular momentum. This result is indeed unexpected, and it seems to be a general property not only of GRB but also of the supermassive Kerr BHs in active galactic nuclei; see, e.g. Ref. 17 for the analysis of M87*.

4. The Prompt and the Afterglow Emission

This section gives the details of the propagation and the radiation of the relativistic outflow, based on the theoretical papers of Refs. 26–29 and the observational papers of Refs. 13, 15, 23, 30–33.

4.1. *The ultrarelativistic prompt emission phase*

Reference 22 investigated the ultrarelativistic prompt emission (UPE) phase of the BdHN I in which the electric field is overcritical, generating an optically thick electron–positron plasma by vacuum polarization. The plasma expands and self-accelerates to ultrarelativistic by converting its internal energy. Eventually, it reaches the transparency point and releases photons in the MeV energy domain. Reference 16 studied the channel of producing electron–positron pairs via high

energy photons interacting with magnetic fields, the motion of these pairs generates a current which induces another dominant magnetic field that screens the original one.

We now focus on the relativistic electron-position plasma that leads to the UPE phase. The hydrodynamics of this plasma have been formulated and simulated in the articles that established the *fireshell* model, and which have been adopted by the BdHN model. Reference 29 considered a Reissner–Nordstrom electromagnetic BH generates the electron–positron pairs. The system is expected to be thermalized to a plasma configuration due to the huge pair density and cross-section of the $e^+ + e^- \rightarrow \gamma + \gamma$ process. The evolution of plasma is governed by the hydrodynamic equations including, the conservation of energy–momentum, the conservation of the baryon number, the rate equation for electron–positron annihilation, and the equation of state. By integrating the equations numerically under the Reissner–Nordström metric and compared with the analytical analysis, the temperature drops as the internal energy are converted to kinetic energy. The plasma Lorentz factor is accelerated to several hundred, and the radiation releases when reaching the transparency radius. Reference 30 adopted a more realistic baryonic environment where the plasma propagates. Baryons are incorporated into the hydrodynamic equations. It is clear by solving the equations that the Lorentz factor of plasma keeps increasing in the beginning until engulfing the baryons, a drop of Lorentz factor occurs, then it goes up again and finally reaches saturation. Reference 31 systematically reviewed the creation and annihilation of the electron–positron pairs, thermalization, oscillation and their applications in GRB observations. The plasma penetrates the low-density region of the SN ejecta, see Refs. 3 and 32 for details, then propagates in the ISM, and radiates, accounting for the prompt emission. For the observations, the light-curve and spectrum of the prompt emission have been successfully fitted by solving the hydrodynamic equations plus a density profile of the circumburst medium. Reference 12 offers an example of GRB 090618, of which the system starts by $\sim 2.5 \times 10^{53}$ erg electron–position plasma. The plasma propagates in the circumburst density of 0.6 cm^{-3}, and collides with dense clouds of mass $\sim 10^{24}$ g at the distance of 10^{15} cm to 10^{16} cm. The plasma finally self-accelerates up to transparency reaching a Lorentz factor ~ 500, thereby producing the observed emission.

We refer the reader to the most recent analysis of the UPE phase in BdHN I presented in Ref. 22, where the physical origin of the UPE phase has been scrutinized taking as a proxy GRB 190114C. The UPE phase of GRB 190114C is observed in the rest-frame time interval $t_{\text{rf}} = 1.9–3.99$ s, by the *Fermi*-GBM in 10 keV–10 MeV energy band. Thanks to the high signal-to-noise ratio of *Fermi*-GBM data, a time-resolved spectral analysis of the UPE emission has evidenced a sequence of similar blackbody plus cut-off power-law spectra (BB + CPL), on ever decreasing time intervals. In it, the inner engine operates in an overcritical electric field regime. The electron–positron pair electromagnetic plasma in presence of a baryon load, *a PEMB pulse*, is therein originated from a vacuum polarization quantum process.

This initially optically thick plasma self-accelerates, giving rise at the transparency radius to the MeV radiation observed by *Fermi*-GBM. For the first time, it has been quantitatively shown how the inner engine, by extracting the rotational energy of the Kerr BH, produces a series of PEMB pulses. Therefore, a quantum vacuum polarization process sequences with decreasing time bins occurs. We compute the Lorentz factors, the baryon loads and the radii at transparency, as well as the value of the magnetic field in each sequence. It has been therefore found there is an underlying fundamental hierarchical structure, linking the quantum electrodynamics regime of the UPE to the classical electrodynamics regime of the GeV emission after the UPE. The PEMB pulses of the UPE have been found to be characterized by the emission of blackholic quanta of energy $\sim 10^{45}$ erg, over a timescale $\sim 10^{-9}$ s.

Let us summarize GRB 190114C. The initial magnetic field left over by the collapse of the accreting NS and rooted in the surrounding material is very strong ($\sim 10^{14}$ G), so it induces a sizeable electric field that surpasses the critical value near the horizon. The overcritical electric field transfers its energy to the electron–positron pairs by the vacuum polarization and is later emitted as the UPE phase of 2.5×10^{53} erg. The magnetic field becomes then screened to a few 10^{10} G in a few seconds,[16] consequently the size of the region above the BH horizon with overcritical electric field (the *dyadoregion*) shrinks, and its energy stored becomes insignificant. This marks the end of the UPE phase and after it, the above inner engine mechanism by which the induced electric field accelerate electrons within a few horizon radii becomes the main channel of taking away the BH rotation energy in form of GeV photons.[17]

4.2. *The afterglow emission phase*

Another part of the plasma hindered by the SN ejecta accelerates the SN outermost shell to mildly-relativistic velocities. The breakout of the plasma (shockwave) from the outermost shell at $\sim 10^2$ s radiate photons of keV energies which explain the observed X-ray flares.[32] The synchrotron emission in the outermost shell accounts for the early afterglow X-ray emission.[13] Rotational energy from the νNS rotational is injected into the SN ejecta, then radiated by the synchrotron emission, accounts for the plateau and late-time ($\sim 10^4$ s) afterglow.[15,25,28] The emission of the νNS as a pulsar becomes directly observable when the synchrotron luminosity fades off below the pulsar radiation luminosity. About ~ 15 days (rest-frame time) after the SN explosion that triggered the BdHN, the optical emission from the nickel decay in the SN ejecta reaches the maximum, there may appear a bump on the optical light-curve.[13,15,35]

References 32 and 34 statistically analyzed the X-ray flares observed in the early afterglow. A general pattern of thermal component of temperature ~ 1 keV was found, suggesting that the flare is generated from a mildly-relativistic expanding shell of Lorentz factor <4 at a distance $\sim 10^{12}$ cm. The observation of flares is consistent with our simulation of $\sim 10^{53}$ erg of plasma impacts on the SN ejecta of

a few solar masses, leading to the formation of a shock propagating inside the SN ejecta until reaching the outermost shell. The density profile and velocity profile of the accelerated ejecta are obtained. Precisely, the shockwave breaks out at $\sim 10^{12}$ cm and the outermost shell is accelerated to Lorentz factor ~ 2–5. This feature was also extensively studied for GRB 151027A.[33] Along with the conversion of the kinetic energy of the outermost shell into radiation, the early afterglow exhibits a steep decay behaviour. Then, the energy injected from the νNS dominates the afterglow, the light-curve shows a plateau followed by a normal power-law decay, shown in Fig. 5. Taking GRB 180728A as an example,[15] from the conversion of angular momentum, the $CO_{\rm core}$ collapses to a fast spinning NS of initial spin period ~ 3 ms. Such a newborn NS allows the presence of multipolar magnetic fields, with a quadrupole magnetic field $\sim 10^{15}$ G and a dipole field $\sim 10^{13}$ G, the spin-down of the νNS injects energy into the outflowing ejecta whose synchrotron emission fits the late-time X-ray afterglow. A comprehensive analysis of the afterglow of a few long GRB afterglows within the above synchrotron mechanism of the BdHN model has been presented in Ref. 25.

5. Conclusion

We can draw some general conclusions with the aid of the BdHN evolution shown in Fig. 6. (a) Our picture starts with a binary system consisting of two main-sequence stars of intermediate mass, say $15M_\odot$ and $12M_\odot$, respectively. (b) At a given time, the more massive star undergoes a core-collapse SN and forms an NS. (c) The
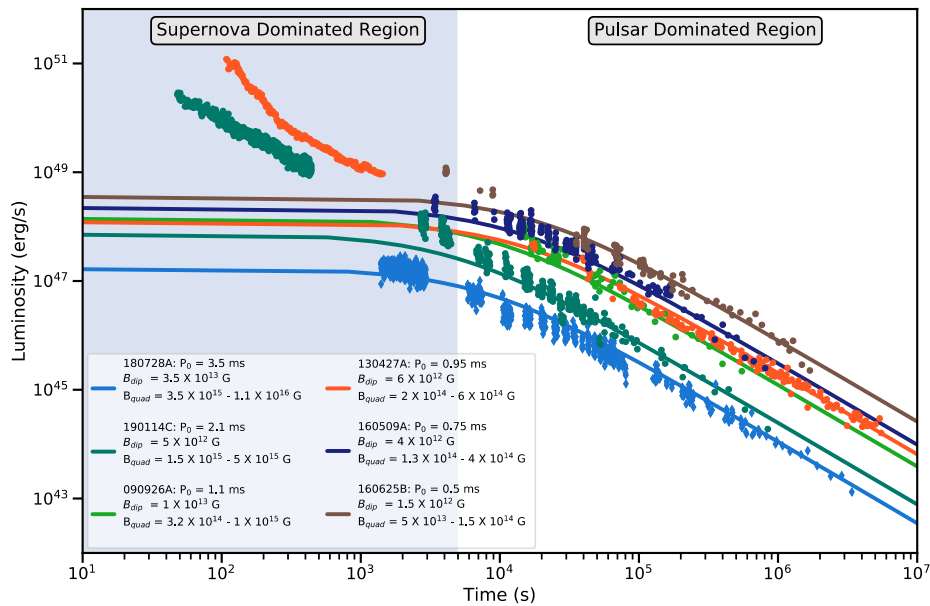
Fig. 5. (Color online) The brown, dark blue, orange, green, and bright blue dots correspond to the bolometric light curves of GRB 160625B, 160509A, 130427A, 190114C and 180728A, respectively. The thick lines are energy injection from the NS spin-down, which energizes the late-time afterglow (white background), while in the early time (blue background) the remaining kinetic energy of the outermost shell of the SN ejecta plays a dominant role. This figure is quoted from Ref. 25.

J. A. Rueda et al.

system enters the X-ray binary phase. (d) The system has overcome binary inter-
actions and common-envelope phases (not shown in the diagram) which have led
to the hydrogen and helium envelopes of the ordinary star to have been stripped
off, remaining a star which is rich in carbon and oxygen, referred to as CO_{core}.
At this stage, the system is a CO_{core}-NS binary, which is considered as the initial
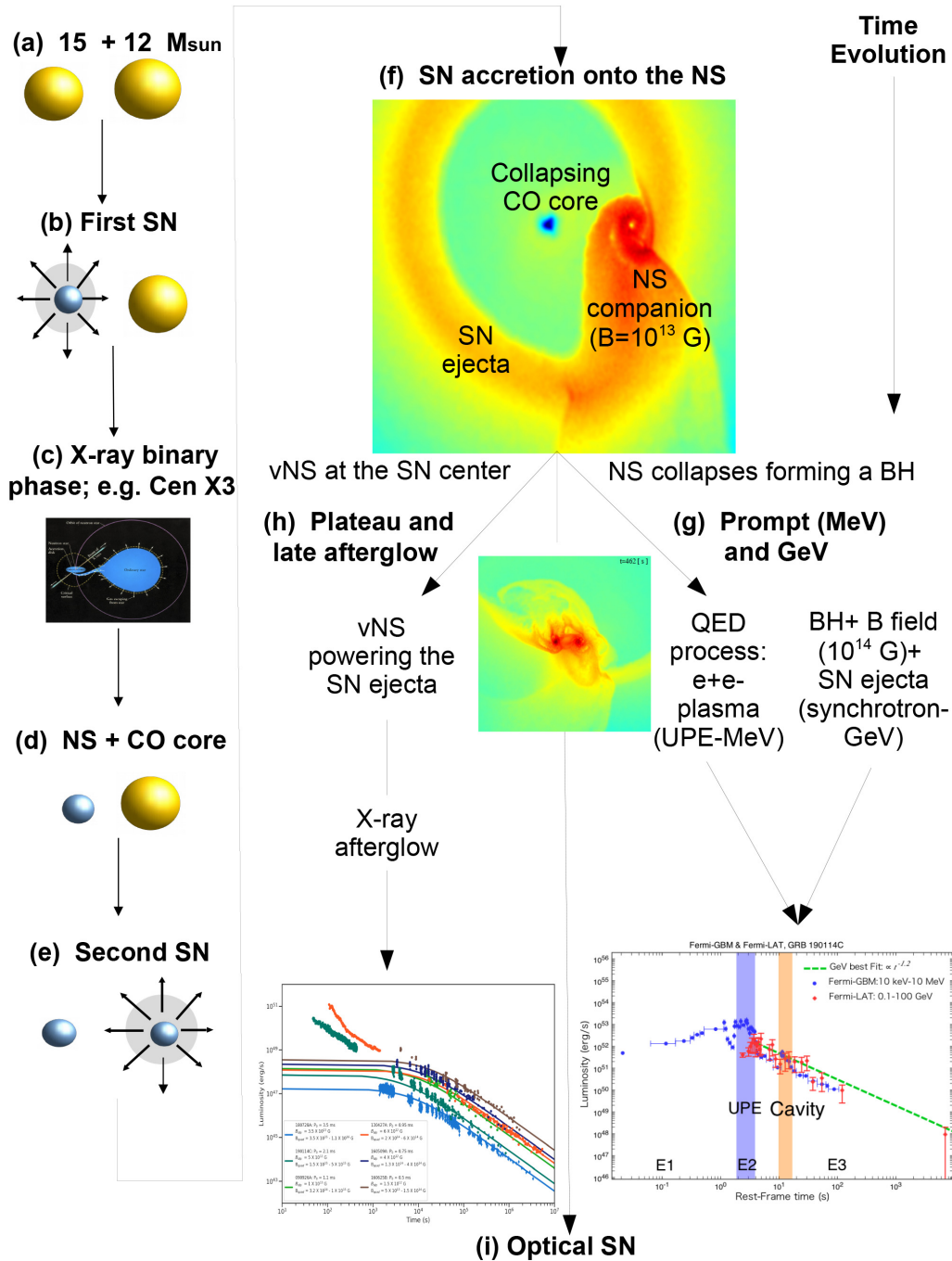
Fig. 6. Diagram of the evolutionary path of BdHN. Including binary evolution, SN explosion, NS
accretion, BH formation, GRB prompt and afterglow emissions and SN appearance. This figure
is quoted from Ref. 25. The content of this figure is explained in detail in the conclusion.

configuration of the BdHN model. (e) At this stage the orbit of the binary has shrink to a period of the order of a few minutes. The CO_{core} explodes into an SN (of type Ic in view of the absence of hydrogen and helium in its outermost layers), expelling several solar masses. These ejecta begin to expand, and a rapidly rotating νNS is left in the centre. (f) Depending on the initial NS mass and binary separation, the SN ejecta accretes onto the NS companion and onto the νNS, forming a massive NS (BdHN II) or BH (BdHN I; this example). At this stage, the system is a new NS and BH binary surrounded by the expanding ejecta. (g) The inner engine composed by the newborn BH, the surrounding magnetic field and ionized plasma is formed, and its activity explains the GRB UPE phase and the subsequent GeV emission. The magnetic field in the inner engine at BH formation is overcritical, so it induces (by gravitomagnetic interaction with the BH spin) an overcritical electric field, so the UPE phase operates in an overcritical regime. A quantum electrodynamical process of vacuum polarization takes place leading to an electron–positron pair plasma pulses (PEMB pulses) that expand to ultrarelativistic velocity reaching transparency with a Lorentz factor of up to hundreds, and emitting MeV photons. The magnetic field is then screened to undercritical values by currents produced by the motion of the electron and positrons, and the inner engine classical electrodynamical process of particle acceleration emitting GeV photons by synchrotron radiation becomes the relevant process of emission. (h) The spin-down energy of the νNS injects energy into the expanding SN ejecta emitting the observed X-ray afterglow by synchrotron radiation. (i) The appearance of the energy release owing to nickel decay in the SN ejecta is observed at optical wavelengths.

Acknowledgments

References

1. J. A. Rueda *et al.*,*J. Cosmol. Astropart. Phys.* **2018** (2018) 006.
2. J. A. Rueda *et al.*, *J. Cosmol. Astropart. Phys.* **2019** (2019) 044
3. L. Becerra, C. L. Bianco, C. L. Fryer, J. A. Rueda and R. Ruffini, *Astropart. Phys. J.* **833** (2016) 107.
4. L. Becerra, F. Cipolletta, C. L. Fryer, J. A. Rueda and R. Ruffini, *Astropart. Phys. J.* **812** (2015) 100.
5. L. Becerra *et al., Astropart. Phys. J.* **852** (2018) 120.
6. L. Becerra, C. L. Ellinger, C. L. Fryer, J. A. Rueda and R. Ruffini, *Astropart. Phys. J.* **871** (2019) 14.
7. F. Cipolletta, C. Cherubini, S. Filippi, J. A. Rueda and R. Ruffini, *Phys. Rev. D* **96** (2017) 024046.
8. C. L. Fryer, F. G. Oliveira J. A. Rueda and R. Ruffini, *Phys. Rev. Lett.* **115** (2015) 231102.
9. C. L. Fryer, J. A. Rueda and R. Ruffini, *Astrophys. J.* **793** (2014) L36.

10. J. A. Rueda and R. Ruffini, *Astrophys. J.* **758** (2012) L7.
11. L. Izzo, J. A. Rueda and R. Ruffini, *Astron. Astrophys.* **548** (2012) L5.
12. L. Izzo *et al.*, *Astron. Astrophys.* **543** (2012) 10.
13. R. Ruffini *et al.*, *Astrophys. J.* **798** (2015) 10.
14. R. Ruffini *et al.*, *Mon. Not. Roy. Astron. Soc.* **504** (2021) 5301.
15. Y. Wang *et al.*, *Astrophys. J.* **874** (2019) 39.
16. S. Campion, J. Rueda, R. Ruffini and S. Xue, *Phys. Lett. B* **820** (2021) 136562, https://www.sciencedirect.com/science/article/pii/S0370269321005025.
17. R. Moradi J. A. Rueda, R. Ruffini and Y. Wang, *Astron. Astrophys.* **649** (2021) 75.
18. R. Moradi, J. A. Rueda, R. Ruffini and Y. Wang, *Euro. Phys. J. C* **80** (2020) 300
19. R. Ruffini *et al.*, *Astrophys. J.* **886** (2019) 82.
20. L. Liang *et al.*, arXiv:1910.12615.
21. R. Moradi *et al.*, arXiv:2103.09158.
22. R. Moradi, Submitted to *Astrophys. J.* (2021).
23. R. Ruffini *et al.*, arXiv:1811.01839.
24. R. Ruffini *et al.*, arXiv:1904.04162.
25. J. A. Rueda, R. Ruffini, M. Karlica, R. Moradi and Y. Wang, *Astrophys. J.* **893** (2020) 148.
26. R. Ruffini, J. D. Melon Fuksman and G. V. Vereshchagin, *Astrophys. J.* **883** (2019) 191.
27. R. M. Wald, *Phys. Rev. D* **10** (1974) 1680.
28. R. Ruffini, *et al.*, *Astrophys. J.* **869** (2018) 101.
29. R. Ruffini, J. D. Salmonson, J. R. Wilson and S. S. Xue, *Astron. Astrophys.* **350** (1999) 334.
30. R. Ruffini, J. D. Salmonson J. R. Wilson and S.-S. Xue, *Astron. Astrophys.* **359** (2000) 855.
31. R. Ruffini, G. Vereshchagin and S. Xue, *phys. Rep.* **487** (2010) 1.
32. R. Ruffini, Y. Wang Y. Aimuratov *et al.*, *Astrophys. J.* **852** (2018) 53.
33. R. Ruffini *et al.*, *Astrophys. J.* **869** (2018) 151.
34. Y. Wang *et al.*, *Mem. Soc. Astron. Ital.* **89** (2018) 293.
35. Y. Wang *et al.*, *Astron. Rep.* **59** (2015) 667.
36. J. A. Rueda *et al.*, *Int. J. Mod. Phys. D* **26** (2017) 1730016.
37. R. Ruffini *et al.*, *Astrophys. J.* **832** (2016) 136.
38. R. Ruffini *et al.*, arXiv:1602.03545.